SMIP06

SMIP06 SEMINAR ON
UTILIZATION OF STRONG-MOTION DATA
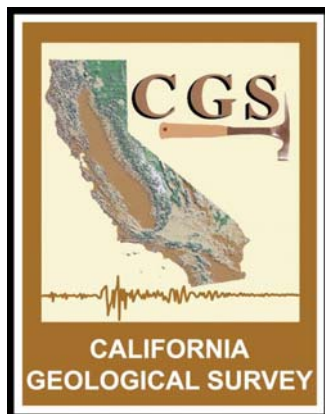
Oakland, California
September 28, 2006

PROCEEDINGS

Sponsored by

California Strong Motion Instrumentation Program
California Geological Survey
California Department of Conservation

Co-Sponsors

California Seismic Safety Commission
California Office of Emergency Services
California Department of Transportation
Office of Statewide Health Planning and Development

The California Strong Motion Instrumentation Program (CSMIP), a program within the California Geological Survey of the California Department of Conservation, records the strong shaking of the ground and structures during earthquakes for analysis and utilization by the engineering and seismology communities through a statewide network of strong motion instruments (www.conservation.ca.gov/CGS/smip). CSMIP is advised by the Strong Motion Instrumentation Advisory Committee (SMIAC), a committee of the California Seismic Safety Commission. Major program funding is provided by an assessment on construction costs for building permits issued by cities and counties in California, with additional funding from the California Office of Emergency Services, the California Department of Transportation, the Office of Statewide Health Planning and Development and the California Department of Water Resources.

In July 2001, the California Office of Emergency Services began funding for the California Integrated Seismic Network (CISN), a newly formed consortium of institutions engaged in statewide earthquake monitoring that grew out of TriNet, funded by FEMA, and includes CGS, USGS, Caltech and UC Berkeley. The goals are to record and rapidly communicate ground shaking information in California, and to analyze the data for the improvement of seismic codes and standards (www.cisn.org). CISN produces ShakeMaps of ground shaking, based on shaking recorded by stations in the network, within minutes following an earthquake. The ShakeMap identifies areas of greatest ground shaking for use by OES and other emergency response agencies in the event of a damaging earthquake.

The CISN Engineering Strong Motion Data Center (www.quake.ca.gov/cisn-edc) is operated by the CSMIP Program in cooperation with the National Strong-Motion Program (NSMP) of the U.S. Geological Survey. The Data Center provides strong-motion data rapidly after an earthquake in California. Users also have direct access to data from previous earthquakes and detailed information about the instrumented structures and sites.

DISCLAIMER

SMIP06

SMIP06 SEMINAR ON
UTILIZATION OF STRONG-MOTION DATA

Oakland, California
September 28, 2006

PROCEEDINGS

Edited by

Moh Huang

Sponsored by

California Strong Motion Instrumentation Program
California Geological Survey
California Department of Conservation

Co-Sponsors

California Seismic Safety Commission
California Office of Emergency Services
California Department of Transportation
Office of Statewide Health Planning and Development

PREFACE

The California Strong Motion Instrumentation Program (CSMIP) in the California Geological Survey of the California Department of Conservation established a Data Interpretation Project in 1989.   Each year CSMIP Program funds several data interpretation contracts for the analysis and utilization of strong-motion data. The primary objectives of the Data Interpretation Project are to further the understanding of strong ground shaking and the response of structures, and to increase the utilization of strong-motion data in improving post-earthquake response, seismic code provisions and design practices.

The M6.0 Parkfield earthquake of September 28, 2004 yielded the most extensive and dense set of strong-motion data in the near source region in California. This set of data was highlighted and presented in the SMIP05 Seminar that was held on May 10, 2005. In June 2005 CSMIP funded six projects to focus primarily on the analysis and interpretation of the extensive data set generated by the Parkfield earthquake.

As part of the Data Interpretation Project, CSMIP holds annual seminars to transfer recent research findings on strong-motion data to practicing seismic design professionals, earth scientists and post-earthquake response personnel. The purpose of the annual seminar is to provide information that will be useful immediately in seismic design practice and post-earthquake response, and in the longer term, useful in the improvement of seismic design codes and practices. The SMIP06 Seminar, held on the second anniversary of the 2004 Parkfield earthquake, is the seventeenth in this series of annual seminars.

The SMIP06 Seminar is divided into four sessions. Session I includes studies of fault rupture processes using the strong-motion data from the Parkfield earthquake. Session II will include engineering implications of the near-fault ground motions and improved ShakeMaps. Session III will include presentation on studies of the responses of two wood-frame buildings and one highway bridge using the data recorded from these structures during the Parkfield earthquake. In Session IV, the Turkey Flat Blind Prediction Experiment will be presented, including an overview of the experiment and of recorded data from the Parkfield earthquake and a review of the blind predictions.

The seminar includes presentations by investigators of six CMIP-funded projects. These six projects are scheduled to be completed by the end of 2006 and the final results will be published in their final reports.

Moh J. Huang, Ph.D., P.E.
Data Interpretation Project Manager

Members of the
Strong Motion Instrumentation Advisory Committee

Main Committee
Chris Poland, Chair, Degenkolb Engineers
Norman Abrahamson, Pacific Gas & Electric Company
Anil Chopra, UC Berkeley
Bruce Clark, Seismic Safety Commission, Leighton & Associates
C. Allin Cornell, Stanford University
Wilfred Iwan, California Institute of Technology
Jerve Jones, Jones & Jones
Michael Keever, Caltrans
Vern Persson, DWR Division of Safety of Dams (retired)
Maurice Power, Geomatrix Consultants
Daniel Shapiro, Seismic Safety Commission, SOHA Engineers
Edward Bortugno (ex-officio), Office of Emergency Services
Robert Anderson (ex-officio), Seismic Safety Commission

Ground Response Subcommittee
Maurice Power, Chair, Geomatrix Consultants
Abbas Abghari, Caltrans
Yousef Bozorgnia, PEER
Brian Chiou, Caltrans
Marshall Lew, MACTEC Engineering & Consulting
Geoffrey Martin, Univ. of Southern California
Ben Tsai, Pacific Gas & Electric Company

Buildings Subcommittee
Chris Poland, Chair, Degenkolb Engineers
Kenneth Honda, URS Corporation
Donald Jephcott, Structural Engineer
Jerve Jones, Jones & Jones
Bret Lizundia, Rutherford & Chekene
Eduardo Miranda, Stanford University
Farzad Naeim, John A. Martin & Associates
John Robb, Structural Engineer
Daniel Shapiro, SOHA Engineers
Chia-Ming Uang, UC San Diego

Lifelines Subcommittee
Vern Persson, Chair, DWR Division of Safety of Dams (retired)
Martin Eskijian, California State Lands Commission
David Gutierrez, DWR Division of Safety of Dams
Michael Keever, Caltrans
LeVal Lund, Civil Engineer
Edward Matsuda, BART
Stuart Nishenko, Pacific Gas & Electric Company

Data Utilization Subcommittee
Wilfred Iwan, Chair, California Institute of Technology
Representatives from each Subcommittee

TABLE OF CONTENTS

<div style="border: 3px solid black; background-color: #d9d9d9; text-align: center;">

SMIP06 SEMINAR ON
UTILIZATION OF STRONG-MOTION DATA

</div>

Harris State Building, 1515 Clay Street, Oakland, California
September 28, 2006

FINAL PROGRAM

8:00 am   **REGISTRATION**

9:15 am   **WELCOMING REMARKS**
   Bruce Clark, Commissioner, Seismic Safety Commission
   Anthony Shakal, Program Manager, Strong Motion Instrumentation Program, California
      Geological Survey

9:25 am   **INTRODUCTION**
   Moh Huang, Strong Motion Instrumentation Program, California Geological Survey

---

<div style="background-color: #ccffcc; text-align: center;">

S E S S I O N   I

</div>

Moderator: *Maurice Power*, Geomatrix Consultants, Inc., SMIAC

9:30 am   **Rupture Process of the 2004 Parkfield Earthquake Utilizing Near-Fault Seismic**
   Records and Implications for ShakeMap
   Douglas Dreger and *Ahyi Kim*, University of California, Berkeley

9:55 am   **Implication of the Rupture Process and Site Effects in the Spatial Distribution**
   and Amplitude of the Near-Fault Ground Motion from the 2004 Parkfield
   Earthquake
   Arben Pitarka, *Nancy Collins*, *Hong-Kie Thio*, *Robert Graves* and *Paul Somerville*, URS
   Corporation

10:20 am   **Questions and Answers for Session I**

10:30 am   Break

<div style="background-color: #ccffcc; text-align: center;">

S E S S I O N   II

</div>

Moderator: *Anil Chopra*, U.C. Berkeley, SMIAC

10:50 am   **Instability Inducing Potential of Near-Fault Ground Motions**
   Dennis Bernal, *Arash Nasseri* and *Yalcin Bulut*, Northeastern University

S E S S I O N III

Moderator: *Vern Persson*, SMIAC

S E S S I O N IV

Moderator: *Wilfred Iwan*, Caltech, SMIAC

RUPTURE PROCESS OF THE 2004 PARKFIELD EARTHQUAKE UTILIZING NEAR-FAULT SEISMIC RECORDS AND IMPLICATIONS FOR SHAKEMAP

Douglas Dreger and Ahyi Kim

Berkeley Seismology Laboratory
University of California Berkeley

Abstract

The September 28, 2004 Parkfield earthquake, arguably the best recorded earthquake ever, allows for detailed investigation of finite-source models, and their resolution. We have developed models using GPS and InSAR geodetic data, and CSMIP and USGS strong motion seismic waveforms independently and jointly. In order to focus on better resolved long wavelength features the seismic data was lowpass filtered at 0.5 Hz. We have investigated the sensitivity of the finite-source models due to station coverage, weighting and smoothing parameters, and seismic velocity structure. The resulting model is consistent with preliminary results using regional broadband and strong motion waveform data (e.g. Langbein et al., 2005; Dreger et al., 2005) as well as with higher frequency seismic waveform only inversions (e.g. Custódio et al., 2005; Liu et al., 2006). The scalar seismic moment was found to be 1.28e25 dyne cm (Mw6.0), the overall rupture length 25 km, the peak slip 58 cm, and the average rupture velocity 2.6 km/s. The rupture was predominantly unilateral to the NW with a small component to the SE. The obtained slip model was used to simulate 3D wave propagation taking into account the velocity contrast across the San Andreas Fault, and a narrow low-velocity fault zone. The results of this analysis suggest observed waveform complexity and amplitudes at stations located in the fault zone could be due to fault zone guided waves.

Introduction

On September 28, 2004 the long awaited Parkfield mainshock occurred 16 years past its expected due date, nearly a full cycle past the regular recurrence interval of 22 years. Fortunately the investment in geophysical monitoring of the region paid off as most systems were kept running. This foresight and persistence by the network operators has lead to the best near-fault geophysical data set of a moderate earthquake to date.

In this study we have developed kinematic finite-source models for the event using the local strong motion waveform data provided by CSMIP and NSMP, as well as coseismic GPS and InSAR deformation data. Independent models for each data set, as well as our preferred joint inversion model are presented.

In Dreger et al. (2005) the automated finite-source inversion method developed by Dreger and Kaverina (2000) was applied to regional broadband waveform data from CISN stations. The kinematic model in that study showed a rupture which nucleated near Gold Hill, and propagated 25 km unilaterally to the NW stopping at Middle Mountain, the opposite of the

1934 and 1966 Parkfield earthquakes. The kinematic model was used to simulate near-fault strong ground motions, and the largest motions were found to be NW of the epicenter. The updated CISN ShakeMap on the other hand shows a bimodal distribution in peak ground motions, where large amplitude motions are also located SE of the epicenter along the Cholame array (CH stations, Figure 1). Therefore an objective of our study is to understand the reason for the bimodal ground motion distribution to ascertain whether it is due to unaccounted for source process or possibly 3D wave propagation in the fault zone.

Data

Strong Motion Waveforms

We used horizontal records from 29 strong motion sites (Figure 1), which provided excellent azimuthal coverage of the ruptured fault. Some sites close to the fault were excluded because they exhibited waveform complexity indicative of fault zone guided wave propagation, which could not be modeled with the assumed 1D velocity model Green's functions.
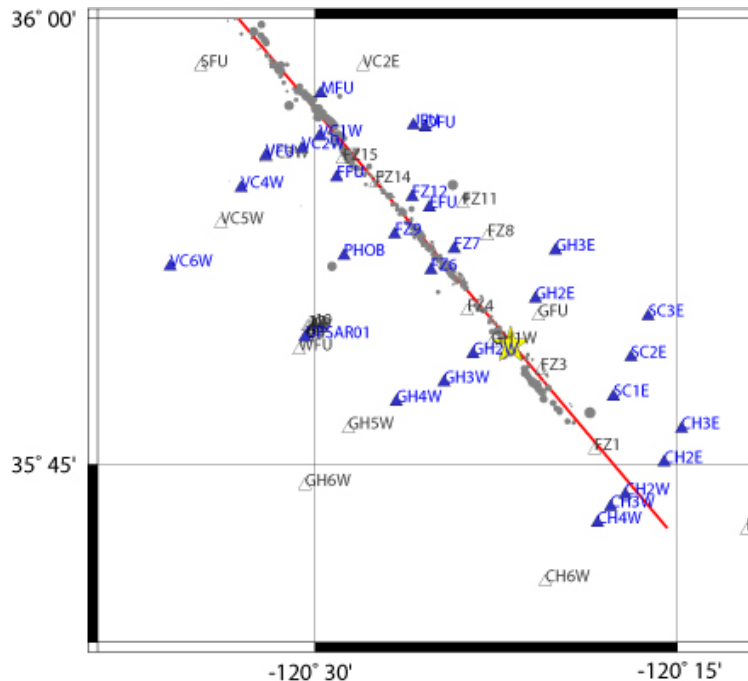
Figure 1. CSMIP and USGS strong motion stations. The filled triangles show the sites used to determine the kinematic source model. The star shows the epicenter and the gray circles background seismicity and aftershocks.

For example, Figure 2 compares north-south records from the CSMIP Gold Hill array (GH1W, GH2W and GH3W, Figure 1). It is evident that the GH1W record has an extended duration compared to the other two stations only a few km to the west. Since GH1W is close to the epicenter, and the faulting mechanism is a nearly vertical dipping, right-lateral strike-slip fault, the motions theoretically should be very small due to the radiation pattern, but as Figure 2 shows they are nearly the same amplitude as the more distant stations. The amplitude and extended duration is likely due to fault zone guided or trapped waves propagating within the low

velocity core of the San Andreas Fault (e.g. Korneev et al., 2003). In this report we will demonstrate with 3D finite-difference modeling that this is likely the case. In any event, for the inversion, it was necessary to exclude the waveforms at sites that exhibited this complexity because the method we employed could not account for guided wave propagation.
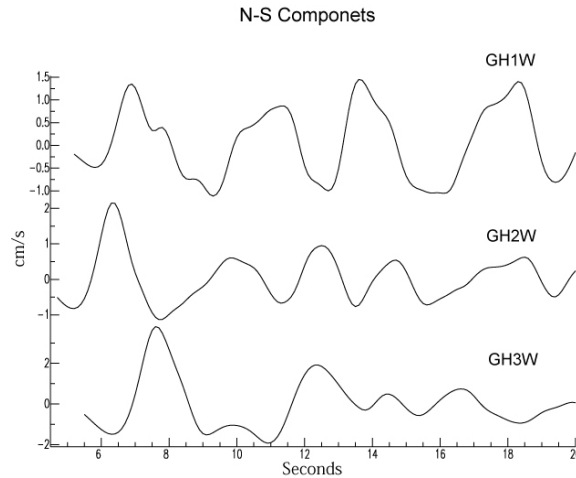
Figure 2. Comparison of N-S component velocity waveforms from stations of the Gold Hill array. GH1W is the site closest to the fault within the low velocity fault core (e.g. Korneev et al., 2000; 2003). This record has several cycles of large amplitude arrivals (actually extending beyond what is plotted). The other two stations located to the west of the fault outside the gouge region have simpler waveforms characterized by a primary initial S-wave pulse.

The waveforms were processed by integrating recorded acceleration to velocity, and lowpass filtering with an acausal Butterworth filter with a corner frequency of 0.5 Hz. The records were then resampled to 10 samples per second. The filtering was done in order to focus on getting a better resolved longer wavelength source process, and because the 1D velocity structures likely could not model high frequency wave propagation.

GPS Deformation

GPS deformation data was obtained from 1 second continuous GPS observations at 13 sites. To obtain the coseismic deformation the 1 second time series were averaged 10 minutes before the event and 2 to 10 minutes afterward. Because of the high sample rate data it is unlikely that much postseismic deformation signal is present in the GPS data set.

InSAR Deformation

The coseismic deformation from ENVISAT InSAR data was obtained from a pre event scene on 7/3/2003 and post event scene on 9/30/2004. We used the interferogram processed by Johanson et al. (2006) in which non-tectonic effects, especially atmospheric changes, and groundwater induced vertical motion were removed. Because the post-event scene is two days after the event there could be some postseismic signal present in the data.

Development of a Kinematic Rupture Model

Method

We use the method of Hartzell and Heaton (1983), which is the same method we used in developing our automated finite-source procedure (Dreger and Kaverina, 2000; Dreger et al., 2005). The multiple time window parameterization of this method allows for some variability in rupture velocity as well as variability in the dislocation rise time, and has the advantage of being a linear inversion for the slip distribution.

The fault model is parameterized as a 44 km length by 18 km width fault. The strike is 140 degrees and the dip is 89. The fault orientation was obtained by fitting the single fault plane to the aftershock distribution (Figure 1). The fault extends 29 km NW of the hypocenter and 15 km to the SE. The overall model dimension exceeds what is necessary to fit the data. The fault model is discretized with 792 1 km by 1 km subfaults.

We initially tested variable rake models, but found that the results were strike-slip, and therefore in subsequent modeling we assumed a constant rake of 180 degrees. Focal mechanisms reported in Thurber et al. (2006) for background seismicity and aftershocks support this assumption.

We allowed 12 time windows each with a dislocation rise time of 0.6 seconds with each subsequent time window offset by 0.3 seconds giving a total rise time range from 0.6 to 3.6 seconds. All 12 time windows yields 9504 free parameters though our subsequent sensitivity modeling revealed that most of the slip was contained in the first 6 time windows.

To stabilize the inversion we employ slip positivity using the non-negative least squares routine (Lawson. and Hanson 1974), spatial smoothing and moment minimization constraints. We examine the smoothing weight and data weighting parameter space to find the optimum solution with a trial and error approach.

Because we lowpass filtered the seismic waveform data at 0.5 Hz it is not necessary to use site amplification terms. Liu et al. (2006) used records from the Coalinga earthquake recorded at Parkfield stations to determine relative site amplification terms as a function of frequency. Some stations show broadband amplification, but most others show a frequency dependent site response. Generally their amplification factors for f<0.5 were relatively small, and the sites with the largest factors tended to be the fault zone sites we eliminated due to guided wave signatures in the waveforms.

Because the velocity differs across the fault (Michaels and Eberhart-Phillips, 1991; Michelini and McEvilly, 1991; Thurber et al., 2006) we performed inversions using both a single velocity structure as well as a two velocity model case. Our preferred inversion utilizes two 1D velocity models to represent the contrast across the fault. The velocity models after Liu et al., (2006) are shown in Table 2.

The use of simplified velocity structure can lead to artificial absolute time shifts between Green's functions and the observed records. Therefore we required that the observed first arriving S wave at each site be aligned with the S-wave arrival from the Green's function for the hypocenter following the approach of Wald et al. (1991). Table 1 lists the stations and the applied time shifts.

Independent Inversions

We performed inversions of each data set independently and the results of these inversions are compared in Figure 3. The results show some common features, namely that the rupture propagated from the hypocenter to the NW, and that the highest slip was located 10-20km northwest of the hypocenter. In general these results are consistent with those reported in Langbein et al. (2005) and Dreger et al. (2005), which utilized regional distance stations. However in detail the three models differ.

Seismic Waveform Inversion

The kinematic model obtained with only seismic waveform data (Figure 3a) shows some slip located close to the hypocenter; however the largest asperity is 10 to 20 km to the NW. The slip is generally found to be located below a depth of 5 km, and is shallower than 15 km. Slip shallower than 5 km in the model is not well constrained. This model also has some low levels of slip to the south of the hypocenter that is needed to fit the waveforms from the Cholame array. Thus, there is some indication of a slight bilateral rupture; however the rupture was principally unilateral to the NW. The best fit variance reduction for the seismic waveform data is 69.5%. The scalar seismic moment was found to be 1.35e+25 dyne cm (Mw6.05). Finally, we note that these results are consistent with what we obtained previously (e.g. Langbein et al., 2005; Dreger et al., 2005) with the regional seismic waveforms and near-fault GPS data.

Geodetic Inversion

The inversion results for the geodetic data also show shallow slip extending about 25 km NW of hypocenter. The GPS inversion (Figure 3b) tends to have slip concentrated in two asperities, one at the hypocenter and the other 10 to 20 km to the NW. The InSAR result (Figure 3c) on the other hand tends to have slip in a continuous band, though it is peaked at the two ends. Both inversions are consistent with the seismic result in terms of the overall rupture dimension, and the fact that the slip is shallower than 15 km. The two geodetic results also seem to have more significant SE-ward slip, which extends as much as 10 km to the SE. The best fit variance reductions for the two independent inversions were found to be 97.0% (GPS) and 74.8% (InSAR).

The relatively higher slip in the InSAR only model might be due to included postseismic deformation since the post-event scene is 2-days after the mainshock. The scalar seismic moment for the GPS inversion was found to be 1.25e+25 dyne cm (Mw6.03), and was 1.73e+25 (Mw6.12) for the InSAR inversion. The GPS scalar moment is about 7% less than the seismic model indicating that our coseismic estimates of GPS deformation are reasonable. The InSAR

scalar moment is about 28% higher than the seismic estimate indicating that some postseismic deformation may be included.
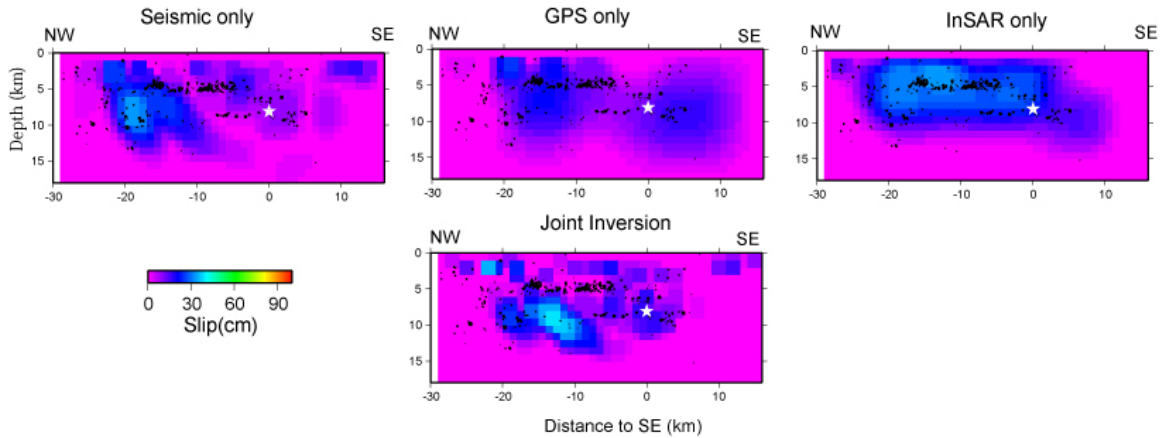

Figure 3. a) Seismic only inversion. b) GPS only inversion. c) InSAR only inversion. d) Joint inversion of all three data sets. The hypocenter is marked by the white star.

Joint Inversion

The preferred model, in which the three data sets were inverted simultaneously, is presented in Figure 3d. This model is consistent with our preliminary model with local and regional seismic and GPS data (Dreger et al., 2005) in that there are two primary asperities, one near the hypocenter, and the other 10-20km northwest of the hypocenter.

The slip in this model is also complementary (or anti-correlated) with the postseismic slip determined by Johanson et al. (2006), and is also complementary to the distribution of aftershocks. Most notable is the lack of slip in the region of the seismicity streak at 5 km depth. The slip shallower than 2 km depth is not well constrained. The scalar seismic moment in this model is 1.28e25 dyne-cm (Mw6.0) with a peak slip of 58cm.

Since different data sets with different numbers of observations are used in the joint inversion it is necessary to weight them relative to each other. This was done by generating a tradeoff plot in which the fit to the data was compared to the relative weight of each data set. In Figure 4a we show the weight of the InSAR+GPS data relative to the seismic waveform data. An inflection in the curves occurs at weight of 3000, where a larger weight would better fit the geodetic data at the detriment of the fit to the seismic waveforms. With a weight of 3000 the fit of all three data sets remains close to their respective best fits, and therefore this value is considered reasonable. Next, we assume the obtained data weight, and then find the smoothing weight again using a tradeoff curve (Figure 4b). Here we find the largest value of smoothing that still retains an acceptable level of fit to all data sets. Again we look for an inflection where there is a discernable change in the fit to the data. An optimal smoothing weight of 0.002 was found from the analysis.

The variance reductions for each data set in the joint inversion were less than obtained from each of the independent inversions as expected, however they remained high; 66.9% (seismic), 90.1% (GPS) and 54.7% (InSAR). The seismic waveform and GPS fits are very close

to their respective maxima, however the InSAR fit dropped by 20%. The joint inversion scalar moment is close to what was obtained in the seismic and GPS inversions, but substantially less than the InSAR result. Thus, it appears that the inversion is fitting the coseismic component of the InSAR observations leaving unmodeled the postseismic deformation.

a)

b)
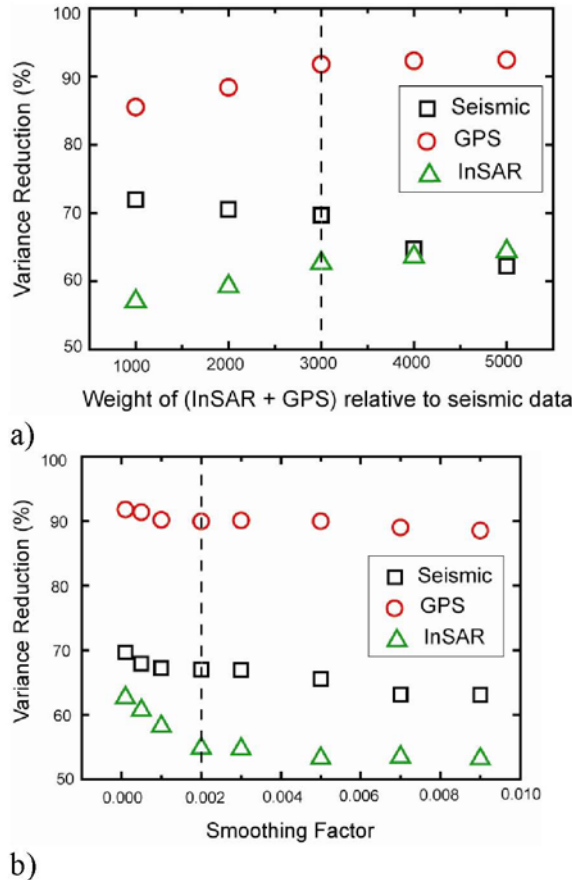
Figure 4. a) Weight of the InSAR+GPS data relative to the seismic waveform data vs. model fit. b) For the optimal weight the smoothing factor vs. model fit. In each case the preferred value is marked by the dashed line, which was chosen based on the point where there is a change in the slope of each curve.

We performed a series of inversions with seismic+GPS and seismic+GPS+InSAR to evaluate the effect of the InSAR data, and found that it provided additional constraint without dominating the inversion. Because the InSAR data provides substantially better coverage than either the GPS or the seismic sites we prefer to include it in the joint inversion.

The fit to the seismic waveforms as shown in Figure 5 is quite good. We included the waveforms from the Cholame array to investigate the possibility of SE-ward rupture. We can fit some of those stations (CH2E, CH3E, CH4W) very well; however there are problems at other stations located closer to the fault. For example we under predict CH2W. The CH2W waveforms are more complex with several additional cycles of motion. Although this is a fault zone signature, we left this station in the inversion to specifically test the hypothesis of SE-ward rupture. The small amount of SE-ward slip in the preferred model is needed to explain the Cholame records in general, but it is not sufficient to describe the high amplitudes and waveform

complexity. The site factor determined by Liu et al. (2006) for this station is only 1.12 so not using site factors do not appear to be the cause of the misfit.
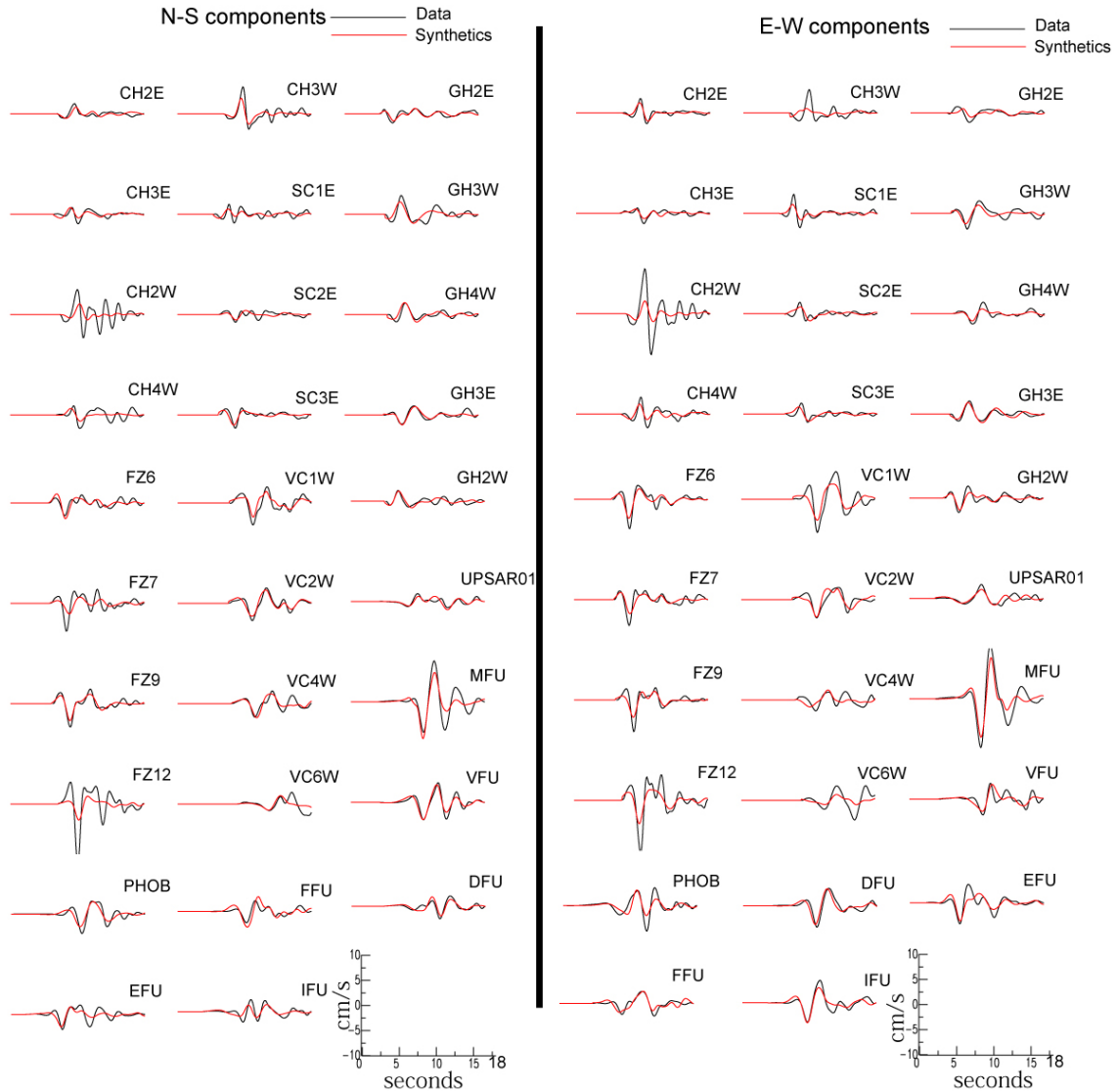
Figure 5. Comparison of data (black) and synthetics (red) for the joint inversion. The left panel shows the NS component and the right panel the EW component. The amplitude scale is in cm/s and the time scale shows seconds.

Although the seismic only inversion fits the Cholame stations better they are still fit worse than other stations used in the inversion. Another problematic station is FZ12, which is located close to the main trace of the SAF (Figure 1). For this station we only fit half of the amplitude. Interestingly we fit the nearby EFU records very well. In the next section we present 3D simulations that take into account the velocity contrast across the fault as well as a low velocity fault zone that produces the observed waveform complexity and extended duration at sites located within the fault zone. Based on that analysis we believe that the elevated amplitudes

at the near-fault stations of the Cholame array and also the FZ1 site (not used in the inversion due to fault zone waveform complexity) is due to fault zone guided wave effects.

The fit to the geodetic data is also very good. Figure 6 shows the fit to the GPS data, and Figure 7 shows the fit to the InSAR data. This plot also shows that the assumed fault geometry based on fitting the plane to the seismicity is consistent with the differential deformation imaged by InSAR.
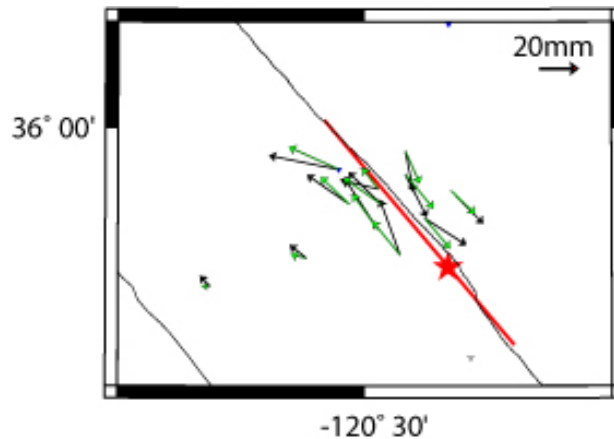
Figure 6. Comparison of observed (black) and simulated (green) GPS deformation. The hypocenter is shown by the star and surface projection of the fault plane by the red line.
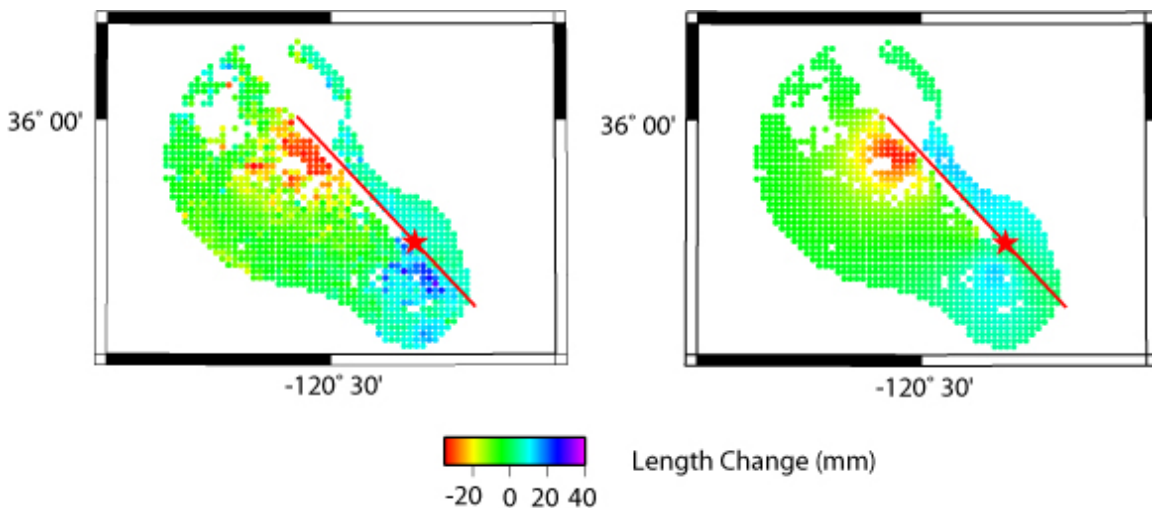
Figure 7. Observed line length change (left) is compared to predictions (right) for the preferred finite-source model. This image is for an ascending orbit. The data was edited by Johanson et al. (2006) to remove decorrelated pixels due to atmospheric disturbance.

The best average rupture velocity was found to be 2.6km/s (Figure 8). We did examine the possibility of super-shear rupture, but did not find a significant improvement in fit. Fletcher and Spudich (2006) investigated the data from the UPSAR array where they were able to determine the slowness and azimuth of the incident wavefield and were able to map the rupture

propagation. They concluded that the rupture was sub-shear. The results of Liu et al. (2006) show a highly variable rupture velocity that is on average 2.6 km/s with a maximum of 3.3 km/s.
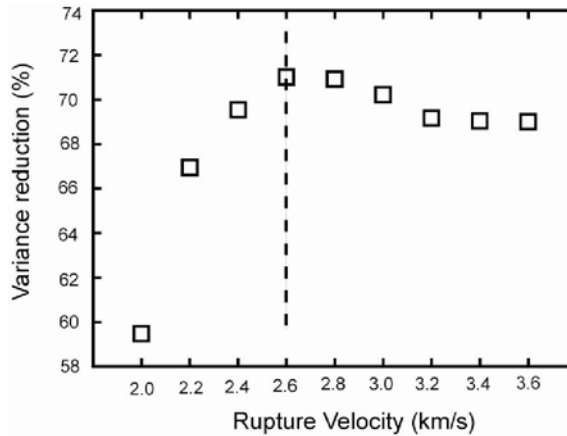
Figure 8. Fit vs. rupture velocity.

The bulk of the slip (93%) occurs in the first 6 time windows. Although some slip occurs in later time windows an examination of the synthetic waveforms indicated that it did not significantly affect the fit to the data, and that it was likely an artifact due to the mapping of propagation effects into the source. The first 6 time windows allow a range in rise time from 0.6 to 2.1 seconds, and we found that the average rise time during the rupture was 1.6 seconds.

Our preferred model compares favorably with the results of Custódio et al. (2005) and Liu et al. (2006). In those studies they used higher frequency waves (1 Hz) and consequently recovered models with shorter wavelength heterogeneity than in our model. They used a non-linear inversion for the slip trigger time and rise time, and reported that the rupture velocity is highly variable, but on average 2.6 km/s, which agrees with our result. They also developed multiple models for different station configurations (Custódio et al. 2005), and different random seeds (Liu et al. 2006), and from those models they obtained average slip models. Our model agrees very well with their average models in terms of the slip distribution. In fact, it is remarkable how similar they are considering the differences in linear vs. non-linear inversions, and their use of only seismic waveform data compared to our use of seismic and geodetic data. One major difference though is that in their models the peak slip is located at the hypocenter asperity, whereas in our model it is in the NW asperity. The similarity in the models as well as the complementary nature of coseismic slip with aftershock seismicity and postseismic deformation (Johanson et al., 2006) suggests the obtained slip model is robust.

Three Dimensional Fault Structure Effects on Ground Motions

There is a pronounced velocity contrast across the San Andreas Fault along the Parkfield segment (Michaels and Eberhart-Phillips, 1991; Michelini and McEvilly, Thurber et al., 2006). There is also evidence of a low velocity fault zone from the analysis of fault zone guided waves (Korneev et al., 2003). Korneev et al. (2003) were able to model the fault zone guided waves using a 200m wide fault zone extending to a depth of 8 km. The fault zone at Parkfield is wide as evidenced by mapped surface faults and where surface slip and creep occurred in the 1966 and

the 2004 Parkfield earthquakes (e.g. Langbein et al., 2005). For example the southwest fault zone likely marks the western extent of the San Andreas Fault system along the Parkfield segment, indicating that the fault zone is on the order of 1 km wide. The 3D model images of Thurber et al. (2006) show a fairly sharp contrast in the northern 2/3 of the fault segment in which velocities are faster on the SW side of the fault. In the vicinity of Gold Hill and southward to the Cholame array there is a 2-3 km wide low velocity zone adjacent to the plotted seismicity that extends from 5 km to about 15 km depth.

We used a 3D elastic finite-difference code, e3d (Larsen and Schultz, 1995), to simulate three-component velocity wavefields for a variety of fault models using a finite-source model derived from the preferred model described above. Simulations were performed using a single 1D structure, two 1D structures on opposite sides of the fault, and finally a sandwiched narrow low velocity zone. In order to generate synthetic records comparable to the fault zone station observations in terms of relative amplitude and duration we needed a low velocity fault zone 750m wide.

For purposes of simplifying the source parameterization we did not use the finite-source model exactly as determined. Although we did use the exact slip distribution, and the constant rupture velocity of 2.6 km/s, we did not use the multiple time window parameterizations for the slip time history. Instead we assumed a constant slip velocity of 80 cm/s and divided the slip at each point in the fault model by this value to obtain the local rise time. The local rise time was then used to define a local Gaussian shaped slip velocity function. Although the model used is not exactly the same as obtained from the inversion it does approximate the kinematic rupture process well, and is sufficient for evaluating 3D velocity structure effects on the near-fault wavefield.

The finite-difference model had dimensions of 80 km in the fault-parallel direction, 50 km in the fault perpendicular direction and 40 km in depth. The fault was centered in the grid. The grid discretization was 250m. The various simulations had minimum shear velocities of 1.5 and 1.0 km/s, and therefore the maximum frequency without significant grid dispersion effects is 0.75 and 0.5 Hz assuming 8 grid points per minimum wavelength.

In Figure 9 we compare results for stations of the Gold Hill array for a 1D reference run, and the 3D model that includes a 750m 1.0 km/s low velocity fault zone. The synthetics were low pass filtered with a corner frequency of 0.5 Hz.

This simulation very nicely illustrates the transition from complex fault zone time histories to simpler impulsive time histories at sites away from the fault, outside the low-velocity zone. Additionally the simulation shows that peak amplitude of the 3D synthetics at GH1W is 3 times higher than the near-nodal 1D reference run synthetics. In fact, the fault zone amplification effect can be greater than this. Differences in local site effects can compound the amplification at fault zone sites. Although the simulated GH1W record is similar to the observations in Figure 2 the simulated duration and period of the fault zone guided waves is not correct. These are a function of the fault zone width and the velocity in the fault zone. It would be possible to obtain better agreement with the observations by considering lower fault zone velocities, though that

would require increasing the resolution of the finite-difference calculation to maintain the same maximum frequency. We plan to do this in future work.
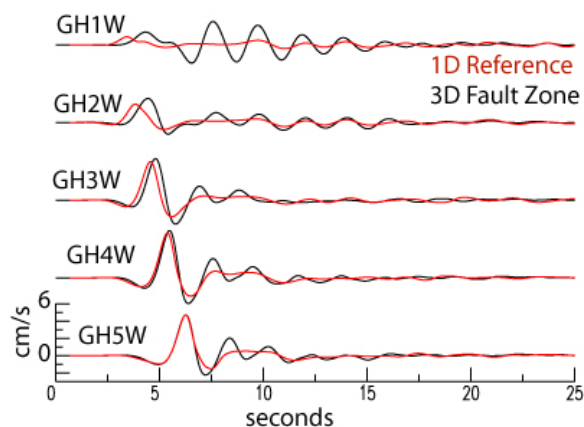

Figure 9. N-S component velocity synthetics for the Gold Hill array. The synthetics were computed with the preferred slip model, and a 3D fault model with a 750m gouge zone.

As shown previously we were able to fit the southern stations of the Cholame array quite well. Stations CH2E, CH3E, CH3W and CH4W are well modeled with fit comparable to that of other stations. Standing out is CH2W, which has a waveform with considerably more complexity and duration. 3D finite-difference synthetics for the Cholame array have the same behavior as the Gold Hill array shown in Figure 9, and therefore it seems that while a small component of southward slip is needed to fit the CH data, as shown above and by Liu et al. (2006), the large amplitudes observed at CH2W and FZ1 are most likely due to the combined effect of 3D fault zone guided waves and local site amplification.

The finite-difference results indicate that 3D fault zone wave propagation has a significant effect, and should be considered when inverting for high resolution images of the rupture process. Of course in order to do this requires a well constrained 3D geologic and velocity model. We will investigate the effect of 3D Green's functions on kinematic source inversions in future work.

Implications for ShakeMap

In Dreger et al. (2005) it has been shown that automated and rapidly reviewed finite-source information can greatly improve near-fault strong shaking estimates in cases where direct observations are not available. This was made clear in the ShakeMap response for the San Simeon earthquake (Figure 10), where the initial ShakeMap failed to portray the high level of shaking to the SE of the event near the towns of Paso Robles and Templeton. The ShakeMap taking the finite-fault rupture extent into account greatly improved the characterization of strong shaking in those areas. The question is how well resolved is a finite-source model obtained with regional distance data?

It is not expected that a finite-source model derived from a handful of regional distance (3 to 300 km) seismic stations would be comparable in detail with the results presented in this

report. Nevertheless, it is important to make this comparison to evaluate how well the regional distance approach does in characterizing slip. Figure 11 compares these two cases. The preferred joint inversion model obtained in this study is considered "truth" since it utilized many more stations at much closer distances, as well as including geodetic data. The regional model represents what can be obtained quickly after the occurrence of an event. As Figure 11 shows the two models do differ, which is not surprising, but it is also clear that they have many similar features such as the rupture extent, the depth range of rupture, the peak-slip and the scalar seismic moment. The slip in both models is focused into two asperities, one near the hypocenter and the other 10 to 20 km to the NW. This comparison shows that while the regional case is limited in its resolution of details of the source the obtained model is sufficient for purposes of including finite-source information in ShakeMap.

PERCEIVED SHAKING	Not felt	Weak	Light	Moderate	Strong	Very strong	Severe	Violent	Extreme
POTENTIAL DAMAGE	none	none	none	Very light	Light	Moderate	Moderate/Heavy	Heavy	Very Heavy
PEAK ACC.(%g)	<.17	.17-1.4	1.4-3.9	3.9-9.2	9.2-18	18-34	34-65	65-124	>124
PEAK VEL.(cm/s)	<0.1	0.1-1.1	1.1-3.4	3.4-8.1	8.1-16	16-31	31-60	60-116	>116
INSTRUMENTAL INTENSITY	I	II-III	IV	V	VI	VII	VIII	IX	X+
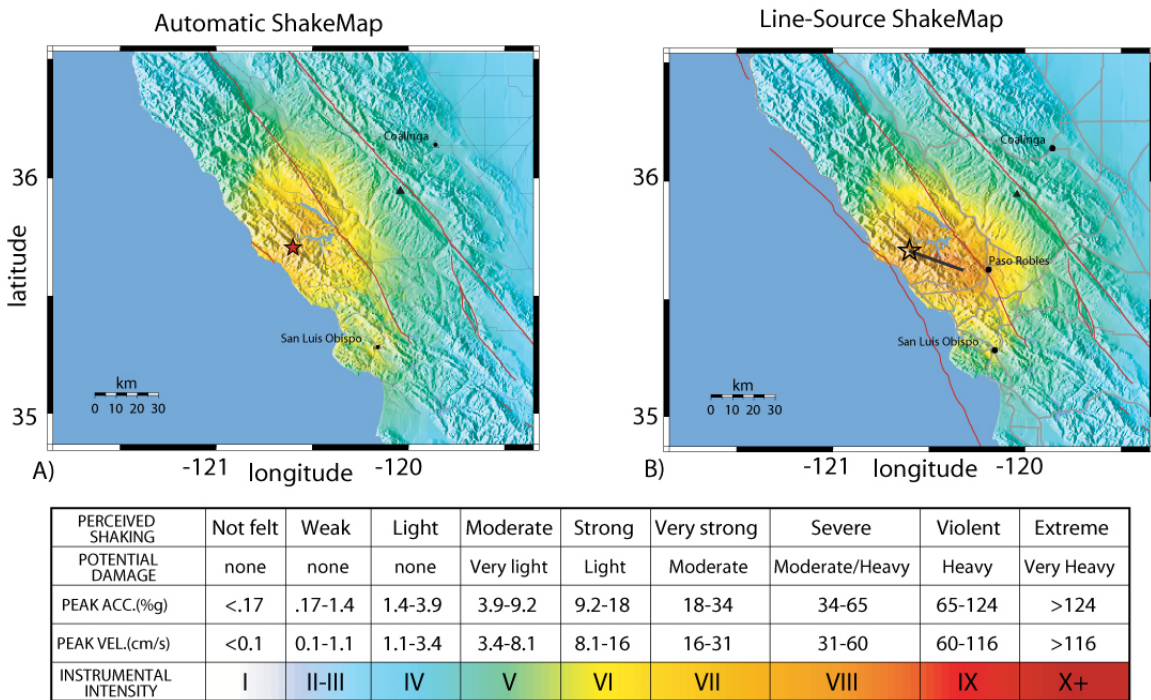
Figure 10. Comparison of (a) initial automatic ShakeMap with one that takes the rupture length determined from rapid finite-source inversion into account (b). The red star shows the epicenter, and the black line shows the extent of rupture. Note that there are no near-fault stations contributing to either map. In fact, the closest contributing stations was 55 km away. The map on the right was found to agree well with a map generated a few days after the event, which took into account the observed motions at several near fault sites (e.g. Dreger et al., 2005).
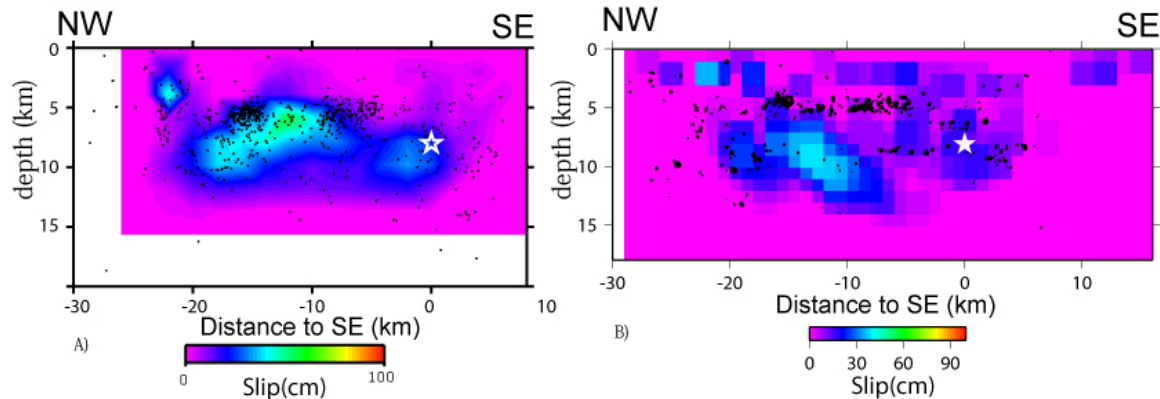
Figure 11. (a) Slip model obtained by inverting 9 three-component, regional distance displacement seismograms. This model was presented at the 2005 SSA meeting. (b) Preferred slip model based on the inversion of 29 two-component, near-fault velocity records, 13 GPS vectors, and InSAR deformation data.

Conclusions

We have developed kinematic finite-source models for the 2004 Mw6.0 Parkfield earthquake using the strong motion data collected by the California Geologic Survey CSMIP program. In addition, to these data we added strong motion records from the USGS NSMP and also GPS and InSAR geodetic data. A combined inversion of the three data sets produces the most constrained results. We find that the preferred slip model is consistent with our previous models obtained by inverting regional distance waveform data (e.g. Langbein et al., 2005; Dreger et al., 2005). This is a very positive result as it demonstrates that the automated regional distance finite-source method developed by Dreger and Kaverina (2000) is capable of recovering the kinematic finite-source rupture process with reasonably high resolution.

As shown by Dreger and Kaverina (2000) for the Mw7.1 Hector Mine earthquake and Dreger et al. (2005) for the Mw6.5 San Simeon earthquake rapidly determined fault slip models may be used to help constrain the level of near-fault strong shaking. In the case of the San Simeon earthquake the finite-source information, namely the length of the ruptured fault was instrumental in accurately characterizing strong shaking levels the day of the earthquake. Subsequently when a few near-event strong motion records became available the ShakeMap using the finite-source information was found to be consistent with the observations.

We incorporated 9 stations located SE of the epicenter in the inversion to try to resolve possible SE-ward rupture since elevated peak ground motions (Shakal et al., 2006) in this region suggest bilateral rupture. The results of our inversions (the seismic only and joint inversion) indicate that there was a small amount of SE-ward rupture, but that overall the 2004 Parkfield earthquake ruptured unilaterally to the NW.

We used our derived slip model to simulate the 3D wavefield for a fault model with an across-fault velocity contrast with a sandwiched low velocity zone. The results show that fault zone guided waves develop in this narrow zone greatly amplifying peak ground motions and producing complex multi-cycle waveforms. Based on this result we conclude that the elevated

motions SE of the epicenter at FZ1, at some sites of the Cholame array, and other sites located close to the fault are in part due to this 3D wave propagation effect.

The implications of this study for ShakeMap is two-fold. First, the similarity between the regional and near-fault finite-source models indicates that an automated regional distance approach is capable of producing reliable results for the rupture dimension and slip distribution. For both the San Simeon and Parkfield earthquakes including rupture length information (from aftershocks in the case of Parkfield) improved the ground motion characterization of ShakeMap. Second, the finite-difference simulation results indicate that near-fault motions can be affected by 3D fault structure. This is something that cannot easily be incorporated in an automated approach. It is therefore necessary to keep in mind that lateral velocity contrasts and fault zone low velocity can significantly increase the level of near-fault ground motions.

References

Custódio S., P. Liu, and R. J. Archuleta (2005). 2004 Mw6.0 Parkfield, California, earthquake: Inversion of near-source ground motion using multiple datasets, *Geophys. Res. Lett.,* 32, L23312, doi:10.1029/2005GL024417.

Dreger, D. S., L. Gee, P. Lombard, M. H. Murray, and B. Romanowicz (2005). Rapid Finite-Source Analysis and Near-Fault Strong Ground Motions – Application to the 2003 Mw6.5 San Simeon and 2004 Mw6.0 Parkfield Earthquakes, *Seismo. Res. Lett.* 76, 40-48.

Dreger, D., and A. Kaverina (2000). Seismic remote sensing for the earthquake source process and near-source strong shaking: A case study of the October 16, 1999 Hector Mine earthquake, Geophys. Res. Lett., 27, 1941-1944.

Eberhart-Phillips, D., and A.J. Michael, 1993, Three-dimensional velocity structure and seismicity in the Parkfield region, central California, J. Geophys. Res., 98, 15,737-15,758.

Fletcher, J. B., P. Spudich, and L. M. Baker (2006). Rupture propagation of the 2004 Parkfield earthquake from observations at the UPSAR array, *submitted to BSSA special issue on the Parkfield earthquake.*

Hartzell, S. H., and T. H. Heaton (1983) Inversion of strong ground motion and teleseismic waveform data for the fault rupture history of the 1979 Imperial Valley, California, earthquake, Bull. Seism. Soc. Am., 73, 1553-1583.

Johanson, I. A., E. J. Fielding, F. Rolandone, and R. Bürgmann (2006). Coseismic and postseismic slip of the 2004 Parkfield earthquake from space-geodetic data, *Bull. Seism. Soc. Am.,* 96, S269-S282.

Korneev, V. A., R. M. Nadeau, and T. V. McEvilly (2003). Seismological studies at Parkfield IX: Fault zone imaging using guided wave attenuation, Bull. Seism. Soc. Am., 93, 1415-1426.

Langbein, J., R. Borcherdt, D. Dreger, J. Fletcher, J. L. Hardebeck, M. Hellweg, C. Ji, M. Johnston,J. R. Murray, R. Nadeau, M. J. Rymer, J. A. Treiman (2005). Preliminary Report on the 28 September 2004, M 6.0 Parkfield, California Earthquake, *Seismo. Res. Lett.* 76, 10-26.

Larsen, S., and C. A. Schultz (1995). ELAS3D: 2D/3D elastic finite-difference wave propagation code, Technical Report No. UCRL-MA-121792, 19pp.

Lawson, C. L. and R. J. Hanson (1974) Solving Least Squares Problems, Prentice Hall, Englewood Clioes, New Jersey.

Lui, P., S. Custódio, and R. J. Archuleta (2006). Kinematic inversion of the 2004 Mw6.0 Parkfield earthquake including site effects, *Bull. Seism. Soc. Am.,* 96, S143-S158.

Michael, A. J., and D. Eberhart-Phillips (1991). Relationships between fault behavior, subsurface geology, and three-dimensional velocity models, Science, 253, 651-654.

Michelini, A., and T. V. McEvilly (1991). Seismological studies at Parkfield, part I: Simultaneous inversion for velocity structure and hypocenters using cubic B-splines parameterization, *Bull. Seism. Soc. Am.,* 81, 524-552.

Shakal, A., H. Haddadi, V. Graizer, K. Lin, and M. Huang (2006). Some key features of the strong-motion data from the M6.0 Parkfield, California, earthquake of 28 September 2004, *Bull. Seism. Soc. Am.,* 96, S90-S118.

Thurber, C., H. Zhang, F. Waldhauser, J. Hardebeck, A. Michaels, and D. Eberhart-Phillips (2006). Three-dimensional compressional wavespeed model, earthquake relocations, and focal mechanisms for the Parkfield, California, region, *Bull. Seism. Soc. Am.,* 96, S38-S49.

Wald, D. J., T. H. Heaton, and D. V. Helmberger (1991). Rupture model of the 1989 Loma Prieta earthquake from the inversion of strong motion and broadband teleseismic data, *Bull. Seism. Soc. Am.,*, 81 1540-1572.

Table 1: Station Locations and Applied Time Shifts

station	lat	lon	time shift (s)	station	lat	lon	time shift (s)
CH2E	35.751	-120.259	1.2	FZ9	35.879	-120.445	1.6
CH3E	35.770	-120.247	1.2	FZ12	35.900	-120.433	1.8
CH2W	35.733	-120.286	1.6	UPSAR01	35.821	-120.507	1.3
CH3W	35.726	-120.296	1.0	PHOB	35.867	-120.048	2.0
CH4W	35.717	-120.305	1.1	EFU	35.894	-120.421	0.4
SC1E	35.788	-120.294	0.9	FFU	35.911	-120.486	0.2
SC2E	35.810	-120.282	1.9	DFU	35.939	-120.425	2.4
SC3E	35.833	-120.27	1.2	JFU	35.939	-120.432	0.8
GH2E	35.842	-120.348	1.8	MFU	35.956	-120.496	0.1
GH3E	35.870	-120.334	1.8	VC1W	35.934	-120.497	0.8
GH2W	35.812	-120.391	1.8	VC2W	35.927	-120.509	0.8
GH3W	35.796	-120.411	1.8	VC4W	35.905	-120.551	1.3
GH4W	35.785	-120.444	1.7	VC6W	35.861	-120.600	1.2
FZ6	35.859	-120.42	1.9	VFU	35.922	-120.534	0.3
FZ7	35.871	-120.404	2.0				

Table 2: 1D Velocity Models

SW of the Fault						NE of the Fault					
Thickness (km)	Vp (km/s)	Vs (km/s)	density (kg/m^3)	Qp	Qs	Thickness (km)	Vp (km/s)	Vs (km/s)	density (kg/m^3)	Qp	Qs
1.0	1.9	1.0	2000	70	35	0.7	2.0	1.1	2000	70	35
1.0	3.4	1.7	2300	270	160	0.7	3.8	2.2	2300	300	180
1.0	4.6	2.4	2300	450	260	0.6	4.3	2.4	2300	340	190
1.0	5.1	3.1	2700	500	300	1.6	4.8	2.7	2300	450	250
1.4	5.6	3.6	2700	550	350	4.0	5.3	3.1	2500	500	300
13.3	6.3	3.6	2800	600	350	6.7	5.8	3.3	2700	550	300
∞	6.8	3.6	2800	680	360	6.2	6.2	3.8	2800	600	350
						4.1	6.8	3.8	2800	650	350
						∞	7.0	4.0	2800	700	400

IMPLICATION OF RUPTURE PROCESS AND SITE EFFECTS IN THE SPATIAL DISTRIBUTION AND AMPLITUDE OF THE NEAR-FAULT GROUND MOTION FROM THE 2004 PARKFIELD EARTHQUAKE

Arben Pitarka, Nancy Collins, Hong-Kie Thio, Robert Graves and Paul Somerville

URS Corporation, Pasadena, California

Abstract

The 2004 M_w6 Parkfield earthquake is the last in a series of several strike-slip earthquakes that have occurred on the same fault located in a zone that marks the transition between a creeping section and a locked section of the San Andreas Fault in central California. Ground motion data recorded at a dense network of near-fault stations installed by California Geological Survey (CGC) and United States Geological Survey (USGS) are unprecedented in terms of quality and characteristics for this type of earthquake in California. Although of moderate size, the earthquake produced near-fault ground motion acceleration that exceeds predictions from empirical ground motion models. At three sites the recorded acceleration was more than 1.0g (Shakal et al., 2005). Very large peak ground velocities of up to 83cm/s were also recorded at both ends of the fault. On the other hand, most of the stations located very near to the fault recorded ground motion with very low acceleration and velocity. In this study we investigate the implication of the rupture kinematics and dynamics, and local site effects in the amplitude and spatial variation of the near-fault ground motion for this earthquake.

Near-Fault Ground Motion Characteristics

Figure 1 shows the map of the Parkfield area and location of 47 CGC and 11 USGS strong motion recording stations used in this study. The Parkfield earthquake occurred on a right lateral segment of the San Andreas fault. The San Andreas fault forms the boundary between the granitic Salinian block on the west and Southern Diablo Range with sedimentary Franciscan terrane on the east (Dickinson 1966). Based on the distribution of aftershocks that occurred immediately after the earthquake the fault length and width were estimated to be 35km and 15 km, respectively (Hardebeck and Michael, 2004). No co-seismic surface rupture appeared, but surface slip began several hours after the main shock (Langbein et al., 2005). The fault plane has a strike angle of 157° and a dip angle of 89°. The shallow underground structure is characterized by the velocity contrast across the fault, with the northeast side about 20% slower in the top 10 km. Below 10 km the velocity contrast gradually diminishes with depth. Most of the strong motion sites are category B using NEHRP classification.

Figure 2 displays the fault-normal component of two selected acceleration time histories recorded at stations PF14 and PF15 located near the northern end of the fault. Their respective spectrograms are shown in figure 3. Station PF14 is located very close to the fault with a fault distance less than 1 km. The 1.3 g ground motion acceleration at this station is the highest peak acceleration recorded during the Parkfield earthquake (Shakal et al., 2005). Station PF15 is
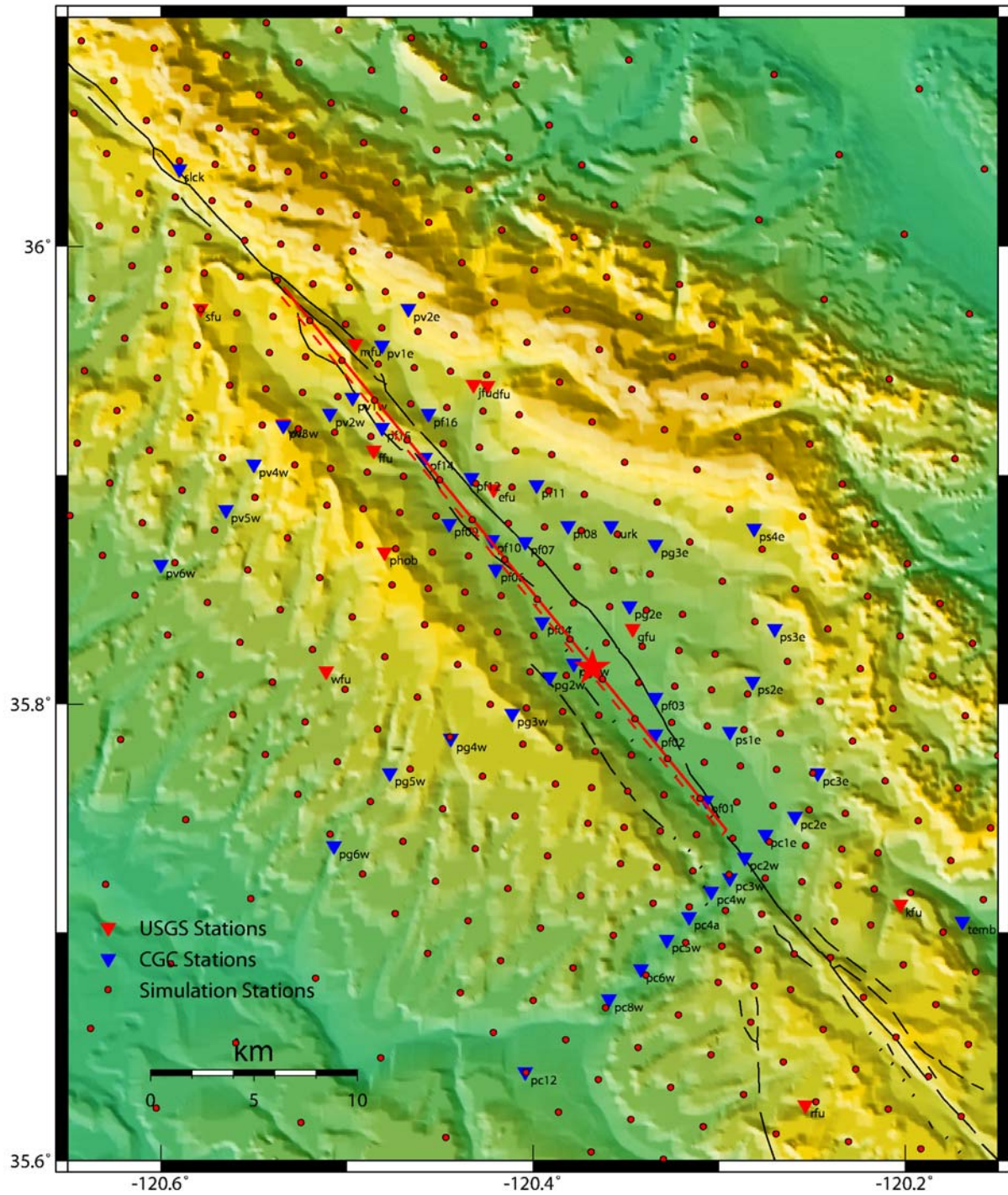
Figure 1. Map of the Parkfield area showing the faults trace (red line), the epicenter of the 2004 Parkfield earthquake (star) and CSMIP and USGS strong motion station locations. Red dots show the location of sites used in mapping simulated ground motion.

located close to station PF14. The distance between the two stations is less than 3.5 km. The differences among the main features of the ground motion at these two stations are a clear illustration of the very complex near-fault ground motion. The acceleration at station PF14 is dominated by two source related large pulses, and a very short time duration. The pulses are energetic at a very narrow frequency band between 1Hz and 3Hz. In contract, the acceleration time history at station PF15 has a much smaller amplitude and longer duration. Most energetic phases at this station have different arrival times and distinct frequency contents that are centered at 1Hz, 2.5 Hz. and 5Hz, respectively. Coda waves are mainly small amplitude pulses with a 1 sec period. Such striking dissimilarities between neighboring stations are also observed at other regions near the fault trace. They are indicatives of fault zone effects that mainly suppress the high frequency signals of the ground motion while increasing its duration.

The comparison between the recorded peak acceleration and that predicted by the empirical attenuation model of Abrahamson and Silva (1997), for both fault-normal and fault-parallel components shown in Figures 3a and 3b, indicates that the stations that recorded ground motion below the expected value are all located within less than 1 km from the fault. In contrast, stations with higher than expected acceleration are clustered at fault distances between 2-4 km. At longer distances the recorded ground motion is slightly smaller than that predicted by the attenuation model at all analyzed frequencies. The generally low-level ground motion can be explained by the fact that this was a low stress drop event. The difference between fault-normal and fault-parallel components remains significant up to at least 3.3Hz. This is an interesting observation. It indicates that the rupture directivity for strike-slip event remains effective even at high frequencies.

These general observations indicate that the wide-spread differentiated near-fault motion may have been caused mainly by fault zone effects and local site effects. As it will be shown below, our study does not rule out the possibility of increased ground motion in some small areas near the north end of the fault where our rupture dynamics model shows small patches of larger stress-drop. Studies of fault-zone trapped waves have delineated a 150 m-wide fault zone characterized by low velocity and cracked rock (Li et al., 2006; Thurber et al., 2003). The width of the fault zone and that of damaged rock may vary along the fault. The fault zone weakens the high-frequency motion generated at the crack tip while amplifying trapped waves propagating along the fault. As a direct consequence, the scattered waves generated inside this zone, dominate the ground motion at near fault stations where the relatively low amplitude coda waves increase the ground motion duration significantly.

Local Site Effects

We used the recoded motion from the 1983 $M_w6.5$ Coalinga earthquake to estimate the elastic local site response at Parkfield array stations that recorded both earthquakes. The stations used in analyses of local site effects are shown in Figure 4. The Coalinga earthquake occurred about 30 km NE of the epicenter of the Parkfield earthquake (Eberhart-Phillips, 1989). Given its large epicentral distance from the array, we assumed that the incoming motion from the Coalinga earthquake was the same at all Parkfield stations. The site effect was calculated as the ratio between the smoothed amplitude spectrum of recorded motion at each station and the reference
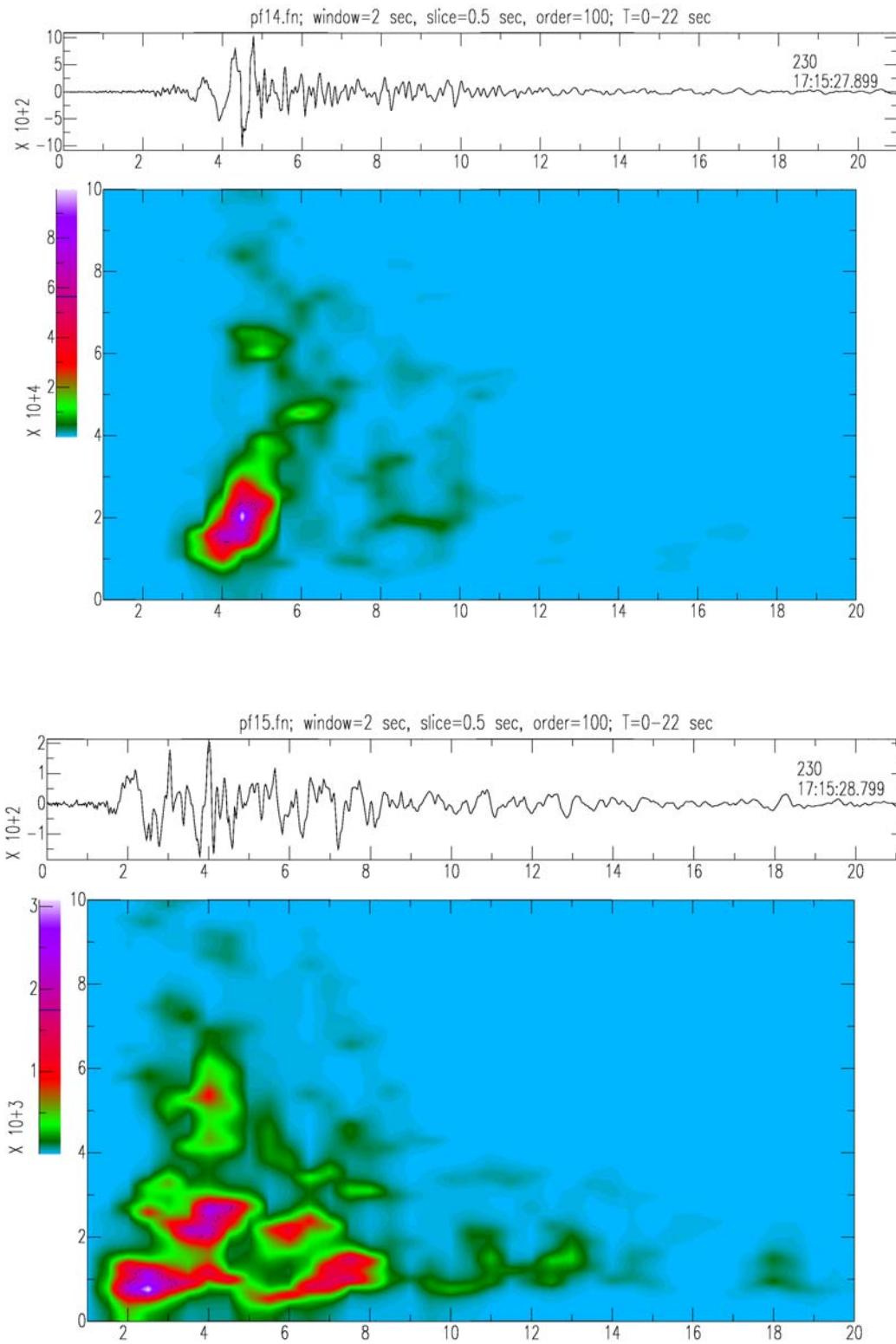
Figure 2. Spectrograms of recorded acceleration at stations PF14 (top panel) and PF15 (bottom panel). Acceleration unit is cm/s. Note that the peak spectral acceleration at PF14 is 30 times higher than that at PF15.
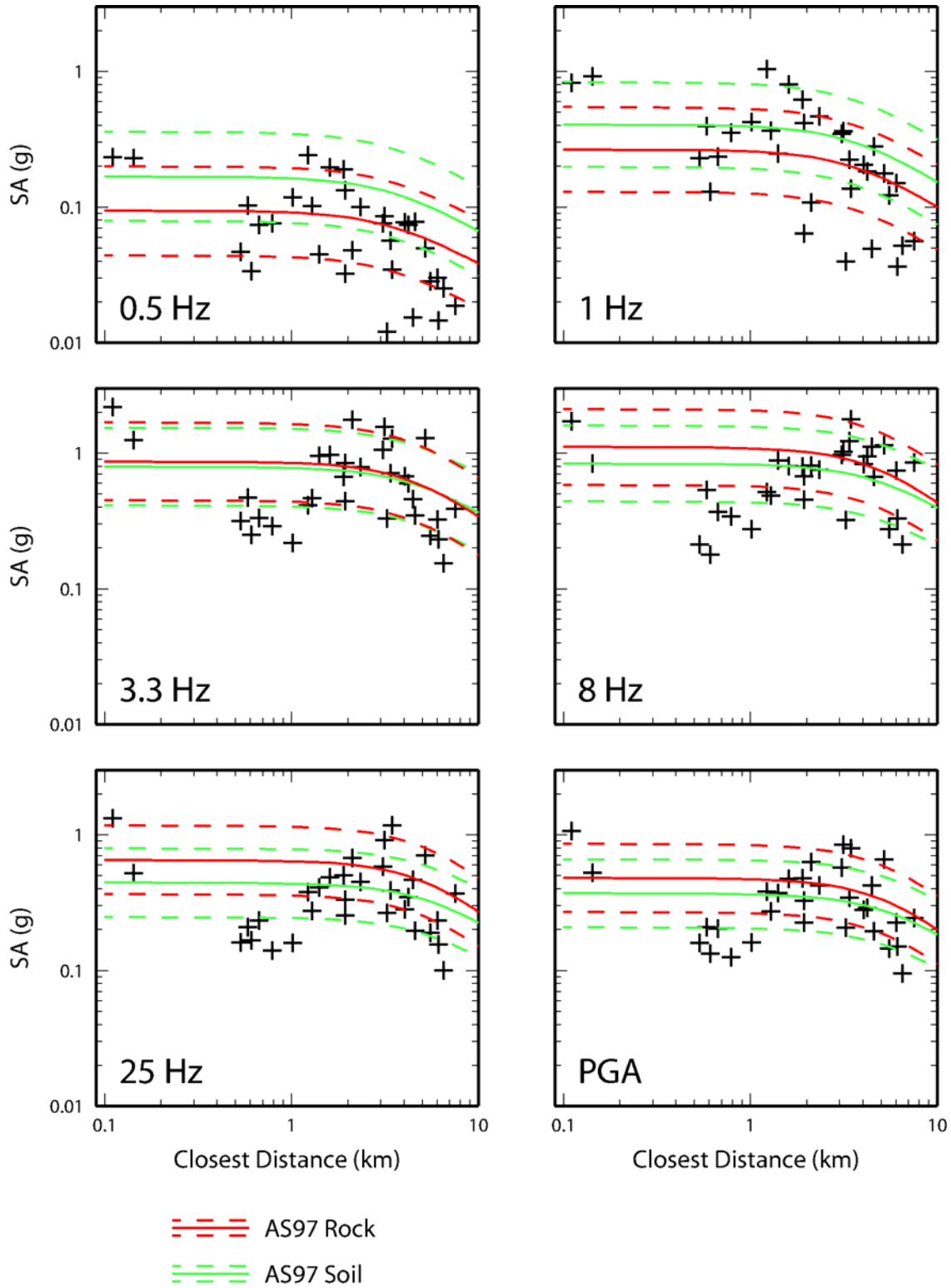
Figure3a. Comparison of recorded spectral acceleration (crosses) and the Abrahamson and Silva (1997) empirical attenuation model for fault normal component.
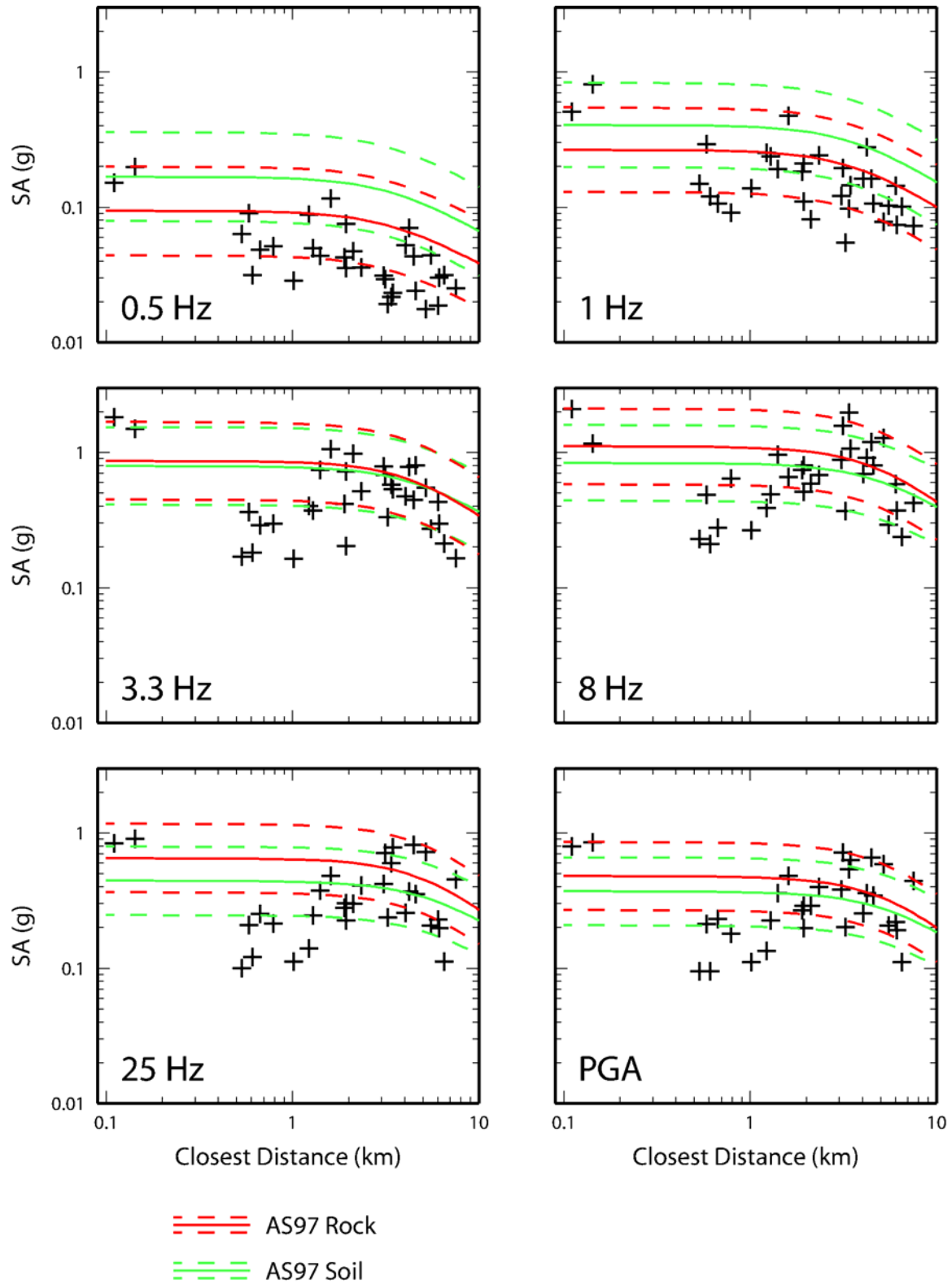
Figure3b. Comparison of recorded spectral acceleration (crosses) and the Abrahamson and Silva (1997) empirical attenuation model for fault parallel component.

spectrum calculated as the log average of all smoothed spectra. In order to reduce possible discrepancies due to the velocity contrast in the fault region the reference spectrum was calculated separately for stations on the east and west side of the fault. The calculated spectral ratio at a given frequency was considered as the local amplification factor.

The amplification factors estimated at frequencies 0.5Hz, 1Hz, 3Hz, 8Hz, 12Hz and 25 Hz are shown in Figure 5. In this figure closed blue circles correspond to amplitude ratios larger than 1, indicating amplification, and green circles correspond to amplitude ratios smaller than 1, indicating deamplification. A circle's radius is proportional to the corresponding amplification factor. The biggest site amplification of 3.6 is observed at 1Hz at station PF14. Our analyses indicate that site effects at this site have amplified the ground motion on a broad frequency range. Based on this result we believe that the very high acceleration observed at this station is mainly due to site effects and to a lesser extent to fault rupture effects. This is also supported by another study of local site effects at station PF14 and nearby sites (Haddadi et al., 2006). According to their investigation of ground motion acceleration record at station PF16 which was clipped during the Parkfield earthquake, the peak acceleration may have exceeded 2.5g. Also ground motion records from aftershocks of the 2004 Parkfield earthquake, 1983 M6.5 Coalinga earthquake and M6.0 San Simeon earthquake at station PF14, PF16 and their vicinity are characterized by elevated amplitudes at these particular sites. Based on waveform analyses they demonstrated that the cause of the amplification is the local site effects.

Clear trends in the amplification factors that reflect site effects are the followings:

1. The fault zone amplifies the ground motion at frequencies 1Hz and lower. The amplification is more pronounced at sites located in both ends of the fault. Note that 1Hz falls in the frequency range where also the directivity effect is expected to amplify the fault-normal component of ground motion for this type of earthquake. At most of the sites located within 1km from the fault, fault zone and site effects deamplified the ground motion acceleration, and amplified the ground motion velocity.

2. High frequency site effects are negligible at stations near the southern end of the fault where the ground motion was relatively high.

Rupture Kinematics

Inversion Method

The method for determining the slip time history and slip distribution on the fault is similar to that developed by Hartzell and Heaton (1983). The fault plane is discretized into a grid of subfaults. We then impose a slip band propagating over the fault plane starting at hypocenter. The individual sets of grid points that are contained within a slip band at any time step are combined into one large set that are cast into a normal equation of the form Ax=b where A contains the Green's functions from every grid point to every station, x is the vector containing the slip value that we are trying to solve for, and b the vector containing all the data. The normal equation is solved using a least squares solver with positive constraint (we do not allow for

reverse slip). Our method allows for variable rake, in which case every original grid point is split into two grid points where the new rake angles are different from the original by + and – 45° respectively, so that the same positivity constraint can be used. In order to stabilize the solution we applied spatial smoothing constraints as well as smoothing of the two perpendicular rake vectors. The smoothing and damping parameters used in solving the linear equations are determined by trial-and-error.
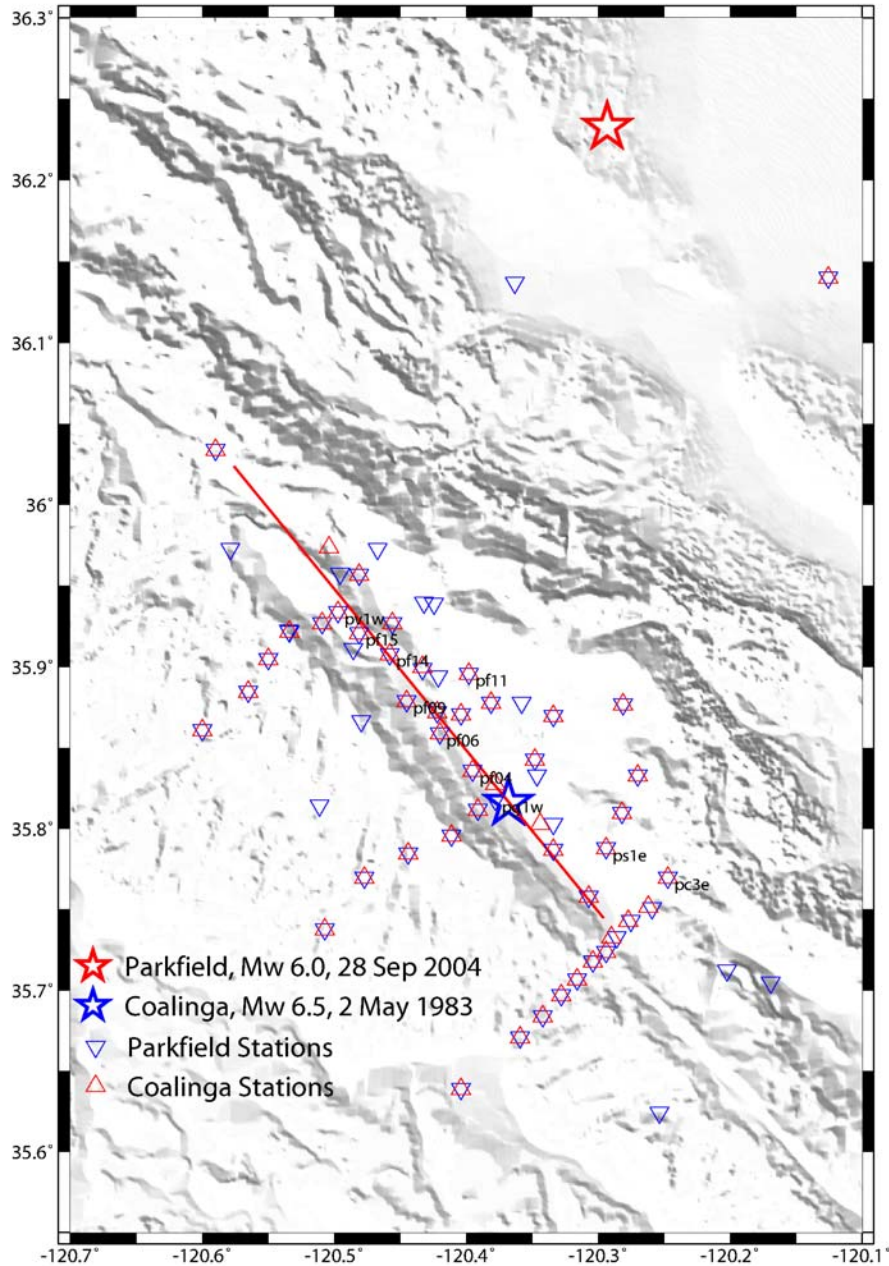
Figure 4. Map of the Parkfield area showing the location of the stations that recorded 2004 Parkfield earthquake (blue triangles) and Coalinga earthquake (red triangles). Also shown are the epicenter of the Parkfield earthquake (blue star) and the epicenter of the Coalinga earthquake (red star).
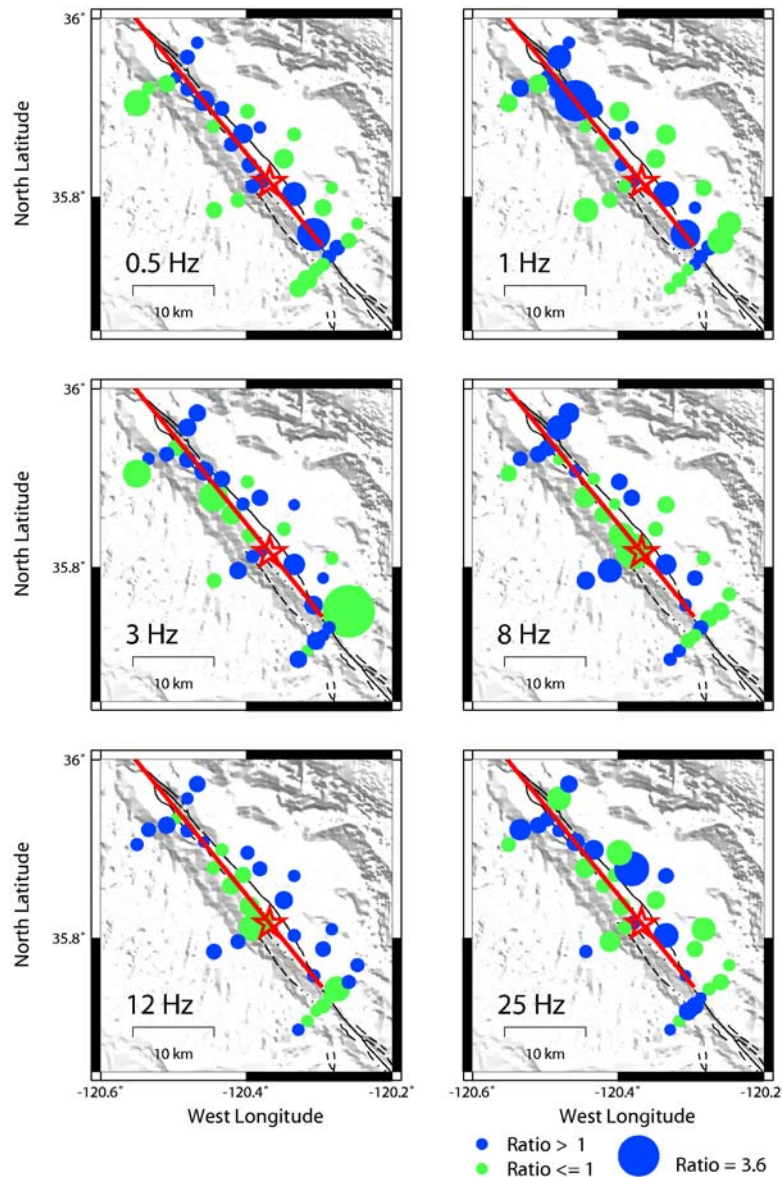
Figure 5. Site effect amplification factors estimated at stations that recorded the Coalinga earthquake. A circle's radius is proportional to the amplification factor. Blue circles indicate amplification and green circles indicate deamplification. Note that the largest amplification of 3.6 was observed at 1Hz at station PF14 which also recorded the highest acceleration during the 2004 Parkfield earthquake

We set up the rupture plane as single fault plane with a strike angle of 140.8^o and dip angle of $89^o.$ The length of the fault plane is 35 km and the width 16 km. The depth to the top of the fault is 0.1 km. In our inversion we used ground motion data recorded at stations with the fault distance smaller than 30 km. We excluded most of the stations with fault distance less than

1 km. These stations were excluded from the inversion for several reasons. First, with our current representation of the fault surface by a single plane, stations that are very close to the fault may project on the wrong side of the fault plane. Second, some of these stations are affected by the 3D structural heterogeneities in the fault zone that are not presented in the 1D velocity models used in generating the Green's functions.

The original acceleration data were integrated to velocity and band-pass filtered at 0.1-1 Hz. The 1D velocity models shown in Table 1a and 1b were used to calculate Green's functions for sites located on the east and west sides of the fault, respectively. The two models differ from each other in the top 10 km, with the west side model being 20% faster in the top 10 km (e.g. Thurber et al., 2003). The west side 1D velocity model was derived from wave path calibration analyses in the region.

Since we inverted relatively high frequency ground motion velocity the 1D Green's functions were also corrected for local site effects using site-specific amplification factors. These factors were derived using the empirical relations of Borcherdt (1994) and V_S^{30} value. Although very simplistic, the correction improves the quality of the slip inversion. In our trial inversions we varied the maximum rupture velocity between 2.5 and 3.5 km/s, but found that 3.0 km/s gave the best waveform fit. We used 20 time widows with duration of 0.8 sec and superposed by 0.4 sec.

Table 1a. 1D Velocity Model Parameters. East of the Fault

Thick.	Vp	Vs	Density	Qp	Qs
0.002	1.70	0.35	2.00	80	20
0.004	1.80	0.55	2.00	80	30
0.006	1.80	0.80	2.00	80	40
0.008	1.90	0.90	2.00	100	40
0.010	2.00	1.00	2.00	100	40
0.070	2.40	1.30	2.00	200	60
0.20	2.66	1.40	2.00	50	60
0.20	3.24	1.80	2.00	50	80
0.50	3.28	1.90	2.00	50	105
1.00	3.60	2.07	2.10	100	110
2.00	3.76	2.17	2.20	200	120
3.00	5.35	3.10	2.60	200	130
3.00	5.65	3.26	2.60	200	140
16.00	6.37	3.68	2.81	200	150
12.00	7.76	4.48	3.25	600	170
4.00	7.90	4.56	3.30	700	180
0.00	7.99	4.61	3.33	1000	200

Table 2a. 1D Velocity Model Parameters. West of the Fault

Thick.	Vp	Vs	Density	Qp	Qs
0.002	1.70	0.35	2.00	80	20
0.004	1.80	0.55	2.00	80	30
0.006	1.80	0.80	2.00	80	40
0.008	1.90	0.90	2.00	100	40
0.010	2.00	1.00	2.00	100	40
0.070	2.40	1.30	2.00	200	60
0.20	2.80	1.50	2.00	50	60
0.20	3.60	2.00	2.00	50	80
0.50	3.86	2.23	2.01	50	100
1.00	4.23	2.44	2.12	100	110
2.00	4.71	2.72	2.28	200	120
6.00	5.95	3.44	2.67	200	130
16.00	6.37	3.68	2.81	200	150
12.00	7.76	4.48	3.25	500	170
4.00	7.90	4.56	3.30	700	180
0.00	7.99	4.61	3.33	1000	200

**Inverted Slip Model**

Figure 6 shows the distributions of final slip, and slip vector on the fault plane. Figure 7 shows contour lines of the rupture initiation time. The waveform fits for selected stations used in the inversion is shown in Figure 8. The slip is concentrated in two large areas that occupy about 30% of the fault. The maximum slip of 40 cm is observed in a shallow slip area in the northern part of the fault. The average rake angle is 180 degrees. It indicates that this event was predominantly right-lateral strike slip. The total moment amounts to 1.53×10^{25} dyne.cm, corresponding to a moment magnitude of 6.1.

The only region with substantial shallow slip is in the northern part of the fault. Elsewhere the slip is relatively deep. The patch of slip located in the southern edge of the fault seems to be controlled by the large ground motion observed at nearby stations. Although not well resolved, because of its proximity to the fault boundary, the slip in the southern part of the fault indicates that the fault rupture propagated bilaterally. It quickly stopped in the southern part of the fault, probably due to a strong barrier. The ruptured fault segment is situated between a locked segment to the south and a creeping segment to the north.
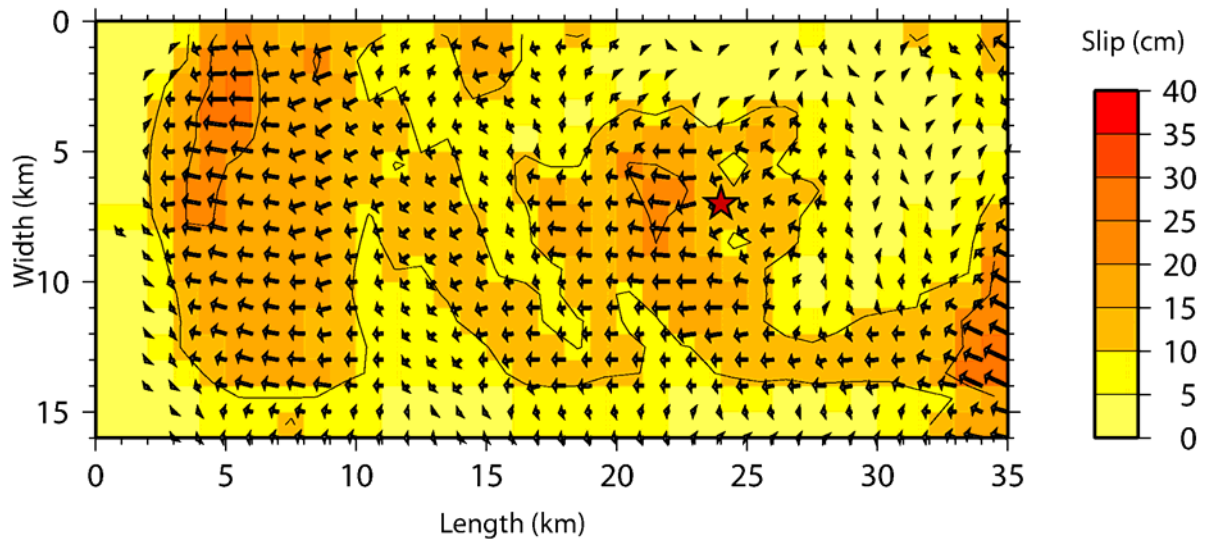
Figure 6. Total slip and final slip vector distribution for the kinematic rupture model obtained by inverting near-fault ground motion velocity in the frequency range 0.01-1.0 Hz.
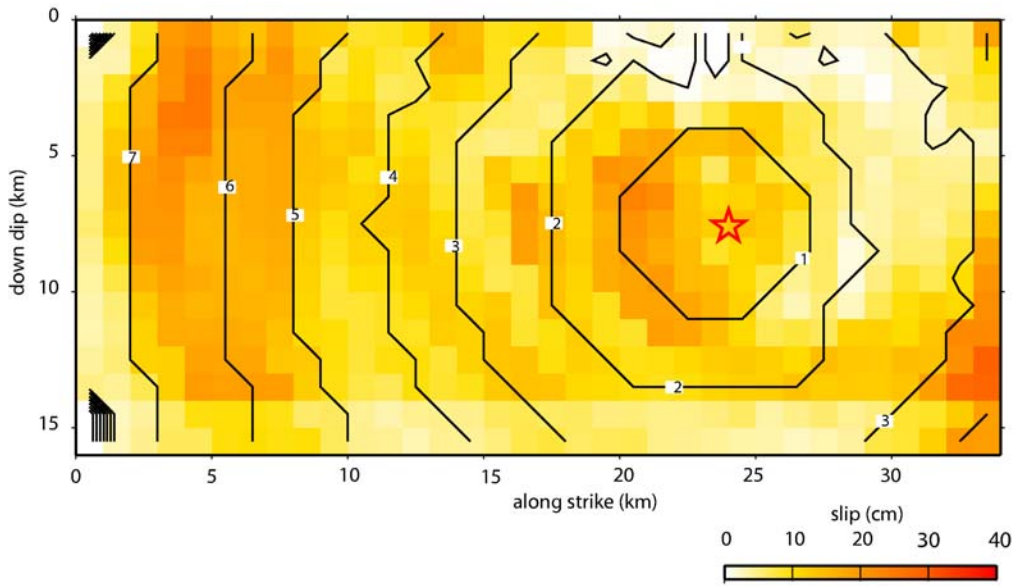
Figure 7. Contour lines of kinematic rupture time initiation.
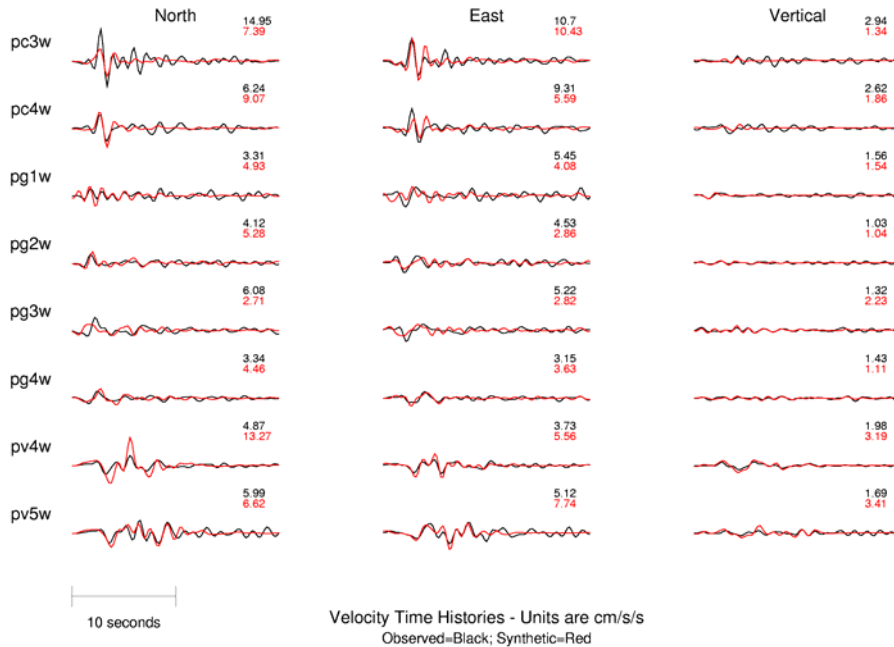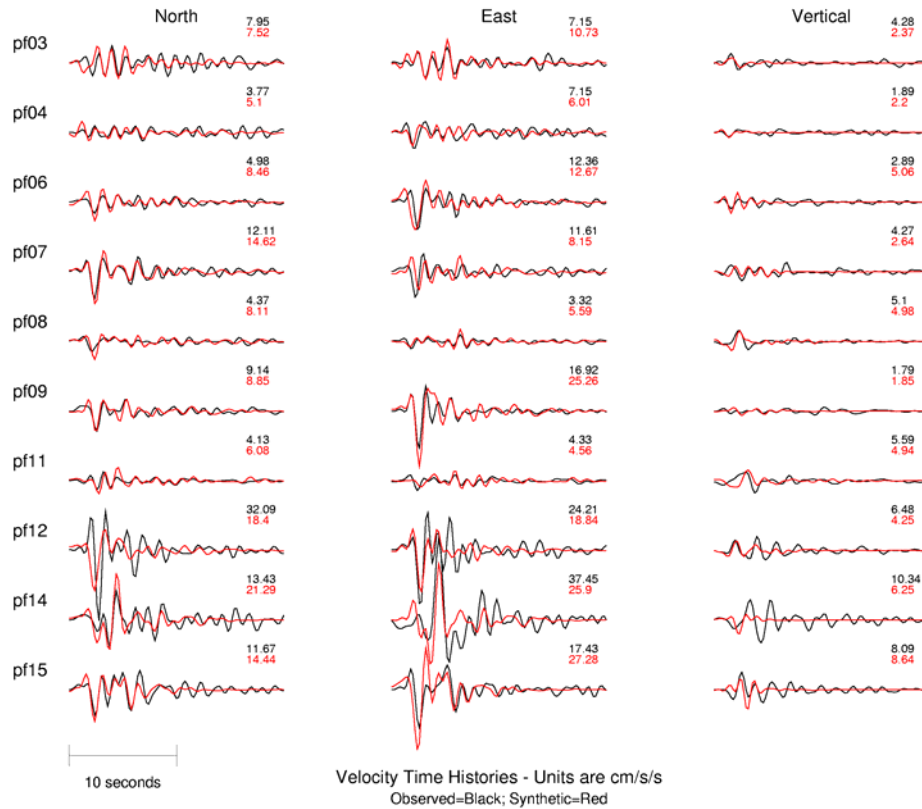
Figure 8. Comparison of recorded (black) and synthetic ground motion velocity (red) calculated with the kinematic model at CGS and USGS stations shown in the upper panel and lower panel, respectively.

The maximum rupture speed in our preferred model is 3.0 km/s. The kinematic rupture model indicates that the rupture speed increased as the rupture propagated away from the initiation point. The rupture gradually came to a stop in the northern end of the fault as opposed to an abrupt stop in the south where our kinematic model shows that the rupture speed was supershear for a short distance.

The shallow slip observed in the north and rupture directivity contributed to the seismic energy at frequencies above 1Hz at sites north of epicenter. We concluded that the increase in ground motion amplitude observed at stations located near the north end of the fault was caused by combined site effects and local rupture process effects. In contrast, in south at stations PS1E and PC3E neither the site effects nor rupture directivity were strong enough to be considered key factors in affecting the ground motion amplitude. In fact most of the stations in this area recorded relatively weak motion. It is possible that the larger ground motions observed at stations PS1E and PC3E were caused by the large amplitude shock wave created when the rupture in the southern part of the fault went supershear. We will elaborate more on this topic in the following section.

Rupture Dynamics

Inversion Technique

Our procedure for obtaining the dynamic rupture model of the earthquake is similar to the inversion procedure proposed by Dalguer (2002). His procedure is based on a trial-and-error technique in which the spatial distributions of the dynamic rupture parameters are obtained by step-by-step modifications that improve both the waveform fit between the recorded and calculated data, and the fit between the kinematic and dynamic final slip and initial rupture time (e.g. Pitarka and Dalguer, 2003; Pitarka, 2005). In the first step of the inversion we use a kinematic rupture model to develop initial dynamic rupture parameters that are necessary for performing spontaneous rupture modeling. We start with the kinematic slip history given on a regular grid in the fault plane. The slip history is imposed as a boundary condition in a finite-difference calculation of the stress time history on the fault. The 3D finite-difference method solves the wave equation for heterogeneous media (Pitarka, 1999). The stress time history is then used to estimate dynamic rupture parameters such as dynamic stress drop, static stress drop, and strength excess. The inversion scheme starts with this initial dynamic rupture parameterization. We also assume that the spatial distribution of the slip weakening displacement is similar to that of the final kinematic slip, and its value is 25% of the kinematic final slip. The rupture modeling trials consist of executions of a 3D finite-difference computer program that models spontaneous rupture propagation. After each execution the dynamic rupture parameters are gradually modified. The first iterations are used to constrain the dynamic stress drop. The inversion procedure ends when the spatial distributions of the final slip and rupture time in the dynamic model are similar to those in the kinematic model, respectively. In the final iterations we make small modifications to slip weakening displacement Dc and strength excess aiming at further improving the fit between the synthetic and recorded ground motion velocity seismograms.

Spontaneous Dynamic Rupture Modeling Technique

We use the staggered grid 3D-FD method with variable spacing of Pitarka and Dalguer (2003) to model wave propagation and rupture dynamics on the fault. The rupture dynamics on the fault is modeled by using the so-called the "inelastic fault zone" formulation proposed by Dalguer and Day (2004). The rupture process is controlled by a simple slip weakening law as proposed by Andrews (1976).

Fault Parameterization

The numerical techniques for calculating stress from the slip on the fault require the time history of the slip to be smooth. This condition cannot be met by our kinematic slip model. Therefore in order to initiate the dynamic rupture inversion scheme for the Parkfield earthquake we used the kinematic model of Liu et al. (2006). In their non-linear inversion the geometry and location of the fault is similar to those used in our kinematic model. Their model was obtained by inverting the near-fault ground motion velocity, band-pass filtered at 0.1-1.0 Hz. In their technique the slip rate function is smooth. It is approximated by an appropriate combination of sine and cosine functions representing the accelerating and decelerating parts of the slip rate, respectively.

In our spontaneous rupture modeling we assumed that the fault slipped with a rake angle of 180 degrees. The FD grid spacing of 250 m used in our numerical simulation insured accurate wave propagation modeling up to 0.5 Hz. The best estimates of the final slip and initial rupture time distributions resulted from our dynamic rupture inversion are shown in Figure9. For comparison, in this figure, we also show the targeted final slip and initial rupture time distributions from the kinematic rupture model of Liu et al. (2006). Our dynamic slip model matches well the kinematic slip model. Most importantly we succeeded to match very well details of the kinematic initial rupture time distribution, too.

Dynamic Fault Rupture Model

The preferred dynamic fault rupture model is shown in Figure 10. The rupture parameters that we obtained through our spontaneous rupture modeling include the dynamic stress drop, static stress drop, strength excess, and slip weakening displacement.

The average stress drop is very low, less than 2 MPa. Elevated stress drops of about 5-10 MPa are concentrated in several small areas throughout the fault. Because of their relatively high stress drop, these areas of energy bursts can generate near-fault ground motion with locally large acceleration. The strength excess, which is one of the factors that controls the fracture energy, is low throughout the fault, except for the southern part where combined effects of high strength excess and low dynamic stress drop have caused the rupture to quickly stop. The rupture speed seems to have been larger than the shear-wave speed around the hypocenter and along a small portion of the southern end of the fault.
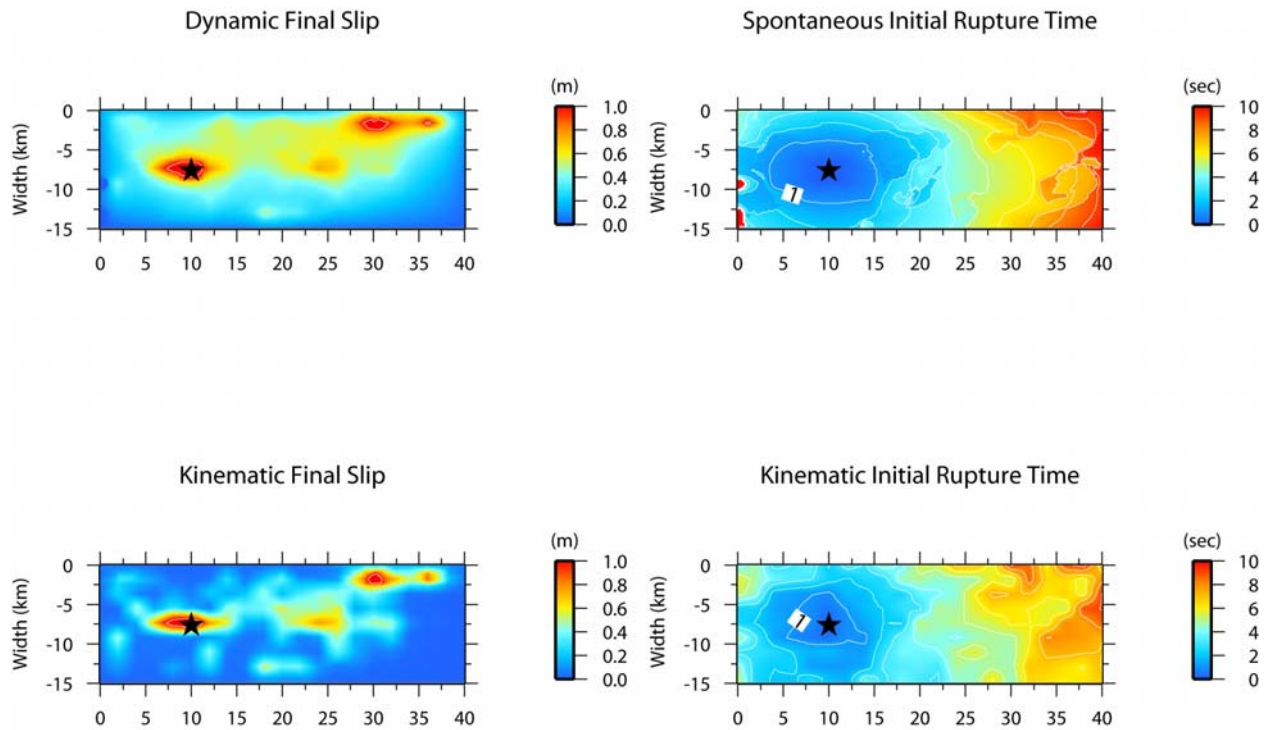
Figure 9. Comparison of dynamic (upper panels) and kinematic (lower panels) rupture models. Left panels show the final slip and the right panel show the initial rupture time. The kinematic model is from Liu et al. (2006).

Discussion

The unprecedented relatively dense ground motion recordings of the 2004 M_w6 Parkfield earthquake demonstrated that near-fault ground motion of shallow strike-slip earthquakes can be extremely variable. The degree of variability for this earthquake was related more to site conditions, including fault zone effects, rather than source effects. The observation of alternated very low and very high ground motion at many sites located close to the fault, and our investigation of site effects support this conclusion.

Our study cannot give a definitive answer to the question of how much the rupture process was responsible for the localized but very high acceleration observed near the fault. Unfortunately due to the numerical requirement, our kinematic and dynamic rupture models cannot resolve the process of generation and propagation of ground motion energy at frequencies higher than 1Hz. Nevertheless there are indications that a small portion of the fault in the south ruptured with a supershear speed. As predicted by numerical and laboratory experiments this could lead to localized high acceleration at small areas offset from the fault, similar to what was observed during this earthquake. Our investigation of site effects support an important conclusion of this study that the very large ground motion at station PF14 which recorded the highest acceleration of 1.3g, was mostly due to site effects, whereas the elevated ground motion to the south of epicenter (stations PS1E and PC3E) was probably due to the shock wave generated locally as a result of the supershear rupture in that region. This is a speculation that needs further
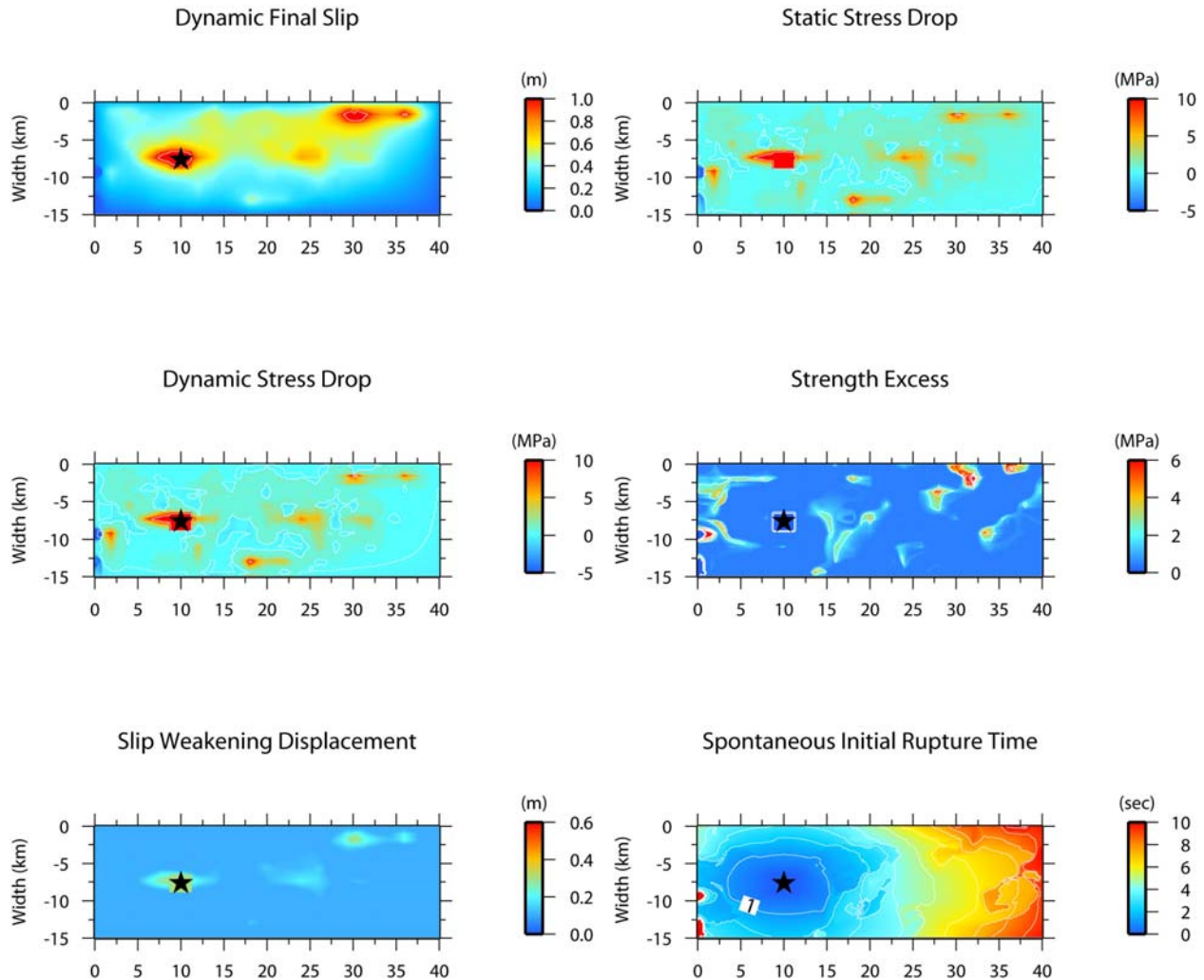
Figure 10. Dynamic rupture model of the 2004 Parkfield earthquake obtained by a trial-and-error inversion scheme and 3DFDM spontaneous rupture modeling. Star indicates the rupture initiation point.

investigations of the source process with higher resolution modeling and 3D wave propagation effects.

Our study leaves open the discussion about the possibility that a part of the spatial variation of high frequency ground motion was generated by very small asperities on the fault. These asperities are characterized by large stress drop and high slip velocity. These observed difference between fault-normal and fault parallel motion, which is an indication of rupture directivity effects, shows that near-fault ground motion from strike-slip earthquakes of moderate magnitude, such as the 2004 Parkfield earthquake, is affected by the rupture directivity at frequencies as high as 3 Hz.

Given the complexity in the observed ground motion and the band-limited information on the source process obtained for this earthquake it is interesting to see how well our broad-band

numerical simulation techniques perform in terms of predicting the average ground motion, the maximum ground motion and spatial variation of peak acceleration.

We simulated the recorded acceleration time history up to 10 Hz at all near-fault stations. In the simulation we used our kinematic model presented here and the technique of Graves and Pitarka (2004). The simulation technique combines deterministic and stochastic approaches to model the low frequency and high frequency parts of the acceleration time history. The simulated acceleration was finally corrected for site effects using site category and V_S^{30} values obtained from Wills et al. (2000).

Figure 11 shows the goodness of fit between the simulated and recorded ground motion. In general the spectral acceleration is matched very well at all considered periods. A negligible bias is observed. In Figure 12 we have plotted the recorded and simulated peak spectral acceleration as a function of distance at several periods, and compared it with the attenuation model of Abrahamson and Silva (1997) for this type of earthquake. The comparison shows that on average the ground motion from the Parkfield earthquake follows the existing empirical attenuation model. The simulation fails to produce the observed near-fault spatial variation of spectral acceleration. This is not surprising since, because of lack of information about the local underground structure at all strong motion sites, our simulation was mostly driven by the source process. Our study suggests that in order to capture wave propagation effects due to fault zone structure and local site conditions, 3D Green's functions and site specific corrections based on direct measurements of velocity are needed. Applying site-specific corrections, derived from the Coalinga earthquake data analyses, to the simulated peak acceleration and peak velocity results in a more favorable comparison (shown in Figure 13), especially north of epicenter.

Our main conclusion is that the relatively high and low peak acceleration, and the extremely spatially variable near-fault ground motion observed during the 2004 Parkfield earthquake were mostly driven by the local wave propagation and site effects. Unless such site effects are known, the broad-band strong motion simulation can not reproduce the ground motion variability very well. On the other hand the numerical simulation technique yields much better results than the ground motion empirical models in predicting spatial ground motion distribution and variability since it allows a better representation of the source process and underground structure characteristics.

Acknowledgements

References

Abrahamson,N.A. and W.J. Silva (1997). Empirical response spectral attenuation relations for shallow crustal earthquakes, *Seismological Res. Letters* **68**,94-127.

Andrews,D.J. (1976). Rupture velocity of plane-strain shear cracks, J.Geoph. Res., 81, 5679-5687

Borcherdt, R. (1994). Estimates of site-dependent response spectra for design (methodology and justification). *Earthquake Spectra*,10(4),617-653.
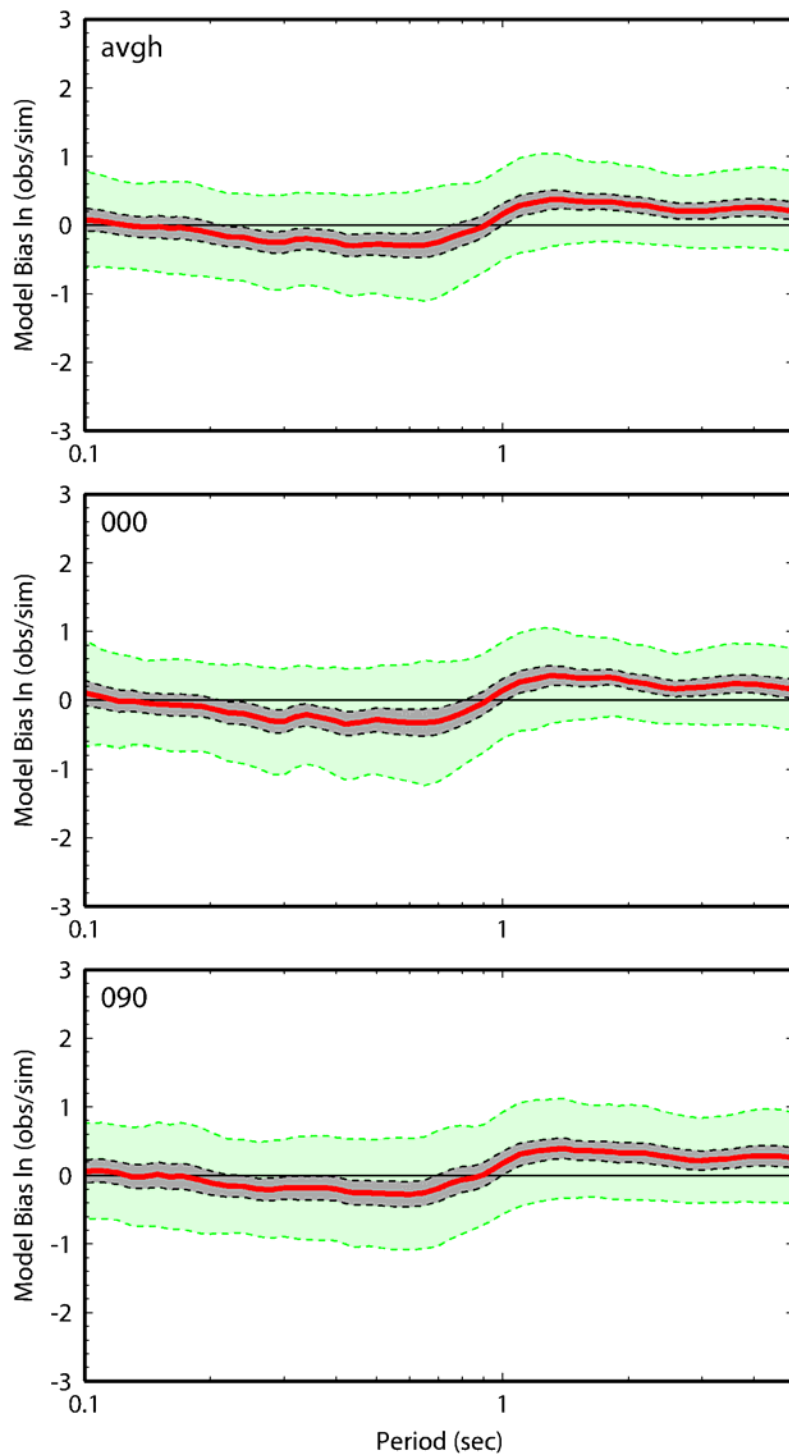
Figure 11. Spectral acceleration goodness-of-fit computed for the average of both horizontal components (top panel), fault parallel component (middle panel), and fault-normal component (bottom panel) for the Parkfield earthquake. Red line plots mean model bias averaged over all sites. Gray shading denotes 90% confidence interval of the mean and green shading denotes interval of one standard deviation.
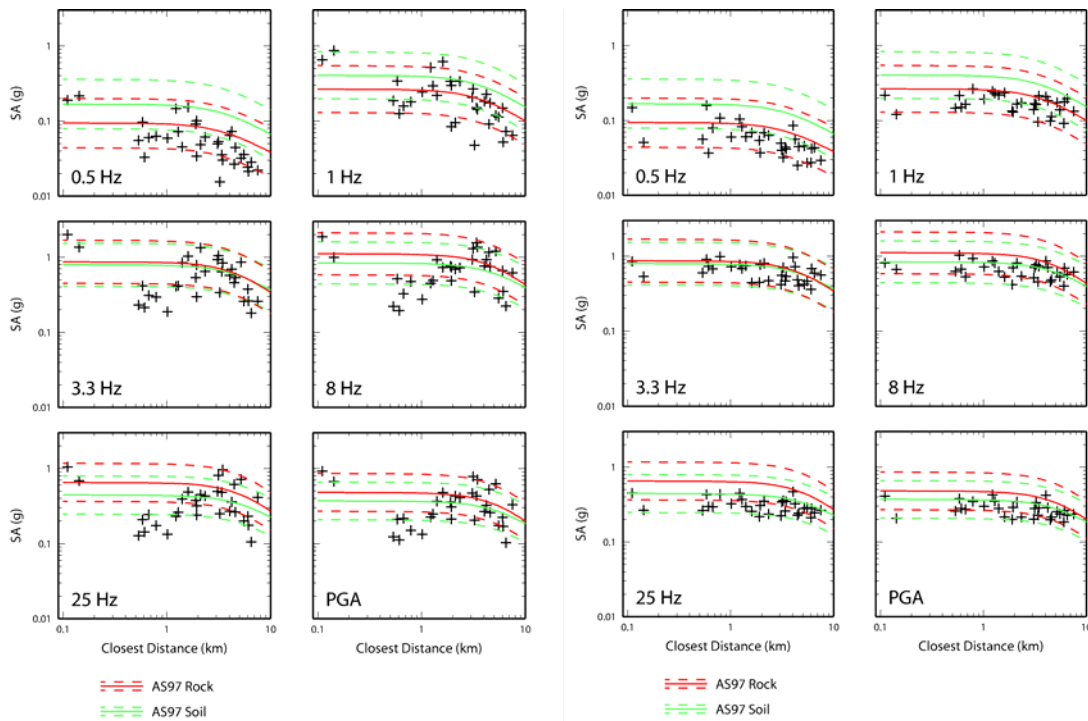
Figure 12. Comparison of recorded (left panels) and simulated (right panels) horizontal spectral acceleration indicated by crosses. Also shown are the Abrahamson and Silva (1997) empirical attenuation models for rock (red lines) and soil (green lines) site condition.
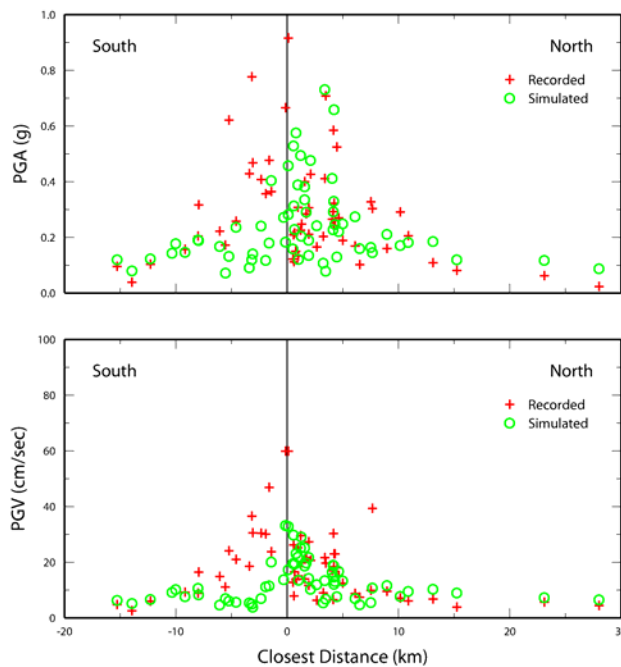
Figure13. Comparison of recorded (crosses) and simulated (circles) peak ground acceleration and peak ground velocity. The simulated values include site corrections. At sites that recorded the Coalinga earthquake the site correction was derived from theanalyzes of weak motion data recorded during the Coalinga earthquake.

Dickinson, W.R. (1966). Structural relations of San Andreas fault system, Cholame Valley and Castle Mountain Range, California. *Geological Society of America Bulletin*, **77**, 707-725.

Dalguer L. (2002). Strong motion prediction based on dynamic fault modeling. 2002 Report on MEXT Project.

Dalguer, L.A. and S.M.Day (2004) Split nodes and fault zone models for dynamic rupture simulations. EOS Trans. AGU, 85(47), Fall Meet.Supl. Abstract S41A-0944.

Eberhart-Phillips, D. (1989). Active faulting and deformation of the Coaling aniticline as interpreted from three-dimensional velocity structure and seismicity, *Journal of Geophysical Research*, **94**(13),15,565-15,586, 10.1029/89JB01390.

Eberhart-Philips,D., and A.J. Michael (1993). Three-dimensional velocity structure, seismicity,and fault structure in the Parkfield Region, central California, *Journal of Geophysical Research*,98,15,737.

Graves, R. and A. Pitarka (2004). Broadband time history simulation using a hybrid approach. Proceedings of the 13th World Conference on Earthquake Engineering, Vancouver, Canada, August 1-6, 2004, Paper No. 1098.

Haddadi,H.,A.Shakal,E.Kalkan,and P.Roffers (2006) On the strong ground shaking at the Fault Zone 16 and nearby ststions of Parkfield array. *Seism.Res.Lett.*,**77**,244.

Hardebeck, J.L., and A.J. Michael (2004). Earthquake locations before and after the 2004 M6.0 Parkfield earthquake, *AGU Fall Meeting Abstracts*, 85 (47).

Hartzell , S.H., and T.H. Heaton (1983). Inversion of strong ground motion and teleseismic wavefor data for the fault rupture history of the 1979 Imperial Valley, California earthquake. Bull.Seism.Soc.Am. **73**, 1553-1583.

Langbein,J., R.Borcherdt, D.Dreger, J.Fletcher, J.L. Hardebeck, M.Hellweg, C.Ji, M.Johnston,J.R.Muray, and R.Nadeau (2005). Preliminary report on the 28 September 2004, M6.0 Parkfield, California earthquake, *Seismological Res.Lett.*, **76**,10-26.

Liu, P., S.Custodio and R.J. Archuleta (2006). Kinematic inversion of the 2006 M_w6.0 Parkfield earthquake including site effects. *Bull. Seism.Soc.Am.* (in press).

Li,Y-G.,P.Chen, E.S. Cochran,J.E.vidale, and Th. Burdette (2006). Seismic evidence for rock damage and healing on the San Andreas fault associated with the 2004 M6 Parkfield earthquake. . *Bull. Seism.Soc.Am.* (in press).

Pitarka, A. (1999). 3D elastic finite-difference modeling of seismic motion using staggered grids with nonuniform spacing. *Bull.Seism.Soc.Am.* **89**, 54-68.

Pitarka A., and L. A. Dalguer (2003). Estimation of dynamic stress parameters of the 1992 Landers earthquake. *EOS Trans.AGU, 84(46). Fall Meeting Supp. Abstract*. S52A-0109.

Pitarka A. (2005) Rupture dynamics of the 1989 Loma Prieta earthquake , Seismolocal Research Letters, Vol 76, Nr.2., 252.

Shakal, A., V. Graizer, M. Huang, H. Haddadi, and K. Lin (2005). Strong-motion data from the M6.0 Parkfield earthquake of September 28,2004. *Proceedings of SMIP05 Seminar on Utilization of Strong Motion Data, Los Angeles, CA*, 1-18.

Thurber,C., S.Roecker,K.Roberts,M.Gold,L.Powell,and K.Rittger (2003). Earthquake locations and three-dimensional fault zone structure along he creeping section of the San Andreas fault near Parkfield, CA: Preparing for SAFOD. *Geophys.Res.Lett.* **3**, 1112, doi: 10.1029/2002GL016004.

Wills,C., Petersen, M.,Brayant,W.,Reichle, M.,Saucedo, G.,Tan,S.,Taylor,G.,Treiman,J. (2000). A site condition map for California based on geology and shear-wave velocity. *Bull.Seism.Soc.Am.* **90**,6B, S187-S208.

INSTABILITY INDUCING POTENTIAL OF NEAR FAULT GROUND MOTIONS

Dionisio Bernal[1], Arash Nasseri[2] and Yalcin Bulut[2]

[1]Civil and Environmental Engineering Department, Center for Digital Signal Processing, Northeastern University, Boston, MA.
[2] Graduate Student, Northeastern University, Boston, MA,

Abstract

Gravity imposes a lower bound on the strength needed for stable response. Collapse spectra are plots of this strength vs. period for constant values of a parameter that characterizes gravity. The paper contains formulas for collapse spectral ordinates for near fault conditions and shows that the collapse mechanism in buildings is not statistically dependent on whether the excitation is near fault or far field. Safety against instability can be predicted using the provided expressions and results from a pushover analysis. The near fault condition is not found to be a critical consideration from an instability perspective.

Introduction

Dynamic instability is a phenomenon whereby the seismic response of a structure changes from vibration to unbounded drift in a single direction. Since the consequence of dynamic instability is complete collapse, characterization of this limit state is of paramount importance for the formulation of performance based seismic design guidelines. The salient feature of the instability phenomenon is the fact that it is abrupt. Indeed, as shown by Husid (1967), Jennings and Husid (1968), Takizawa and Jennings (1980) and Bernal (1990) for simple systems, and by Bernal (1992a, 1992b, 1998) using models of multistory structures, the influence of gravity on inelastic seismic response is generally small except for a small range of values where the strength of the system is near a threshold bellow which the response grows without bound. The situation is exemplified in fig.1 which depicts the maximum displacement at the first level of a model of a ten story building for increasing levels of a scaling factor that multiplies the ground motion amplitudes. The figure, which compares results from first order and second order nonlinear dynamic analyses shows that the maximum response is little affected by P-delta except in a restricted region near the strength for which instability occurs.

The behavior exemplified in fig.1 is typical and shows that the important issue in design is not assessing amplifications of the displacement response due to P-delta effects but establishing means to quantify the safety margin against the instability limit state. Note that the foregoing is not in harmony with the amplification approach that for many years has been used to consider P-delta effects in the analysis of buildings for wind, dead and live loads. Specifically, the amplification perspective is misleading because it suggests that the issue is one of "adjusting" the estimated response and this is not so. Plainly, since inertial loads during seismic excitation are not independent of structural characteristics the P-delta effect needs to be considered as a reduction in lateral stiffness, not as an added load. As noted, the important task from a practical

perspective is to characterize the instability limit in a way that is useful from the point of view of a designer that needs to ensure that safety against instability is adequate.
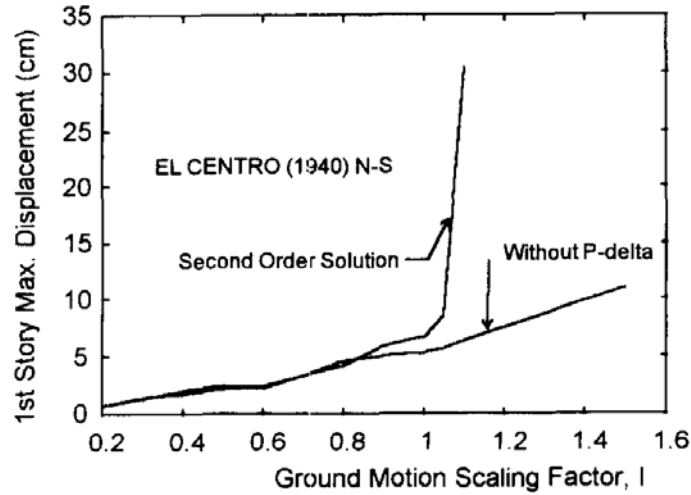

Fig.1 Maximum response at level#1 in a 10-story model of a steel frame

It is not difficult to see that experimental investigations to determine the collapse threshold or realistic structures subjected to earthquakes are impracticable. Virtually all the research in this area, therefore, is analytical. In this regard it is worth noting that formulation of high fidelity models for buildings that undergo large inelastic displacements is a very difficult task. For example, quantifying the participation of floor systems in providing lateral stiffness as a function of response history and amplitude is one of many items that can be listed as difficult to model accurately. An indication of the degree of simplification is the fact that while collapse takes places "downward", all our models for buildings predict it as large "lateral displacements".

Having accepted that analytical predictions of collapse are necessarily uncertain we must nonetheless move forward and make the best possible estimation given the constraints. While the "best" analytical prediction is in principle that obtained from a 3-D model that accounts for soil-structure interaction, non-structural element contributions, and which models the load-deformation relation of each structural element in as much detail as the state of knowledge allows, this model is generally impractical. In arriving at a practical solution one seeks, of course, to maximize reductions in the computational burden while adding the least possible uncertainty to the results. A brief summary of modeling related decisions made in this study is presented later in the paper and details can be found in the full report that appears in (Ref.1).

Assertions made in the previous paragraphs regarding instability are qualitative and independent of the specific characteristics of the ground motion. It has become increasingly clear in the past few decades, however, that records obtained in the close vicinity of the causative fault differ substantially from those in the far field and this has prompted concern on the adequacy of using design guidelines that have been validated using far field records in checking structures located close to known faults. The special feature of strong motion records obtained near faults is the fact that they often contain large velocity pulses of relatively long periods and/or large permanent displacements (Sommerville 1997, Rodriguez-Marek 2000). Prior to the project

reported on this paper research carried out on response to near fault motions had focused on characterizing the effect of near fault on linear and nonlinear effects, primarily on SDOF oscillators (MacRea,2001 and Mavroeidis,2004). The studies from these and other references produced consistent results and at present some modern codes (IBC-2004, FEMA356, ATC40) have incorporated near fault effects as modifiers of the elastic spectral ordinates (Table.1).

Table 1. Near fault modification factors for the acceleration (N_a) and velocity region (N_v) of the elastic response spectrum – as given in the IBC-2003 Code.

		N_a			N_v			
Type	Source	= 2 km	5 km	10km	= 2 km	5 km	10km	15km
A	M>7 SR≥5mm/yr	1.5	1.2	1.0	2.0	1.6	1.2	1.0
B	Not satisfying A or C	1.3	1.0	1.0	1.6	1.2	1.0	1.0
C	M=6.5 SR=2mm/yr	1.0	1.0	1.0	1.0	1.0	1.0	1.0

The question of whether or not structures located in the near fault require special treatment when it comes to the evaluation of the safety against instability is the basic question addressed in this study. For buildings in sites that are not too close to the seismic source the safety against this failure mode can be evaluated in terms of base-shear strength, shape of the controlling mechanism and the peak ground motion parameters and effective duration of the design motion (Bernal 1993, 1998). The research reported here shows that this framework can be used for near fault conditions also.

The paper is organized as follows. The first section following this introduction presents a summary of the existing methodology for characterizing instability, originally developed without regard for the frequency content of the records. The next section considers the development of statistical formulas for predicting collapse spectral ordinates for near fault conditions. Following the collapse spectra section the paper presents the results of a study on the instability of multistory structures. The results in this section are based on the examination of 3 structures varying from 6 to 20 stories in height. A summary and critical review of the findings concludes the paper.

Dynamic Instability Fundamentals

We adopt the definition that a structure subjected to a certain input is stable if small increases in the magnitude of the excitation result in small changes in the response. We begin by recalling that static stability can be ascertained by inspecting the eigenvalues [λ] of the effective tangent stiffness. In particular, since these eigenvalues represent generalized scalar stiffness values in the configuration of the associated eigenvectors [ϕ], static stability requires that all the terms in [λ] be positive. An equivalent more intuitive statement is that a structure is stable if the

change between any two equilibrium positions requires positive work from external forces. An obvious example of an unstable system is a ball on a slope. If one holds the ball in equilibrium by applying an external horizontal force and then allows it to move down the slope slowly to a new position the external work (not including gravity) is obviously negative. This example also shows that instability is associated with a specific direction, i.e., the ball roles down but not up. The parallel in a structural system is that the structure will deform "spontaneously" (with the help of gravity) in the direction of the eigenvector associated with the negative eigenvalue, not in other directions.

Configurations that are statically unstable can occur during dynamic response without resulting in collapse so the attainment of negative eigenvalues is a necessary but not a sufficient condition for dynamic instability. A mathematical discussion of how inertia provides the transient stabilizing forces that allow the system to "survive" configurations that are statically unstable is presented in Bernal (1998). Here, instead of repeating the mathematical treatment we clarify the basic behavior using a simple physical analogy. Consider, as shown in fig.2, the situation wherein a disc (to keep the problem in 2D) rests on a line whose concavity fluctuates dynamically from upward to downward. The disk represents the structure; the condition with upward concavity the times when the structure is statically stable and downward concavity that when yielding is so extensive that the tangent stiffness is insufficient to provide static stability. It should be apparent at this point that incursions into the downward concavity do not necessarily imply that the disc is going to roll down the surface and fall off. Namely, the outcome will depend on how long an unstable condition persists. Although the analogy is not precise, since in the situation of fig.2 the disc tends to return to a unique equilibrium position and this is not true in the structure, this flaw does not invalidate the basic idea which is that statically unstable configurations are necessary but not sufficient for dynamic instability.
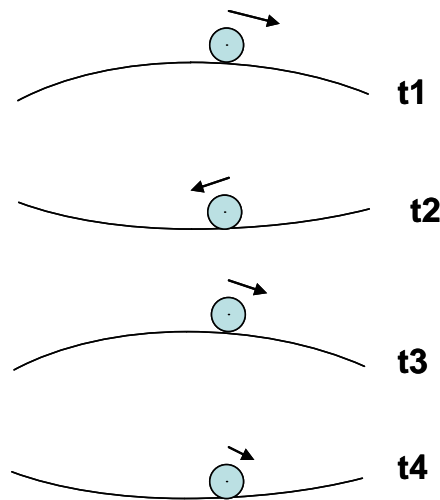

Fig.2 Analogy used to describe the ability of a structure to dynamically survive configurations that are statically unstable.

While it may appear at first glance that sufficient inelasticity to result in statically unstable configurations during earthquake response is unlikely, a closer look can dispel this first impression. The key point is that for negative eigenvalues to be attained there is no need for inelasticity to be such that the structure is rendered a mechanism. The point is illustrated in fig.3 which shows the variation of the fundamental buckling eigenvalue as a sequence of hinges progress up the structure. The structure in the figure is 6 stories high and the gravity load has been taken at a representative value, in particular, the buckling eigenvalue with no hinges is 10, which implies that the elastic buckling load is 10 times larger than the gravity loading condition considered. As the figure shows, if a wave of hinges that engages the beams of the lower 2 stories plus the column bases exists at any point the structural configuration is, from an instantaneous perspective, unstable.
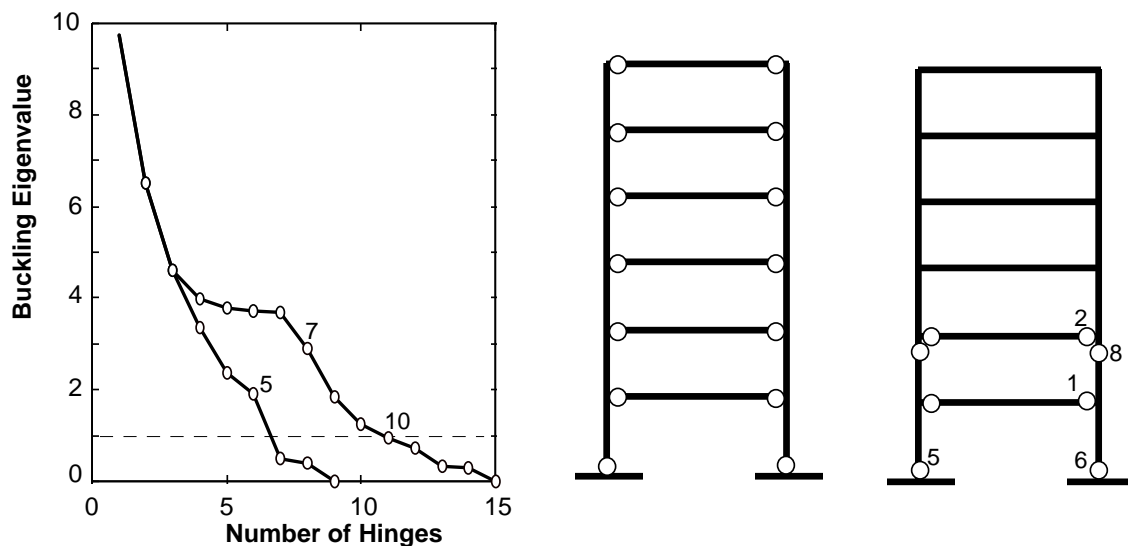

Fig.3 Buckling eigenvalue as a function of the distribution of plastic hinges

Characterizing the Effect of Gravity in the Load Deformation Behavior

The theory needed to formulate and analyze a full detailed model of a structure including nonlinearity and second order geometric effects is well established. Note that we do not imply here that it is easy or even possible to make a model that captures all the complexities of the real situation but simply that once the basic assumptions are made a material and geometrically nonlinear representation of a system can be formulated and analyzed. A direct check of the safety against instability by performing nonlinear dynamic analysis of a full model of each building is, however, impractical for routine application and for this reason simplified procedures compatible with the level of complexity of typical seismic provisions are necessary. Furthermore, it is in the reduced parameterization of a simplified method that the key parameters that affect behavior become clear and show which structural modifications have significant effect on the safety against instability and which do not.

The Stability Coefficient in a SDOF System

A parameter that has been widely used in simplified characterizations of second order gravity effects is the so called stability coefficient θ. The stability coefficient has been the subject of much discussion in the technical literature and is sometimes the source of confusion when sight is lost of the fact that there is no such thing as "the exact stability coefficient" for a multistory structure that responds nonlinearly, just like there is no such thing as "the ductility" at a given instant. The stability coefficient is non-dimensional parameter defined such that when multiplied by the first order elastic stiffness it gives the reduction in stiffness resulting from P-delta.

To clarify consider a rigid column supported at the base by a pin plus a nonlinear rotational spring. The column is assumed massless and weight is assumed concentrated at the tip as depicted in fig.4a. The load deformation relationship including the effect of the weight acting on the deformations can be easily computed and used to obtain the second order response. It is not difficult to see that the second order load deformation curve is obtained (in the simple situation of fig.4) by subtracting a constant slope from the first order curve. If we normalize the reduction in slope by the initial elastic slope one gets θ. In a MDOF system there is no unique load deformation curve and, even after one decides what function of the load to plot vs. what deformation the difference between the first order and second order curves is not, in general, a constant reduction in slope.
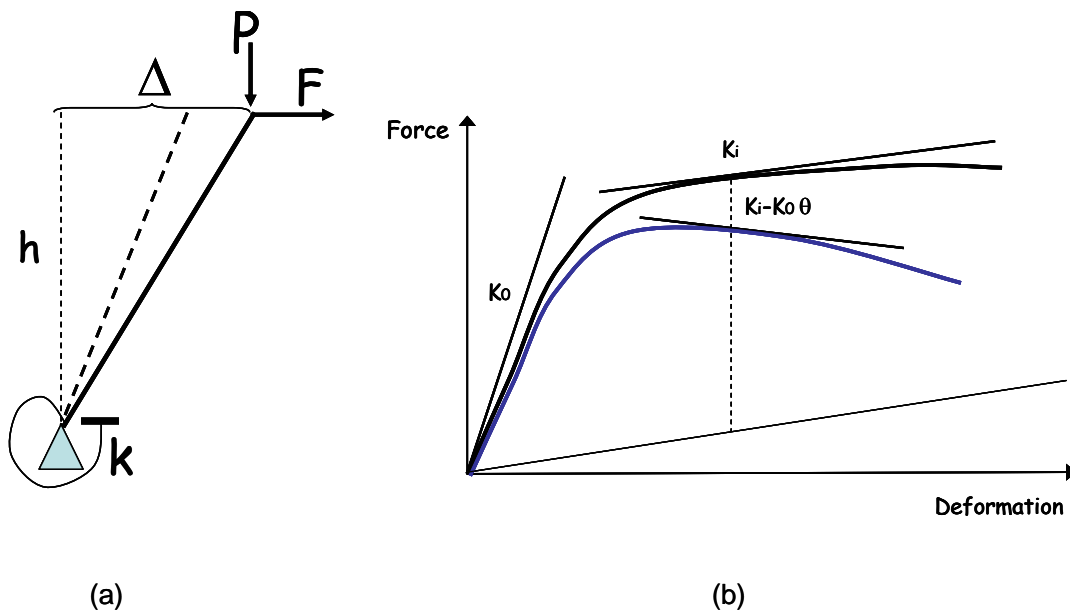

(a)   (b)

Fig.4 a) Rigid Column with rotational base spring b) First and second order load deformation curves.

The Stability Coefficient in a MDOF System

In a SDOF the value of θ is equal to the inverse of the elastic buckling eigenvalue. The buckling definition offers a tempting extension of the stability coefficient to the MDOF case but there is a need to be careful because the real question is not whether the definition is easily computed but whether the value is a good indicator of how gravity affects the potential for dynamic instability in buildings. To be explicit, if one tentatively accepts that there is a way to arrive at a SDOF model whose collapse occurs at the same ground motion intensity that produces instability in the real building, the question is whether a θ based on the elastic buckling eigenvalue is a good indicator of the difference between the first order and the second order load deformation of this SDOF system.

The answer, in general, is that the buckling based θ is not a good indicator and the reason has to do with the fact that in a MDOF system the reduction in slope of the load deformation due to P-delta depends on the predominant shape of the structure during the response and this shape, at large amplitudes can differ notably from the elastic buckling shape. Since in a first approximation the elastic buckling mode of a building is a straight line one concludes that the elastic buckling based θ should be reasonable when the governing mechanism is a global tilt.

Retaking the basic idea that θ is a way to specify how to pass from the first to the second order load deformation curve one has

Slope of 2nd order load deformation = Slope of 1st order - θ (Slope of first order at the origin)

from where one gets

$$\theta = \frac{\text{1st order slope} - \text{2nd order slope}}{\text{1st order at origin}} \tag{1}$$

MDOF to SDOF Reduction

The motivation for obtaining a reduction of the building to a SDOF system resides in the fact that instability can be characterized in terms of a few parameters in the SDOF case. In other words, if one can estimate when instability is imminent in a SDOF and has a procedure to reduce a multistory building to a SDOF then safety against instability in the building can be estimated without the need to perform nonlinear time history analysis of the full model. Reduction of a set of dynamic equilibrium equations to a single equation introduces approximation by necessity. The simplest approach to affect the reduction is by assuming a shape and solving for the amplitude. In this regard it should be noted that even in the simplest case of a linear system and a constant shape the solution is still not unique since there are various alternatives that arise from how the inevitable error is treated. To illustrate consider the equations of motion for earthquake input for a linear system which, neglecting damping can be written as

$$M\ddot{u} + Ku = -Mr\ddot{x}_g \tag{2}$$

To reduce the system to a SDOF we take

$$u \approx \phi Y \tag{3}$$

where ϕ is an assumed shape and Y is the amplitude. Substituting eq.3 into (2) gives

$$M\phi\ddot{Y} + K\phi Y = -Mr\ddot{x}_g + \varepsilon \tag{4}$$

where ε is a residual term that is needed because eq.3 is an approximation and eq.4 has been written as an equality. Since the left hand side of eq.4 has one unknown one can decide to satisfy the equality at a given DOF or, more generally, one can make any weighted sum of the terms in ε equal to zero and solve for the corresponding Y. Namely, with the weights listed in the vector φ one pre-multiplies by φ^T and taking $\varphi^T\varepsilon = 0$ gets the SDOF equation

$$\varphi^T M\phi\ddot{Y} + \varphi^T K\phi Y = -\varphi^T Mr\ddot{x}_g \tag{5}$$

Note that eq.5 depends not only on the assumed shape ϕ but also on the weights φ. The selection of $\varphi = \phi$ is, of course, common but is not forced by any compelling reason. Anyway, the point we set out to make is that even in the simplest case of linear behavior there are choices on how one arrives at the SDOF equation. In a study of instability the situation is much more complex because the assumption of a single dominant shape is not sufficiently general. Specifically, the shape of the structure when the response is not yet near collapse is governed by a shape that can usually be taken as the first mode but as the structure approaches failure the shape of the controlling mechanism dominates and this shape can vary notably from that of the first mode. A possibility that comes to mind is to perform a reduction using more than one shape but this is not a viable option since the characterization that is truly tractable is based on a SDOF model. The other possibility, initially examined by Pique (1976) and developed in detail for instability analysis by Bernal (1993) is to generalize the constraint in eq.3 as

$$u \approx Yf_Y \tag{6}$$

In other words, we assume a shape that is amplitude dependent. In Bernal (1993, 1998) and in the research reported here the amplitude dependent shape is taken as the sequence of deformed patterns that result from a pushover analysis using a mass proportional lateral load distribution. Description of the details of the SDOF reduction for the amplitude dependent shape is unnecessary for the present objectives and is thus skipped for brevity; the interested reader can find the details in the original references.

SDOF Reduction

1. Perform a first order pushover analysis with a load distribution that is proportional to the story weights (uniform in the case or regular buildings). From this analysis extract the

maximum base shear that the structure can withstand, V_u, and the parameters that define the shape of the final mechanism (see fig.5).

2. Calculate two stability coefficients. One that governs when the dominant shape is not far from the first mode, θ_0, and the other which accounts for the shape of the mechanism θ_m. The formulas are:

$$\theta_0 = \frac{g\tau}{\omega_0^2 h} \tag{7}$$

$$\theta_m = \Omega\theta_0 \tag{8}$$

with

$$\Omega = \frac{1 + 2N(1 - \dfrac{E}{h} - 0.5\dfrac{G}{h})}{\dfrac{G}{h}(1 + 2N(1 - \dfrac{E}{h} - 0.67\dfrac{G}{h}) + \dfrac{1}{3N}} \tag{9}$$

where ω_0 = fundamental frequency of the elastic structure in the direction considered, h, G and E are defined in fig.5, N = number of stories, g = acceleration of gravity and τ = ratio of total vertical load to the inertial weight used to compute the fundamental frequency (typically around 1.1 since it is reasonable to assume a reduced live load during the extreme event).
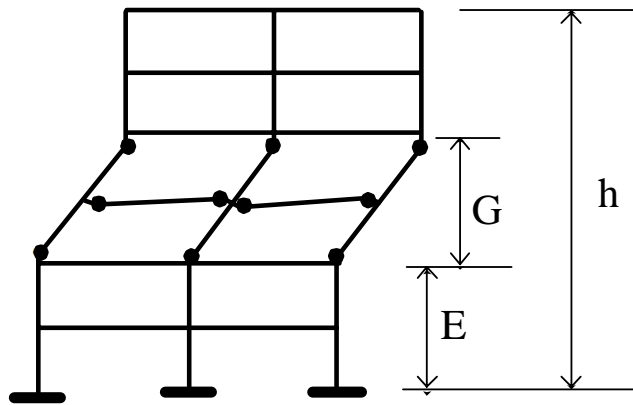

Fig.5 Parameters that define the critical mechanism

The SDOF to investigate instability has a unit mass and a damping equal to the damping of the fundamental mode, the envelope of its first order load deformation curve is assumed elasto-plastic with a yield level given by the shear V_u and the elastic stiffness is selected such that the elastic period is

$$T_e = \frac{T_1}{\sqrt{Q}} \tag{10}$$

where T_1 is the period of the fundamental mode in the structure (in the direction of analysis) and

$$Q = 1 + \theta_m - \theta_0 \qquad (11)$$

The second order curve is obtained from the first order one by using the effective stability coefficient

$$\theta_e = \frac{\theta_m}{Q} \qquad (12)$$

The first and second order load deformation relations (per unit mass) are illustrated in fig.6.
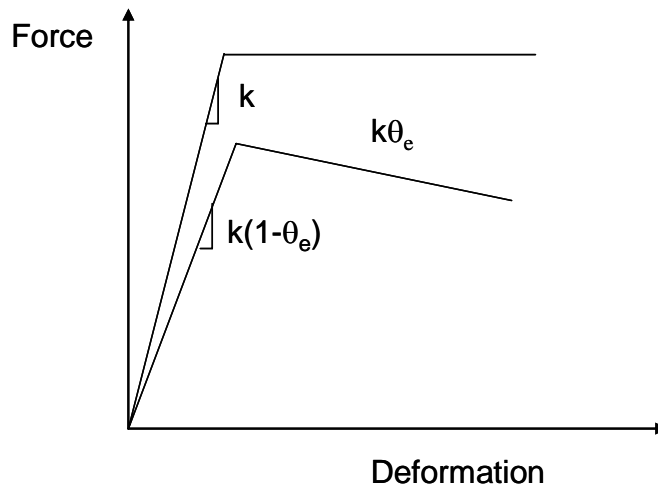

Fig.6 First and second order curves of SDOF reduction for instability analysis

A check against instability can be carried out by subjecting the SDOF reduction described previously to a set of appropriate ground motion time histories. The need to have explicit ground motions and to perform non-linear dynamic analyses, however, detracts from practicality. A much more practical approach consists in characterizing the collapse level response in terms of the relevant parameters of the SDOF reduction and the critical parameters of the ground motion using the concept of collapse spectra (Bernal 1993, 1998).

Collapse Spectra

Collapse spectra are plots vs. period (based on the initial elastic stiffness) of the minimum yield strength (per unit mass) of a SDOF for which the response is stable. These spectra can be viewed as the limit to which inelastic spectra converge when the ductility is arbitrarily large and second order effects are considered. Collapse spectra are conveniently plotted for a specific record for a constant stability coefficient. To aid clarity, the collapse spectrum for a record obtained during the Parkfield event of 2004 is depicted in Fig.7 for two values of the stability coefficient. Collapse spectra are little affected by damping so it is

customary to use 5% of critical damping based on the initial first order elastic characteristics of the SDOF system.
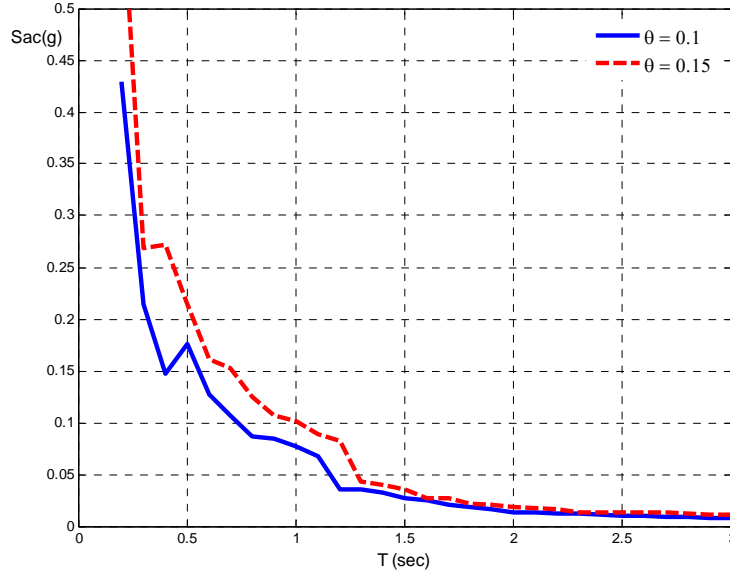

Fig.7 Collapse spectra for Parkfield 9/28/04 Vineyard Canyon 3 west station projected to the fault normal direction

Procedures to estimate elastic and inelastic spectra in terms of peak ground motion parameters and ductility (in the inelastic case) have long been available (Newmark and Hall 1982, Ridell 1979). Statistical formulas for collapse spectra were developed for systems with elasto-plastic and degrading stiffness hysteresis by Bernal (1993) using a set of far field records. At the mean level the formula for the elasto-plastic hysteresis is

$$S_{ac} = \frac{5PGV.t_{0.9}{}^{0.5}\theta^{0.75}}{T^{1.42}} \leq \frac{36PGD \cdot t_{0.9}^{0.2}\theta^{0.75}}{T^{1.86}}$$ (13)

where PGV and PGD stand for peak ground velocity and peak ground displacement, T is the period in sec. and $t_{0.9}$ is the effective duration of the ground motion, defined as the time over which the cumulative integral of the squared acceleration goes from 5% to 95% of its total value at the end of the record. The estimation of the minimum base shear strength for which the response is stable is taken as

$$V_c = S_{ac}M$$ (14)

where S_{ac} is the collapse spectral ordinate for the fundamental period and effective stability coefficient and M is the total inertial mass of the building.

Collapse Spectra for Near Fault Motions

The SDOF reduction and the concept of collapse spectra are general but extension to the near fault condition requires determining 1) if the formulas for S_{ac} developed for the far field hold for near fault motions and 2) if the uniform load distribution is adequate for predicting the collapse mechanisms that controls when the motions are impulsive.

In this research the first question was initially examined by carrying out an extensive statistical study using a collection of 43 records obtained during the M=6 Parkfield earthquake of 09/28/04. In the study the motions were first projected in the fault normal and fault parallel directions and the analysis was carried for each set separately. It was found that eqs14 and 15 predicted the collection of collapse spectra well so, on the basis of these data it did not appear that special considerations were needed for defining S_{ac} for near fault conditions. In this regard it is worth noting that while there was some difference in results between the fault parallel and the fault normal directions the differences were not sufficiently large to warrant special treatment.

Nevertheless, since the Parkfield event of 2004 is relatively low magnitude (M=6) and directivity effects in near fault motions are more prevalent in large magnitude events it was judged prudent to look at a second ensemble of near fault records before arriving at conclusions. To do this a number of records that displayed significant near fault effects were identified and the ones chosen for analysis are listed in Table 2. The motions in Table 2 were also projected in the fault normal and fault parallel orientations and the analysis was carried out independently in each direction. In contrast with the Parkfield data the analysis in this case did suggest that special expressions for predicting Sac for near fault conditions may be useful.

Table 2. Near fault records used in the study to complement the Parkfield data.

Number	Location	Date	Mw	Station	Distance (km)	Strike Angle	Angle		Rotation Angle
							Chanel 1	Chanel 2	
1	Kobe, Japan	16-Jun-95	6.9	TAZ	0.4	45	0	90	140
2	Nahanni-Canada	23-Dec-85	6.8	SITE2	5.2	160	240	330	5
3	Tabas-Iran	16-Sep-78	7.11	TAB	1.2	330	344	74	256
4	Imperial Valley,CA	15-Oct-79	6.5	E04	6	143	140	230	274
5	Imperial Valley,CA	15-Oct-79	6.5	E05	2.7	143	140	230	274
6	Imperial Valley,CA	15-Oct-79	6.5	E06	0.3	143	140	230	274
7	Imperial Valley,CA	15-Oct-79	6.5	E07	1.8	143	140	230	94
8	Imperial Valley,CA	15-Oct-79	6.5	EMO	1.2	143	270	0	324
9	Supersition Hills,CA	24-Nov-87	6.4	PTS	0.7	130	225	315	355
10	Loma Prieta CA	17-Oct-89	6.9	LGP	3	130	0	90	220
11	Loma Prieta CA	17-Oct-89	6.9	STG	8.3	130	0	90	40
12	Erzincan, Turkey	13-Mar-92	6.63	ERZ	2	125	0	90	214
13	Landers, CA	28-Jun-92	7.2	LUC	1.1	335	0	75	233
14	Northridge, CA	17-Jan-94	6.7	JFA	5.2	120	292	22	280
15	Northridge, CA	17-Jan-94	6.7	RRS	6	120	228	318	344
16	Northridge, CA	17-Jan-94	6.7	SCG	5.1	120	52	142	160
17	Northridge, CA	17-Jan-94	6.7	SCH	5	120	288	18	291
18	Northridge, CA	17-Jan-94	6.7	NWS	5.3	120	316	46	76
19	Chi Chi, Taiwan	20-Sep-99	7.6	TUC052	0.8	60	0	90	90
20	Chi Chi, Taiwan	20-Sep-99	7.6	TUC068	0.2	60	0	90	90
21	Chi Chi, Taiwan	20-Sep-99	7.6	TUC075	0.6	60	0	90	270
22	Chi Chi, Taiwan	20-Sep-99	7.6	TUC129	1.5	60	90	0	0

The statistical analysis used to arrive at the expressions for collapse spectra is summarized next.

1. Data on collapse spectra was generated from simulations.

For each of the records in Table 2, S_{ac} was computed by running nonlinear second order dynamic analysis with different strength levels until the minimum strength to prevent instability was identified. This was done for $\theta = \{0.05, 0.1, 0.15, 0.2\}$ for systems varying in period from 0.2 to 6.0 seconds.

2. The collapse spectra were normalized to $GMP \cdot t_{0.9}^{\gamma}$ where GMP was PGA, PGV or PGD and γ is a constant taken as 0, 0.1, 0.2 etc up to 1.0.

A total of 33 plots of coefficient of variation (COV) vs. period for the generated collapse spectra were obtained. For each ground motion parameter there is an exponent of the effective duration that minimizes the COV in the region where the parameter is most effective in reducing the spread. A plot of COV for the 3 optimal combinations $GMP \cdot t_{0.9}^{\gamma}$ is depicted in fig.8 for the fault normal and the fault parallel directions for $0 \leq T \leq 3$ sec. Note the level of the COV, between 0.3 and 0.4 when the appropriate normalization is selected, is typical of statistical work for the definition of spectra (Newmark and Hall 1982). Results for T> 3 sec. can be found in Ref.1.
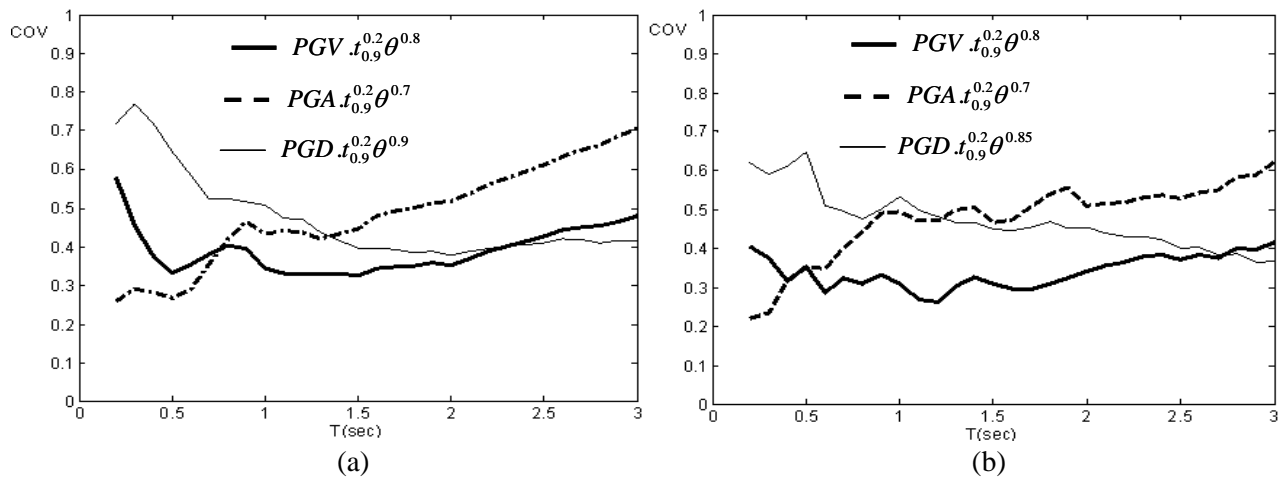

(a)   (b)

Fig. 8- COV of normalized collapse spectra to different peak ground parameter
a) fault normal component b) fault parallel component

3. The expression given in eq.15 was postulated and the free parameters $\{\alpha, \beta, \gamma, \lambda\}$ selected to minimize the spread between the predictions and the data.

$$S_{ac} = \frac{\alpha\, \theta^{\beta}\, GMP\, t_{0.9}^{\lambda}}{T^{\gamma}} \tag{15}$$

The units of S_{ac} are the same as the units in PGA or those in PGV divided by sec. or in PGD divided by sec^2. The optimum values for the free parameters are listed in Table 3.

Table 3. Optimal values of the free parameters in eq.15

GMP	Fault Normal				Fault Parallel			
	α	β	γ	λ	α	β	γ	λ
PGA	1.53	0.7	0.2	0.57	1.97	0.7	0.2	0.42
PGV	12.05	0.8	0.2	1.51	10.04	0.8	0.2	1.17
PGD	42.66	0.9	0.2	1.94	61.91	0.85	0.2	2.21

Although the coefficients in Table 3 were obtained by minimization over a fixed frequency band, in practice it is best to use the eq.15 without imposing fixed transitions because this avoids discontinuities. In particular, at any period one simply takes S_{ac} as the smallest value obtained from any of the 3 possible normalizations. A quick appreciation of the accuracy of eq.15 when compared to the simulated data can be developed from fig.9, which shows predictions and simulations at the mean level.
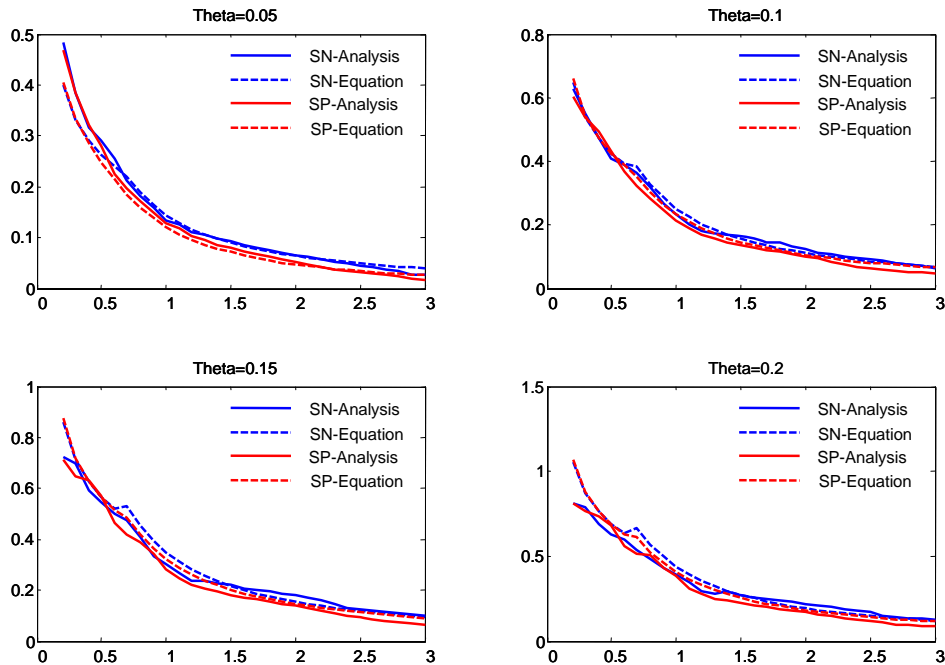

Fig.9. Comparison of actual Sac from numerical analysis with Sac from eq.15 and the coefficients in Table 3 (mean level results, in g's).

Instability Limit Reduction Factor (R$_c$) and the Instability Severity Index (ISI)

Before moving on to multistory buildings it is useful to pose the question: is the near fault condition critical regarding instability? The key to answering this in a meaningful way is to look

at it from a perspective that is entirely dependent on frequency content and duration. An index that satisfies the previous requirement is the ratio of the minimum strength needed to ensure that the response is elastic to the strength bellow which instability takes place. Note that this ratio is the limit that instability imposes on the classical reduction factor R which codes have long used to estimate the strength level that needs to be provided in design as a fraction of the elastic response level. We have, therefore

$$R_c = \frac{S_{ae}}{S_{ac}} \tag{16}$$

The interest lays in determining whether R_c is typically larger or smaller in the near fault than in the far field, where a large value means that instability does not pose a strong limit. For this purpose one can define an Instability Severity Index (ISI) as the inverse of the ratio of the R_c value associated with the near fault condition divided by some R_c for the far field that serves as a reference, specifically

$$ISI = \frac{1}{\dfrac{R_c^{near\,fault}}{R_c^{far\,field}}} \tag{17}$$

Substituting the expressions for R_c in terms of S_{ac} and S_{ae} one finds that ISI can also be written as

$$ISI = \left(\frac{S_{ae}^{far\,field}}{S_{ae}^{near\,field}} \right) \left(\frac{S_{ac}^{near\,field}}{S_{ac}^{far\,field}} \right) \tag{18}$$

In eq.18 the first ratio is always less than or equal to one because the near field effect either increases the elastic spectral ordinate or leaves it unaffected. One gathers then, that for ISI to be greater than unity (i.e., for the near fault condition to be "more severe" in the sense that we're here characterizing it, the increase in the minimum strength to prevent collapse has to be larger than the reduction of the first term. Plainly, if the near fault condition requires x% increase in elastic strength and y% increase in the minimum strength for stability then we say that the near fault condition is severe (i.e., ISI >1) if y > x.

Fig.10 plots ISI where S_{ac} is obtained from eqs.13 and 15 for the far field and near fault condition respectively and S_{ae} is computed using the well known Newmark-Hall elastic response Spectrum construction approach with the near fault effect considered using the factors in Table.1. While fig.10 corresponds to a specific set of parameters, the qualitative behavior displayed holds for a wide range, namely: ISI is typically less than unity for short periods and for rather long periods but can exceed one in some intermediate range. Although the results show clear differences in the fault normal and fault parallel directions we refrain from making observations on this regard because the information in Table 1 is not direction specific. The fact that ISI is less than unity for long periods is consistent with what one anticipates from a qualitative reasoning since long period structures necessarily fail by crawling and the near fault motion is less capable of forcing this mechanism given the small number of significant pulses. In the short period range the reason is less intuitively evident but mathematically it derives from the

fact that the increase in the elastic spectral ordinate is larger than the increase in the strength to prevent collapse.
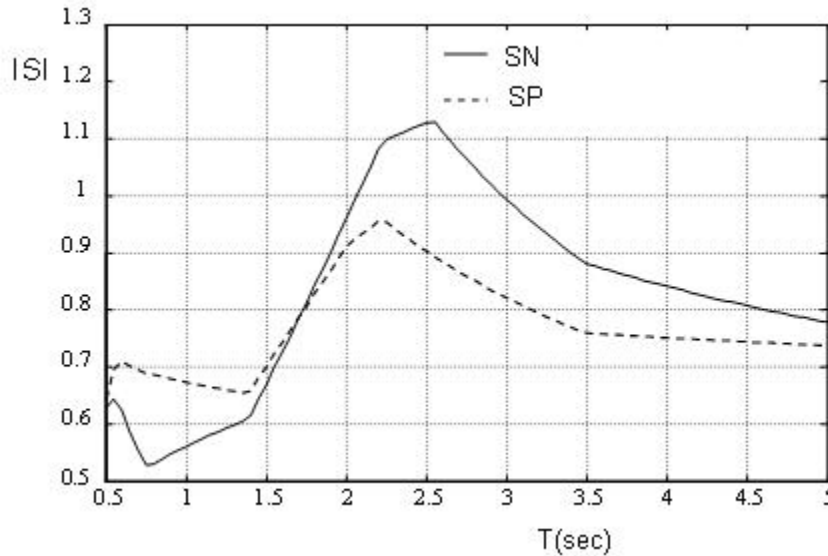

Fig.10 Instability Severity Index vs period (PGV/PGA=0.124 sec, PGD/PGV=0.48 sec $\theta = 0.1$, $t_{0.9} = 10$ sec, Na=1.2, $N_v = 1.6$ (from Table 1))

Examination of Multistory Structures

In this part of the research 3 multistory structures were considered and results computed for a large ensemble of records from the Parkfield event and for 9 motions taken from the set that appears in Table 2. The study can be subdivided into two large sections: 1) computation of ISI indices and 2) investigation of the accuracy that can be attained in predicting instability using the SDOF reduction approach described previously and the collapse spectral ordinate expression presented as eq.15 (with the coefficients in Table 3).

Mathematical Modeling

As noted earlier in the paper, the formulation of an accurate model for a 3-D structure to investigate the response up to collapse from instability is difficult. In this study a significant simplification resulted because all the structures considered are regular in plan so little is lost by using a 2D model to represent the structure. An issue that was of some concern is whether a lumped plasticity model would introduce significant error in the estimation of the collapse threshold when compared to results obtained with a distributed plasticity. The idea is that since the loss of tangent stiffness is much more gradual in the distributed plasticity model the plastic hinge simplification could prove unduly conservative. The matter was investigated by preparing two models for a 20 story structure, one where plasticity in the elements was modeled with plastic hinges and the other using fiber elements. The results showed that, at least for the type of sections used in the buildings (standard W shapes) the difference in the collapse intensity was

nominal so, for computational convenience, all models were formulated using the plastic hinge simplification. Gravity loads not acting on lateral load resisting frames were added into the models by means of an auxiliary unstable linkage that added to the geometric stiffness computation. All the buildings considered resist lateral forces through steel moment frames so the hysteretic behavior at the critical sections was assumed elasto-plastic. Moment axial force interaction was considered in the yield criterion for columns and the effect of the initial stress existing at the onset of the earthquake (due to the gravity loading) was modeled. Damping was taken to be Rayleigh type with 2% assigned to the first and second frequencies of the elastic model. As is standard, the masses were lumped at the floor levels. The boundary condition at the base, in all cases, was assumed fixed. Table 4 gives all the relevant information needed for subsequent discussion in the buildings. Sketches of the floor plans and elevations are given in Fig.11.

Table 4. Parameters of the buildings needed in the investigation of instability

Building	h (ft)	Mechanism Parameters			Period (sec)	Effective Stability Coefficient θ_e
		V_u (kips)	E	G(ft)		
6-story	82.5	902.7	0	17.5	1.58	0.119
9-story	122	2270.3	0	57	2.04	0.070
20-story	246	596.9	0	90	2.71	0.083

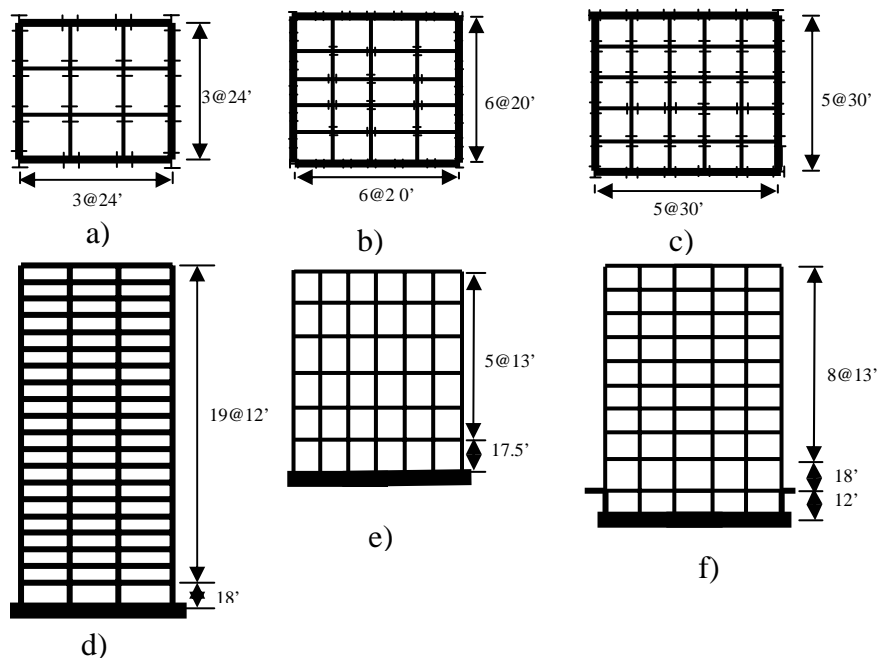

Fig.11 Floor plans and elevations of the buildings used in the multistory study

ISI Indices

The ISI index given by eq.18 can be computed for a particular near fault motion (instead of statistically) if one chooses a far field record to use as a reference. For the multistory structures we selected 10 far field records as references and computed the ISI for 23 records from Parkfield and for 9 of the records in Table 2. The results for the case of the motions from Table 2 are summarized in Table 5. The results show that the mean value of ISI is not far from unity, which is what one anticipates based on the results obtained in the SDOF analysis.

Table 5a. ISI indices for 6-story building

6-Story Building		Far Field Earthquakes									
		F1	F2	F3	F4	F5	F6	F7	F8	F9	F10
Near Field Earthquakes	N1[1]	1.15	0.78	0.71	0.80	0.86	0.80	1.44	0.87	1.15	1.64
	N2	0.91	0.62	0.56	0.63	0.68	0.63	1.14	0.69	0.91	1.30
	N3	1.50	1.03	0.93	1.04	1.12	1.04	1.88	1.13	1.51	2.15
	N4	1.69	1.16	1.05	1.17	1.27	1.18	2.12	1.28	1.70	2.42
	N9	0.66	0.45	0.41	0.46	0.50	0.46	0.83	0.50	0.67	0.95
	N10	0.86	0.59	0.53	0.60	0.65	0.60	1.08	0.65	0.87	1.23
	N12	1.36	0.93	0.84	0.94	1.02	0.95	1.70	1.03	1.37	1.95
	N14	1.39	0.95	0.87	0.97	1.05	0.97	1.75	1.05	1.40	2.00
	N19	1.03	0.71	0.64	0.72	0.77	0.72	1.29	0.78	1.04	1.48
Mean		1.17	0.80	0.73	0.81	0.88	0.82	1.47	0.89	1.18	1.68
COV		0.29	0.29	0.29	0.29	0.29	0.29	0.29	0.29	0.29	0.29

1. Refers to the # in Table 2.

Table 5b. ISI indices for 9-story building

9-Story Building		Far Field Earthquakes									
		F1	F2	F3	F4	F5	F6	F7	F8	F9	F10
Near Field Earthquakes	N1	0.60	0.29	0.16	0.44	0.35	0.27	0.43	0.35	0.36	0.37
	N2	1.35	0.66	0.36	0.99	0.78	0.62	0.97	0.78	0.81	0.84
	N3	1.59	0.78	0.43	1.17	0.92	0.73	1.14	0.92	0.95	0.99
	N4	2.33	1.15	0.62	1.72	1.35	1.07	1.67	1.35	1.40	1.46
	N9	0.62	0.31	0.17	0.46	0.36	0.29	0.45	0.36	0.37	0.39
	N10	1.71	0.84	0.46	1.26	0.99	0.78	1.22	0.99	1.02	1.07
	N12	0.88	0.43	0.24	0.65	0.51	0.41	0.63	0.51	0.53	0.55
	N14	1.68	0.83	0.45	1.24	0.97	0.77	1.20	0.97	1.00	1.05
	N19	1.14	0.56	0.31	0.84	0.66	0.53	0.82	0.66	0.69	0.72
Mean		1.32	0.65	0.35	0.98	0.77	0.61	0.95	0.77	0.79	0.83
COV		0.43	0.43	0.43	0.43	0.43	0.43	0.43	0.43	0.43	0.43

Table 5c. ISI indices for 20-story building

20-Story Building		Far Field Earthquakes									
		F1	F2	F3	F4	F5	F6	F7	F8	F9	F10
Near Field Earthquakes	N1	1.11	0.44	0.62	0.56	0.86	0.37	0.80	0.87	0.75	0.74
	N2	1.86	0.75	1.04	0.95	1.44	0.63	1.34	1.46	1.25	1.25
	N3	3.67	1.47	2.06	1.87	2.85	1.24	2.64	2.88	2.48	2.46
	N4	2.94	1.18	1.65	1.50	2.28	0.99	2.11	2.31	1.98	1.97
	N9	1.13	0.45	0.63	0.57	0.87	0.38	0.81	0.88	0.76	0.76
	N10	1.61	0.65	0.90	0.82	1.25	0.54	1.16	1.26	1.09	1.08
	N12	1.25	0.50	0.70	0.64	0.97	0.42	0.90	0.98	0.84	0.84
	N14	1.36	0.55	0.76	0.69	1.05	0.46	0.98	1.07	0.92	0.91
	N19	1.77	0.71	0.99	0.90	1.37	0.60	1.27	1.39	1.19	1.19
Mean		1.86	0.74	1.04	0.94	1.44	0.63	1.33	1.46	1.25	1.24
COV		0.48	0.48	0.48	0.48	0.48	0.48	0.48	0.48	0.48	0.48

Table 5d. Far field records used in the study

Far Field Earthquakes	F1	El centro (1940) NS
	F2	Imperial Valey 1979/09/15
	F3	Loma Prieta 1989/10/18
	F4	Kern County 1952/07/21
	F5	Big Bear 1992/06/28 08:05
	F6	Landers 1992/06/28 04:58
	F7	Northridge 1994/01/17 12:31
	F8	Petrolia 1992/05/25 11:06 PDT
	F9	Victoria , Mexico 06/09/80 03:28
	F10	Whittier Narrows 1987/10/01 14:42

Instability Predictions

        The critical item from a practical perspective is whether one can estimate the collapse threshold intensity with adequate accuracy using a procedure that lends itself to practical implementation. As noted at the outset, the framework introduced by Bernal (1993, 1998) is based on reducing the multistory structure to a SDOF system that has a certain effective stability coefficient and strength and whose first order period is closely connected to that of the first mode of the building in the direction of analysis. The basic idea is that the safety margin against instability can be characterized as the ratio of the base shear strength of the mechanism to the base shear strength for which instability is imminent. The safety against instability computed in this manner can be also be interpreted as a scaling factor that if applied to the ground motion definition renders the safety margin equal to one. The adequacy of the SDOF reduction can be checked, therefore, by comparing the scaling factor that is needed to induce instability with the scaling factor predicted using the SDOF reduction. There are two ways to perform the comparison: one is by computing the collapse spectral ordinate for a given record from its definition, i.e., by performing nonlinear second order analysis and the other is by using the estimate that can be obtained from the peak ground motion parameters and the statistical expression given by eq.15. In the report presented in Ref.1 results are given for both options and

for all the Parkfield records but here we limit the presentation to the case of the motions taken from Table 2 and to the estimate of S_{ac} obtained from eq.15. The results are summarized in Table 6.

Table 6a. Summary of instability scaling factor predictions for 6-story building

6-Story Building		Fault Normal			Fault Parallel		
		Actual	Prediction	Ratio	Actual	Prediction	Ratio
Near Field Earthquakes	N1	1.50	2.19	0.68	3	1.92	1.56
	N2	8.00	4.87	1.64	5	1.92	2.61
	N3	1.20	1.05	1.14	1.2	1.46	0.82
	N4	1.50	1.77	0.85	2.7	3.37	0.80
	N9	1.40	1.45	0.96	2.5	3.09	0.81
	N10	1.30	1.36	0.95	1.7	2.13	0.80
	N12	1.90	1.58	1.21	2.2	2.88	0.76
	N14	1.05	1.26	0.83	1.3	1.53	0.85
	N19	1.03	0.79	1.30	0.9	0.99	0.91
			Mean	1.06		Mean	1.10
			COV	0.28		COV	0.56

Table 6b. Summary of instability scaling factor predictions for 9-story building

9-Story Building		Fault Normal			Fault Parallel		
		Actual	Prediction	Ratio	Actual	Prediction	Ratio
Near Field Earthquakes	N1	8.50	4.38	1.94	6.1	4.36	1.40
	N2	16.20	9.73	1.67	14	4.35	3.22
	N3	1.70	2.11	0.81	4	3.31	1.21
	N4	2.25	3.53	0.64	7.5	7.64	0.98
	N9	4.20	2.91	1.45	12	7.02	1.71
	N10	2.20	2.73	0.81	7.5	4.83	1.55
	N12	4.50	3.15	1.43	4.25	6.53	0.65
	N14	1.75	2.51	0.70	3.5	3.47	1.01
	N19	2.00	1.58	1.27	1.4	2.24	0.63
			Mean	1.19		Mean	1.37
			COV	0.39		COV	0.57

Table 6c. Summary of instability scaling factor predictions for 20-story building

20-Story Building		Fault Normal			Fault Parallel		
		Actual	Prediction	Ratio	Actual	Prediction	Ratio
Near Field Earthquakes	N1	7.00	3.98	1.76	5.25	4.37	1.20
	N2	14.10	8.83	1.60	11.5	4.36	2.64
	N3	1.40	1.91	0.73	3.5	3.32	1.05
	N4	1.75	3.21	0.55	5.25	7.66	0.69
	N9	3.75	2.64	1.42	7.5	7.04	1.07
	N10	1.90	2.48	0.77	5.5	4.84	1.14
	N12	4.75	2.86	1.66	4.5	6.54	0.69
	N14	2.20	2.28	0.96	3.3	3.48	0.95
	N19	1.50	1.43	1.05	1.3	2.24	0.58
			Mean	1.17		Mean	1.11
			COV	0.39		COV	0.55

As can be seen from the results, the predictions of the SDOF approach with the statistical expressions are conservative in the mean and provide sufficient accuracy to be useful for practical design.

Conclusions

In multistory structures subjected to strong earthquake plasticity travels along the height of the structure in a wave like fashion. Analyses show that the distribution of plastic hinges during the response can be sufficiently extensive for the effective second order stiffness to develop negative eigenvalues opening up the potential for instability. An important aspect about instability during earthquake response is the fact that its conceptualization through pseudo-static reasoning is misleading. As the paper repeatedly notes, the correct framework is not one of amplifications but of ensuring that the strength provided is sufficiently larger than that bellow which instability can be anticipated.

An indicator of how the P-delta effect interacts with the type of record is the ratio of the minimum strength needed for elastic response to the minimum strength needed to prevent instability, R_c. On the premise that design is carried out for a certain fraction of the demand computed for elastic response one concludes that the relevance of P-delta increases as R_c decreases. Results show that for large fundamental periods R_c is generally larger for near fault conditions than in the far field, indicating that being at close distances from the fault is not a critical situation for tall flexible structures from an instability perspective (provided that the elastic demand is adequately estimated). The situation can be reversed in the intermediate period range (say from 1.5 to 3 seconds) for some conditions but the reductions in R_c are typically modest and not a source for major concern. The previous observations apply both in the fault normal and fault parallel orientations although the fault normal direction is consistently the one where the effect being described is more pronounced.

Acknowledgement

References

Bernal D. (2006). Instability inducing potential of near-fault ground motions, CSMIP *report on data interpretation project*.

Bernal, D.(1990). P-D effects and instability in the seismic response of buildings, *Report no. CE-90-14*, Northeastern University, Boston, MA.

Bernal, D. (1991). "Dynamic instability in buildings", *Proceedings of the 6th Canadian Conference on Earthquake Engineering*, Toronto, pp. 85-92.

Bernal, D. (1992a). "Instability of buildings subjected to earthquakes", *Journal of Structural Engineering*, ASCE, Vol. 18, No.8, pp. 2239-2260.

Bernal, D. (1992b). Dynamic instability in buildings subjected to earthquakes, *Report no. CE-92-14, Northeastern University*, Boston, MA, 1992.

Bernal, D. (1998). "Instability of buildings during seismic response", *Engineering Structures,* vol.20, No.4-6, pp.496-502.

Bray, J.D. and Rodriguez-Marek, A. (2004) "Characterization of forward-directivity ground motions in the near-fault region". *Soil Dynamics and Earthquake Engineering,* 24, 815-828.

Husid, R. (1967). Gravity effects on the earthquake response of yielding structures, *Earthquake Engineering Research Laboratory*, California Institute of Technology, Pasadena.

Jennings P.C. and Husid, R. (1968). "Collapse of yielding structures under earthquakes", *Journal of Engineering Mechanics*, ASCE, Vol94, No.5, pp.1045-1065.

MacRae, G.A., Morrow, D.V. and Roeder, C.W., (2001), "Near fault ground motion on simple structures", *Journal of Structural Engineering,* ASCE, Vol.127, No.9, pp.996-1004.

Mavroeidis G.P., Dong, G. and Papageorgiou A.S., (2004). "Near-fault ground motions, and the response of elastic and inelastic single-degree-of-freedom (SDOF) systems", *Earthquake Engineering and Structural Dynamics*, Vol.33 pp.1023-1049.

Newmark, N. M., and W. J. Hall (1982). Earthquake spectra and design, *Earthquake Engineering Research Institute*, Oakland, California.

Pique, J. (1976). On the use of simple models in nonlinear dynamic analysis, *report R76-43* Massachusetts Institute of Technology Cambridge, MA

Riddell, R. and Newmark, N.M.(1979). Statistical analysis of the response of nonlinear systems subjected to earthquakes *Res. Report R76-43*, University of Illinois, Urbana, Ill.

Somerville, P., Smith, N., Graves, R. and Abrahamson, N. (1997). "Modification of empirical strong motion attenuation relations to include the amplitude and duration effects of rupture directivity" *Seismological Res. Letters,* 68(1), 199-222.

Takizawa, H. and Jennings, P. (1980). "Collapse of a model for ductile reinforced concrete frames under extreme earthquake motions", *Earthquake Engineering and Structural Dynamics,* Vol.8, pp.117-144.

DEVELOPMENT OF IMPROVED INTENSITY MEASURES AND IMPROVED SHAKEMAPS FOR LOSS ESTIMATION AND EMERGENCY RESPONSE

Eduardo Miranda, Marios Kyriakides and Qiang Fu

John A. Blume Earthquake Engineering Center
Stanford University

Abstract

An improved measure of ground motion intensity that is well correlated with structural and many kinds of nonstructural damage is presented. The proposed intensity measure is based on the peak interstory drift demand computed using a simplified continuous model that consists of a combination of a flexural beam and a shear beam. This new intensity measure accounts for the influence of higher modes and for concentrations of lateral deformation demands along the height of buildings. It is then proposed to compute this new intensity measure at all stations that recorded a seismic event in order to generate improved ShakeMaps for loss estimation and emergency response. The 2004 Parkfield event is used to illustrate both concepts.

Introduction

Interest in seismic hazard and the performance of structures in earthquakes has steadily increased in recent years. This interest has expanded from the seismology and earthquake engineering communities to national, state, county, city and local public officials, owners of critical facilities and utilities, emergency response organizations, insurance and other financial institutions, the media and the general public. In particular, there is a growing need for information of the intensity of earthquakes and their possible effects on structures within a few minutes of moderate and large magnitude events. Recent technological developments in instrumentation, storage, data transmission and increased computational power have allowed the generation and dissemination of valuable information of earthquakes in near real time. The most widely known example is ShakeMap which is computed and distributed within minutes of a seismic event and provides an instrumental measure of ground motion intensity.

Over the years various parameters have been proposed and used as measures of ground motion intensity. Of particular interest are parameters that are closely correlated to structural and nonstructural damage and that therefore can be used as demands parameters to identify whether damage is likely to occur and the severity of the damage. While it is possible to use response parameters of detailed nonlinear models of structures, these models require a great deal of information about the structure, require a significant amount of time to be developed, debugged and calibrated, require large computational power to run as well as many hours for interpreting their results, thus making the latter approach not practical for rapid assessment of large inventories buildings in urban areas. Therefore, there is a need for simplified ground motion intensity measures that require only a minimum amount of information, require only small

amount of computation and yet their results are useful in identifying the capability of a ground motion to cause damage in structures.

The objective of this work is to summarize the results of an investigation whose main objectives were to develop improved ground motion intensity measures and improved ShakeMaps for loss estimation and emergency response, as well as to illustrate the computation and use of these new tools by using ground motions recorded during the 2004 Parkfield earthquake.

Commonly Used Intensity Measures

Existing approaches to characterize ground motion intensity for design, loss estimation and emergency response typically fall in one of the following categories:

(a) *Using peak ground motion parameters such as peak ground acceleration (PGA) or peak ground velocity (PGV)*. For example, in ShakeMap the instrumental intensity is computed from empirically-derived relations between Modified Mercalli Intensity (MMI) and PGA and PGV (Wald, et al. 1999a). When generating instrumental intensity ShakeMaps, the instrumentally-derived MMI is first computed from the PGA-MMI empirical relationship and if the instrumental intensity value determined from peak acceleration is equal or larger than VII, then the instrumental intensity derived from the the PGV-MMI empirical relationship is used (Wald, et al. 1999a).

(b) *Using response spectral ordinates at a few selected periods.* ShakeMap also produces information of 5% damped pseudo-acceleration spectral ordinates at 0.3s, 1.0s and 3.0s for earthquakes with magnitudes larger than 5.5. While originally envisioned as a pre-event planning tool and in a time when rapid data was not available, *HAZUS* has recently been enhanced to facilitate rapid post-event evaluation of damage and loss using ShakeMap data (Kircher, 2003). *Hazus* uses the peak response of linear single-degree-of-freedom systems with periods of vibration of 0.3s and 1.0s available in ShakeMap to estimate damage and losses to buildings and other types of structures.

(c) *Using peak ground motion parameters and response spectral ordinates at a few selected periods.* This approach is a combination of the two previously described approaches. This approach was recently incorporated in the ATC-54 (Guidelines for utilizing strong-motion and ShakeMap data in post-earthquake response) in which PGA, and spectral ordinates at 0.3s and 1.0s are used for post-earthquake evaluation of existing buildings by comparing the acceleration demand computed with ShakeMap acceleration data to the design lateral-force coefficient (Rojahn et al., 2003).

(d) *Using the linear spectral ordinate at the fundamental period of the building.* Current codes in the United States, such as the *International Building Code* (ICC 2000), define earthquake hazard in terms of acceleration spectral ordinates at the first mode period of vibration, *Sa(T1)*. This approach was also used in the ATC-54 project for post-earthquake evaluation of existing buildings in order to estimate the peak roof displacement (Rojahn et al., 2003). The use of the pseudo acceleration spectral ordinate at the fundamental period of the building has also been extensively used to characterize the ground motion intensity in SAC (Cornell et al.

2002) and PEER (Deierlein, et al., 2003; Miranda and Aslani, 2003; Krawinkler and Miranda, 2004; Moehle and Deierlein, 2004).
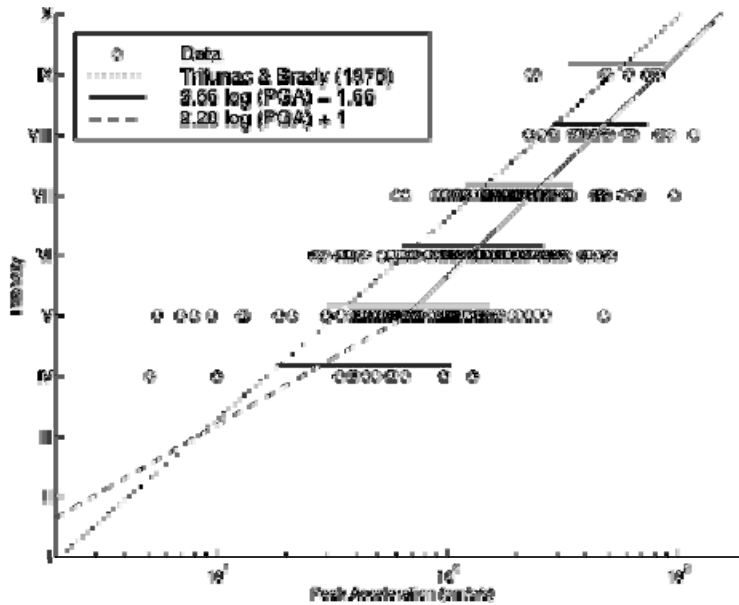
Figure 1. Empirical relationship between PGA and MMI used im ShakeMap (Wald et al. 1999b).

The empirical relationship between PGA and MMI that is incorporated in the generation of ShakeMaps is shown in figure 1. As shown in this figure there is a significant scatter between PGA and MMI. For example, according to Wald et al. (1999b) areas subjected to peak ground accelerations of 300 cm/s^2 (31%g) could be associated with Modified Mercalli Intensities of V, VI, VII or VIII. This means that a PGA=0.3g could produce damages ranging from "very light damage" to "moderate to heavy damage". Similarly, according to figure 1 a MMI of V could have been produced by peak ground acceleration ranging from values as small as 5 cm/s^2 to values as large as 450 cm/s^2 (a peak ground acceleration almost two orders of magnitude larger!). Analytical work, as well as observations of earthquakes effects, including records of strong ground motion, consistently indicate that PGA is not a reliable parameter on which to base evaluations of seismic risk (ATC 1982; Aptikaev, 1980; Borg, 1980; McCann et al. 1980; Kennedy et al. 1984). Although a slightly better correlation is obtained using peak ground velocity for higher intensity levels, the correlation remains relatively low. One of the fundamental problems of using peak ground motion parameters to characterize the intensity of ground motion is that they do not differentiate between the seismic intensity on structures with different dynamic characteristics (different periods of vibration).

Using spectral ordinates offers a significantly better approach to characterize the ground motion intensity of different types of structure. The main advantage of this approach is that it incorporates information about the frequency content of the ground motion, hence it is able to account for differences in seismic intensity for systems with different periods of vibration. However there are two main shortcomings with this approach: (1) cannot account for possible

concentrations of deformation demands in certain stories; and (2) the response of higher modes is neglected.

Improved Ground Motion Intensity Measure

Structural damage and many types of damage to nonstructural components are primarily the result of lateral deformations that occur from the relative displacement between consecutive floors. In particular, many studies have concluded that the structural response parameter that is best correlated with seismic damage is the peak interstory drift ratio (Algan 1982; Sozen 1983; Qi and Moehle 1991; Gülkan and Sozen 1999), which is defined as the difference in lateral displacements in between two consecutive floors normalized by the interstory height. Therefore, parameters that provide direct estimates of interstory drift demands in buildings constitute more reliable measures of ground motion intensity.

In 1997, Iwan introduced a simple and direct measure of drift demand for earthquake ground motions called the *drift spectrum* (Iwan 1997). Like the response spectrum, the drift spectrum is based on a relatively simple linear model. However, the drift spectrum differs from the response spectrum in that it is based on a continuous shear beam rather than a single-degree-of-freedom (SDOF) system. The most important advantages of this new powerful tool are that it takes into account the fact that interstory drift demands are not uniformly distributed along the height of buildings and considers the contribution of higher modes. Therefore, the drift spectrum results on more accurate estimations of maximum interstory drift demands than does the response spectrum. In his study, Iwan strongly recommended the use of drift spectrum in structural design and concluded that the drift spectrum was particularly useful in estimating drift demands in buildings subjected to pulse-like ground motions.

For many buildings, the shear beam model can lead to reasonable estimations of interstory drift demands. This is particularly true in the case of moment-resisting frame buildings whose beams are significantly stiffer than the columns and where axial deformations in the columns are negligible. In such cases, modes of vibration will be relatively similar to those of a shear beam. However, in buildings with bracing or shear walls or for moment-resisting buildings where the lateral stiffness provided by the columns is significant relative to that provided by the beams or where axial deformations are significant, the use of a shear beam is not an adequate model.

In this study an improved ground motion intensity measure is proposed referred to as *generalized interstory drift spectrum*, which is based on a continuous model that consists of a combination of a flexural beam and a shear beam, rather than only a shear beam. By modifying one parameter this model can consider lateral deformations varying from those of a flexural beam to those of shear beam. Hence, Iwan drift spectrum is a particular case of the proposed intensity measure. Furthermore, it permits to account for a wide range of modes of deformation that represent more closely those of multistory buildings. Mode shapes, modal participation factors and period ratios required to compute the response of the model are all computed with closed-form solutions and are a function of only one parameter. Hence, providing a highly efficient computational tool which only requires a minimum amount of information in order to

be used. It can be used for analysis of individual buildings or for large groups of building within urban areas.

The simplified model consists of a linear elastic continuum model. Continuum models have been proposed before for approximating the response of buildings to wind or seismic forces. For a review of previously-proposed models the reader is referred to Miranda and Taghavi (2005) and Miranda and Akkar (2005). The proposed continuum model consists of a combination of a flexural cantilever beam and a shear cantilever beam deforming in bending and shear configurations, respectively. It is assumed that along the entire length of the model, both beams undergo identical lateral deformations. Furthermore, mass and lateral stiffness are assumed to remain constant along the height of the building.

While assuming the mass to remain constant along the height of buildings is reasonable for most buildings, assuming that the lateral stiffness remains constant along the height of the building is perhaps only a reasonable assumption for one to three-story buildings. However, Miranda and Taghavi (2004) have shown that the product of modal shapes and modal participation factors as well as period ratios are relatively robust and are not significantly affected by reductions in lateral stiffness, provided that no abrupt reductions exists. In the same study, it was similarly shown that reductions of mass along the height of the building also do not affect significantly the dynamic characteristics of the model. It should be noted that Miranda and Taghavi (2005) provided expressions to estimate the dynamic characteristic of non-uniform buildings, but concluded that, in many cases, using the dynamic characteristics of uniform models could provide reasonable approximations to the dynamic characteristics of non-uniform models.

As shown by Miranda and Akkar (2005), the response of a uniform shear-flexural model when subjected to an horizontal acceleration at the base $\ddot{u}_g(t)$ is given by the following partial differential equation:

$$\frac{\rho}{EI}\frac{\partial^2 u(x,t)}{\partial t^2} + \frac{c}{EI}\frac{\partial u(x,t)}{\partial t} + \frac{1}{H^4}\frac{\partial^4 u(x,t)}{\partial x^4} - \frac{\alpha^2}{H^4}\frac{\partial^2 u(x,t)}{\partial x^2} = -\frac{\rho}{EI}\frac{\partial^2 u_g(t)}{\partial t^2} \qquad (1)$$

where ρ is the mass per unit length in the model, H is the total height of the building, $u(x,t)$ is the lateral displacement at non-dimensional height $x=z/H$ (varying between zero at the base of the building and one at roof level) at time t, c is the damping coefficient per unit length, EI is the flexural rigidity of the flexural beam and α is the lateral stiffness ratio defined as

$$\alpha = H\sqrt{\frac{GA}{EI}} \qquad (2)$$

where GA is the shear rigidity of the shear beam. The lateral stiffness ratio, α is a dimensionless parameter that controls the degree of participation of overall flexural and overall shear deformations in the continuous model and thus, it controls the lateral deflected shape of the model. A value of α equal to zero represents a pure flexural model (Euler-Bernoulli beam) and a value of $\alpha \rightarrow \infty$ corresponds to a pure shear model. Intermediate values of α correspond to multistory buildings that combine overall shear and flexural lateral deformations.

The mode shapes of the simplified model are given by (Miranda and Taghavi, 2005):

$$\phi_i(x) = \sin(\gamma_i x) - \gamma_i \beta_i^{-1} \sinh(x\beta_i) - \eta_i \cos(\gamma_i x) + \eta_i \cosh(\beta_i x) \tag{3}$$

where β_i and η_i are nondimensional parameters for the ith mode of vibration which are given by

$$\beta_i = \sqrt{\alpha^2 + \gamma_i^2} \tag{4}$$

$$\eta_i = \frac{\gamma_i^2 \sin(\gamma_i) + \gamma_i \beta_i \sinh(\beta_i)}{\gamma_i^2 \cos(\gamma_i) + \beta_i^2 \cosh(\beta_i)} \tag{5}$$

and γ_i is the eigenvalue of the ith mode of vibration corresponding to the ith root of the following characteristic equation:

$$2 + \left[2 + \frac{\alpha^4}{\gamma_i^2 \beta_i^2} \right] \cos(\gamma_i) \cosh(\beta_i) + \left[\frac{\alpha^2}{\gamma_i \beta_i} \right] \sin(\gamma_i) \sinh(\beta_i) = 0 \tag{6}$$

Periods of vibration corresponding to higher modes can be computed as a function of the fundamental period of vibration of the building T_1 by using period ratios computed as

$$\frac{T_i}{T_1} = \frac{\beta_1 \gamma_1}{\beta_i \gamma_i} \tag{7}$$

Since the masses are assumed to remain constant, the modal participation factors Γ_i can be computed with the following equation:

$$\Gamma_i = \frac{\displaystyle\int_0^1 \phi_i(x)dx}{\displaystyle\int_0^1 \phi_i^2(x)dx} \tag{8}$$

Integrals shown in equation (8) can be solved in closed-form solution. Readers interested in these closed-form solutions are referred to Miranda and Akkar (2005). As shown by these equations, mode shapes and modal participation factors, which control the spatial distribution of seismic demands, are fully defined by only one parameter, the lateral stiffness ratio α.

The contribution of the ith mode of vibration to the lateral displacement (relative to the ground) at non-dimensional height $x=z/H$ at time t is given by

$$u_i(x,t) = \Gamma_i \phi_i(x) D_i(t) \tag{9}$$

where Γ_i is the modal participation factor of the ith mode of vibration, $\phi_i(x)$ is the amplitude of ith mode at nondimensional height x, and $D_i(t)$ is the relative displacement response of a SDOF system, with period T_i and modal damping ratio ξ_i corresponding to those of the ith mode of vibration, subjected to ground acceleration $\ddot{u}_g(t)$. The product $\Gamma_i \phi_i(x)$ controls the spatial variation of the contribution of the ith mode to the total response, while $D_i(t)$ controls its time variation. Assuming that the structure remains elastic and that it has classical damping, the displacement at non-dimensional height $x=z/H$ at time t is given by

$$u_i(x,t) = \sum_{i=1}^{\infty} \Gamma_i \phi_i(x) D_i(t) \tag{10}$$

Equation (10) indicates that the estimation of relative displacements along the height of the building require consideration of an infinite number of modes of vibration. However, Taghavi and Miranda (2005) and Reinoso and Miranda (2005) have shown that for most buildings considering three to six modes in each building direction is enough to capture the main aspects of the response of buildings subjected to earthquakes. Therefore, equation (10) can be reduced to

$$u_i(x,t) \approx \sum_{i=1}^{m} \Gamma_i \phi_i(x) D_i(t) \tag{11}$$

where *m* is the number of modes contributing significantly to the response.

Taghavi and Miranda (2005) compared acceleration response computed with the simplified model to that computed with detailed finite-element models of a ten-story steel moment resisting frame building and a twelve-story reinforced concrete building whose properties were available in the literature. Additionally, they compared acceleration demands computed with the model to those recorded in four instrumented buildings in California that have been subjected to earthquakes. In all cases, it was shown that the simplified model provided very good results. More recently, Reinoso and Miranda (2005) compared acceleration demands computed with the simplified continuous model to that recorded in five high rise buildings in California in various earthquakes. However, those studies did not compare displacement response.

As part of this study the ability of the simplified model to estimate displacement time histories and peak lateral displacements was evaluated. As an illustration Figures 2 to 5 show examples comparing relative displacement (relative to the base of the building) time histories of two instrumented buildings in California. It is noted that these analyses have been conducted assuming that the lateral stiffness and mass of the continuous system remains constant along the height of the building and that the damping ratio is the same for all modes included in the analysis, therefore the models were fully defined by using only three parameters, namely the fundamental period of vibration of the building, a damping ratio that characterizes the damping in the model and the lateral stiffness ratio. In equations 9 to 11 one could use different damping ratios for computing $D_i(t)$ for each mode. However, for simplicity and in order to keep the number of parameters to a minimum, here it has been assumed that the damping ratio is the same for all modes. Furthermore, the base of the model has been assumed as fixed and torsional deformations have been neglected. As shown in these figures, despite the important simplifications, the model is capable of capturing relatively well the peak and the most important features of the lateral deformation response of the buildings.
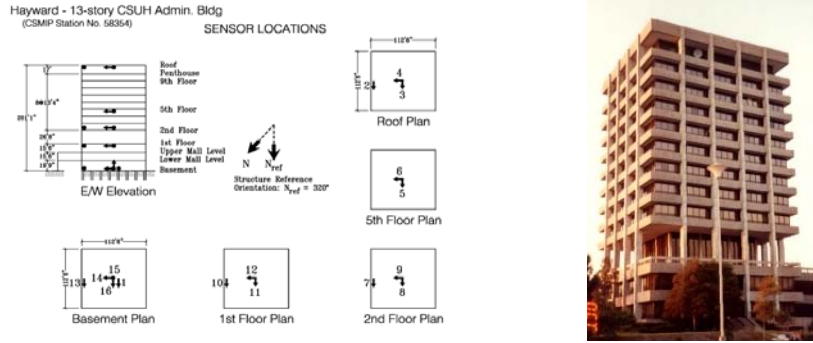
Fig 2. Sensor location and photograph of a 13-story RC building in California (CSMIP station 58354).
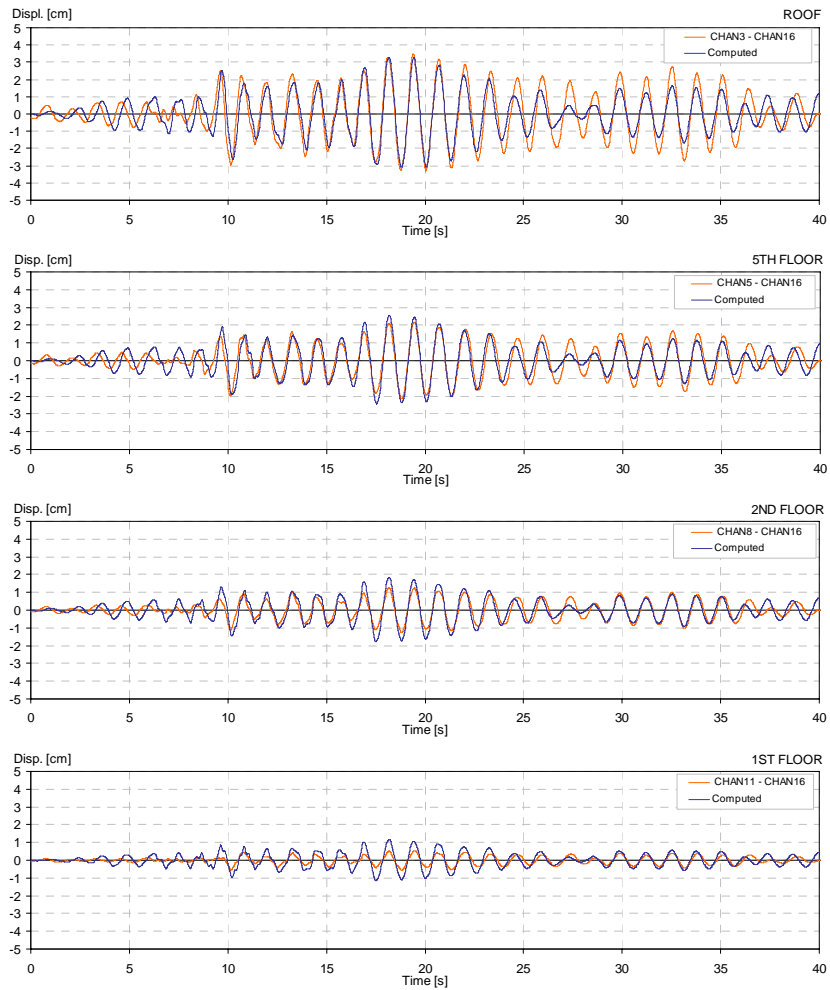
Fig. 3. Comparison of computed and recorded relative displacements in the NS components of the 13-story building in Hayward California during the 1989 Loma Prieta earthquake.
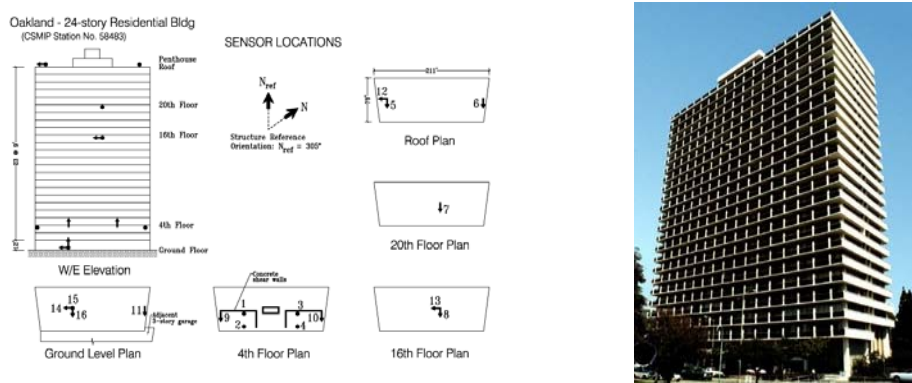
Fig. 4. Sensor location and photo of a 24-story RC building in California (CSMIP station 58483).
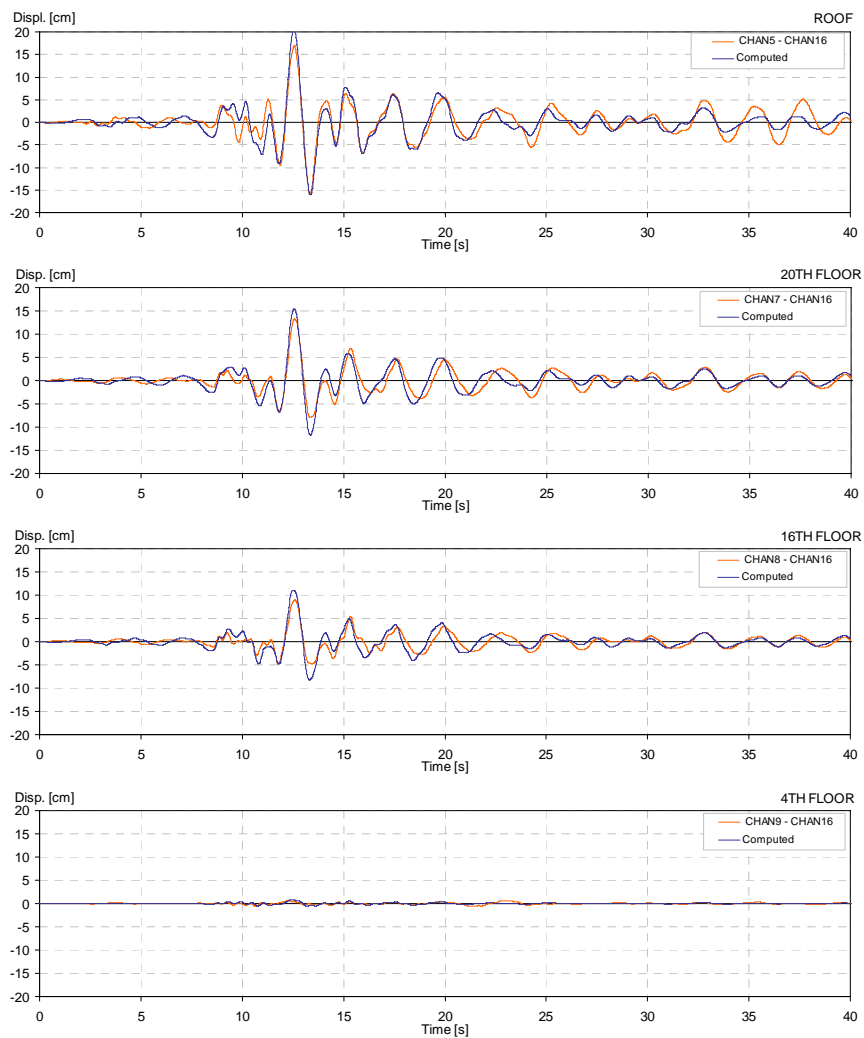
Fig. 5.   Comparison of computed and recorded relative displacements in the NS components of the 24-story building in Oakland California during the 1989 Loma Prieta earthquake.

The interstory drift ratio at the jth story of a building can be computed as

$$IDR(j,t) = \frac{1}{h_j} \sum_{i=1}^{n} \Gamma_i \left[\phi_i(x_{j+1}) - \phi_i(x_j) \right] D_i(t) \tag{12}$$

where h_j is the floor to floor height of the jth story, n is the number of modes in the building, and $\phi(x_{j+1})$ and $\phi(x_j)$ are the mode shape values corresponding to the jth+1 and jth floor computed with equation (3), respectively. If the interstory height is assumed to remain constant along the height of the building, it can be shown that for buildings with 6 or more stories a relatively good estimation of the interstory drift at non-dimensional height $x=z/H$ at time t can be computed with

$$IDR(j,t) \approx \theta(x,t) = \frac{1}{H} \sum_{i=1}^{\infty} \Gamma_i \phi_i'(x) D_i(t) \tag{13}$$

where H is the total building height above ground, $\theta(x,t)$ is the rotation in the simplified model at height x at time t, and $\phi_i'(x)$ is the first derivative of the ith mode shape $\phi_i(x)$ with respect to non-dimensional height x. The derivative of the mode shapes with respect to non-dimensional height x is obtained by taking the derivative of Eq. (3) with respect to x as follows:

$$\phi_i'(x) = \gamma_i \cos(\gamma_i x) - \gamma_i \cosh(\beta_i x) + \eta_i \gamma_i \sin(\gamma_i x) + \eta_i \beta_i \sinh(\beta_i x) \tag{14}$$

The ordinates of the *generalized interstory drift spectrum* (GIDS) are defined as the maximum peak interstory drift demand over the height of the building and are computed as

$$IDR_{max} \equiv \max_{\forall t,x} |\theta(x,t)| \tag{15}$$

The generalized interstory drift spectrum is a plot of the fundamental period of the building in the abscissas versus IDR_{max} in the ordinates. Similarly to the response spectrum, the GIDS provides seismic demands for a family of systems with different periods of vibration. However, instead of having ordinates of maximum relative displacement, maximum relative velocity or maximum acceleration of SDOF systems, the GIDS provides a measure of peak interstory drift demands, which is a demand parameter that is better correlated with damage in buildings. In particular, the GIDS provides a rapid estimation of peak interstory drift demand in buildings with different periods of vibration.

As mentioned before, if the same damping ratio is used for the m contributing modes, then the model is fully defined by using only four parameters: (1) the fundamental period of vibration of the building, T_1; (2) a modal damping ratio that represents the damping ratio in the building, ξ; (3) the lateral stiffness ratio α; and (4) the building height, H. Since the derivative of the modes, modal participation factors and period ratios can be computed in closed-form solution, the GIDS is computationally very efficient, requiring just a few seconds in most personal computers. If empirical relations between building height and fundamental period are used, the number of parameters is then further reduced from four to three.
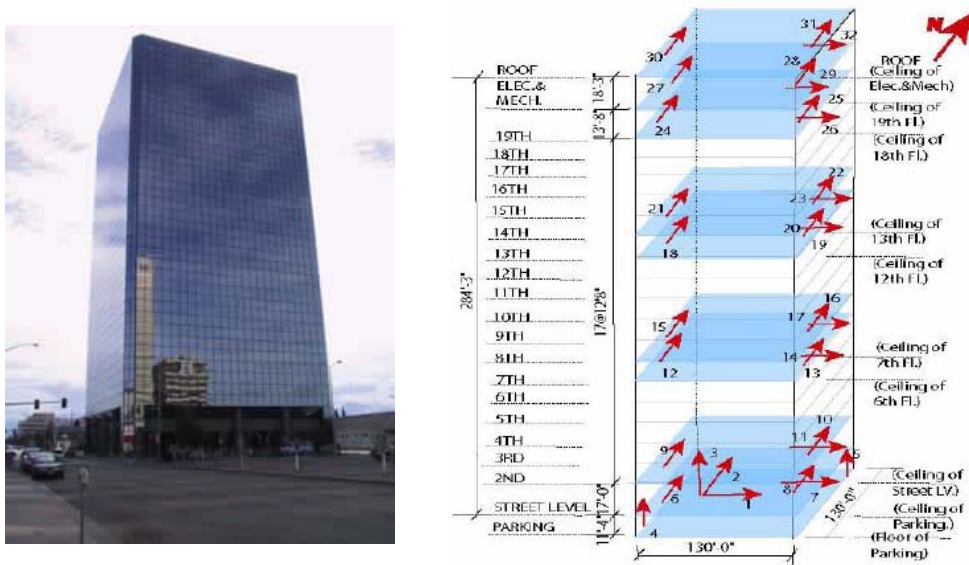
Fig. 6. Photograph and instrumentation layout of the Atwood Bldg. in Anchorage Alaska.

Validation of the simplified contious model for capturing interstory drifts is more complicated because most instrumented buildings only have accelerometers installed at 3 or 4 locations along the height. However, the United States Geological Survery has recently deployed dense instrumentation arrays in a few buildings. Figure 6 show the photograph and instrumentation layout of the Atwood building which is located in Anchorage, Alaska. As shown in this figure sensor are located at consecutive floors in the first and second floors, 7th and 8th floors, 13th and 14th floors, and 19th, 20th and 21st floors, which allows the computation of interstory drifts at the 1st, 8th, 14th, 20th and 21st floors.

On December 15th, 2003 a magnitude 3.7 earthquake occurred only at 18 km from the building. Although the event was very small, still it triggered the instruments and very high quality recording were obtained. Figure 7 shows a comparison of interstory drift time histories computed with the simplified model and those computed through double integration and substraction of acceleration time histories recorded in consecutive floors in the building. It can be seen that with exception of the first floor where the match is not good in the rest of the stories the results of the simplified model are remarkably good, especially if one considers the simplicity of the model.

Another building that offers a unique opportunity to validate the simplified continuous model is the Millikan library of the campus of the California Institute of Technology (CalTech). The instrumentation in this building was recently improved and now sensors are available on all floor levels. A photograph of the building and sketches of its plan and elevation are show in figure 8.
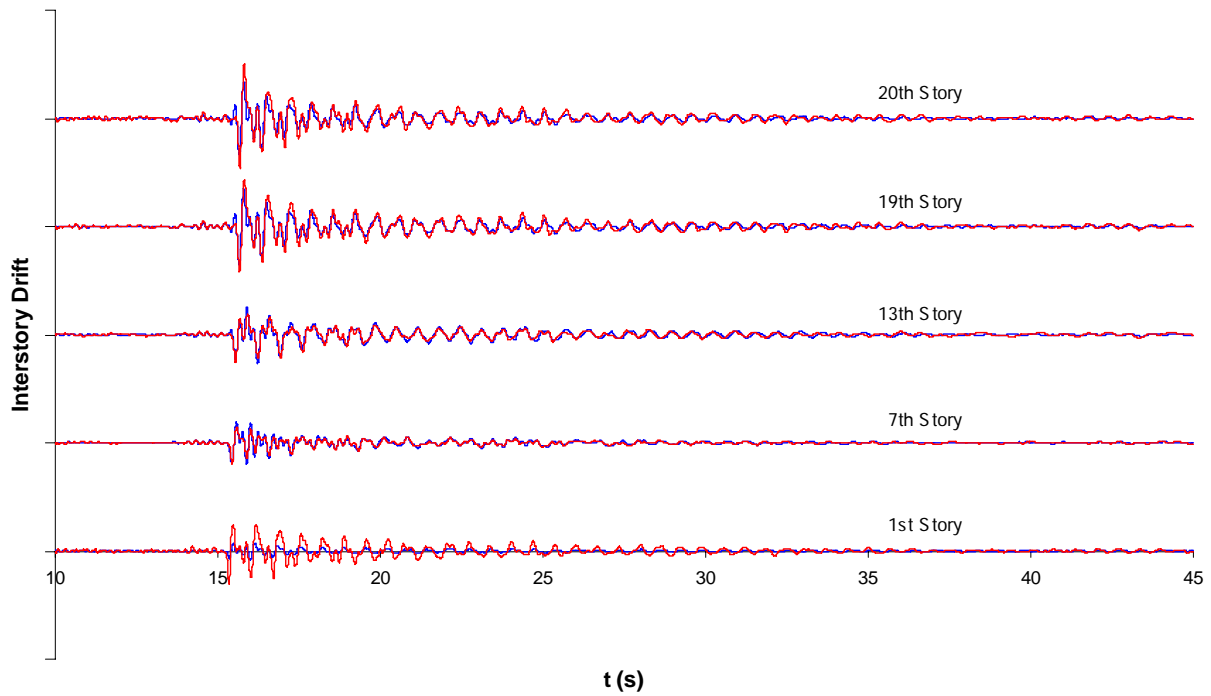
Fig. 7. Comparison of 'recorded' and computed interstory drift time histories in the Atwood Bldg. in Anchorage Alaska.
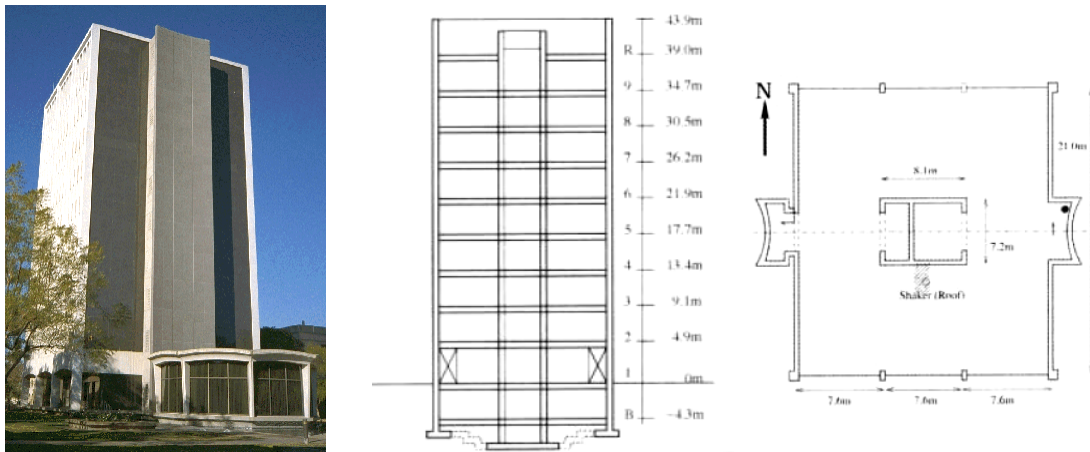
Fig.8. Photograph and instrumentation layout of the Millikan library on Pasadena, CA.

On September 4th, 2002 the Yorba Linda earthquake occurred within the Los Angeles metropolitan region. The event had a magnitude on 4.6. Although the event was small it triggered all instruments and high quality records were obtained. Figure 9 compares interstory drifts computed with the simplified continuous model and those computed from recorded accelerograms. Again it can be seen that the results are very good, especially if one considers the level of difficulty.
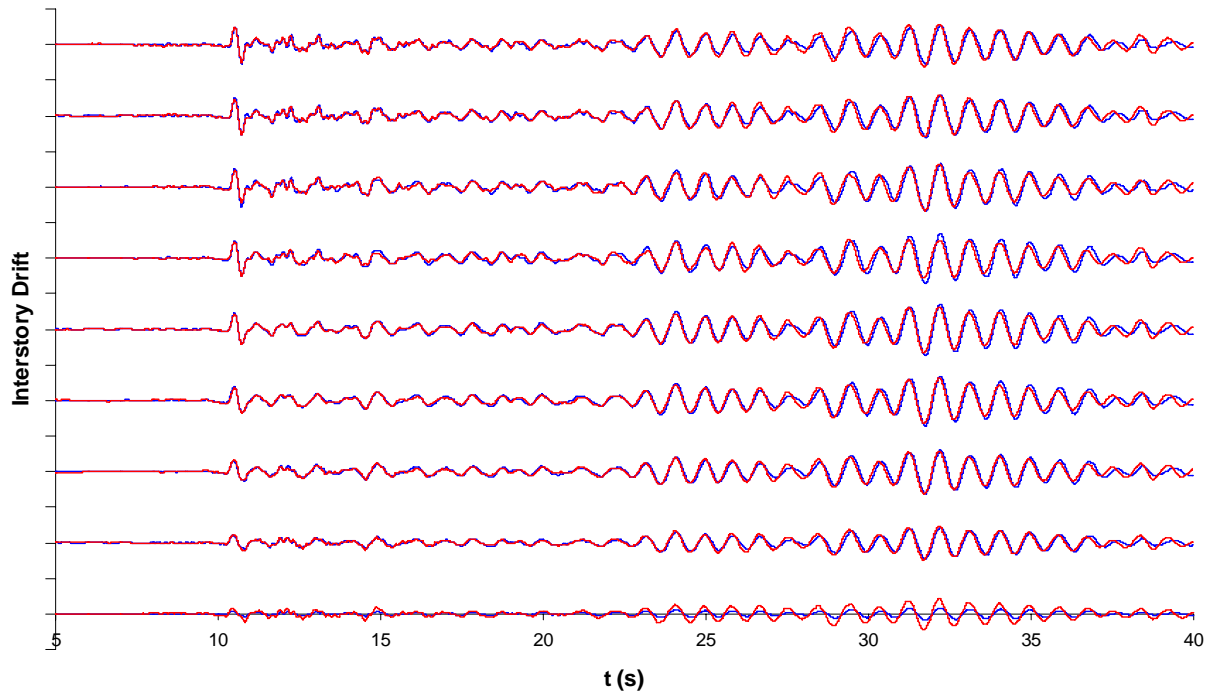
Fig. 9. Comparison of 'recorded' and computed interstory drift time histories in the EW component of the Millikan library on Pasadena California..

Improved ShakeMaps

Improved maps were computed and plotted for the 2004 Parkfield event. The area that was considered in shown in Fig. 10, where the trace of the San Andreas fault running in the NW-SE direction. The peak interstory drift was computed with all ground motions that recorded this event in the facility of the fault. This is equivalent to placing instrumented simplified models at all recording stations prior to the earthquake. This is shown schematically in Figure 11.

Improved Shake Maps provide direct estimates of interstory drift ratios that might have occurred in the area if buildings with a wide range of periods of vibration would have been there. Improved maps were computed for north-south and east-west components. Additionally, improved Shake Maps were also computed and generated for fault-normal and fault parallel directions.
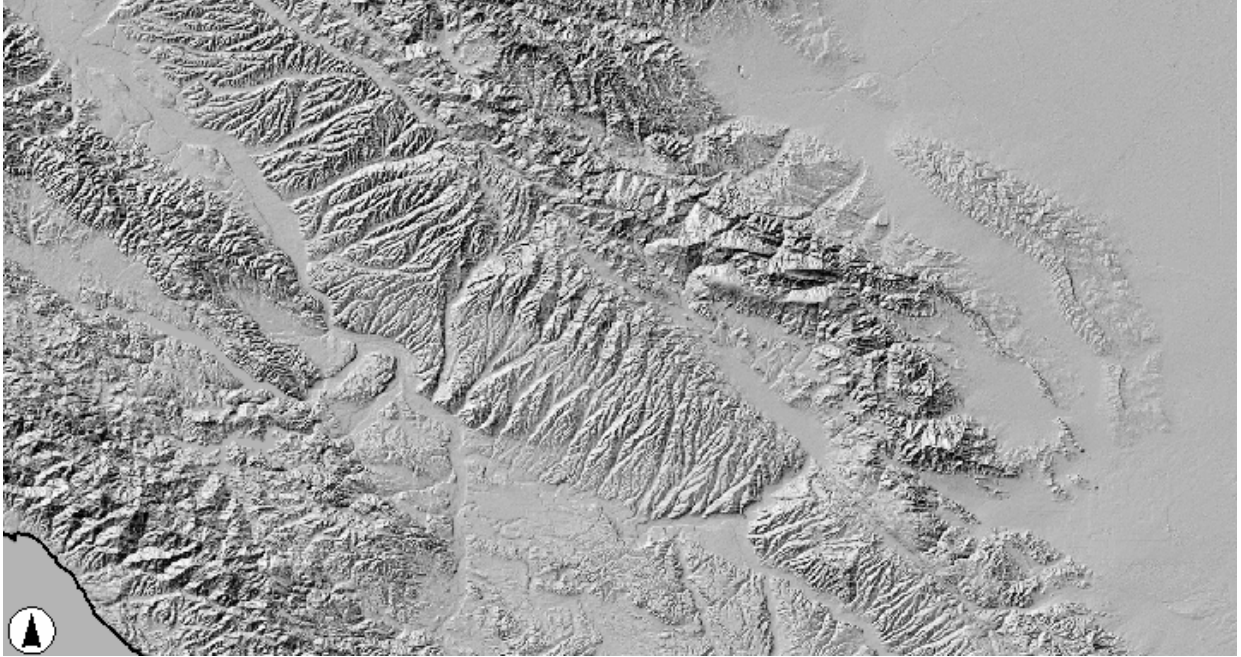
Fig. 10 Region in the vicinity of the 2004 Parkfield earthquake that was used in this study.
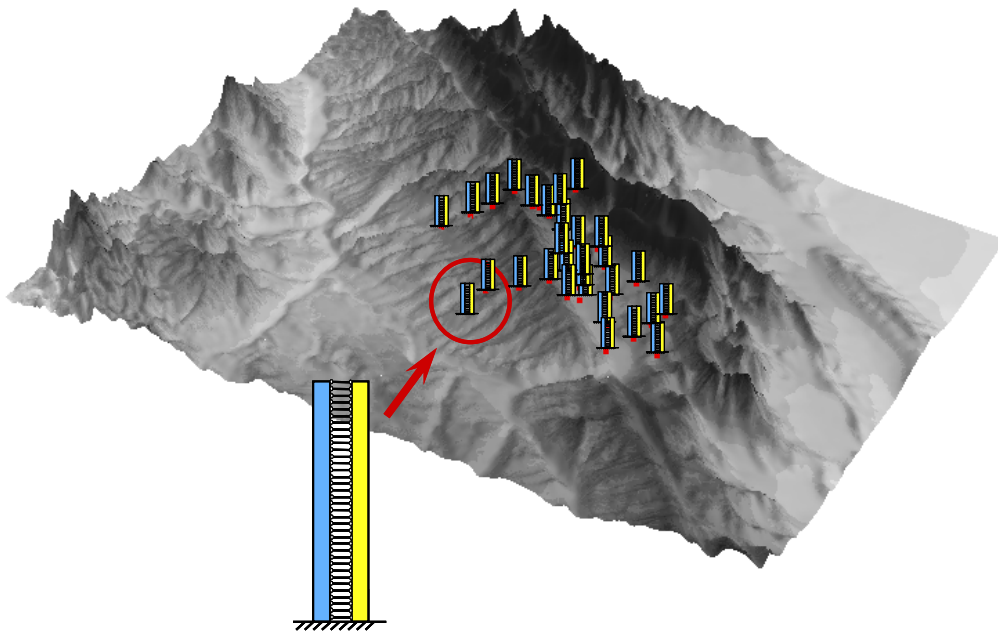
Fig. 11 Ground motion stations for which continuous models were used to compute and display improved shake Maps.
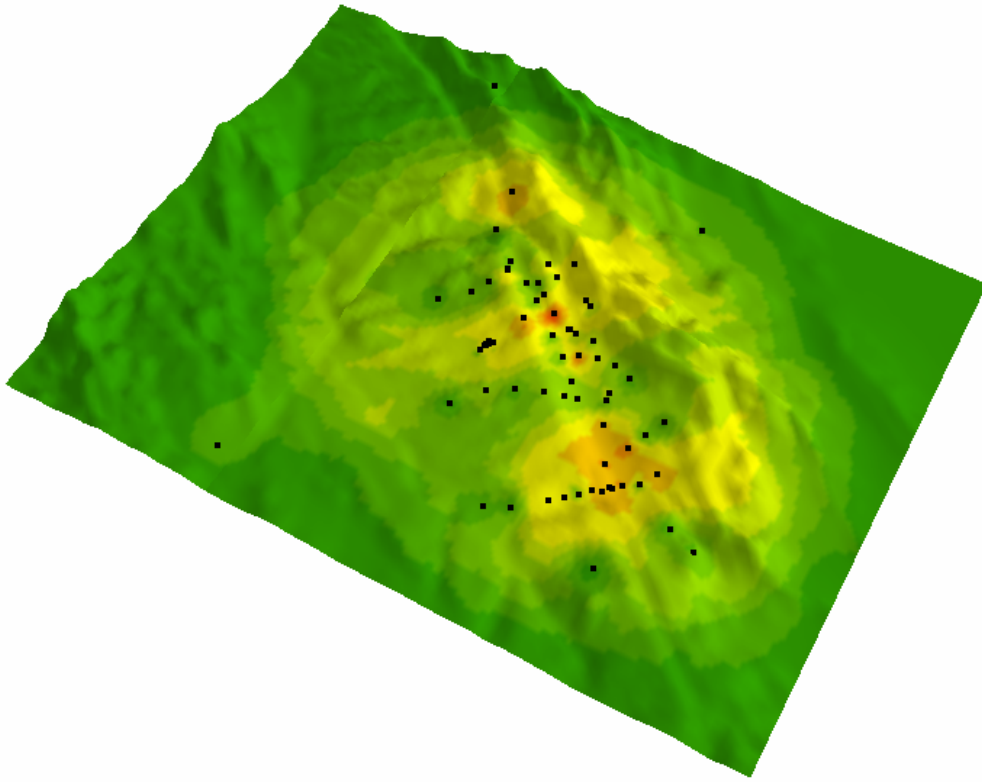
Fig. 12 Interstory drift map in the fault normal direction.
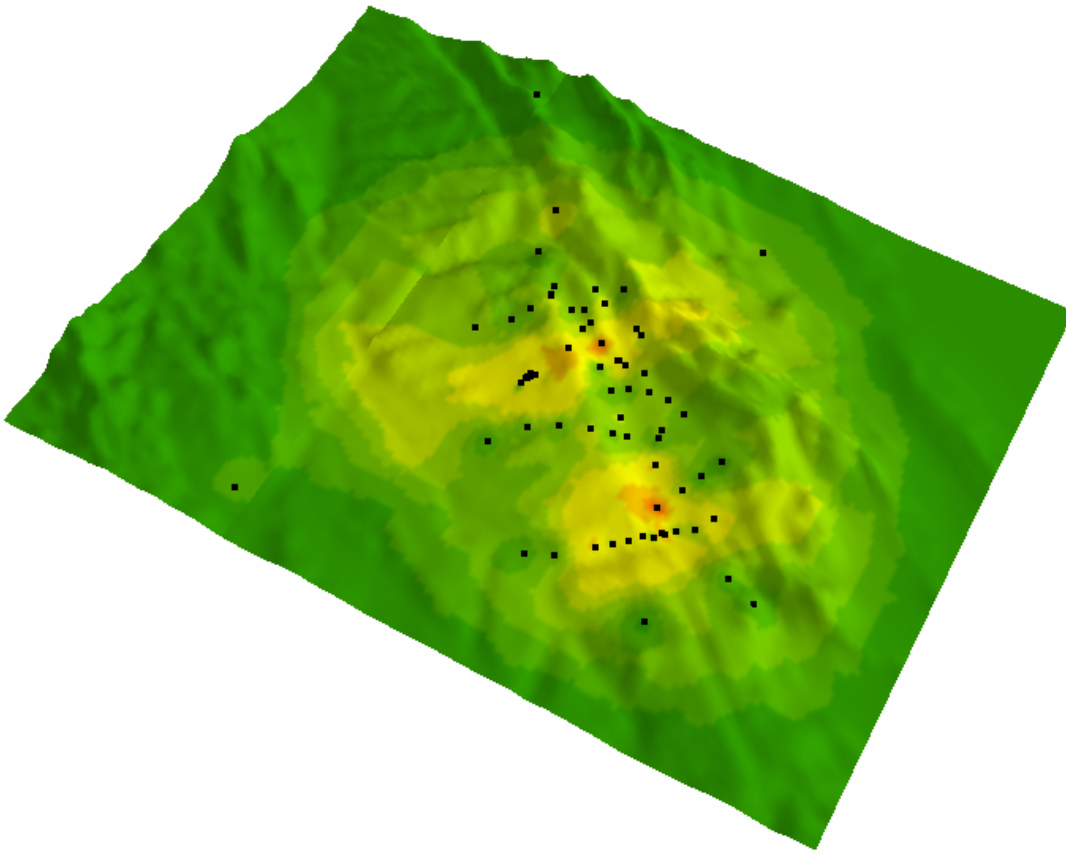
Fig. 13. Interstory drift map in the fault parallel direction.

Summary and Conclusions

New analytical tools for rapid building seismic response estimation aimed at rapid seismic performance assessment of large inventories buildings in urban areas have been presented. The simplified seismic analysis tools make use of continuum models consisting of a flexural beam coupled with a shear beam. Unlike sophisticated analysis models that require a significant amount of information of the buildings being analyzed and are computationally very demanding, the proposed analytical tool is fully defined by only three or four parameters. That is, only one or two parameters in addition to those required to define a linear elastic single degree of freedom system. Seismic response computation using the proposed analytical tool takes only fractions of a second in most personal computers, hence allows for the rapid assessment of hundreds of buildings, within few minutes after an earthquake. It should be noted that the proposed analytical tool has not been developed as replacement of more refined and accurate models. In particular, the proposed tool is not aimed at providing accurate estimates of interstory drift demands for buildings experiencing strong nonlinearities. However, together with information of drifts at which inelastic behavior is initiated, this tool is useful in identifying when yielding and possible damage is likely to occur and provides information on whether large interstory drifts are likely to occur in a structure.

The simplified building model, the generalized interstory drift spectra and the improved Shake Maps can be particularly helpful for the following applications: (1) Screening tool to identify buildings that are likely candidates for more detailed analyses; (2) Screening tool to identify buildings and urban regions that are more likely to be damaged in future earthquakes; (3) As a tool to conduct parametric studies to identify structural parameters or ground motion parameters that increase seismic demands on buildings; (4) Planning tool for emergency managers and city officials by using motions from previous ground motions or synthetic ground motions for studying possible damage in future events; (5) For rapid loss estimation of large inventories of building, and (6) To provide emergency managers and city officials early performance estimates within minutes of a seismic event.

Acknowledgements

References

Algan, B.B. (1982). "Drift and damage considerations in earthquake resistant design of reinforced concrete buildings," *PhD thesis*, University of Illinois, Urbana-Champaign, Ill.

Chopra, A.K., and Chintanapakdee, C. (2001). "Drift spectrum vs. modal analysis of structural response to near-fault ground motions," *Earthquake Spectra*, EERI, 1**7**(2), 221-234.

Cornell, C.A., Jalayer, F. Hamburger, R.O. and Foutch, D.A. (2002). "The Probabilistic Basis for the 2000 SAC/FEMA Steel Moment Frame Guidelines," *Journal of Structural Engineering*, Vol. 128, No. 4, pp. 526-533.

Deierlein, G.G., Krawinkler, H. and Cornell, C.A. (2003). "A framework for performance-based earthquake engineering." *Proceedings of 2003 Pacific Conference on Earthquake Engineering*.

Iwan, W.D. (1997). "The drift spectrum: a measure of demand for earthquake ground motions," *J. Struct. Engrg.,* ASCE, 123(4), 397-404.

Kircher, C.A. (2003). "Near-Real-Time Loss Estimation Using HAZUS and ShakeMap Data," *Proceedings SMIP03 Seminar on Utilization of Strong-Motion Data.*, May 22, 2003, Oakland, California, pp. 59-66.

Krawinkler, H., and Miranda, E. (2004). "Performance-based earthquake engineering," Chapter 9 of *Earthquake engineering: from engineering seismology to performance-based engineering*, Y. Bozorgnia and V.V. Bertero, Editors, CRC Press.

McCann, M.W., Sauter, F. and Shah, H. C. (1980), "A technical note on PGA-intensity relations with applications to damage estimation", *Bulletin of the Seismological Society of America*, Vol. 70, No. 2, pp. 631-637.

McJunkin, R. and Shakal, A. (1983) "Parkfiled strong-motion array," *California Geology*, February 1983, pp. 61-67.

Miranda, E. and Aslani, H. (2003). "Probabilistic response assessment for building-specific loss estimation." *Report PEER 2003/03,* Pacific Earthquake Engineering Research (PEER) Center, Richmond, California.

Miranda, E., and Taghavi, S. (2005). "Approximate floor acceleration demands in multi-story buildings. I: Formulation." *J. Struct. Eng.*, 131(2), 203–211.

Miranda, E., and Akkar, S. (2005). "Generalized interstory drift demand spectrum," accepted for publication in *J. Struct. Eng.*, 132, No. 6, pp. 840-852.

Moehle, J.P., and Deierlein, G.G. (2004). "A framework for performance-based earthquake engineering" *Proceedings of 13th World Conference on Earthquake Engineering*, Paper #679, Vancouver, Canada.

Qi, X., and Moehle, J. P. (1991). ''Displacement design approach for reinforced concrete structures subjected to earthquakes.'' *Rep. No. EERC/UCB-91/02*, Earthquake Engineering Research Center, University of California, Berkeley, Calif.

Rojahn, C., C.D. Comartin and S.A. King (2003). "Guidelines for Utilizing Strong-Motion and ShakeMap Data in Post-Earthquake Response (ATC-54)," *Proceedings SMIP03 Seminar on Utilization of Strong-Motion Data*., May 22, 2003, Oakland, California, pp. 47-58.

Taghavi, S., and Miranda, E. (2005). "Approximate floor acceleration demands in multi-story buildings. II: Applications." *J. Struct. Eng.*, 131(2), 212–220.

Wald, D.J., V. Quitoriano, T. Heaton, C.F. Scrivner and C. Worden (1999a), "TriNet ShakeMaps: rapid generation of peak ground motion and intensity maps for earthquakes in Southern California," *Earthquake Spectra*, Vol. 15, No. 3, pp. 537-555.

Wald, D.J. et al. (1999b), "Relationships between peak ground acceleration, peak ground velocity, and modified Mercalli intensity in California," *Earthquake Spectra*, Vol. 15, No. 3, pp. 557-564.

STUDY OF WOOD-FRAME BUILDING RECORDS
FROM THE PARKFIELD AND SAN SIMEON EARTHQUAKES

Daniel Sutoyo and John Hall

Department of Civil Engineering
California Institute of Technology, Pasadena

Abstract

In order to develop seismic codes that can effectively mitigate damage to wood-frame construction under seismic activity, the dynamic characteristics of wood-frame buildings must be well understood. Toward this end, this data interpretation project focuses on the dynamic behavior of low-rise wooden shearwall buildings under large seismic motions. The procedure includes determining the modal parameters and extracting hysteretic characteristics from the available records.

Overview

Low-rise wood-frame buildings are the predominant wood-frame construction in North America. In California, 99% of all residences are constructed of wood (Camelo 2002). Due to the ubiquitous nature of wood-frame construction, it is surprising that wood-frame building behavior is not fully understood. Progress is being made though as this topic has attracted a lot of government and research attention in recent years, primarily because of huge economic losses in '94 Northridge earthquake. Advancement in wood-frame research has been made through the collaboration of Federal Emergency Management Agency (FEMA) and the Consortium of Universities of Research in Earthquake Engineering (CUREE). The ultimate goal of such work is to make the basis of building codes more rational. The project covered five main areas: testing and analysis, field investigations, building codes and standards, economic aspects and education and outreach (Camelo 2002).

As part of the CUREE project, Camelo and Beck performed system identification with the computed program MODE-ID (Beck 1987) on several wooden buildings California Strong Motion Instrumentation Program (CSMIP) sites. The results show that there is clear amplitude dependence; fundamental frequencies were lowest and damping estimates were highest in the time frame of the strongest seismic activity (Camelo 2003). An important feature from the analysis was the high damping estimates. The values ranged from 15-20%, which are several times more than that of steel or concrete structures.

The current project extends the work of Camelo (2003) to two buildings at higher shaking levels. Since the estimated damping values include energy dissipated by hysteretic action, the current project also seeks to extract hysteretic characteristics of these buildings. The project has six main objectives:

1) Apply different system identification methods to obtain modal estimates. Specifically, observe if various methods conclude on high damping values for wood-frame construction. Investigate methods that include but are not limited to: SDOF time domain methods, random decrement method, frequency curve fitting methods, and Hilbert and Wavelet Transforms.

2) Using the most appropriate system identification technique, perform detailed system identification studies on two structures, Parkfield school and Templeton hospital building, for recently obtained earthquake records. The focus will be on natural frequency and damping as a function of response amplitude.

3) Extract hysteretic parameters of walls and diaphragms from the recorded time histories.

4) Perform system identification studies on components of buildings, such as diaphragms, to determine their dynamic characteristics.

5) Create numerical models to simulate the measured responses. Models will be used to confirm the estimates of various system identification methods, validate the hysteresis extraction procedures and validate the component identification process. A particular interest will be the large damping values.

6) Interpret all of the results for the benefit of code development.

Buildings and Records

Parkfield school and Templeton hospital buildings are chosen as test subjects for analysis. Previous studies have successfully been conducted at these locations, and there is a plethora of records and documentation from past studies contained within the CSMIP database. The databases contain several records of these buildings at different amplitudes of shaking, including the record for the largest peak structural acceleration in a wood-frame building at 128% g.

Parkfield School
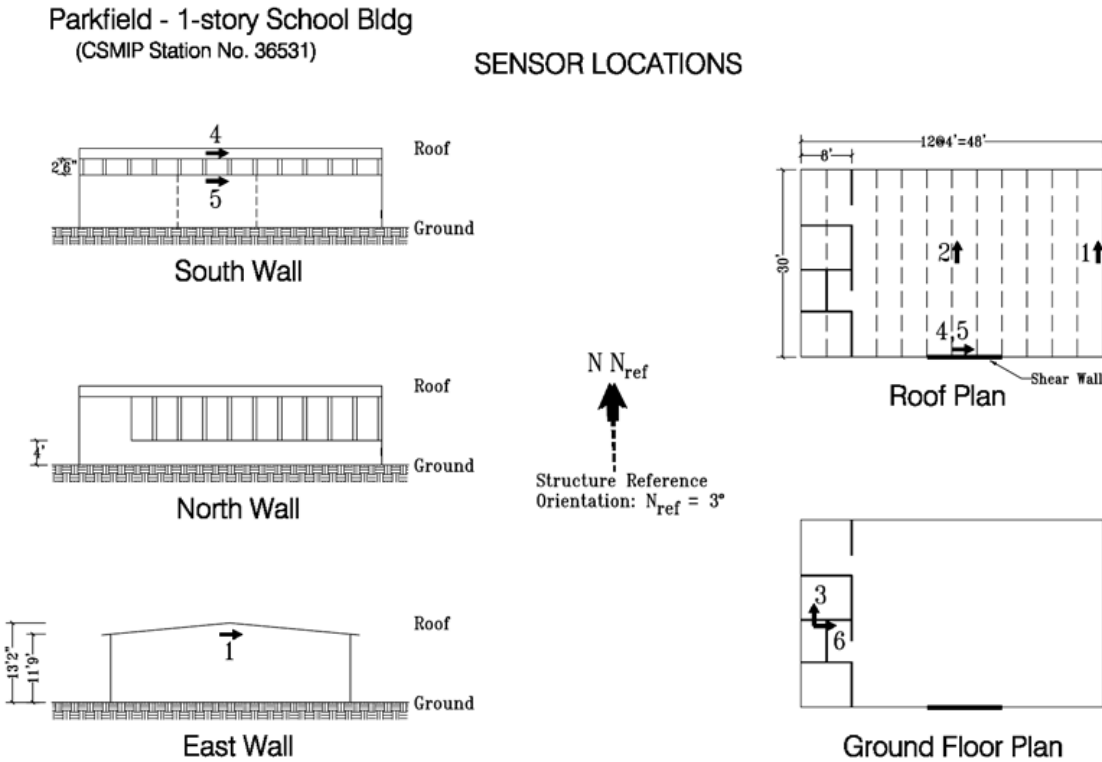
Figure 1: A schematic of Parkfield school building displaying the locations of all six sensors.

The Parkfield school building, built in 1949, is a rectangular wood-frame building with dimensions of 48' by 30' (Figure 1). There are a total of six accelerometer channels on the building. Channels 3 and 6 are the ground reference and taken as the excitation when using MODE-ID. Two channels are in the N-S (transverse) direction and two are in the E-W (longitudinal) direction. Figure 2 displays the acceleration time histories recorded during the 2004 Parkfield earthquake.
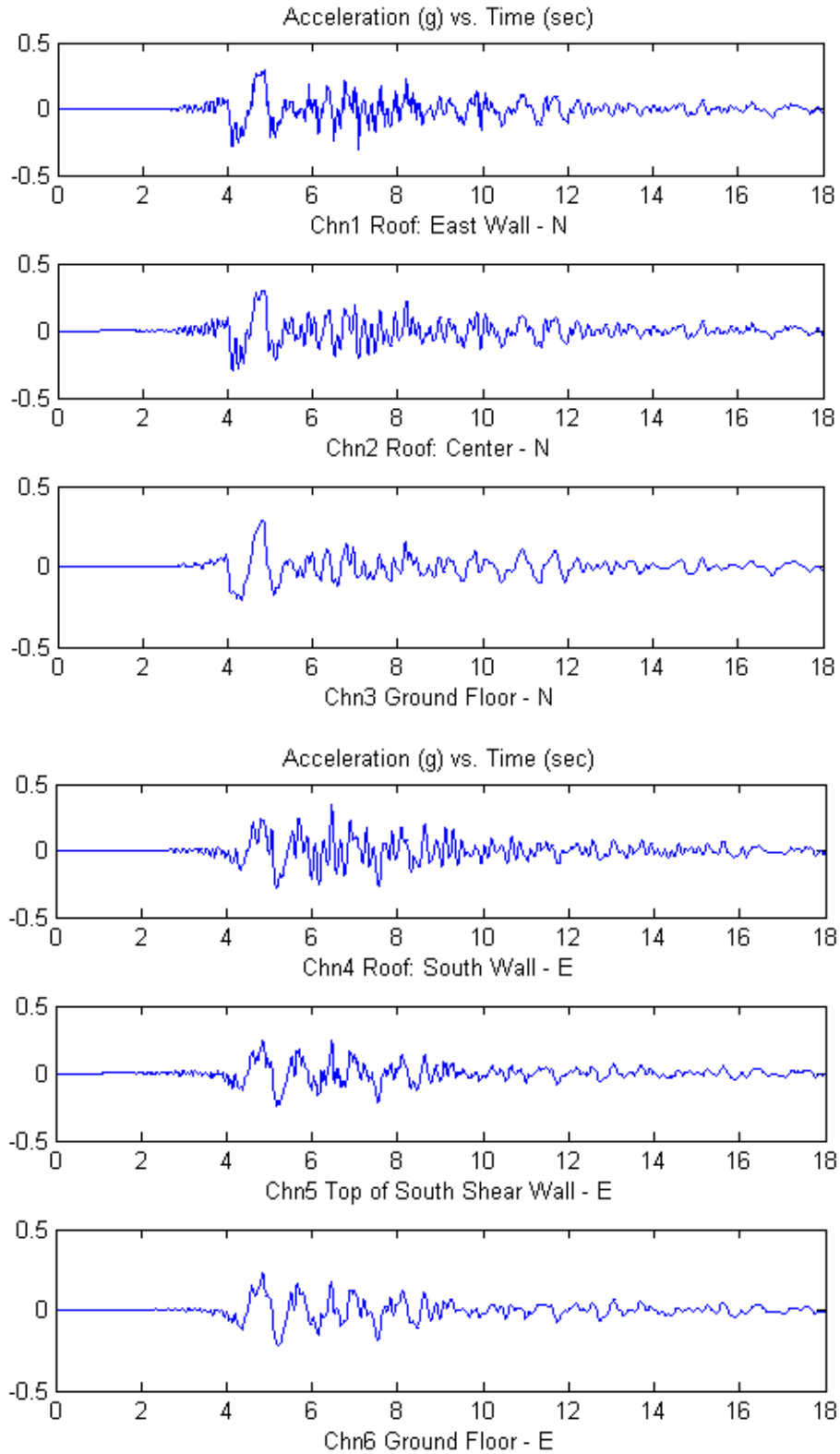
Figure 2: Acceleration time histories that were recorded from the Parkfield school building during the 2004 Parkfield earthquake.

Templeton Hospital

The Templeton hospital building, built in the 1970s, has an irregular shaped building plan spanning the dimensions of 336' by 277' (Figure 3). There are a total of nine accelerometer channels on the building. Channels 1 (vertical), 2 (E-W) and 3 (N-S) are the ground reference sensors. There are three channels for each N-S and E-W direction. Figure 4 displays the acceleration time histories recorded during the 2003 San Simeon earthquake.
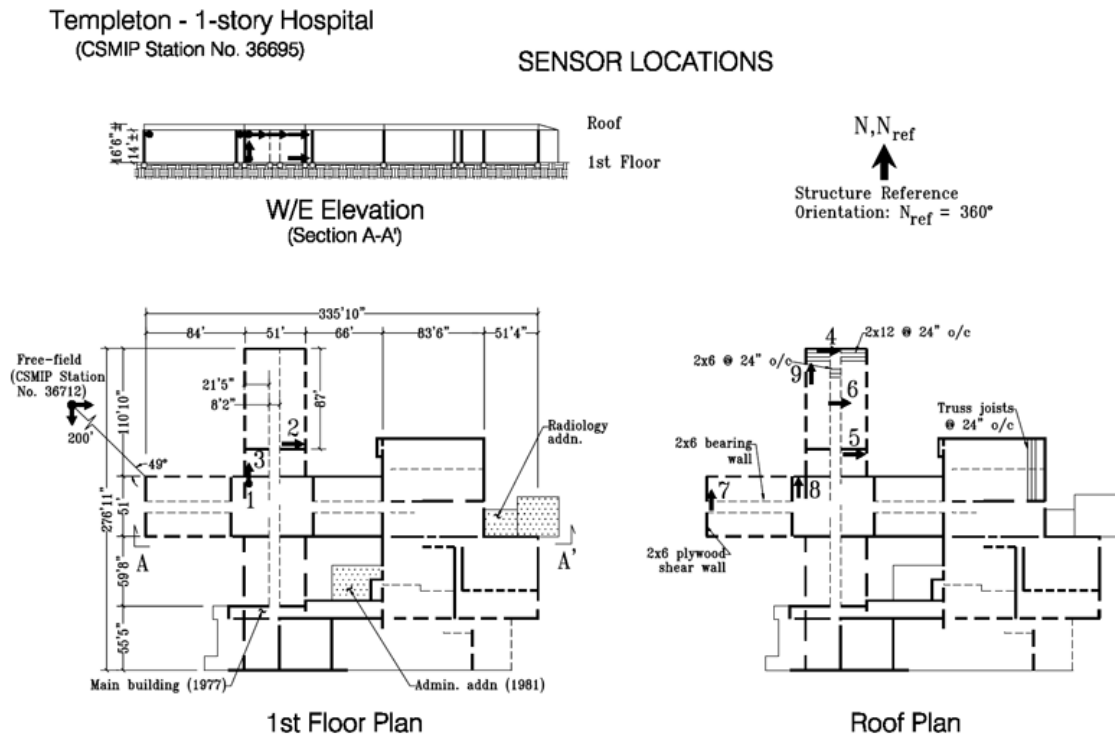
Figure 3: A schematic of Templeton hospital building displaying the locations of all nine sensors.
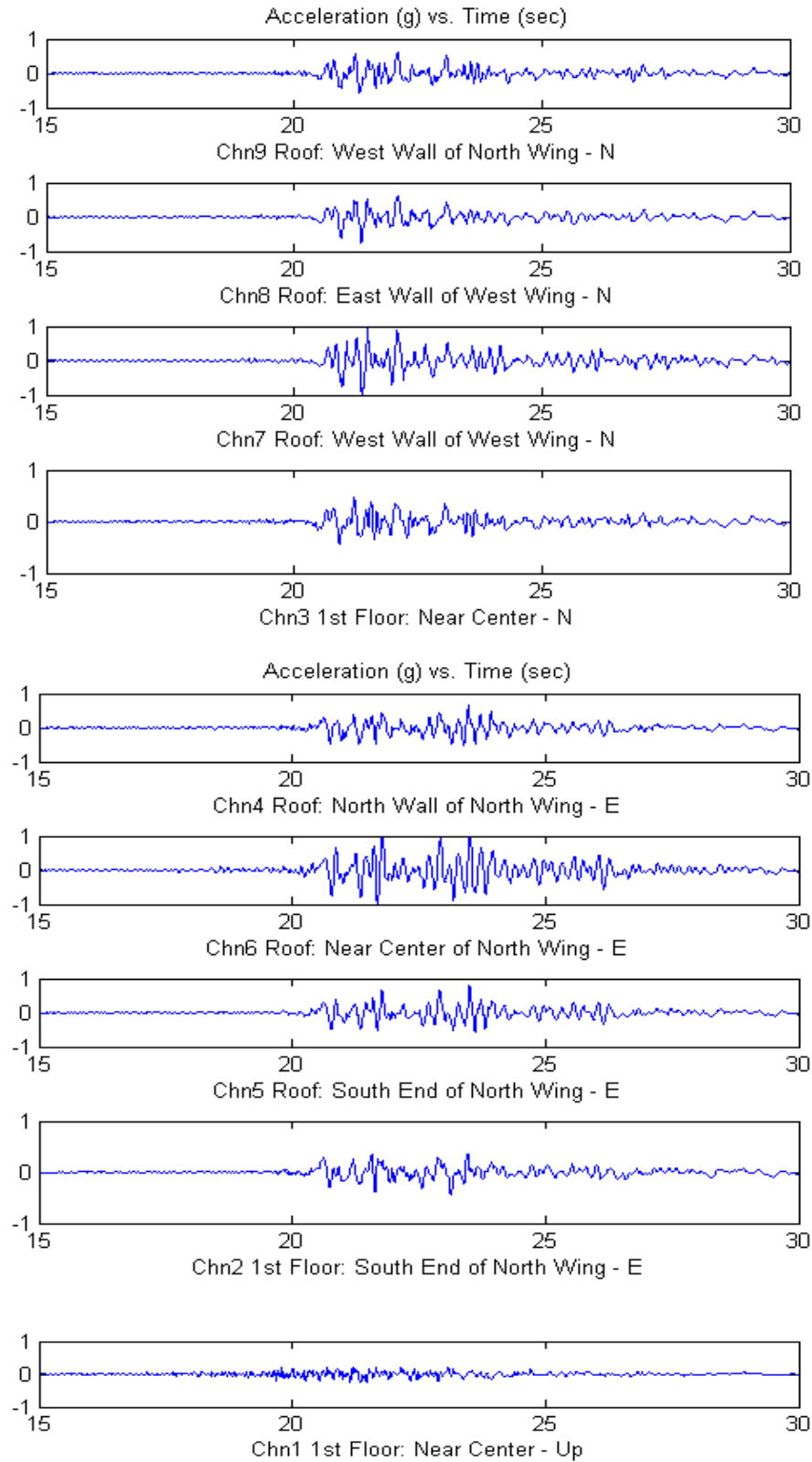
Figure 4: Acceleration time histories that were recorded from the Templeton hospital building during the 2003 San Simeon earthquake.

System Identification

Various system identification schemes were explored, but MODE-ID is selected for its robustness. MODE-ID utilizes modal identification and a modal minimization routine (Beck and Beck 1985). Modal identification estimates modal parameters of a linear dynamic model from the responses of a structure. This application of system identification can be performed in the time domain without the need to develop a structural model by constructing mass, stiffness and damping matrices (Beck, 1978).

Without discussing all the other methods in detail, most of them are ad-hoc, requiring special conditions not met in practice with real seismic response records. Assumptions can be made to improve the results of other methods, but this process requires specific tailoring of the records. However, this is not to say MODE-ID is the only method that is suitable for analyzing real seismic records. Other estimation methods like Bayseian approaches and particle filtering could be suitable as well (Ching, et al.2004). Furthermore a frequency domain MODE-ID can be employed through Parseval's Inequality (Werner 1987).

MODE-ID can handle multiple inputs in order to find the modal parameters from seismic motions recorded from a structure. Inputs for MODE-ID include the ground excitation records, measured structural response histories and initial modal estimates. The modal parameters estimated for each mode are the frequency, damping factor, normalized modeshape, participation factors and initial displacement and velocity. MODE-ID has been extensively applied to earthquake and other dynamic data. In short MODE-ID is based on a nonlinear least-squares output-error method. The measure of fit between the recorded and calculated response is optimized by a modal minimization algorithm (Beck and Beck 1985).

To minimize the measure-of-fit, the program performs a series of sweeps in which optimization is performed one mode at a time. Optimization within each mode is by the method of steepest descent with respect to the modal frequency and damping (Beck and Jennings 1980). Additional information and detailed mathematical background can be found in the MODE-ID user guide and in EERL Report 85-06. Both are listed in the reference section.

Results

Parkfield School

The Parkfield school building is only one story tall. It is expected that the dominant response will largely consist of the fundamental N-S, E-W and torsional modes. The frequency, damping and modeshape estimates are presented in Table 1 and Figure 5. In addition to the 2004 Parkfield earthquake, records from two smaller earthquakes in 1993 and 1994 are considered in order to provide a range of response amplitudes. Note from Figure 5 that the modes are coupled and so are not purely N-S, E-W and torsional.

Table 1.   Parkfield school building frequency and damping estimates calculated from MODE-ID. The peak structural acceleration is provided for each earthquake

Earthquake	Frequency (Hz) E-W	Damping Ratio (%) E-W	Frequency (Hz) N-S	Damping Ratio (%) N-S	Frequency (Hz) T	Damping Ratio (%) T
4.2 M 0.123 g 04/04/1993	7.3	12.3	8.6	14.5	9.8	11.3
4.7 M 0.201 g 12/20/1994	6.5	10.7	8.2	14.0	19.2	11.1
6.0 M 0.30 g 09/28/2004	5.26	12.9	6.01	12.9	13.1	8.9

The 1993 and 1994 earthquakes have been reanalyzed and compared to the results of Camelo and Beck in CUREE Publication No. W-11. The values are found to be consistent. Since the magnitudes of the earthquake in 1993 and 1994 are similar, the reported modal frequency and damping estimates are comparable with the exception of the damping ratios of the torsional mode. A reason for this difference is not evident. With the addition of the records from 2004, amplitude dependence can be observed. The larger response amplitudes are accompanied by lower frequencies and higher damping values.

The analysis done on full-duration records displays high damping estimates as have been noted in previous studies. Damping is inherently difficult to estimate accurately with any method (Beck and Beck 1985). The credibility of a 20% damping ratio in wood-frame buildings needs to be investigated since steel or concrete buildings generally have values of 3 to 5%. For MODE-ID, a linear viscous damping is assumed. The meaning of a linear damping value that is fit under conditions of nonlinear response is currently under study.

E-W Mode

N-S Mode

Torsional Mode
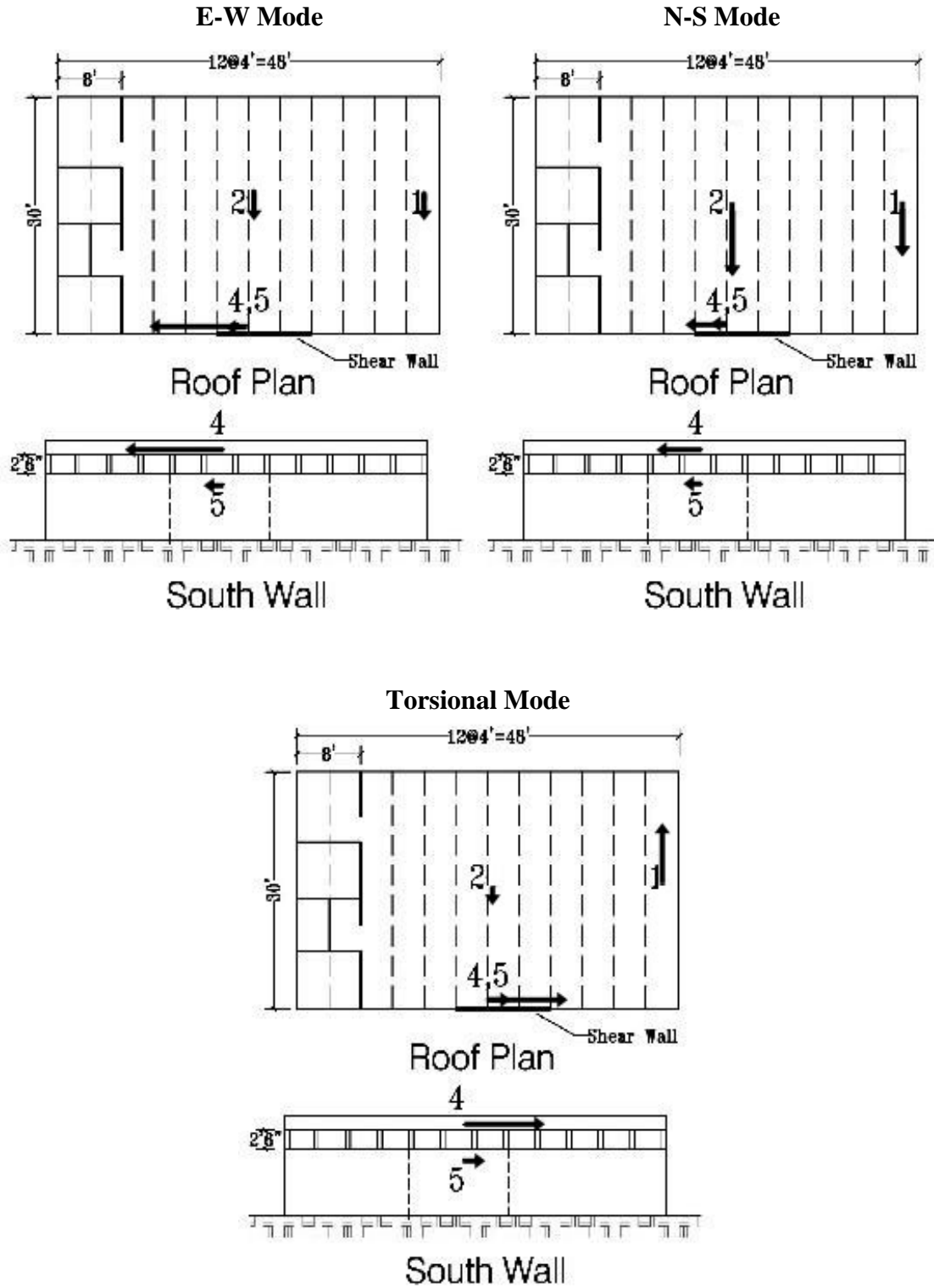
**Figure 5: First three modeshapes of the Parkfield school building
generated from the 2004 Parkfield earthquake**

Another observation that can be inferred from Table 1 is that the damping estimates in the N-S are generally greater than those of the E-W modes. This may be related to the fact that the north and south walls have less shear wall contribution due to a substantial area designated for windows, as shown in Figure 6.

North Wall   East Wall

South Wall   West Wall
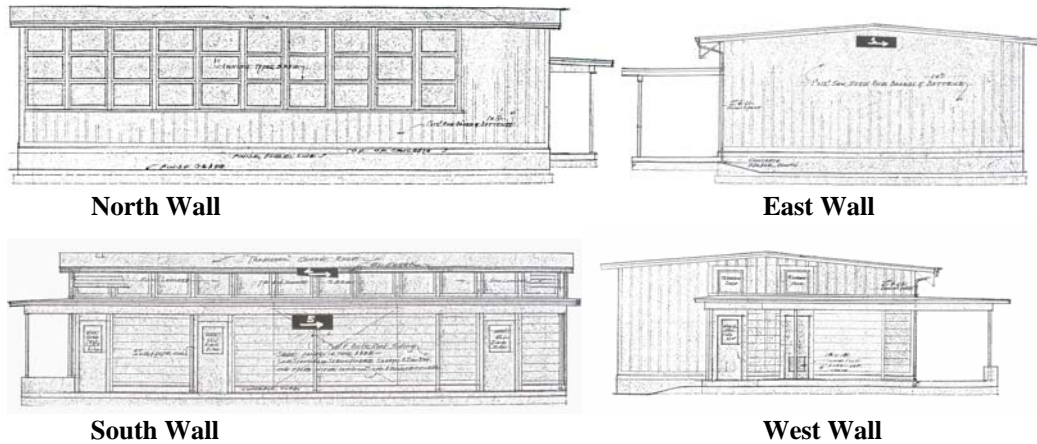
Figure 6. Elevation views of the Parkfield school building

A windowing analysis is also performed on the 2004 Parkfield records through MODE-ID. Results are presented in Figure 7 (frequencies) and Figure 8 (damping). A two-second window with 50 % overlap was chosen because it is the smallest window that results in consistent convergence. Windowing reveals the change in modal frequency and damping during the earthquake.

From Figure 7 it is apparent that the building did reach nonlinear motions as each fundamental frequency changed during the course of the response. Following the locus of the estimated fundamental frequencies of the building, the initial frequencies are around the 7.5 Hz range when the initial motion was recorded. The building's frequencies decrease as the magnitude of the ground response increases, reaching significantly lower values during the time of the strongest ground shaking at around 5 seconds (Figure 2). As the ground motion subsides, the building's frequencies revert to the initial frequencies. This probably indicates the building sustained no significant damage.

The window analysis on damping estimates (Figure 8) shows that damping fluctuates greatly throughout the earthquake shaking. Another observation is that even at lower ground motions, the damping ratio still display values of 12-20%, which are high relative to steel and concrete buildings. As mentioned previously, the issue of high damping values is currently under study.
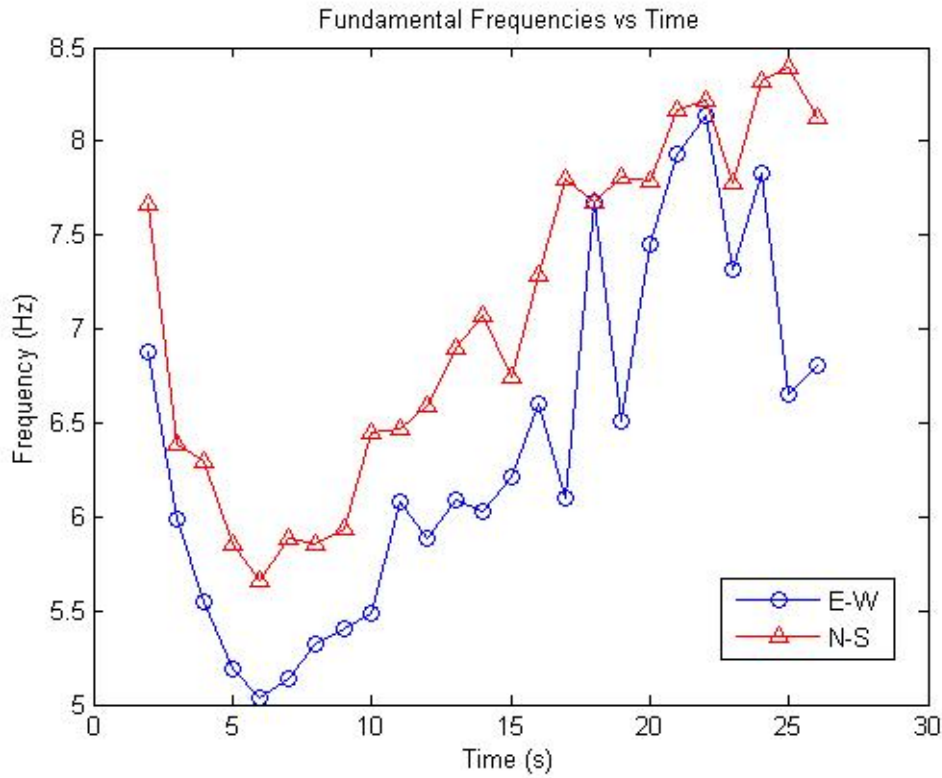
Figure 7: **Amplitude dependence of the E-W and N-S mode frequency estimates for Parkfield School building. The window analysis is performed on the 2004 Parkfield earthquake.**
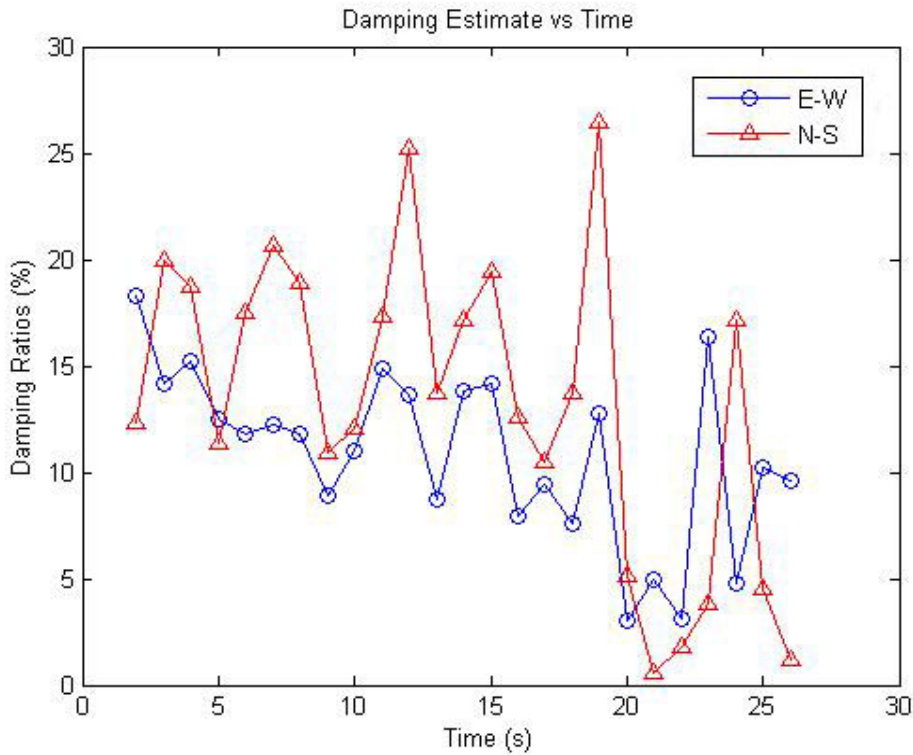
Figure 8. Amplitude dependence of the E-W and N-S mode damping estimates for Parkfield School building. The window analysis is performed on the 2004 Parkfield earthquake.

Templeton Hospital

Frequency, damping and modeshape estimates are presented in Table 2 and Figure 9. The first mode involves mostly transverse motion of the west wing, and the second mode is mostly north wing. Both wings contribute to the third mode. The instrumentation layout allows only the study of the north western wings of this very asymmetric building.

Table 2 contains result for the M 6.5 earthquake in 2003, three of its aftershocks and another smaller earthquake in 2005. Results seem to be consistent to the observations made from the analysis of the Parkfield school building. The amplitude dependence of the modal parameters is shown in Figures 10 and 11. Refer to Figure 4 for the acceleration time histories of the 2003 San Simeon earthquake.

Table 2.   **Templeton hospital building frequency and damping estimates calculated from MODE-ID. The peak structural acceleration is provided for each earthquake**

Earthquake	Frequency (Hz) West Wing	Damping Ratio (%) West Wing	Frequency (Hz) East Wing	Damping Ratio (%) East Wing	Frequency (Hz) Mode 3	Damping Ratio (%) Mode 3
6.5 M 1.3 g 12/22/03	4.77	15.75	5.0	16.6	7.42	17.2
.031g 02/09/04 aftershock	7.09	21.1	7.4	11.6	10.7	16.0
.073g 05/02/04 aftershock	6.6	20.6	6.7	13.4	9.2	11.4
.217 g 10/02/04 aftershock	6.6	15.4	5.8	17.5	8.1	14.0
4.4 M .017 g 05/16/05	7.3	20.0	7.0	12.1	9.9	8.9

West Wing Mode

North Wing Mode
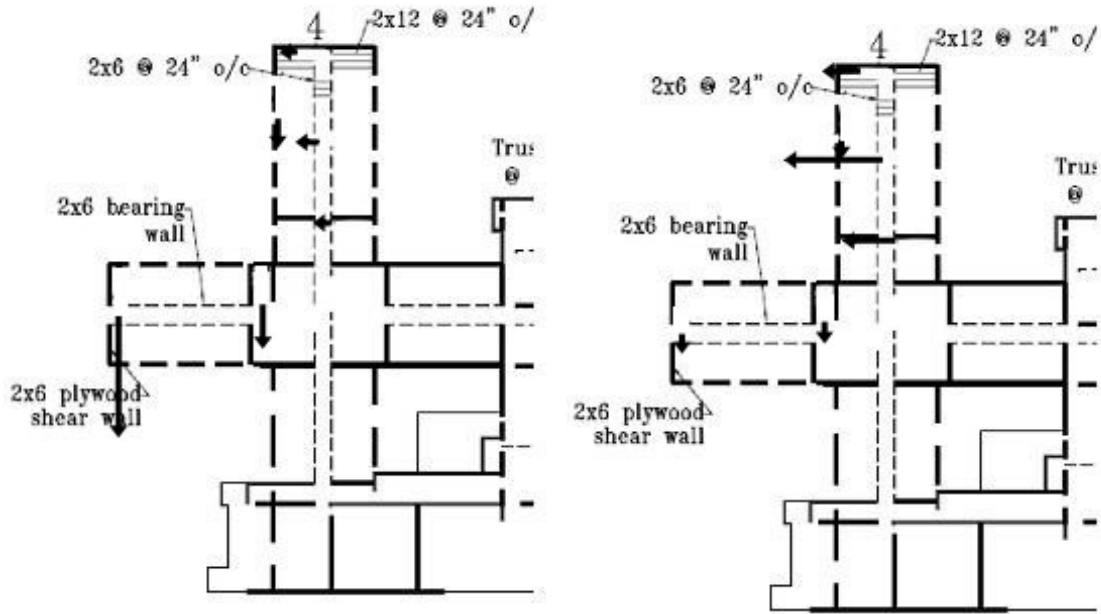
Mode 3
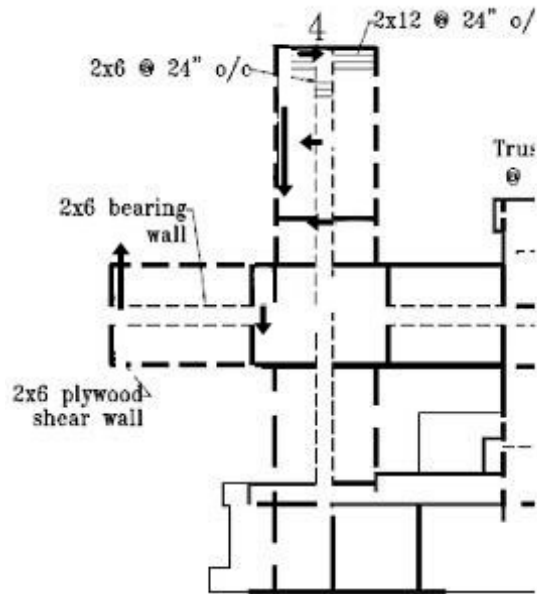
**Figure 9: First three modeshapes of the Templeton hospital building
generated from the 2003 San Simeon earthquake**
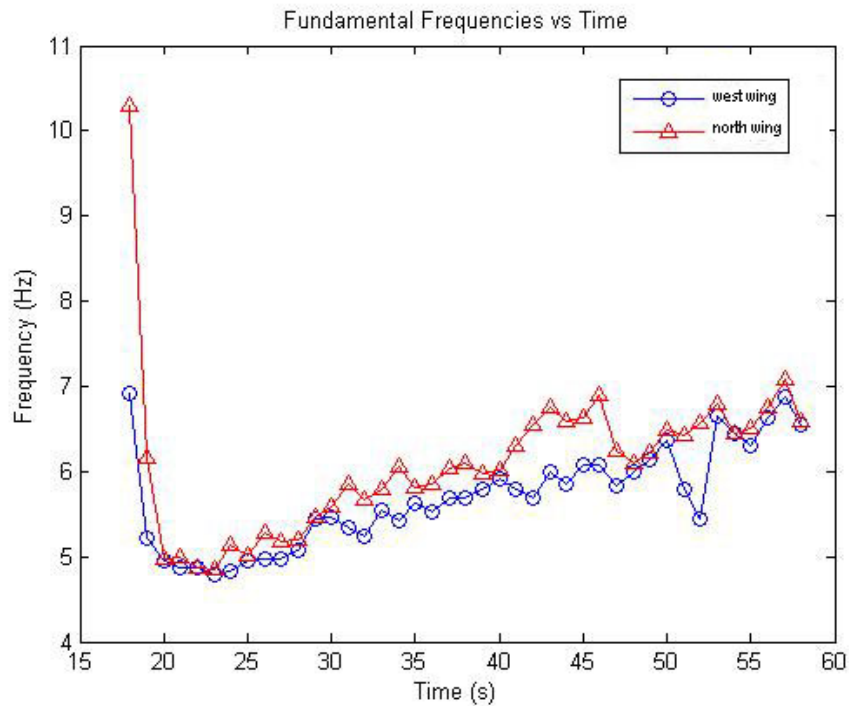
Figure 10: Amplitude dependence of the west wing and north wing frequency estimates for Templeton hospital building. The window analysis is performed on the 2003 San Simeon earthquake.
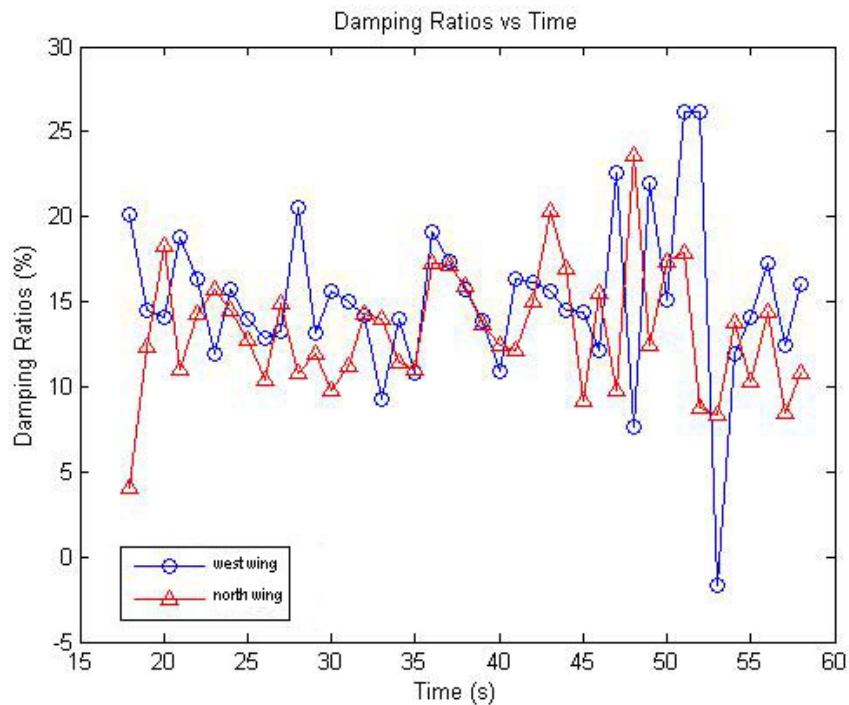
Figure 11: Amplitude dependence of the west wing and north wing mode damping estimates for Templeton hospital building. The window analysis is performed on the 2003 San Simeon earthquake.

Hysteresis Characterization

General Concepts

One of the major characteristic of wood-frame buildings is pinching hysteresis. As loading progresses and the deformation of the connection increases, wood fibers are crushed and a nail may begin to yield. If the loading is reversed, the nail moves through the gap formed by the crushed wood fibers. Through each cycle of displacement, depending on the amplitude of the motion, the wood is increasingly indented by the nail. This creates extra spacing wherein the nail will displace with reduced opposing force (Judd 2004).

It is imperative to accurately map hysteresis curves since they play a pivotal role in creating a better nonlinear model. Fortuantely, many of the commercial products that provide nonlinear analysis have the option to input a hysteresis model. The hysteretic behavior of a structure plays a crucial role in many current approaches to seismic performance-based analysis and design. Thus, many experiments have been performed to record hysteretic data for wood shear walls and other subassemblies. An example that illustrates the pinching behavior is show in Figure 2. Although thus test was for a single-nail connection, similar behavior is observed for wall and diaphragm components and for entire structures.
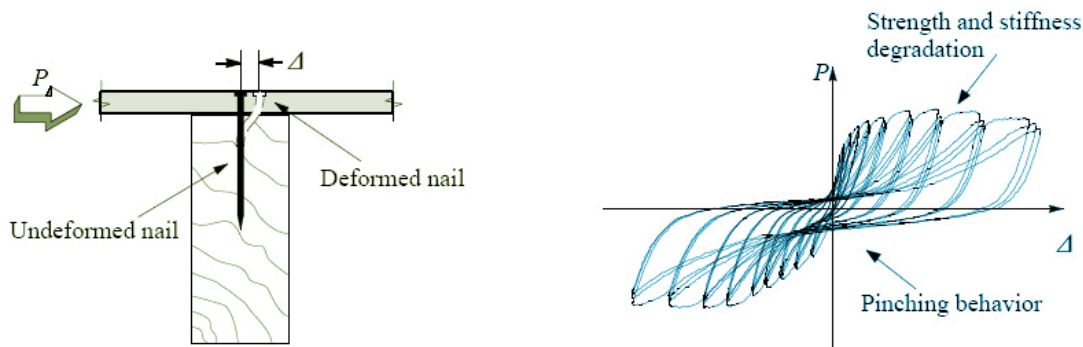
Figure 12. Illustration of the nailed sheathing connection and pinching hysteresis curve (Judd 2004).

Extraction of hysteretic characteristics of wood-frame building components can lead to an understanding of the pinching and degradation behavior as well as reveal the extent to which the building response extends into the nonlinear range. The process involves the construction of a hysteresis curve by plotting time history pairs of restoring force across the component (on the vertical axis) and relative displacement across the component (on the horizontal axis). The ability to compute the restoring force and relative displacement requires that sufficient instrumentation be present.
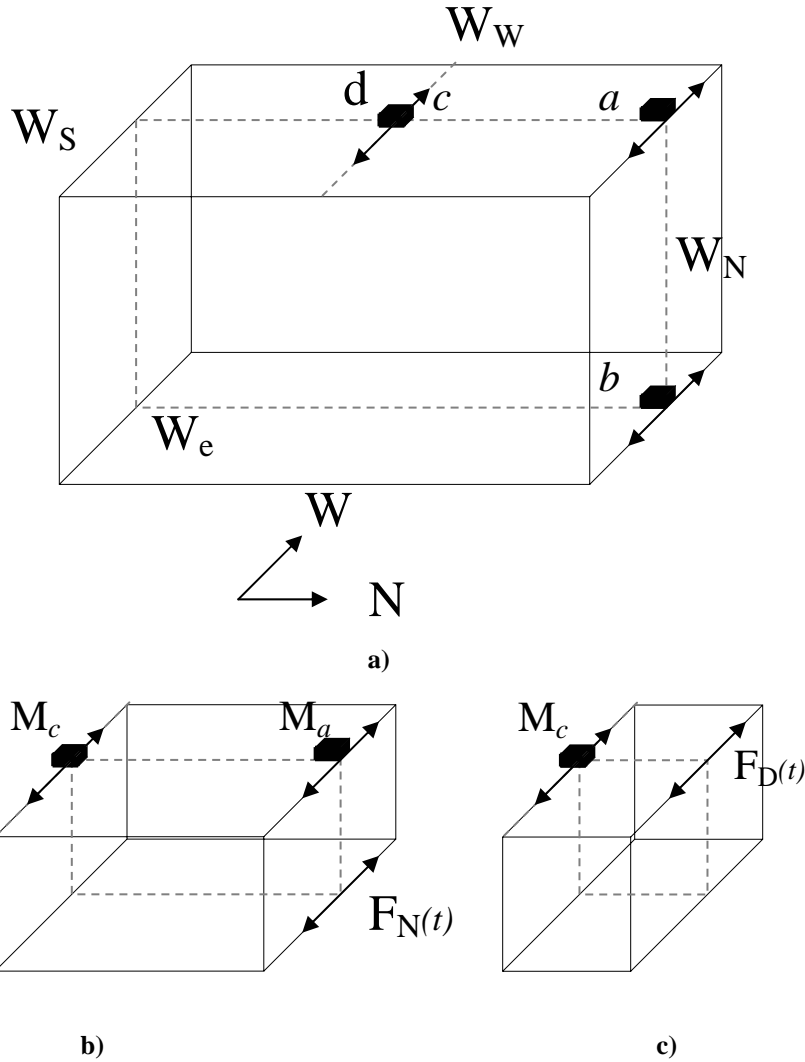
Figure 13: Illustrative example of the free body diagram concept to calculate a hystersis curve.

Consider the simple structure shown in Figure 13a as an example, consisting of north, south, east and west walls (W_N, W_S, W_E and W_W) and a diaphragm (D) with earthquake acceleration records obtained at *a*, *b* and *c* in the E-W direction. It is desired to plot the hysteretic curve for the north wall. To obtain the restoring (shear) force time history, a free-body diagram (FBD) is needed as shown in Figure 13b. The north wall is cut at mid-height and the diaphragm at mid-span as shown, with the cuts extending through the east and west walls. In the E-W direction, the restoring force at the diaphragm cut is set to zero based on an assumption of symmetric response, and the forces on the east and west walls are taken as zero because they would be out of plane, leaving only the restoring force F_N on the north wall. The E-W equation of motion is shown below in Equation 1

Equation 1. Force balance equation derived from FBD Figure 13b

$$F_N(t) = m_a \ddot{x}_a + m_c \ddot{x}_c$$

where m_a and m_c are tributary masses for the free body at a and c and $\ddot{x}_a$ and $\ddot{x}_c$ are the recorded accelerations at a and c, gives $F_N(t)$ directly. The relative displacement $x_{a\text{-}b}(t)$ across the north wall is obtained by subtracting the doubly integrated acceleration records at a and b. Pairs of $F_N(t)$ and $x_{a\text{-}b}(t)$ are then plotted.

The situation for the diaphragm is different because the shear varies substantially along the diaphragm, being maximum at the ends. The procedure employed here extracts the restoring (shear) force $F_D(t)$ at the quarter point and uses a free body consisting of one quarter of the diaphragm and adjacent pieces of the east and west walls cut at mid-height as shown in Figure 13c. With similar assumptions as made previously, only $F_D(t)$ is present and is determined from Equation 2

Equation 2: Force balance equation derived from FBD Figure 13 c

$$F_D(t) = m_c \ddot{x}_c$$

The relative displacement in this case is $x_{c\text{-}a}(t)$, obtained by subtracting the doubly integrated acceleration records at c and a.

Hysteresis Characteristics Results

Using the free body concept described in the previous section, attempts are made to retrieve the hysteretic characteristics of the Parkfield school and Templeton hospital buildings. Results for the Parkfield school are shown in Figure 14a (east wall), 14b (diaphragm), 15c (top part of south wall) and 15d (bottom part of south wall). For example, calculations performed for the hysteresis curve in Figure 14a are based on Equation 1, with the north wall in Figure 13 representing the east wall of the Parkfield school, and channels a, b and c in Figure 13 being channels 1, 3 and 2, respectively, at Parkfield school (see Figure 1). Since the ground motion is assumed to be uniform, it does not matter that channel 3 is not located directly under Parkfield school's east wall. For the masses m_c and m_a in Figure 13b, artificial values in the ratio of 1.3 to 1.0 are employed. The use of artificial values means that the force scale in Figure 14 is meaningless, but the shape of the hysteresis curve is not affected since this depends only on the ratio of m_c to m_a.

The computed hysteresis curve in Figure 14a shows evidence of pinching in the larger excursions, but not nearly as clear as that in Figure 12 obtained from a controlled laboratory experiment. Results for the south wall in Figure 14c and d can be described similarly. In the latter cases, some filtering of the displacement histories had to be done to remove long-period errors. The computed hysteresis curve for the diaphragm (Figure 14b) doesn't seem to have any realistic trends. The same can be said for the computed hysteresis curve for the north wall of the north wing of the Templeton hospital show in Figure 15, which also used the procedure described by Equation 1 and Figure 13.

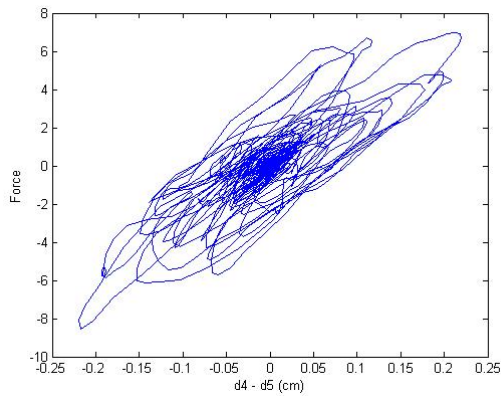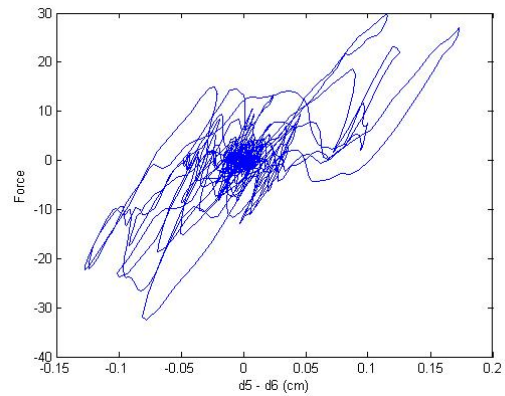**Hysteresis Curve of East Wall**
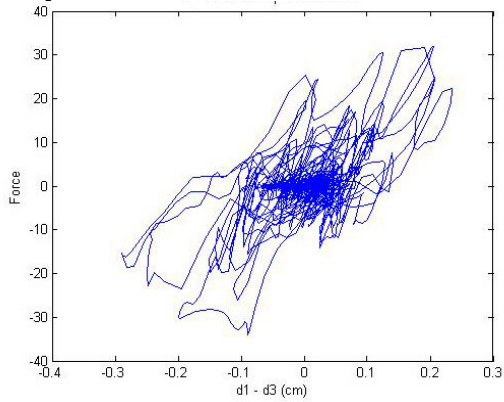
Hysteresis Curve of Diaphragm

a)
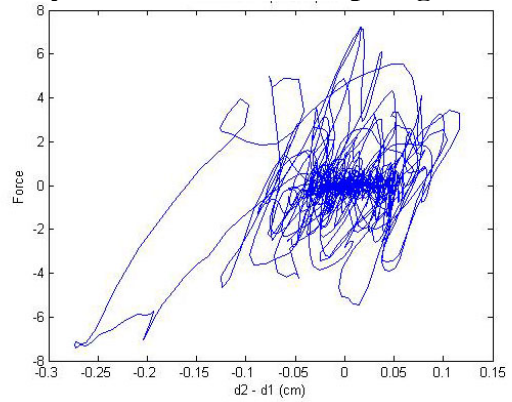
b)

Hysteresis Curve of Upper South Wall

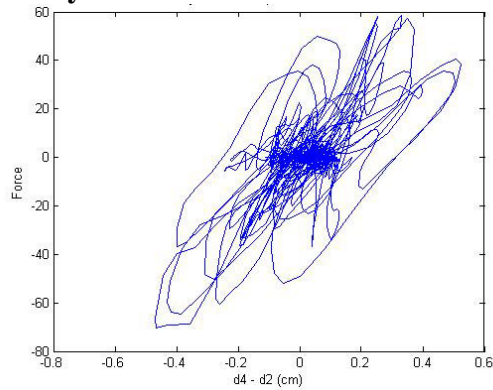**Hysteresis Curve of Lower South Wall**

c)

d)

Figure 14: Hysteresis curves of Parkfield school building

Hysteresis Curve of North Wall

Figure 15: Hysteresis curve of Templeton hospital building's north wall of its north wing

Conclusions

This study has observed significant amplitude dependence of the modal frequencies, decreasing for higher amplitude of shaking, and high damping values identified for the seismic response of wood-frame buildings. These results are in agreement with previous findings. A 25% to 30% drop in frequency during the stronger earthquakes examined here was typical. A damping ratio, more or less constant over the earthquake, at about 15% to 20% was also typical. A detailed study employing finite element models is planned to further investigate these behaviors.

An attempt to retrieve the hysteretic characteristics of wall and diaphragm components was hampered by errors inherent in the process employed. This process will also be a focus of the future finite element studies to determine what improvements in calculation process and instrumentation arrays can increase the accuracy of the computed hysteresis curves.

References

Beck JL. (1978). *Determining Models of Structures from Earthquake Records.* EERL Report No. 78-01, California Institute of Technology, Pasadena, Calif.

Beck JL. (1996) "System Identification Methods Applied to Measured Seismic Response," *Proceedings11th World Conference on Earthquake Engineering*, Acapulco, Mexico, June.

Beck RT., Beck JL. (1985). *Comparison Between Transfer Function and Modal Minimization Methods for System Identification.* EERL Report No. 85-06, California Institute of Technology, Pasadena, Calif.

Beck JL, Jennings PC. (1980). "Structural Identification Using Linear Models and Earthquake Records." *Earthquake Engineering and Structural Dynamics*, 8, 145-160.

Camelo V., Beck JL., Hall JF. (2002). "Dynamic Characteristics of Woodframe Structures." *CUREE Publication No. W-11*. CUREE Richmond, Calif.

Camelo VS, Beck JL, Hall JF. (2003). *Dynamic Characteristics of Woodframe Buildings*. Thesis, California Institute of Technology, Pasadena, Calif.

Ching J. Beck JL. Porter KA., Shaikhutdinov R. *Real-Time Bayesian State Estimation of Uncertain Dynamical Systems.* EERL Report No. 2004-01, California Institute of Technology, Pasadena, Calif.

Filiatrault A., et al. (2001). "Shake Table Tests of a Two-Story Woodframe House". *Element 1 Research Meeting, January 12, 2001*, CUREE-Caltech Woodframe Project, San Diego, Calif.

Foliente GC. (Ed.) (1994). "Analysis, Design and Testing of Timber Structures Under Seismic Loads." *Proceedings of a Research Workshop*, University of California, Forest Products Laboratory, Richmond, Calif.

Isoda H., Folz B., Filiatrault A. (2002). "Seismic Modeling of Index Woodframe Buildings." *CUREE Publication No. W-12*. CUREE Richmond, Calif.

Judd J., Fonseca F., (2004). Hysteresis Model Parameters for Nailed Sheathing Connections in Wood Shear Walls.

Mitrani J., Beck JL. (2003). User's Guide for MODE-ID Version 6.0. COMET website: http://comet.caltech.edu/sn_home.asp

Werner SD, Beck JL, Levine MB. (1987). "Seismic Response Evaluation of Meloland Road Overpass Using 1979 Imperial Valley Earthquake Records." *Earthquake Engineering and Structural Dynamics,* 15, 249-274.

SEISMIC RESPONSE OF THE HWY 46/CHOLAME CREEK BRIDGE DURING THE 2004 PARKFIELD EARTHQUAKE

B. Tom Boardman[1], Anthony V. Sanchez[2], Geoff Martin[3],
Zia Zafir[1], Edward Rinne[1] and Joe Tognoli[2]

[1]Kleinfelder, Inc., [2]TY Lin International, and [3]University of Southern California

Abstract

A Caltrans designed concrete slab bridge is located southwest of the 2004 M_w 6.0 Parkfield rupture zone. Peak horizontal accelerations of 1.0g and absolute displacements of 4 inches were measured with six CSMIP accelerometers on the bridge, and one free-field accelerometer east of the bridge. Ground motions resulted in longitudinal soil displacements in front of the abutments and around the bent piles due to the structure swaying back and forth. Based on our displacement analyses using the measured ground motions, we found that the current Caltrans seismic design approach results in a close match with the measured bridge displacements.

Introduction

The City of Parkfield is located within the northwest trending Cholame Valley between Hwy 101 and Interstate 5 in central California. The prominent geologic feature of the Valley is the highly active San Andreas Fault system that has ruptured multiple times in this area over the last 150 years. Moderate to large earthquakes were recorded in 1857, 1881, 1901, 1922, 1934, and 1966. Based on this high level of seismicity, the California Geologic Survey (CGS) installed over 50 strong motion accelerometer stations throughout the Cholame Valley to gather strong motion data resulting from an earthquake (Fig. 1). The accelerometers are installed in low, fiberglass huts anchored to a reinforced concrete pad bearing on the ground surface. The strong motion array is monitored and maintained by the CGS Strong Motion Instrumentation Program (CSMIP).

The State of California Department of Transportation (Caltrans) constructed the bridge along Hwy 46 in 1954, and widened it by 11 feet in 1979. The five-span, pile supported, reinforced concrete slab bridge is 130-ft long, 44-ft wide and spans Cholame Creek (Fig. 2 & 3). The original structure is supported on 16-inch diameter, CIDH piles at the bents and abutments. The widened portion is supported on driven 16-inch octagonal piles at the bents, and 10-inch square piles at the abutments. A monolithic, diaphragm abutment was used on the west end of the bridge. The east end of the original bridge is supported on a seat abutment with asbestos sliding sheets, while the widening consists of a diaphragm abutment. The 12-inch thick, reinforced concrete wingwalls are connected to the bridge deck. A 3-inch asphalt concrete overlay tops the 18-inch thick slab deck.

On the evening of September 30, 1955 the legendary actor James Dean was driving west on Hwy 46 in his silver Porsche Spyder 550 to race in Salinas, California. Unfortunately, another driver erroneously pulled directly in front of him at the intersection of Hwy 41 and Hwy 46 and Mr. Dean was killed in the resulting accident. If the other driver could have avoided the accident, James

Dean would have soon driven over the 1-year old Cholame Creek Bridge, towards an unknown future in Hollywood and beyond.

The bridge and abutments are underlain alluvial soils consisting of medium dense silty sands and stiff silty clays within the Cholame Creek drainage basin. The sedimentary Paso Robles Formation underlies the site with depth. A total of eight soil borings have been drilled at the site. Groundwater was apparently encountered at depths of 10 to 20-ft below ground surface at the time of the field investigations in 1953 and 1977, however the depth of the groundwater at the time of the earthquake is unknown. The site is classified as Type D soil conditions per Caltrans (2004).

On June 28, 1966 the San Andreas Fault ruptured to the southeast across Hwy 46, within 500 feet of the Cholame Creek Bridge. A free-field CSMIP accelerometer was in place (Cholame 2W) beside the bridge, and measured horizontal ground accelerations as high as 0.6g. Caltrans Bridge Inspection Reports after the earthquake note that the bridge deck shifted east approximately 1-inch at the seat abutment, the bridge approaches settled on the order of ½ inch, both wing walls at the east abutment had diagonal cracks, hairline cracks were present at the tops of the bent piles, and a ½-inch gap was present at the ground surface around the piles at Bent #5. The cracked wing wall on the southern edge of the east abutment was removed as part of the bridge widening in 1979.
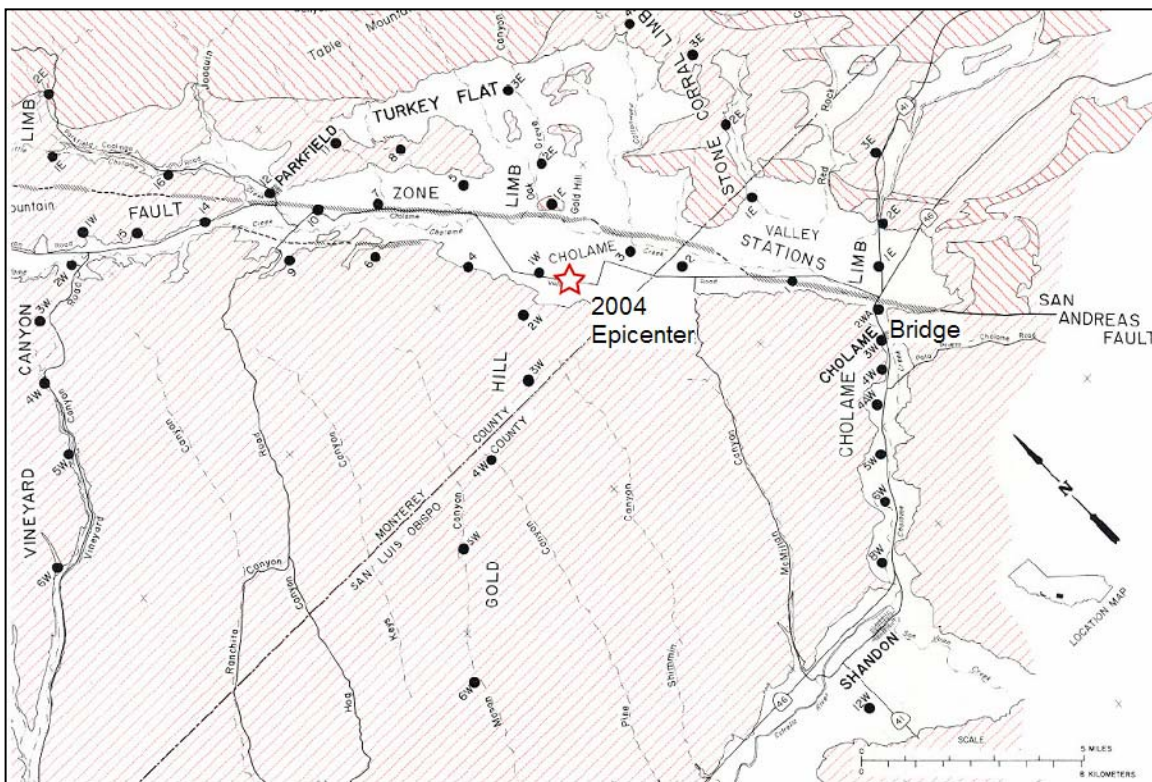
Figure 1. Bridge Location and Parkfield Strong Motion Array Locations
(Original map by McJunkin and Shakal, 1989)
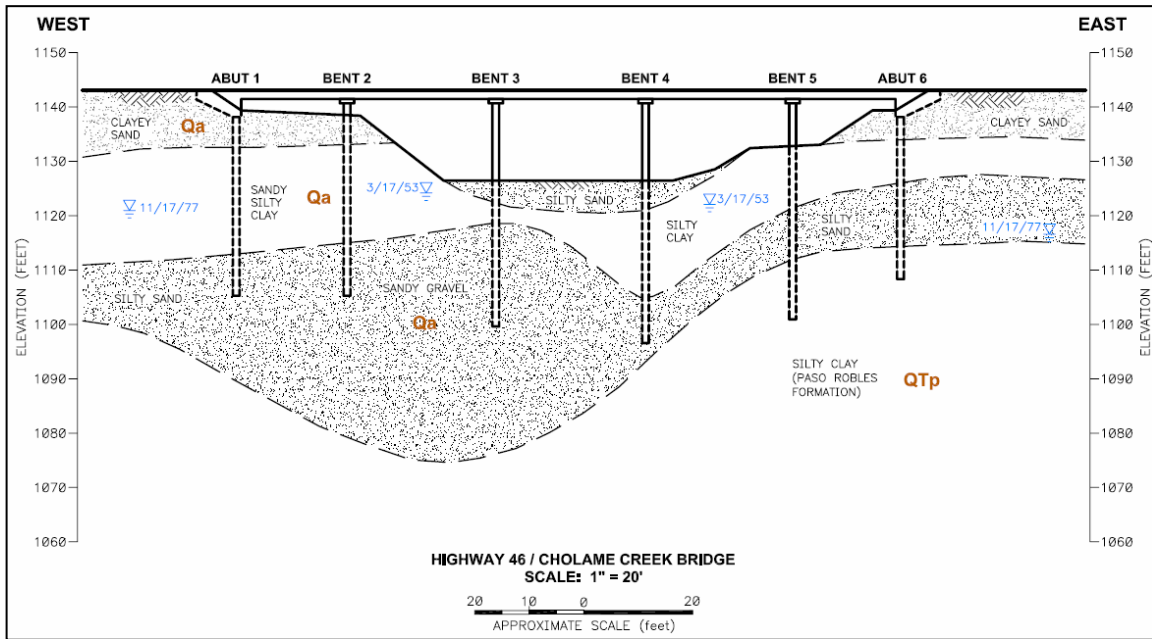
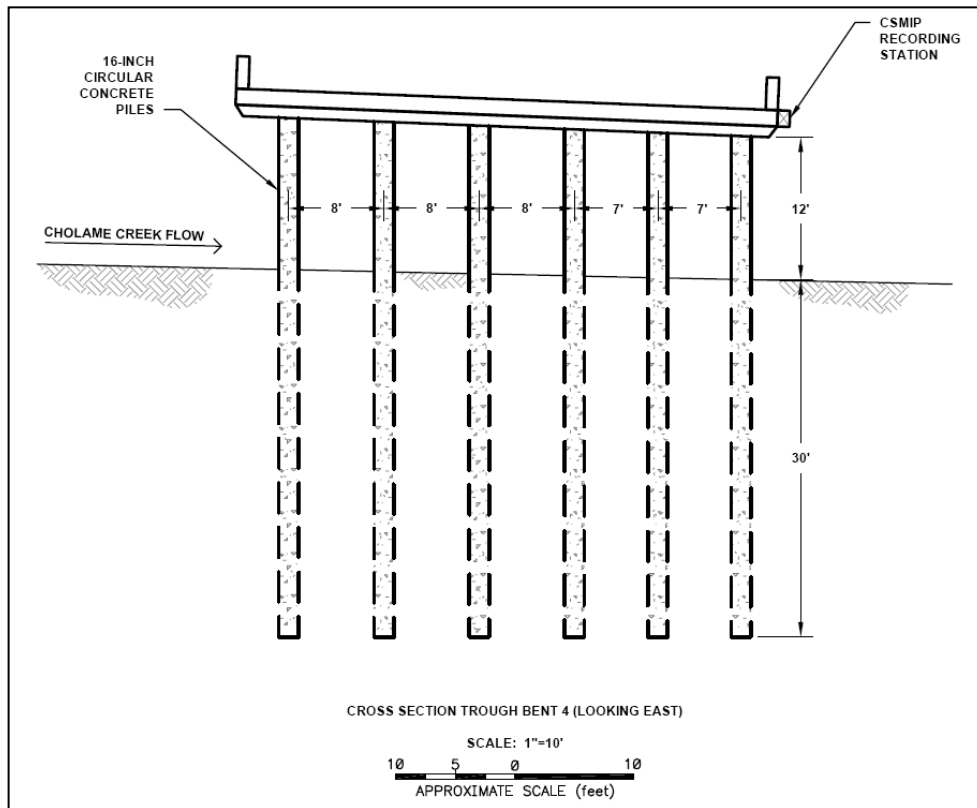**Figure 2. Bridge Elevation and Subgrade Conditions**

Figure 3. Bridge Cross Section

The magnitude M_w 6.5 San Simeon earthquake occurred on December 22, 2003 approximately 50 miles west of the site. The bridge deck experienced peak acceleration values of 0.2g and absolute displacements of approximately 1.4-inches during the far-field event.

The 2004 M_w 6.0 Parkfield Earthquake

On September 28, 2004 the highly anticipated Parkfield earthquake finally occurred. The right-lateral, strike-slip San Andreas Fault ruptured to the northwest (away from the Cholame Creek Bridge), with discontinuous surface rupture occurring over 20 miles along the fault. Surface rupture on the order of 1 to 2 inches was noted, and evidence of liquefaction was observed (sand boils) in two locations along Cholame Creek northwest of the bridge. While the active trace of the fault is only 500 feet to the east, the fault rupture zone did not pass by the site. The earthquake epicenter is shown on Fig. 1. Free-field acceleration time histories were recorded 200-feet east of the bridge at Cholame 2W (Station 36228), as well as on the southern edge of the bridge deck at the west abutment, center and east abutment (Station 36668). The Cholame 2W and bridge time histories recorded by the CSMIP are shown on Fig. 4 and 5. These time histories can be downloaded off the CSMIP web site.

Free-field motions were recorded in the north-south (360 deg) and east-west (90 deg) directions, while the bridge motions were recorded in the transverse and longitudinal bridge directions. As the bridge has little skew (4 degrees), and the centerline (~ N63°E) is essentially perpendicular to the strike of the San Andreas Fault, the longitudinal bridge direction is approximately fault-normal and the transverse bridge direction is approximately fault parallel.

The free-field, fault normal ground motion at the bridge included a directivity pulse with a peak displacement of 5.2 inches (13.3 cm) at t = 2.94 seconds, peak velocity of –21.9 in/sec (-55.5 cm/sec) at t = 3.24 seconds, and a peak acceleration of 0.53g at 3.34 seconds. These are relatively high values for a M_w 6.0 earthquake. It was interesting that the peak displacement preceded both the peak velocity and peak acceleration. Another interesting observation was that the displacement pulse occurred towards the fault to the east. Thus demonstrating that near-field pulses can come from both directions, regardless of the location of the project relative to the fault rupture zone. A summary of the peak accelerations, velocities and displacements recorded at Stations 36228 and 36668 are listed in Table I.

Table I. Summary of Peak Ground Motions at Bridge During 2004 M_w Parkfield Earthquake

Station	Acceleration (g's)	Velocity (in/sec)	Displacement (inches)
Cholame 2W, 90 deg	0.60 @ 3.34 sec	-24.9 @ 3.22 sec	4.9 @ 3.00 sec
Cholame 2W, 360 deg	0.37 @ 3.12 sec	-17.4 @ 3.00 sec	3.0 @ 2.84 sec
Bridge, Longitudinal	1.05 @ 3.34 sec	-20.4 @ 3.15 sec	4.3 @ 2.94 sec
Bridge, Transverse East Abutment	0.99 @ 3.36 sec	-17.1 @ 3.26 sec	2.0 @ 3.13 sec

Caltrans inspected the bridge the day of the earthquake and noted that the ground motions resulted in longitudinal soil displacements of 1 to 2-inches in front of the abutments, and approximately ½ inch around the rows of bent piles, due to the structure swaying back and forth. Structural damage consisted of diagonal cracking of the northern wing wall at the east abutment, minor cracking around the perimeter of all the bent piles at the connection to the bridge deck, and transverse cracking through the asphalt concrete at each bridge approach. Caltrans concluded that the damage was not serious and repairs were not necessary.
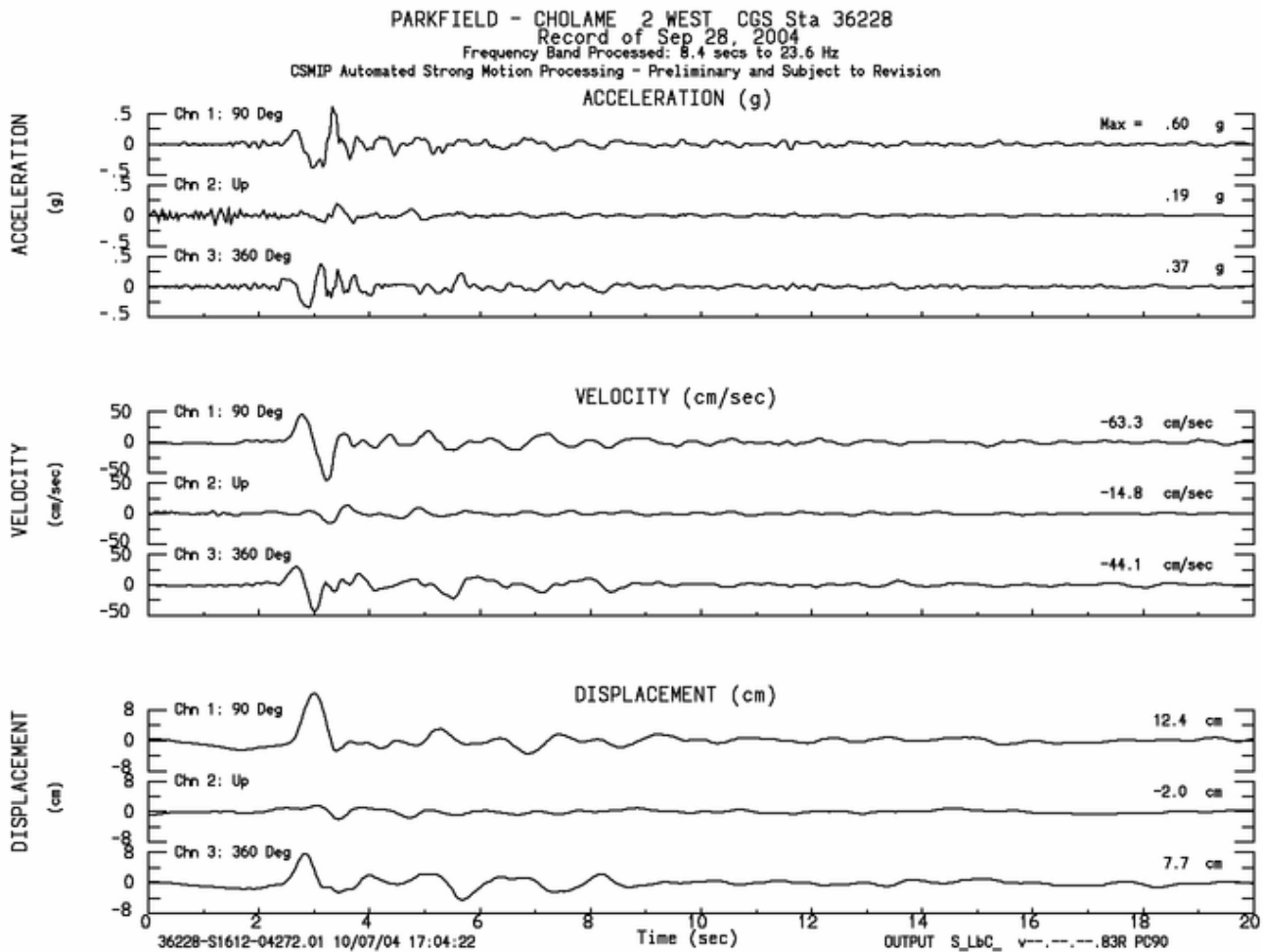
Figure 4 Cholame 2W Time Histories Recorded by CSMIP

During our August 26, 2005 site visit we noted circumferential, hairline cracks around the tops of all the piles. Epoxy repairs had been made on each of the Bent 2 piles. We reviewed all the Caltrans bridge inspection reports since bridge construction in 1954. Pile top cracks are noted in the March 22, 1971 report for nearly all the piles, indicating that the original cast-in-place piles were damaged in the 1966 seismic event. No pile cracking is noted for the new driven piles from November 1979 to June 2004. However, pile top cracking is noted for both the original and bridge

widening piles in the September 28, 2004 report immediately after the recent earthquake. Thus, the pile top cracking observed in our field visit likely resulted from the two M_w 6.0 seismic events.
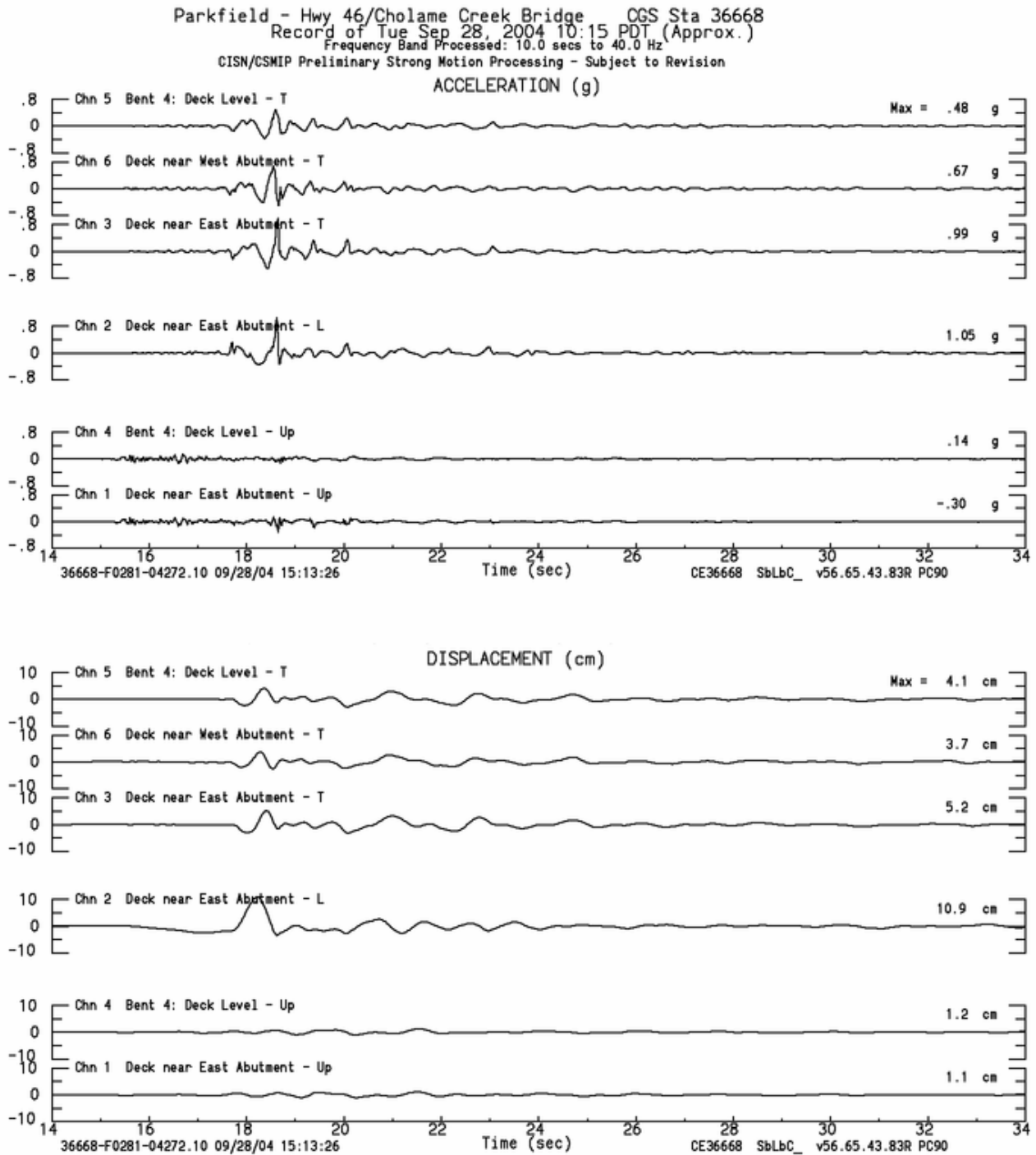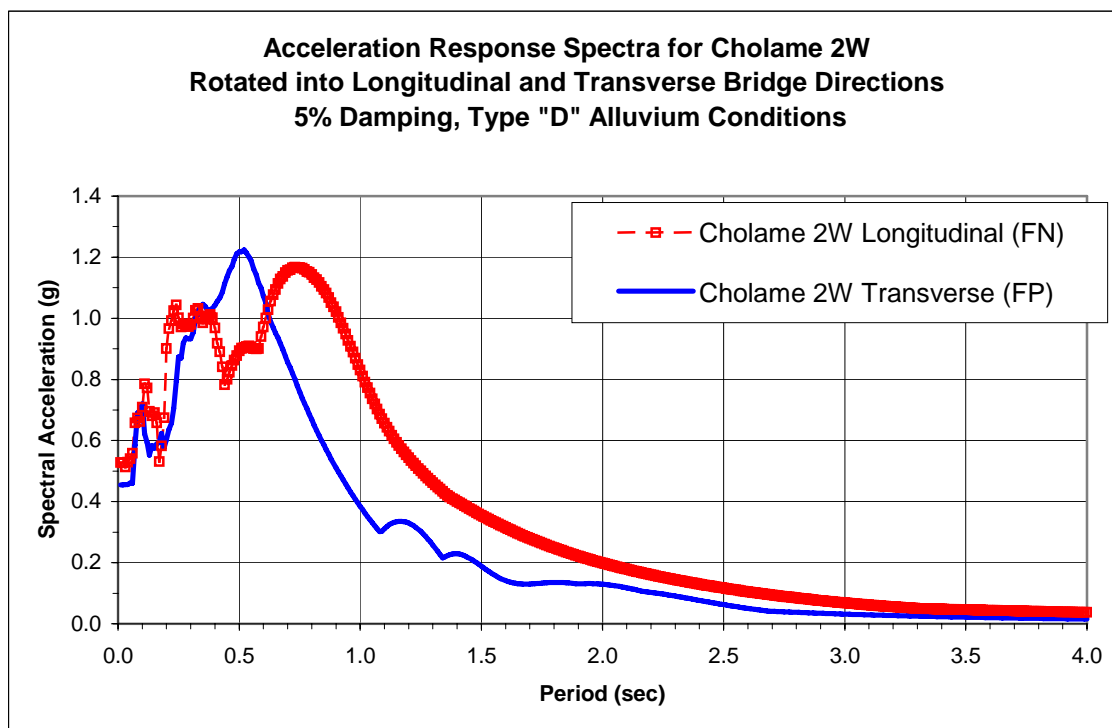

Figure 5 Hwy 46/Cholame Creek Bridge Time Histories Recorded by CSMIP

Figure 6. Cholame 2W Acceleration Response Spectra for 2004 M_w 6.0 Event

The free-field acceleration time histories from the Cholame 2W Station were rotated into the longitudinal (~ N63°E) and transverse (~ N27°W) directions of the bridge to develop site-specific acceleration response spectra for the analyses (Fig. 6). The time histories were downloaded off the CSMIP web page, and no further corrections were made. It is our understanding that the CSMIP time histories have already been frequency band processed and baseline corrected.

Bridge Displacement Analysis

Description of the Structural Model

A 3D dynamic finite element model was used to analyze the Hwy 46/Cholame Creek Bridge. A "spine" model was developed in the SAP2000 program with a single line of frame elements used at the cg of the superstructure. The bents were modeled with frame elements located at the cg of the cap, and frame elements for each column/pile. Effective section properties were used. The bridge profile, curved alignment and skewed bents and abutments were accounted for in the model.

The bent piles were first modeled with idealized boundary conditions - fixed at 5 pile diameters (6.7 ft) below the ground surface (bgs). Subsequently, the model was refined to include pile-soil springs to represent the soil stiffness. First linear soil springs were used to represent an

equivalent secant stiffness, later non-linear springs were used. Soil springs were developed from p-y curves generated using the LPILE5 program.

The abutments were modeled with a pair of linear springs, longitudinal and transverse, at the cg of the bridge deck. We developed equivalent linear abutment springs by combining passive pressures against the abutment, and lateral forces from the piles. The passive pressures were based on the Caltrans recommended value of 20 kips/in per foot of wall width, modified for wall height.

The pile stiffness values (32 kips/in for 10-inch piles and 45 kips/in for 16-inch piles) were based on a force-displacement relationship developed using the software LPILE5 for the site-specific piles and soil conditions. The bridge model is shown on Fig. 7, 8 and 9. The abutment springs were confirmed to remain within their linear elastic range under loading from the 2004 M_w 6.0 event, by comparing the calculated lateral abutment forces to the assumed abutment capacity per typical Caltrans design guidelines.

The SAP2000 model was used to perform three basic types of analyses:

1. Response Spectrum Analysis (Elastic Dynamic Analysis per Caltrans)
2. Linear Time History Analysis
3. Non-linear Time History Analysis

For the response spectrum analysis, displacements were multiplied by a modification factor of 0.70 to account for increased damping (15%) due to a high level of soil mobilization at the piles and abutments. This is consistent with Caltrans (1995) MTD 20-4 for seismic retrofits of short, stiff bridges with monolithic abutments. For the time history analysis runs were made both with 5% and 15% damping ratio.

The site-specific ground motions from the Cholame 2W Station were input into the model as the seismic loading. Both response spectra (Fig. 6) and acceleration time histories were used. The ground motions were rotated into the longitudinal and transverse directions of the bridge.
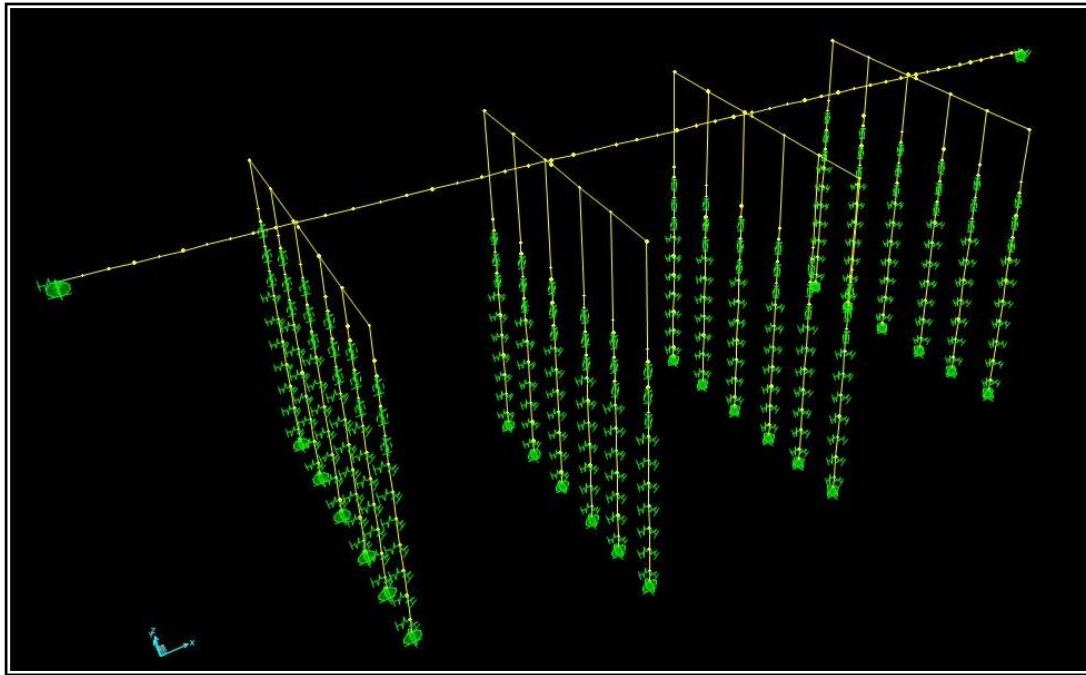
Figure 7. SAP2000 Model of Bridge Structure with Soil-Pile Springs
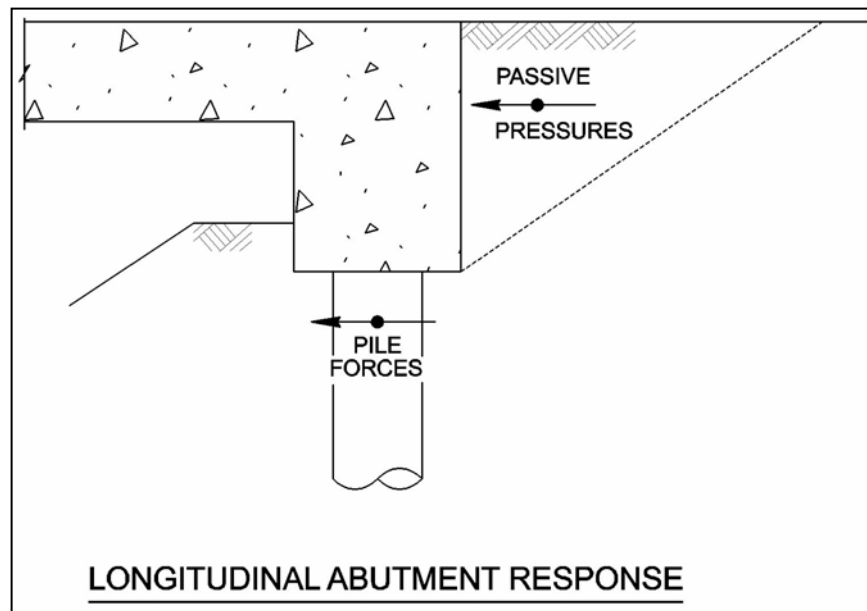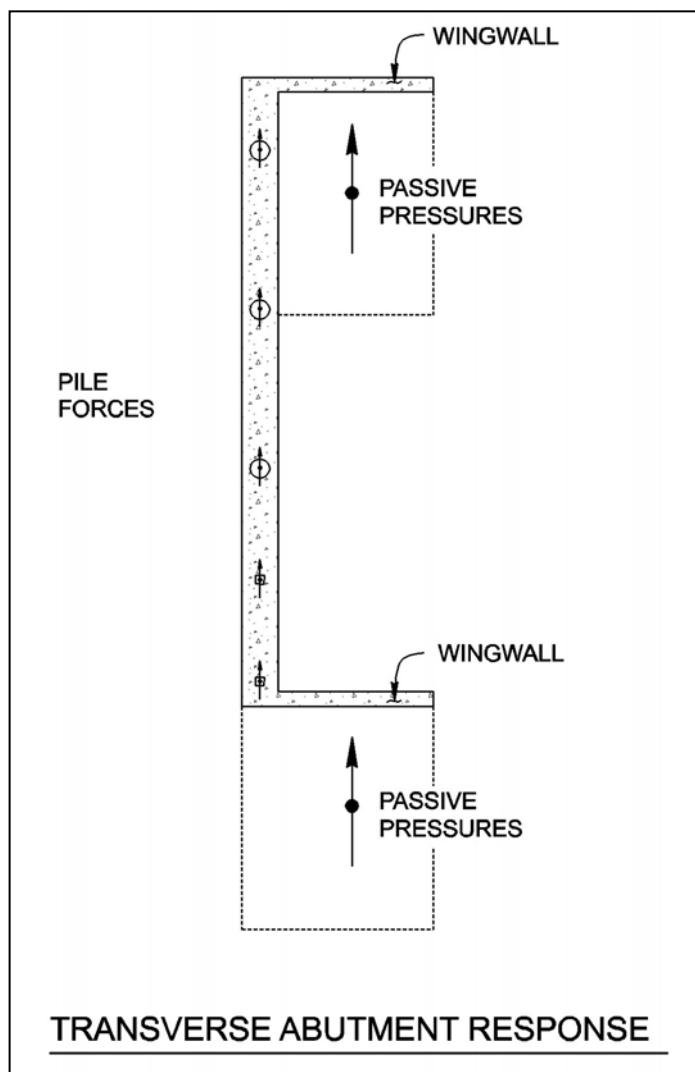

Figure 8. Longitudinal Forces at Abutment

Figure 9. Transverse Forces at Abutment

Discussion of Results

The goal of the bridge analysis was to compare the measured bridge displacements with those calculated following typical Caltrans design guidelines with the Cholame 2W spectra. Accordingly, the first step was to estimate the relative bridge displacements of the bridge deck. The displacements listed in Table I are absolute values. The relative longitudinal and transverse bridge displacements are the absolute values minus the rotated free-field displacements measured at Cholame 2W. The peak relative bridge displacements at the east abutment (Abutment 6) are as follows:

- Longitudinal direction. 0.94 inches (2.38 cm) *at the same time as the peak longitudinal (fault normal) free-field displacement pulse* (t = 2.94 seconds). The relative displacement was only 0.35 inches (0.93 cm) at the time of the peak longitudinal bridge acceleration (t = 3.34 seconds).

- Transverse direction. 0.84 inches (2.14 cm) *at the same time as the peak transverse (fault parallel) bridge acceleration* at the east abutment (t = 3.36 seconds). The relative displacement was essentially zero inches (0.012 cm) at the time of the peak transverse free-field displacement (t = 3.12 seconds).

Comparisons between the free-field and bridge deck time history displacements are shown on Fig. 10 and 11.

Response Spectrum Analysis Results

Results showed over 90% mass participation each for the fundamental longitudinal and transverse modes, with periods of 0.38 and 0.37 seconds respectively. Running 25 modes provided over 99% mass participation each in the two lateral directions. Modeling assumptions were varied in the form of foundation and abutment stiffness values in order to evaluate the effect on the calculated displacements. The design assumptions and peak east abutment displacement results are summarized in Table II.

Table II. Summary of Response Spectrum Analysis Results for Cholame 2W Ground Motions, 5% Damping

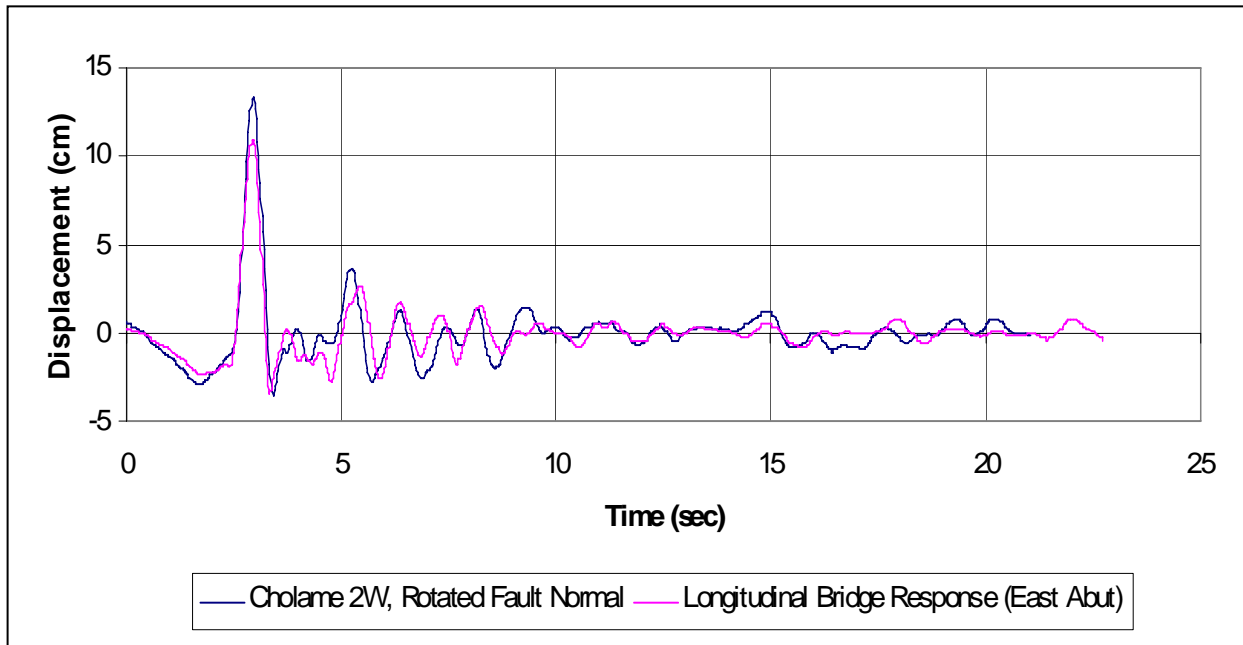| Design Assumption	Longitudinal Displacement (inches)	Transverse Displacement (inches)
Assumed depth to fixity of 5 pile diameters	1.44	1.52
Bent pile springs only in upper 8-feet of pile	1.32	1.41
Bent pile springs along full length of piles assuming "sand" subgrade	1.45	1.51
Bent pile springs along full length of piles assuming "stiff clay" overlying "sand" subgrade	1.32	1.45

Figure 10. Measured Displacement Time History Comparison in Longitudinal Direction
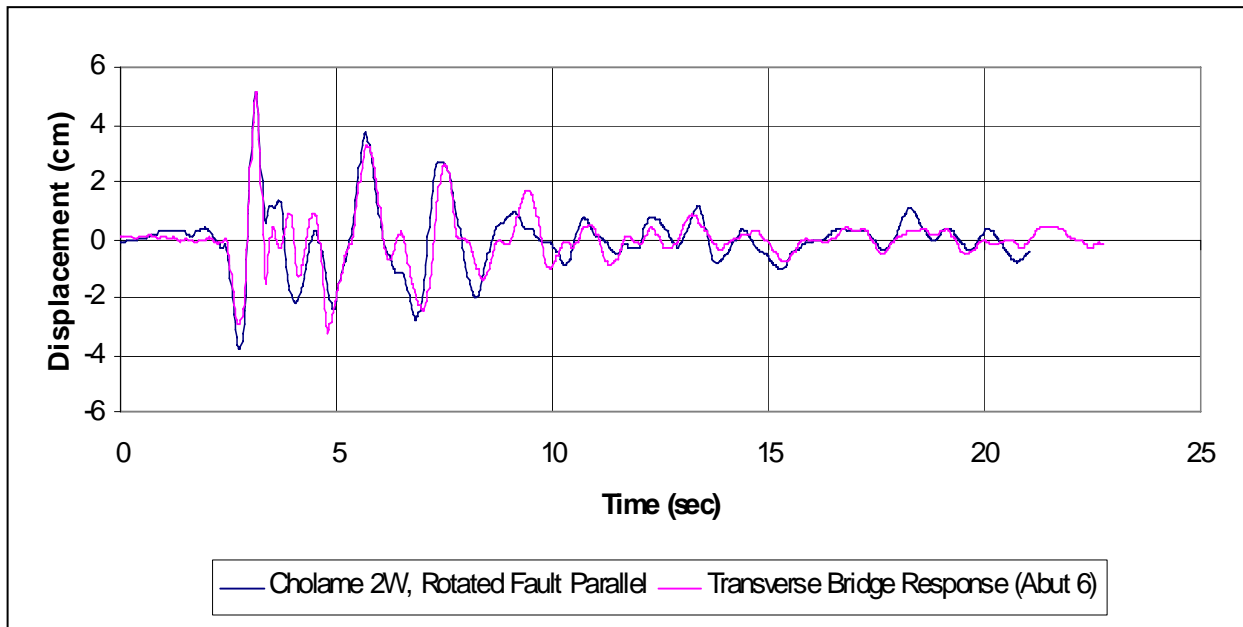

Figure 11. Measured Displacement Time History Comparison in Transverse Direction

Using a displacement reduction factor of 0.70 to account for the assumed higher damping of 15% for the short, stiff bridge (Caltrans 1995) results in longitudinal and transverse displacements on the order of 1 inch for each of the design assumptions. The estimated value of 1 inch is reasonably close to the measured relative displacements values of 0.94 inch (longitudinal) and 0.84 inch (transverse).

Time History Analysis Results

The free-field ground motions from Cholame 2W were rotated into longitudinal (~ N63°E) and transverse (~ N27°W) directions and applied to the bridge model simultaneously. Linear abutment springs were assumed for each model as the ultimate capacity of the abutments was not exceeded during the response spectrum analyses. However, both linear and nonlinear soil-pile springs were used to evaluate the effect on the results. Nonlinear soil-pile springs were modeled in SAP2000 using nonlinear links in the upper portion of the piles. The design assumptions and peak east abutment displacement results are summarized in Table III.

**Table III. Summary of Time History Analysis Results for
Cholame 2W Ground Motions, 5% Damping (except as noted)**

Design Assumption	Longitudinal Displacement (inches)	Transverse Displacement (inches)
Bent pile springs only in upper 8-feet of pile	1.23	1.56
Bent pile springs along full length of piles assuming "stiff clay" overlying "sand" subgrade	1.09	1.43
Bent pile springs along full length of piles assuming "sand" subgrade	1.44	1.53
Bent pile springs along full length of piles assuming "sand" subgrade, *15% damping*	0.93	1.19
Bent pile springs along full length of piles assuming "sand" subgrade, nonlinear springs	1.26	1.53
Bent pile springs along full length of piles assuming "sand" subgrade, nonlinear springs and *15% damping*	0.92	1.15

The use of nonlinear soil-pile springs in the upper portion of the pile did not have a significant effect on the results. However, using 15% damping (Caltrans 1995) in the time history analysis reduced the calculated deck displacements significantly. These reduced values are reasonably close to the measured relative displacements values of 0.94 inch (longitudinal) and 0.84 inch (transverse).

Displacement Demand Assessment

A displacement demand assessment was performed on the Hwy 46/Cholome Creek Bridge to put the measured displacements and damage patterns resulting from the 2004 M_w 6.0 Parkfield seismic event into perspective. The assessment followed current Caltrans seismic design and

retrofit guidelines. The design level spectrum (ARS) was based on a magnitude M_w 7.5 earthquake on the San Andreas Fault with a peak ground acceleration of 0.7g for Type D soil conditions (Mualchin, 1996). Displacement demands for the M_w 7.5 design event were determined using the standard 5% damped ARS curve above. An elastic displacement reduction factor of 0.70 was then applied to account for an increased damping ratio of 15% for the short, stiff bridge in accordance with Caltrans Memo to Designers (MTD) 20-4 (1995). This resulted in a longitudinal displacement demand of 1.8" and transverse displacement demands varying from 1.6" at Bent 2 to 2.0" at Bent 5.

Capacity Assessment

A capacity assessment was performed utilizing moment-curvature analysis. The short piles at Bent 2 were found to be the most critical for the bridge due to their reduced displacement capacities and increased shear demand. However, the results of the assessment indicate that the piles have adequate displacement capacity and shear strength to withstand the Caltrans design level seismic event. The results are summarized below:

Table IV Transverse Pile Displacement Assessment at Critical Bent 2

Displacement Demand reduced by factor of 0.7, Δ_{dem}	Yield Displacement, Δ_y	Ductility Demand, μ_Δ (Δ_{dem}/Δ_y)	Displacement Capacity, Δ_u	Displacement Demand/Capacity, Δ_{dem}/Δ_u
1.8"	0.58"	3.1	8.7"	0.21

Table V Pile Shear Assessment at Critical Bent 2

Plastic Shear Demand, V_p	Design Shear Demand, $V_o = 1.3\,V_p$	Factor1*Factor 2 at $\mu_\Delta = 3.1$	Shear Capacity, $\phi\,V_n$	Shear Demand/Capacity, $V_o / \phi V_n$
18 kips	24 kips	2.7*1.05 = 2.8	46 kips	0.51

Furthermore, results of the pile moment-curvature analysis show that under the displacement demands of about 1" measured during the 2004 event, cracking of the cover concrete and yield of the reinforcement is expected. This correlates well with the damage documented in the Caltrans inspection reports. The table below summarizes the results of the moment-curvature analysis for a typical 16" diameter pile. Displacements were calculated by assuming a 10-ft effective column/pile length, which is appropriate for the critical Bent 2 piles.

Table VI Results of the Pile Moment-Curvature Analysis at Critical Bent 2

Pile Damage Description	Criteria	M (k-in.)	ϕ (10^{-3}/in.)	Δ (in.)
1. Cracking of cover concrete	f_c = 530 psi (tension)	324	0.025	0.17
2. First yield of reinforcement	f_y = 68,000 psi	976	0.278	0.51
3. Idealized yield	$M_p/M_y * \phi'_y$	1100	0.313	0.58
4. Concrete spalling	ε_c = 0.005	1150	1.30	2.2
5. Plastic hinge failure	ε_{cc} = 0.016	1082	5.33	8.7

CONCLUSION

The seismic response of the Hwy 46/Cholame Creek Bridge was studied under a grant from the CSMIP. The goal of the evaluation was to compare the measured bridge deck displacements with those calculated using typical Caltrans design guidelines. The free-field acceleration time histories from the Cholame 2W Station were rotated into the longitudinal and transverse bridge directions to develop the site-specific acceleration response spectra.

Both response spectra and time history analyses were performed using a variety of design assumptions for the bridge foundation. Based on our displacement analyses, we found that using the current Caltrans bridge design guidelines with the Cholame 2W spectra resulted in a close match with the measured bridge displacements during the 2004 M_w 6.0 seismic event. As the measured bridge displacements were much lower than the estimated pile capacity, the minor pile top cracking noted after the recent earthquake is consistent with the capacity assessment for the bridge.

Acknowledgements

References

Caltrans (2004), Seismic Design Criteria Version 1.3, State of California Department of Transportation, February 2004.

Caltrans (1995), Memo to Designers 20-4, Attachment A, March 1995

McJunkin, R.D. and Shakal, A.F., (1989). "Parkfield Strong-Motion Array, Monterey and San Luis Obispo Counties" *California Geology.,* March 1989, pp. 61-67.

Mualchin (1996), "California Seismic Hazard Map 1996." Based on Maximum Credible Earthquake (MCE). California Department of Transportation. 1996

OVERVIEW OF THE TURKEY FLAT
GROUND MOTION PREDICTION EXPERIMENT

Charles R. Real[1], Anthony F. Shakal[1], Brian E. Tucker[2]

[1] California Geological Survey, Sacramento, CA
[2] GeoHazards International, Palo Alto, CA

Abstract

Recognizing the wide variability of methods and often conflicting results of seismic response analyses used for design and construction in the early 1980's, the California Geological Survey (CGS) established the Turkey Flat Site Effects Test Area in 1987, and within two years a *blind* test was conducted to predict the test area's low-strain seismic response. Test results focused on the need to reduce uncertainties in the geotechnical parameters that drive site response codes. Fifteen years later, the array recorded the September 28, 2004 M6.0 Parkfield Earthquake at a fault-rupture distance of only 5 km. A blind test has been conducted to evaluate the ability of current practice to determine the test area's moderate-strain seismic response. This paper provides an overview of the Turkey Flat test site, and describes the rationale for what has become an evolving blind test experiment.

Introduction

The Turkey Flat test area was established to help determine the *state-of practice* in estimating the effects of surface geology on earthquake ground motion (Tucker and Real, 1986, 1988). The California Geological Survey (CGS) joined formation of the IASPEI/IAEE working group on ESG to promote installation of strong-motion arrays specifically designed to study the site-effects phenomenon (Kudo, 2003). CGS's Strong-Motion instrumentation Program (CSMIP) established the Turkey Flat test area in 1987 near the town of Parkfield in the central California Coast Ranges (figure 1).

A clear lack of consensus prevailed in the early 1980's on how soils behave under strong earthquake shaking and their potential to amplify ground motions. The unexpected high level of ground shaking in Mexico City, well above that predicted by contemporary attenuation models, underscored the importance of amplified ground motions caused by linear behavior of high-plasticity clays (Bielak and Romo, 1989).

At the same time advances in soil mechanics began illuminating the importance of non-linear soil behavior at high cyclic strains, and the accompanying de-amplification of ground motions that should be considered when estimating site response in engineering practice (Idriss, 1990). Increasingly complex 2-D and 3-D computer codes were developed to model dynamic soil behavior, providing more opportunity for a wider range of predicted ground motions depending on the constitutive model chosen to represent the soil column on a particular project. There became a clear need to judge the validity of the new models based on a comparison of

model results with actual measurements of ground motion in an objective but decisive manner. This paper provides an overview of the Turkey Flat Experiment and its approach to this challenge, and focuses on what has been learned regarding the design and operation of a site-effects test area over the past 2 decades. A companion paper in these proceedings describes preliminary results of the Strong-Motion Test (Shakal, et al., 2006a).
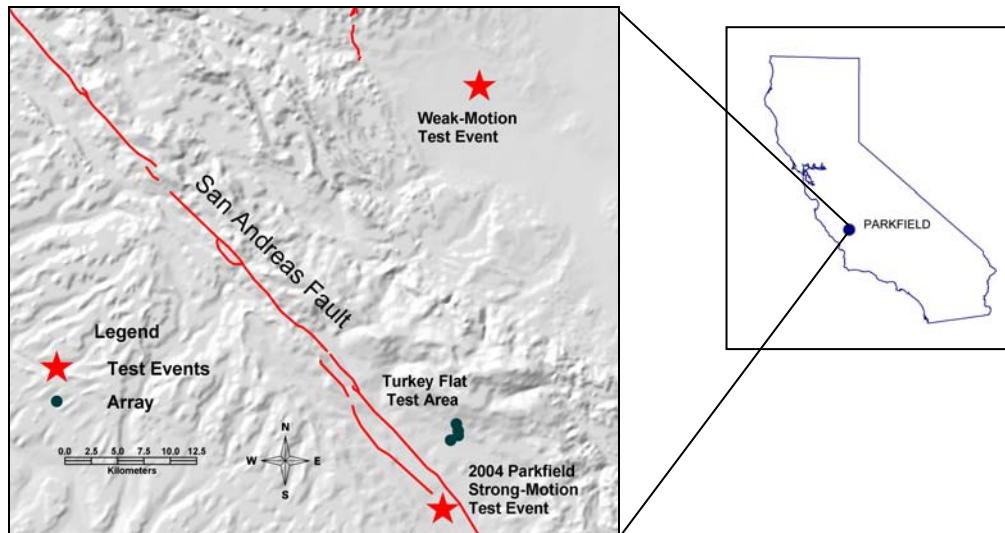

Figure 1. Turkey Flat Site Effects Test Area

Experiment Design

Design of the Turkey Flat experiment was driven by a need to emulate a site response analysis as conducted for a large construction project. The site should be representative of that typically chosen for development, and data provided that are normally attainable in practice. The design was also driven by secondary goals to identify weaknesses and limitations of contemporary site response analyses and to provide a comprehensive database of high-quality geotechnical and seismological data that will continue to facilitate future site-response earthquake engineering research. With these goals in mind it was recognized that although the test site represents only one of an endless variety of site conditions, it is important that the results of the experiment be definitive.

Being among the first international test areas to be established, and knowing that there would be more to follow, it was decided that a site be selected where there is a reasonable likelihood of predicting the correct site response. The rationale being to begin with a simple site before moving to more complicated sites that require complex models and extensive field investigations in order to define the model parameters. If the state-of-practice performs poorly at a geologically simple site, then it is unlikely that it can do better in a more complex site, where the results of a validation test would most likely be less definitive.

Another consideration that bears on experiment design is the site response modeling process. In contrast to an approach where the model is adjusted *a priori* to yield a known site response, a true test of the state-of-practice demands the construct of forward modeling. While valuable for research, inverse modeling is not representative of site response in earthquake engineering practice. Consequently, a blind ground motion prediction test forms the basic framework of the Turkey Flat site response prediction experiment. Assessing the state-of-practice should also include an assessment of the confidence practitioners place on their results, which is incorporated into the blind test process with appropriate consideration in experiment design.

The nature of the experiment requires a broad range of participation, with industry a crucial player. The more sophisticated *state-of-the-art* models reside in the research sector, but these models are not representative of those typically employed in practice. To achieve the goals of the Turkey Flat experiment requires the participation of reputable earthquake engineering firms. Finally, expertise in ground motion estimation is international, so results of the experiment benefit from foreign participation. As the experiment takes on a more serious nature, assuring the desired level of participation requires complete anonymity throughout the experiment; especially in the industrial sector where company reputations may otherwise be affected.

Another requirement for definitive results is the acquisition of high-quality data from which to derive reliable model parameters, and which forms the basis for *ground truth* observations of site response against which prediction results are to be judged. This called for a comprehensive program of geotechnical site characterization and a well-planned high-performance seismic instrument array that must be maintained throughout the operational life of the test site. The scope of the experiment is costly, so a reasonable return on the investment required locating the test site in a seismically active area where a moderate or larger earthquake is imminent.

The secondary goal of identifying the limitations and weaknesses of the various site response estimation processes requires an understanding of uncertainties. To help isolate uncertainties the experiment is conducted in multiple phases, with multiple investigation teams in each phase (figure 2). Three principal phases were identified: 1) *site characterization* to help select an appropriate site response model, and to estimate appropriate model parameters and their uncertainties, 2) a *weak-motion test* to predict the low-strain response of the test site, evaluate the adequacy of the site characterization, provide a preliminary assessment of the state-of- practice, and exercise the entire testing procedure, and 3) a *strong-motion test*, to predict the high-strain response of the test site, quantify nonlinearity of site response, and provide the results necessary to gauge the state-of-practice in site response estimation. Each blind test is conducted in two parts: 1) predictions based on surface rock motions and 2) predictions based on rock motions beneath the sediments. This multi-phase approach allows for tracking the propagation of errors, and helps to distinguish aleatory and epistemic uncertainties. To further isolate uncertainties and assist in the comparison of prediction models, site response predictions were made using a *standard* geotechnical model and a *preferred* geotechnical model derived by each prediction team from the basic field and laboratory measurements.
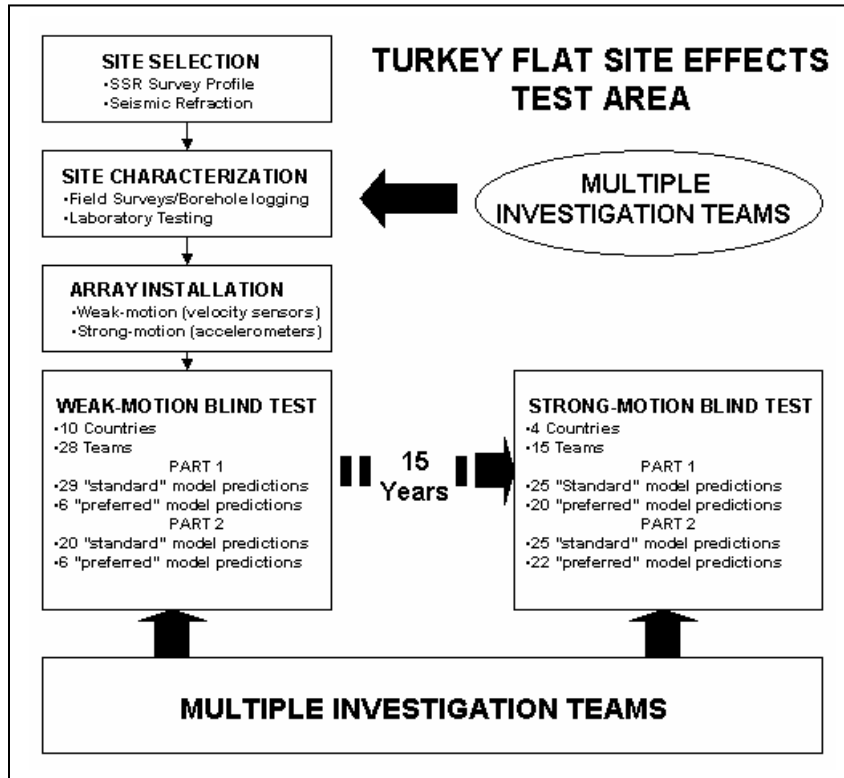
Figure 2. Principal Phases of the Turkey Flat Experiment.

Finally, the highly structured nature and broad scope of the experiment has benefited from expert advice. The Turkey Flat experiment receives oversight from two different advisory groups: an *ad hoc* project steering committee and the Strong-Motion Instrumentation Advisory Subcommittee on Ground Response, both consisting of experts representing practitioners in industry, government, and academia. Having several members who have served since the inception of the Turkey Flat experiment, these groups have provided advice on all aspects of the project including site characterization and the structure of the blind tests.

Site selection

Given the constraints of a geologically-simple site where a moderate event is expected soon and is close enough to experience strong motion, but not too close to be dominated by source effects led to the selection of Turkey Flat (figure 1). The site lies about 5km east of the San Andreas fault, where a characteristic ~M6.0 Parkfield Earthquake was predicted to occur sometime between 1988 and 1992 based on an average historical recurrence interval of 22 years ± 7 (Bakun and Lindh, 1985). Turkey flat is a shallow elongated valley composed of unsaturated Holocene and late Quaternary stiff alluvial terrace sediments overlying basement rocks consisting of Upper Cretaceous and Tertiary sedimentary rocks folded into a southwest plunging syncline (Hanna et al., 1972). Basement rocks outcrop along the western edge of the valley with practically no topographic relief, providing an excellent location for a ground motion reference site. Elevated basement rocks outcrop to the east, where the valley sediments pinch out along the western foot of the southern Diablo range (figure 3).

Beginning in the Fall of 1987 and continuing through Fall 1988, a comprehensive program of site characterization was carried out that included multiple investigation teams, both domestic and abroad, that conducted a broad range of field and laboratory geophysical and geotechnical tests (table 1) (Real and Tucker, 1987; Real and Tucker, 1988c; Tucker et al., 1988). Participants from industry, government, and academia, provided the redundancy of measurements necessary for estimates of uncertainty in site characterization (table 2).

Eight boreholes were drilled through valley sediments into the underlying basement rocks, in which *in situ* testing was performed and rock and sediment samples were acquired for laboratory analysis. All boreholes were cased except one, which provided for improved *in situ* testing of native materials. The cased boreholes were later used for installation of temporary downhole weak-motion sensors and permanent downhole strong-motion sensors. The site-characterization program categorized the Turkey Flat test area as a shallow 25m deep stiff-soil site with a depth to half-width ratio of 1:40, consisting of unsaturated clayey sand and sandy clays derived from the mountain slopes along the eastern edge of the valley (figure 4). Repeated measurements during the wet and dry seasons show the water table remains below the sediment bedrock interface. The interface slopes from the edges toward the valley center with little intervening relief, and is marked by a shear-wave impedance contrast of about 3. Although simple, the site is one where surface geology has a measurable site response, and where 1-D equivalent-linear ground motion models would be expected to perform well. Details of the site-characterization program have been reported (Real, 1988; Real and Tucker, 1988a, 1988b; Real and Cramer, 1992).

Table 1. Participants in Site-Characterization

- Leroy Crandall Associates
- Dames and Moore
- Woodward Clyde Consultants
- Qest Consultants
- Harding Lawson Associates
- Pitcher Drilling Company
- Lawrence Livermore National Laboratory
- California Geological Survey
- Oyo Corporation
- Kajima Corporation

Table 2. Site Characterization Tests

Geophysical/Geotechnical Field	Laboratory
Seismic Refraction (weight drop/explosives)	Unit weight
Seismic Reflection (large air gun)	Liquid limit
Resistivity log	Plastic limit
Spontaneous-Potential Log	Plasticity index
Density log (gamma-gamma)	Sieve analysis
Natural gamma	Moisture content
Downhole velocity (Vp & Vs)	Soil classification
Cross-hole velocity (Vp & Vs)	Consolidation test
Suspension velocity log (Vp & Vs)	Direct shear test
Vertical seismic profile (Vs)	Cyclic triaxial test
Caliper log	Resonance column test
Borehole deviation log	Dynamic torsion test
Pressuremeter test	Triaxial ultrasonic wave velocity
Standard penetration test	
Downhole Q (P & S-wave)	

The Turkey Flat test area instrument array is composed of four recording sites: Rock South (R1), Valley Center (V1), Valley North (V2), and Rock North (R2), with downhole sensors at Rock South (D1), and mid-way (D2) and in the underlying bedrock (D3) at Valley

Center (figures 3-5). Each sensor location consists of 3-component forced-balance accelerometers (details of the instrumentation are provided in figure 5). The strong-motion array was carefully maintained for 17 years by CSMIP. In 2001, 3 years prior to the occurrence of the 2004 Parkfield Earthquake, instrumentation was upgraded to12-bit solid-state digital recorders, which resulted in high-quality records of the Parkfield event. Details of the standard record processing are available (e.g. Shakal et al., 2003).

The CSMIP also established and maintains a 45-station wide-aperture strong-motion array across the Parkfield segment of the San Andreas Fault a few kilometers from the Turkey Flat array (McJunkin and Shakal, 1983). The Parkfield array consists mostly of analog accelerographs and is designed to provide near-fault ground motion data for researching the fault rupture process. The array recorded the 2004 event and has produced an abundance of records that uniquely document a complex rupture process and highly variable near-fault ground motions. These data can provide important insights into the source characteristics of the test event that may be of value in the analysis of Turkey Flat site response. A description of the Parkfield array and a preliminary analysis of records from the 2004 Parkfield event are available (Shakal et al., 2006b).

During Spring 1988, a weak-motion survey of local and regional earthquakes was conducted in order to determine weak-motion empirical transfer functions for each recording site of the strong-motion test area array, and to acquire data to conduct the weak-motion blind test (Cramer, 1990a, 1992, 1995). Velocity sensors were installed at all accelerometer locations on the ground surface and in adjacent boreholes across the test site array (figures 3-5). During the 2 1/2 months of operation 33 local and regional earthquakes were recorded in the magnitude 2-4 range, at distances of 20-230 Km, and azimuths ranging 4°-350°. The SSR technique was used with these data to compute average site transfer functions, which are being used to test the utility of the technique for predicting moderate and high-strain site response in the strong-motion blind prediction test (Cramer, 1995).

In addition to the strong-motion arrays near Parkfield, regional seismograph network coverage by the California Integrated Seismic Network provides accurate locations of local and regional earthquakes.

The Blind Tests

In a blind test high-quality geotechnical data and bedrock motions from a test event recorded at a reference station are distributed to participants as input to the site response estimation process. Participants are then asked to predict bedrock motions beneath the valley (Part 1) and at all other recording sites within and across the valley using the standard geotechnical model, and, if desired, a second set using their preferred geotechnical model. After receiving all predictions from Part 1, the procedure is repeated only this time using the actual recorded ground motions beneath the valley as input (Part 2). With the exception of those recordings used as input motions, all other recorded ground motions across the array are held confidential until all site response predictions are completed. Comparisons are then made between predicted response and observed response.
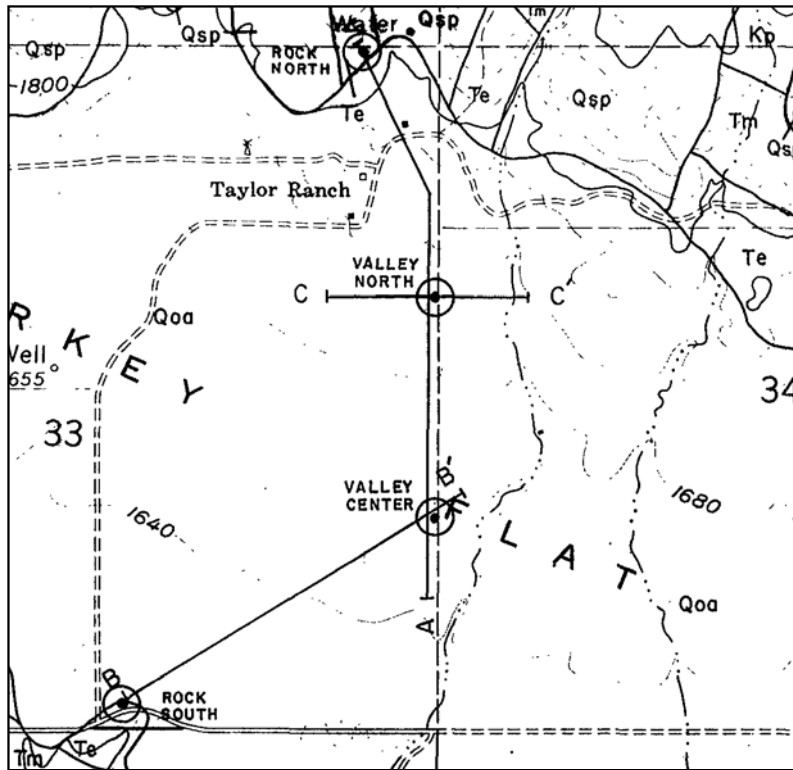
Figure 3. Plan view of Turkey Flat test area showing cross-section lines and location of instrument recording sites.
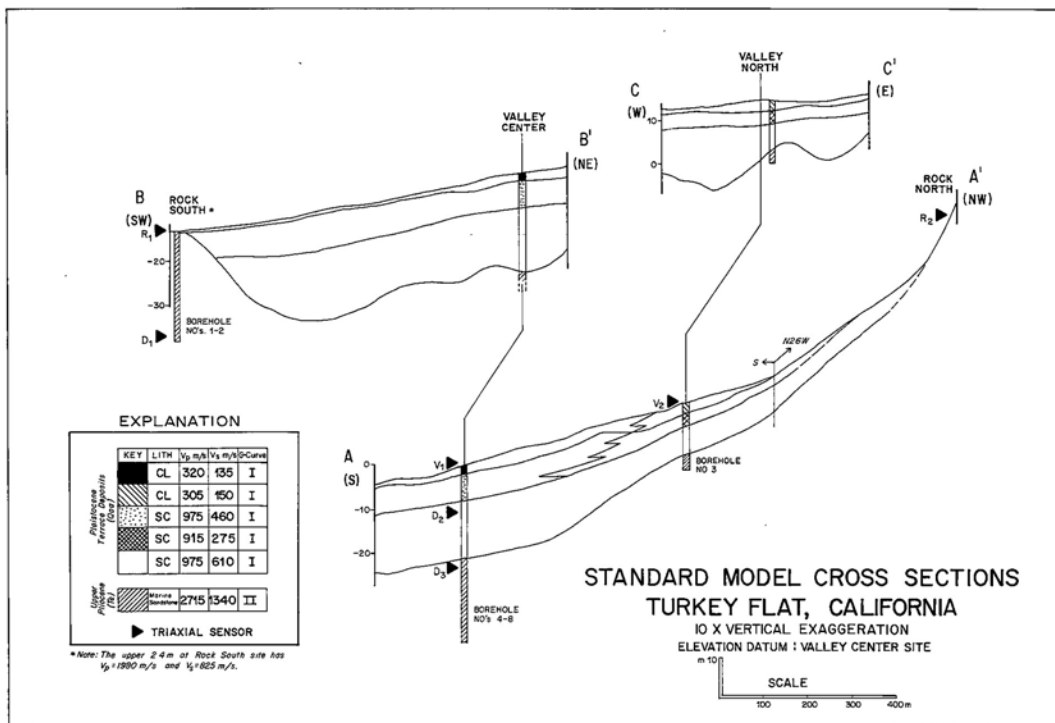

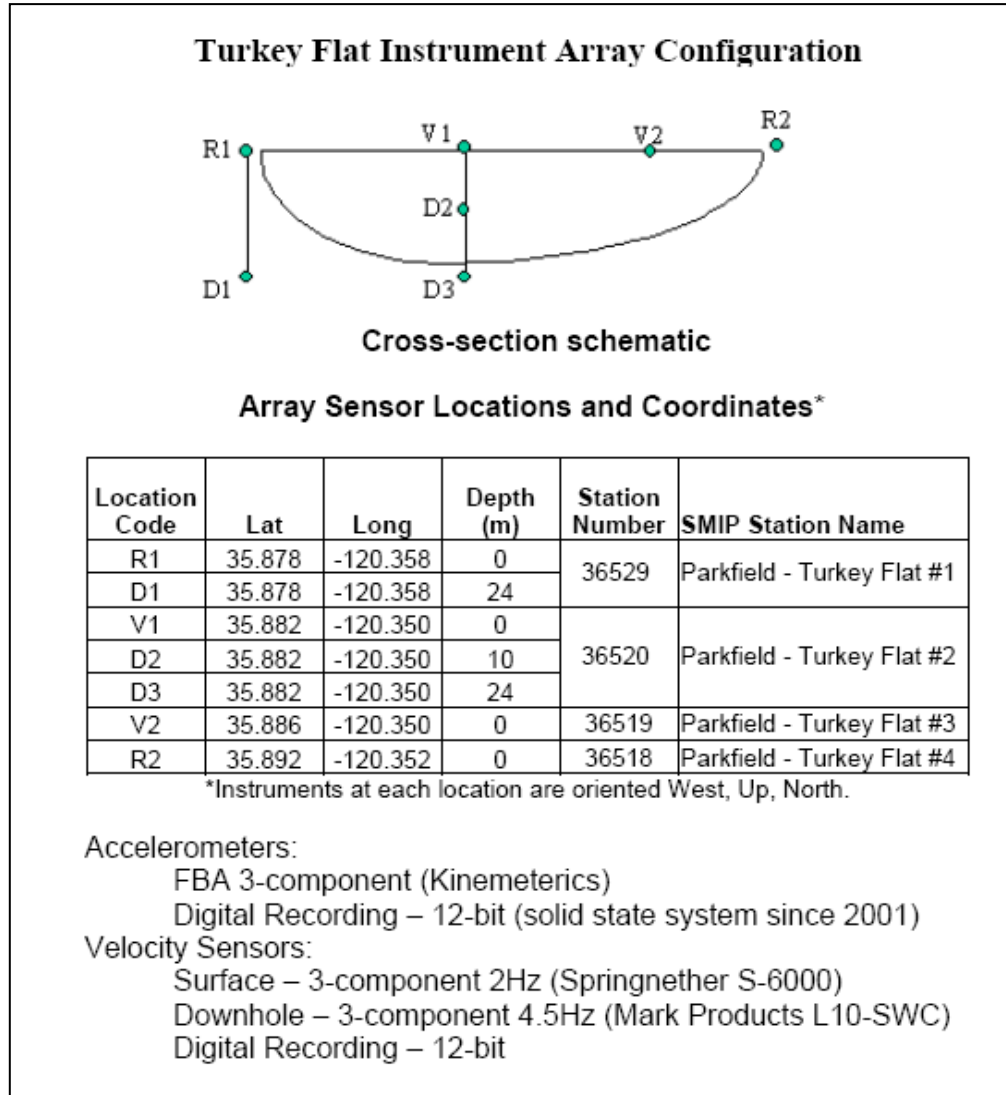Figure 4. Cross-sections of Turkey Flat Test Area.

Figure 5. Turkey Flat array instrument types and locations.

Prediction of earthquake ground motions can be categorized as Class A (considering source, path, and site effects) and Class B (considering only site effects). Because the focus of the experiment is on site effects, the initial blind test predictions are of type Class B, which further constrained the site selection process. Confidentiality of observed site response throughout the blind test process is important because upon completion, should the accuracy of predictions fall short of observations because of suspected path or source effects, a Class A prediction blind test could still be performed at a subsequent stage.

Predicted site response is requested at specific sensor locations, and are in four prescribed forms: 1) acceleration time histories, 2) pseudovelocity response spectra, 3) Fourier amplitude spectral ratios relative to a rock reference site, and 4) peak values of acceleration,

velocity, and displacement. Each form is to include an estimate of uncertainty (standard errors), and is requested to be submitted as digital files and printed plots, both in a prescribed format.

Weak-Motion Blind Test

A M2 event located about 32 km north of the Turkey Flat test site (figure 1) was recorded on 04/27/1988 at the bedrock reference site (Rock South on figure 4). The record was processed and distributed as input motions to the weak-motion blind test (Cramer et al., 1989; Real and Cramer, 1989,1990).

The Turkey Flat weak-motion blind test began Spring 1989 and concluded 16 months later (Cramer and Real, 1990c). There were 28 participants from 10 countries that submitted a total of 29 predictions for Part 1 and 20 predictions for Part 2 based on the standard geotechnical model (tables 3- 4). Eight categories of site response methods were tested in Part 1, and 6 categories in Part 2 (table 4).

Table 3. Participation

Country	No.
Canada	1
China	3
Czechoslovakia	2
France	3
Germany	1
Italy	1
Japan	7
Mexico	1
New Zealand	1
United States	8

Table 4. Categories of site response models tested

Site Response Category		Part 1 (R1-based)	Part 2 (D3-based)
1-D	Equivalent linear	8	5
	Spectral	3	2
	Haskell-like	3	2
	Wave propagation	3	2
2-D	Finite element	5	2
	Wave propagation	3	7
	Boundary element	1	-
3-D	Wave propagation	1	-

Participants were encouraged to submit a second set of predictions based on their preferred geotechnical model which they derived from the basic field and laboratory data. There were 6 submissions for Part 1 and 6 for Part 2.

Each set of predictions was grouped according to their input ground motions, the geotechnical model used, site response model dimensionality, and whether the prediction is optional. They were then statistically compared with observations in all four prescribed forms by computing means, standard deviations, medians, quartiles, and average deviations from observations (Cramer and Real, 1990b,1992). This comparative analysis provided the following results:

- The inter-quartile range of predictions cluster within 10% of their median response, regardless of the geotechnical and site response model used;
- Similarity of shape and frequency of resonant peaks between predicted and observed spectral ratios suggest that layer thicknesses and velocities of the standard geotechnical model are generally reasonable;
- Predictions tend to over estimate the amplitude of the observed ground motions (e.g. figure 6), suggesting that damping in the standard geotechnical model is too low; and,
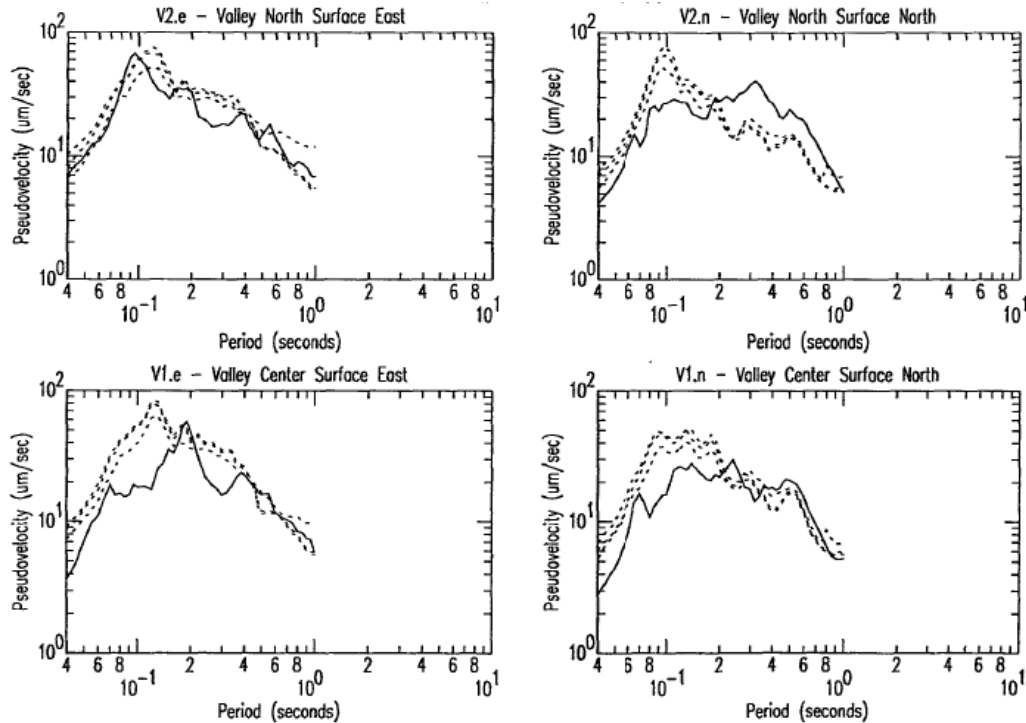- Predictors tend to significantly underestimate the uncertainty of their results.

Figure 6. Predicted horizontal pseudovelocity response spectra (dotted lines quartiles) for Valley North (top pair) and Valley Center (bottom pair) surface sites compared with observations (solid lines) (Cramer and Real, 1990b).

Although the level of participation in the weak-motion test was high, the number of submitted predictions is too small to statistically evaluate performance of the individual site response methods used. However, a comparison of the performance of 1-D methods with that of 2-D and 3-D methods combined indicates no significant improvement using site response methods of higher dimensionality. This might be expected given the relative geologic simplicity of the Turkey Flat test site. Despite the simplicity, however, results indicate that improvements are necessary in site characterization; particularly in reducing the uncertainties in damping and velocity structure. It is worth noting that damping in the standard geotechnical model is biased toward laboratory measurements, which were significantly lower (up to a factor of 10) than damping values obtained by field methods. The results of the blind test suggest the latter may be more reliable. Too few participants submitted predictions based on a preferred model to draw significant conclusions, but of the 6 on hand the one preferred geotechnical model that significantly improved the prediction had increased damping.

Field and Jacob (1993) analyzed the sensitivity of theoretical site response predictions at Turkey Flat to uncertainties in the standard geotechnical model using Monte Carlo simulation. Based on data from the site characterization, they modeled uncertainty distributions for velocity, damping, and layer thicknesses, using a 1-D linear-viscoelastic model to calculate site response for thousands of iterations randomly varying the model parameters according to their uncertainty distributions. The result shows that uncertainties in input parameters produce a large variability in computed site response (e.g. inter-quartile range is 82% of the median response at valley center site). Two important conclusions were drawn from their results: 1) nearly all of the weak-

motion predictions can be considered a success since their average deviations from observations fall within the expected range of uncertainty, and 2) considering the geologic simplicity of the Turkey Flat test site and the comprehensive site characterization program, site response estimates based on a single contemporary geotechnical study elsewhere are likely to be unreliable.

The principal conclusion drawn from these findings is that when estimating the response of a geologically simple, shallow stiff-soil site the geotechnical model may be more important than the method used to calculate response, underscoring the importance of obtaining more accurate estimates of seismic velocity structure and damping during site characterization.

Strong-Motion Blind Test

The M6.0 Parkfield earthquake occurred on September 28, 2004, rupturing the ground surface for a distance of 25 km along the San Andreas Fault, which passed within about 4 km southwest of the Rock South recording site. The main shock was well recorded by the dense Parkfield array, revealing a complex pattern of highly variable ground motions (figure 7).

Near-fault peak accelerations range from .13g to more than 2.5g, while stations separated by only 2-3 km differed by nearly an order of magnitude (Shakal et al, 2006b). Possibly due to source and/or site effects, the high degree of ground shaking variability over short distance is under investigation. No significant directivity is evident from the dense near-field array data, which may be due to bilateral rupture along the San Andreas Fault during the 2004 event (Shakal et al., 2006b).

Turkey Flat lies between the two high acceleration lobes at each end of the fault rupture as shown on figure 7. The main shock produced a peak rock acceleration of 0.245g at station Rock South (surface), and 0.07g at station D3 (rock beneath valley) of the Turkey Flat array (figure 8). The Rock South records were processed and distributed March 2005 for the beginning of the strong-motion blind test (Real and Shakal, 2005; Real et al., 2005), and the D3 records were distributed 7 months later. The deadline for Part 1 predictions was October 2005, and for Part 2 February 2006. Analysis of the submitted predictions is still underway at the writing of this paper, and final results will be available by Fall 2006.

The Turkey Flat strong-motion blind test began March 2005 and is expected to conclude Fall of 2006. There are 15 participating teams from 4 countries that have submitted a total of 92 sets of blind predictions, 45 for Part 1 and 47 for Part 2 of the test. Of the 92 sets of predictions, 18 are from industry, 54 are from academia, and 20 are from government sectors (Table 5). Each *prediction set* corresponds to various sensor locations depending on the level of participation, and varies for Part 1 and Part 2.

Table 6 identifies the various computer codes and model categories being tested. All prediction sets are 1-D analyses except 3 that are 2-D. Also indicated for each code/model being tested are the numbers of prediction sets as described previously that have been submitted for the array, and the number of site response predictions tallied by individual sensor locations (horizontal component pairs) for Part 1 and Part 2, all subtotaled by model category.
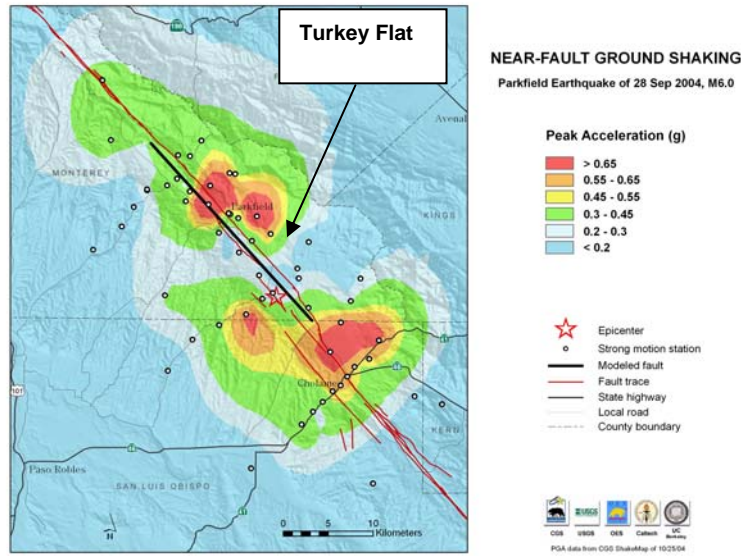
Figure 7. Near-field peak acceleration map of M6.0 2004 Parkfield Earthquake (Shakal et al., 2005)
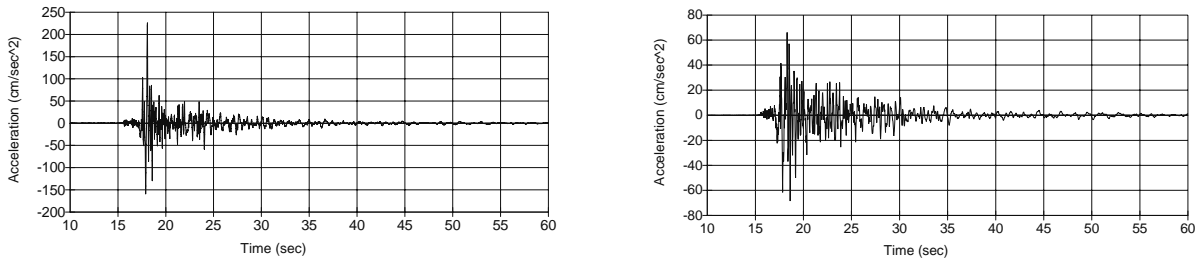

Figure 8. 2004 Parkfield mainshock recorded at (left) Rock South and (right) D3 (rock beneath Valley Center) of the Turkey Flat array.

Table 5. Number of site response prediction sets for Turkey Flat strong-motion test.

Sector	Part 1		Part 2		Total
	Preferred	Standard	Preferred	Standard	
Industry	5	4	5	4	18
Academia	15	11	17	11	54
Government	5	5	5	5	20

The grand total of individual predictions, most provided in the 4 basic forms described previously, exceeds 250 (or more than 500 for individual horizontal components). Thus, the level of participation is believed to be sufficient to draw meaningful conclusions regarding the state-of-practice in site response analysis.

Table 6. Site response codes tested and number of predictions.

Category	Method/Code	No. Sets	Analysis Performed	No. Predictions[2] Part 1	No. Predictions[2] Part 2
Equivalent Linear	SHAKE04	2	1-D	0	4
	SHAKE96B	4	1-D	12	4
	SHAKE91	18	1-D	29	16
	SHAKE72	4	1-D	12	10
	TremorKA	2	1-D	6	2
	TremorN2	2	1-D	6	2
	DeepSoil	6	1-D	12	6
	FDM	4	1-D	12	6
	BESOIL	2	1-D	6	2
	RASCAL	4	1-D	12	4
	SuperFLUSH[1]	2	2-D	6	2
	DYNEQ	5	1-D	15	4
	Subtotal	(55)	Subtotal	(128)	(62)
Nonlinear	DMOD-2[1]	6	1-D	4	10
	DeepSoil	6	1-D	12	6
	TESS	4	1-D	7	4
	FLAC[1]	4	1-D	4	4
	FLAC[1]	1	2-D	0	2
	OpenSees[1]	4	1-D	5	4
	SUMDES[1]	4	1-D	4	4
	NOAHW[1]	2	1-D	6	2
	Subtotal	(31)	Subtotal	(42)	(36)
Other	SSR	2	Empirical transfer function	6	5
	PEXT	2	1-D Source, path, site	6	6
	Subtotal	(4)	Subtotal	(12)	(11)
	Total	90[3]	Total	182	109

[1] Also capable of 2- and/or 3-D analyses. [2] Count is for horizontal component pairs. [3] Two additional sets were submitted that averaged the results from several different codes.

Preferred Soil Models

One major difference between the weak- and strong-motion tests is that the latter required submittal of predictions based on a user-preferred soil model. While only 6 predictions based on a preferred model were submitted for the weak-motion test, 22 were submitted for the strong-motion test. Figure 9 shows preferred velocity and slowness profiles derived from the field measurements by the participants, and indicates substantial variability in judgment among predictors. Slowness is the inverse of velocity, which is linearly related to the time seismic waves spend traveling through each layer. The importance of the near-surface layers is of physical significance as clearly indicated by their longer travel times.
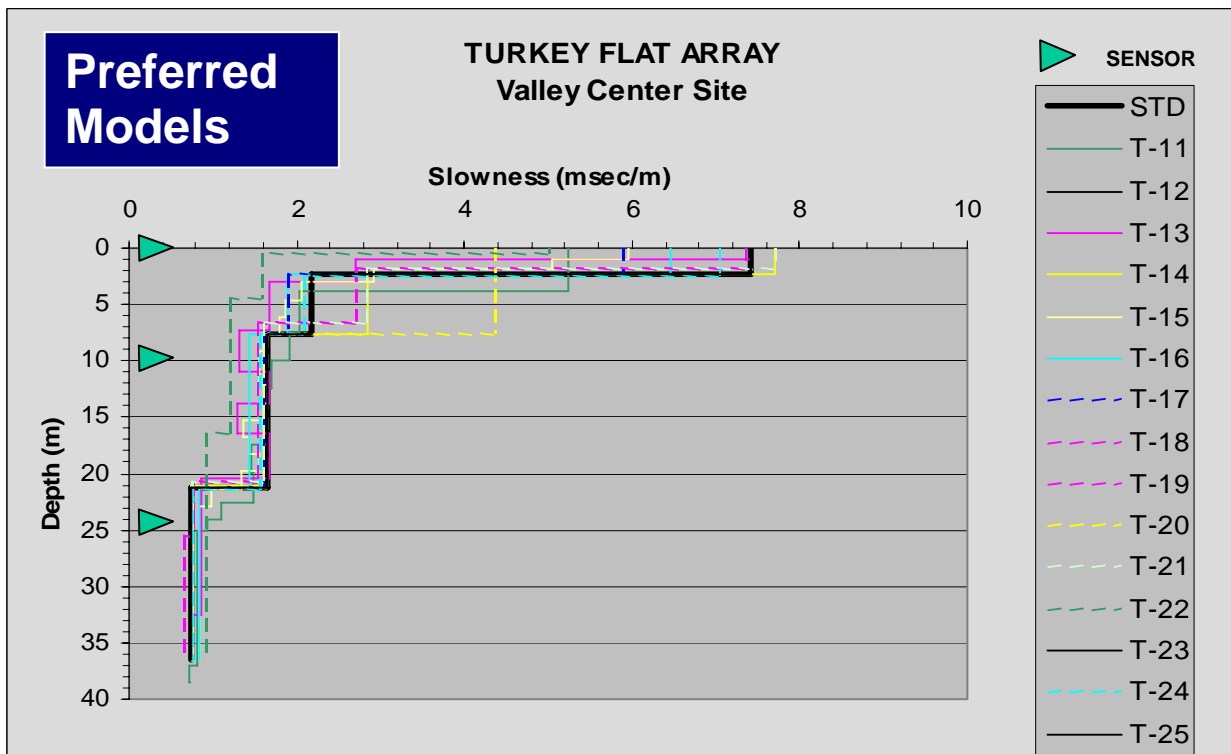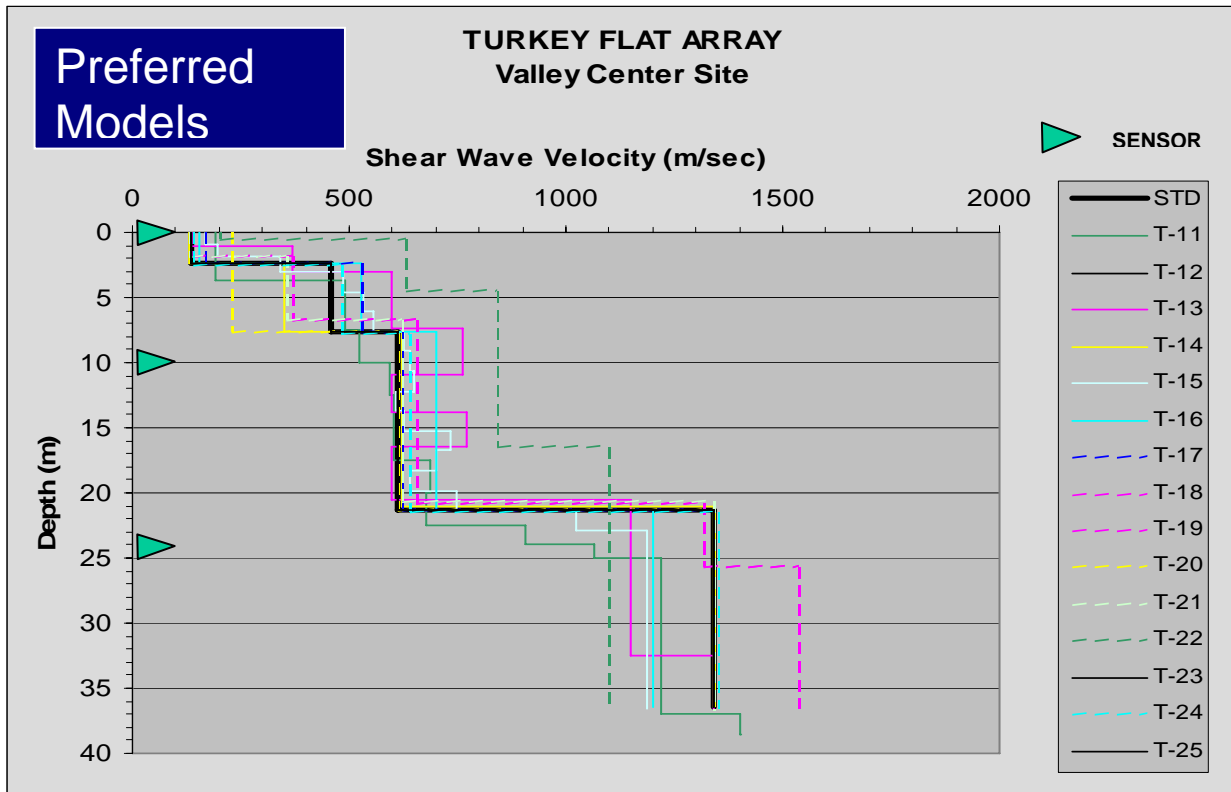
Figure 9. Preferred velocity models used by various predictor teams (indicated by team number).
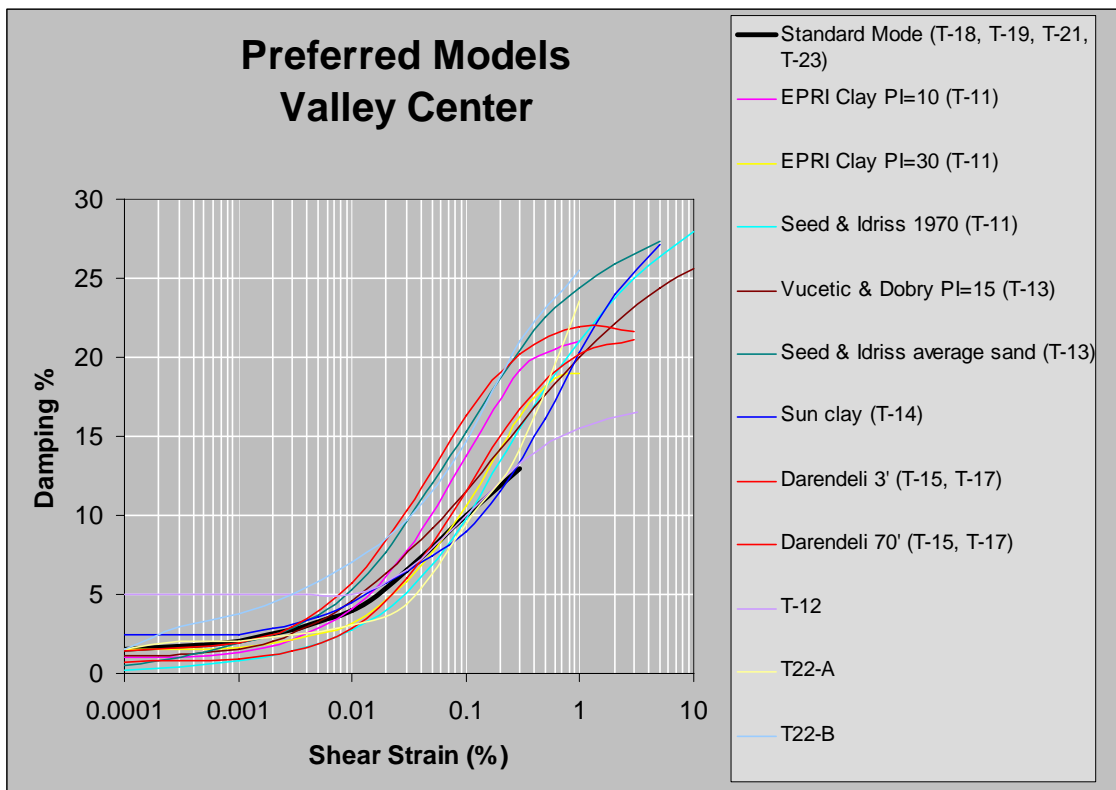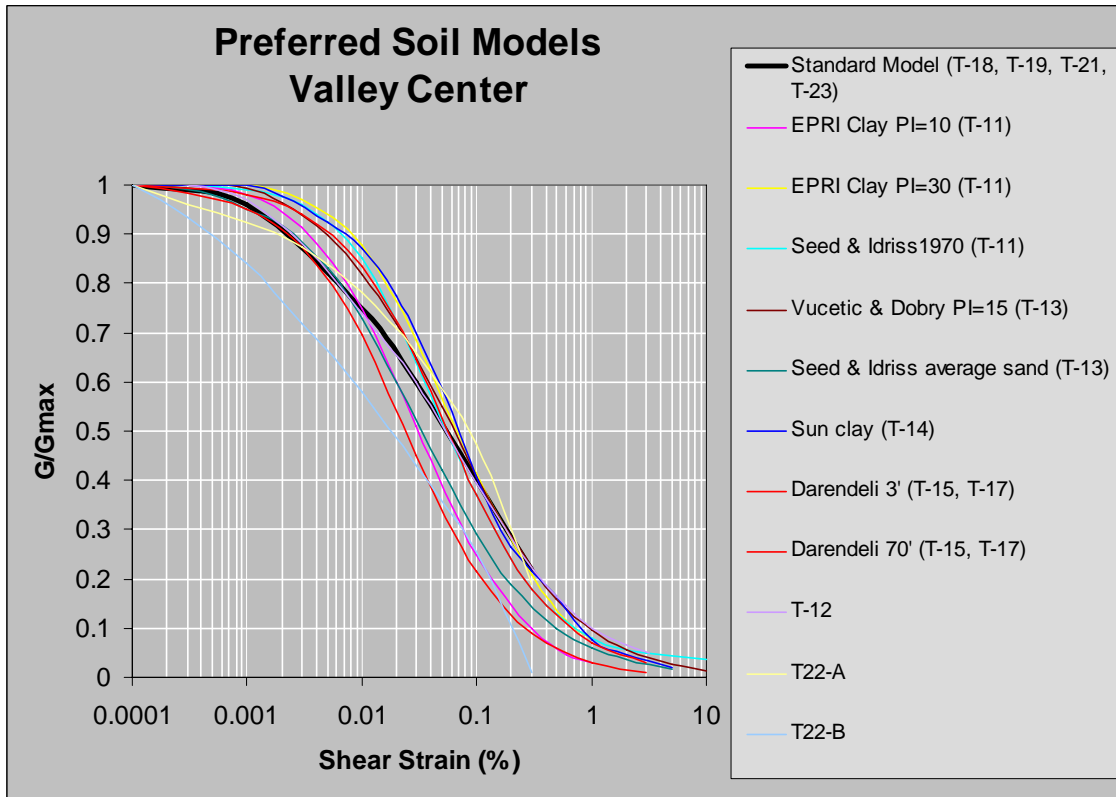
Figure 10. Preferred dynamic soil properties used by the various prediction teams.

Significant advances in site response research have occurred during the 15 years since the weak-motion blind test. Improvements in field and laboratory soil testing and numerous dynamic soil tests made for a variety of soils and representative site conditions have led to a greater understanding of the physics of soil behavior at large strains. The result is a more comprehensive theory of critical state soil mechanics, which has prompted the development of more sophisticated fully nonlinear computer codes and more realistic rheologies to better represent the dynamic behavior of various soil types (Lo Pristi et al., 2004). As a consequence, practice has advanced since the weak-motion test was conducted, which has implications on the soil models chosen for use in the various equivalent-linear and nonlinear codes used in the strong-motion blind test. Variability of the preferred modulus reduction and damping curves used by predictors is shown in figure 10. In addition to these parameters, other parameters not shown that are used in the nonlinear computational models include those used to define the hysteretic behavior of soils under cyclic loading, which are code specific.

Discussion

There are at least two principal issues that are being closely examined that could compromise the integrity of the experiment at Turkey Flat in regards to the strong-motion blind test and its effectiveness in addressing the primary goal of helping to determine the current state-of-practice in estimating site response: 1) improvements in the state-of-practice of site characterization since establishment of the Turkey Flat test site, and 2) potential effects of the source and/or path on ground motions recorded across the array due to the close proximity to the test event surface fault rupture.

The principal issue concerning site characterization is that the uncertainty of site response parameters derived in the late 1980's may be greater than what would result from the current state-of-practice because of interim improvements in field and laboratory testing. If true, this questions the validity of combining circa 1990 practice in site characterization with 2005 practice in site response modeling in order to draw conclusions about the overall reliability of current practice in site response analysis. If today's methods of site characterization are indeed better, then consideration should be given to a supplementary site characterization program at Turkey Flat to perform those tests where improvements have significantly reduced parameter uncertainties in order to obtain improved parameter estimates that would be more representative of the current state-of-practice.

Of the 15 participating teams, one team submitted a Class-A prediction that explicitly considers non-uniform source rupture and full wave propagation through a 1-D linear rheology. Analyses of data from the Parkfield array may further validate whether there are significant source effects at sources distances comparable to Turkey Flat. Consideration might be given to conducting a Class-A prediction blind test if differences between site response predictions and observations cannot be adequately explained by errors in site-effects modeling; particularly if analyses of the Parkfield strong-motion array test event records indicate the likelihood of near-field source effects.

Although the strong-motion blind test is still in progress, experience gained thus far suggest several ways to improve similar blind tests that may be conducted elsewhere in the future. The following is a summary of recommendations:

- To better quantify the performance of current site response estimation analyses will require more redundancy of parameter measurements obtained during site characterization. Multiple measurements of a given parameter by each investigator for each method employed would permit a better estimate of the error distributions, improving the statistical significance of performance results;
- Performing site characterization well in advance of array instrumentation allows for more optimal placement of recording sites and sensors;
- The long wait for significant strong-motion recordings requires a robust program and long-term funding for instrument maintenance for calibration, repairs, upgrades, and constant readiness;
- Statistical robustness in the analysis of prediction results and site response estimation methods requires a high level of participation. Evaluating state-of-practice demands participation by industry, which requires anonymity. Achieving a suitable number of participants may require funding support for their time and effort; particularly for industry participants who work for profit and have less discretionary funding available for research.

Finally, we recommend allowing more flexibility in the format for exchange of prediction results. We chose to adhere to a rigid format that was established 15 years ago for the weak-motion blind test. At that time it was prescribed to be the format that would be used for the strong-motion blind test results as well. Experience showed that this was an obstacle to timely submission and exchange of results. With today's computing technology, the format of results has several alternatives such as spreadsheets, text files, or xml files. Use of more conventional formats would have made the task of transferring site response prediction results much easier.
.

A website has been established to provide updates and disseminate information regarding the Turkey Flat Site Effects Test Area and the blind site response tests:
http://www.quake.ca.gov/turkeyflat.htm.

Melvin and Ruth Taylor, who understood the value of this project and who made their land available for the Turkey Flat, USA Site Effects Test Area.

References

Bakun, W.H., and A.G. Lindh (1985). The Parkfield, California, Earthquake Prediction Experiment. *Science 22 (4714)*, 619-624.

Bielak, J. and M. Romo (1989). Working Group Conclusions on Geotechnical Engineering and Foundations, in, Bertero, V.V. ed., Lessons Learned from the 1985 Mexico Earthquake: *Earthquake Engineering Research Institute Report 89-02*, 56-58.

Cramer, C.H. (1995). Weak-Motion Observations and Modeling for the Turkey Flat, U.S., Site Effects Test Area near Parkfield, California. *Bulletin of the Seismological Society of America 85*, (2), 440-451.

Cramer, C.H (1992). Weak motion observations and modeling for the Turkey Flat, USA, site effects test area near Parkfield, California. *Proceedings of the International Symposium on the Effects of Surface Geology on Seismic Motion, March, 1992, Odawara, Japan 2*. Association for Earthquake Disaster Prevention, Tokyo, Japan, 21-26.

Cramer, C.H., and C.R. Real (1992). A statistical analysis of submitted site-effects predictions for the weak-motion blind prediction test conducted at the Turkey Flat, USA, site effects test area near Parkfield, California. *Proceedings of the International Symposium on the Effects of Surface Geology on Seismic Motion, March, 1992, Odawara, Japan 2*. Association for Earthquake Disaster Prevention, Tokyo, Japan, 15-20.

Cramer, C.H.. *Turkey Flat, USA Site Effects Test Area – Report 6: Weak-Motion Test: Observations and Modeling*. California, Division of Mines and Geology, TR 91-1(1991).

Cramer, C.H. and C.R. Real (1990a). Ground Response to Weak Motions From Local and Regional Earthquakes at The Turkey Flat Site-Effects Test Area Near Parkfield, CA: Observations, Modeling, and Implications for Ground Motion Prediction. *Seismological Research Letters 61*(1), 51.

Cramer, C.H. and C.R. Real. *Turkey Flat, USA Site Effects Test Area – Report 5: Weak Motion Test: Statistical Analysis of Submitted Predictions and comparisons to Observations.* California Division of Mines and Geology, TR 90-2 (1990b).

Cramer, C.H. and C.R. Real. *Turkey Flat, USA Site Effects Test Area – Report 4: Weak-Motion Test: Observed Seismic Response*. California Division of Mines and Geology, TR 90-1 (1990c).

Cramer, C.H., C.R. Real, and B.E. Tucker (1989). The Weak-Motion Test of The Ground-Motion Prediction Phase of The Turkey Flat, USA, Site Effects Test Area Experiment. *Seismological Research Letters 60* (1), 8.

Field, E.H. and K.H. Jacob (1993). Monte-Carlo Simulation of the Theoretical Site Response Variability at Turkey Flat, California, Given the Uncertainty in the Geotechnically Derived Input Parameters. *Earthquake Spectra 9* (4) 669-702.

Hanna, W.F., Burch, S.H., and T.W. Dibblee, Jr. (1972). Gravity, Magnetics, and Geology of the San Andreas Fault Area Near Cholame, California. *U.S. Geological Survey Professional Paper 646-C*.

Idriss, I.M. (1990) Response of Soft Soil Sites during Earthquakes. *Proceedings, Memorial Symposium to honor Professor Harry Bolton Seed 2*, Berkeley, California, 273-289.

Jarpe, S.P., Cramer, C.H., Tucker, B.E., and A.F. Shakal (1988). A Comparison of Observations of Ground Response to Weak and Strong Motion at Coalinga, California. *Bulletin of Seismological Society of America 78* (2), 421-435.

Kudo, K. (2003). IASPEI/IAEE Joint Working Group on the Effects of Surface Geology on Seismic Motion. *International Handbook of Earthquake Engineering and Engineering Seismology 81.7* CD-ROM #2.

Lo Pristi, D. Lai, C., and S. Foti. Geophysical and Geotechnical Investigations for Ground Response Analyses, in, Ansal, A., ed., *Recent Advances in Earthquake Geotechnical Engineering and Microzonation*. Kluwer Academic Publishers, Dordrecht, Netherlands, (2004).

McJunkin, R.D., and A.F. Shakal (1983). The Parkfield Strong-Motion Array. *California Geology 36* (2), 27-34.

Real, C.R., Shakal, A.F., and V. Graizer (2005). Blind prediction test of the response of Turkey Flat Site Effects Test Area to the September 28, 2004 Parkfield Earthquake. *Proceedings of the IASPEI General Assembly, October 2-8, 2005, Santiago, Chile*.

Real, C.R. and A.F. Shakal. *Turkey Flat, USA Site Effects Test Area – Report 7: Strong-Motion Test: : Prediction Criteria and Input Rock Motions*. California Geological Survey, OSMS 05-1 (2005).

Real, C.R., and C.H. Cramer (1992). Site characterization and standard geotechnical model for the Turkey Flat, USA, site effects test area near Parkfield, California. *Proceedings of the International Symposium in the Effects of Surface Geology on Seismic Motion, March 25-27, 1992, Odawara, Japan 2*. Association for Earthquake Disaster Prevention, Tokyo, Japan, 9-14.

Real, C.R. and C.H. Cramer (1990). Turkey Flat, USA, Site Effects Test Area: "Blind" Test of Weak-Motion Soil Response Prediction. *Proceedings of the Fourth U.S. National Conference on Earthquake Engineering 1*, 535-544.

Real, C.R. and C.H. Cramer. *Turkey Flat, USA Site Effects Test Area – Report 3: Weak-Motion Test: Prediction Criteria and Input Rock Motions*. California Division of Mines and Geology TR 89-1 (1989).

Real, C.R. *Turkey Flat, USA Site Effects Test Area – Report 2: Site Characterization*. California Division of Mines and Geology, TR 88-2 (1988).

Real, C.R. and B.E. Tucker (1988a). Ground Motion Site Effects Test Area Near Parkfield, California. *Proceedings of the Sino-American Workshop on Strong-Motion Measurement*, 140-147.

Real, C.R. and B.E. Tucker (1988b). Turkey Flat, USA Site Effects Test Area site characteristics. *Proceedings of the IASPEI/IAEE Joint Working Group on Effects of Surface Geology on Seismic Motion Second Workshop, Tokyo Japan*, 1-22.

Real, C.R. and B.E. Tucker (1988c). Ground Motion Site Effects Test Area Near Parkfield, California. *Proceedings Ninth World Conference on Earthquake Engineering, Tokyo, Japan VIII*, 187-191.

Real, C.R. and B.E. Tucker (1987). Ground Motion Site Effects Test Area at Turkey Flat, California. *EOS, Transactions American Geophysical Union 68*, 1350.

Shakal, A.F., Huang, M.J., and V.M. Graizer (2003). Strong-Motion Data Processing. *International Handbook of Earthquake Engineering and Engineering Seismology Part B*, 967-981.

Shakal, A., H. Haddadi and C. Real (2006a). Recorded data and preliminary review of predictions in the Turkey Flat blind prediction experiment for the September 28, 2004 Parkfield earthquake, *Proceedings of SMIP06 Seminar on Utilization of Strong-Motion Data, September 28, 2006, Oakland, California*, 137-152.

Shakal, A., H. Haddadi, V. Graizer, K. Lin and M. Huang (2006b). Some key features of the strong-motion data from the M6.0 Parkfield, California, earthquake of 28 September 2004, *Bulletin of the Seismological Society of America* **96**, no. 4B, S90-S118.

Shakal, A., Graizer, V., Huang, M., Borcherdt, R., Haddadi, H., Lin, K., Stephens, C., and P. Roffers (2005). Preliminary Analysis of Strong-motion Recordings form the 28 September 2004 Parkfield, California Earthquake. *Seismological Research Letters 76* (1), 27-39.

Tucker, B.E., C.R. Real, and P.Y. Bard (1988). Validation Des Methodes De Prediction Des Effets De Site: L'Experience De Turkey Flat En Californie Centrale. Les Mouvements Sismiques , Reunion de l'AFPS, 16-03-88, Saint Remy les Chevreuse. 344-351.

Tucker, B.E. and C.R. Real (1988). The Design and Operation of a Test Site Near Parkfield, California to Compare and Test Methods of Estimating the Effect of Surface Geology on Seismic Motion. *Proceedings of Workshop on Earthquake Ground-Motion Estimation in Eastern North America*. Electric Power Research Institute EPRI NP 5875, Chapter 15, 1-15.

Tucker, B.E. and C.R. Real. *Turkey Flat, USA Site Effects Test Area – Report 1: Needs, Goals, and Objectives*. California Division of Mines and Geology, TR 86-1 (1986).

RECORDED DATA AND
PRELIMINARY REVIEW OF PREDICTIONS IN THE
TURKEY FLAT BLIND PREDICTION EXPERIMENT
FOR THE SEPTEMBER 28, 2004 PARKFIELD EARTHQUAKE

Anthony Shakal, Hamid Haddadi and Charles Real

California Geological Survey, Sacramento, CA

Abstract

A blind prediction experiment was conducted for the strong-motion data recorded at the Turkey Flat test area during the September 28, 2004 M6.0 earthquake. The motion was predicted at several sites by 15 prediction teams, first based on the observed motion at the edge of the valley, and secondly, based on the observed motion in the rock underlying the valley. Predictions were received from geotechnical firms and researchers, both in the US and internationally. A workshop was held to preliminarily review and compare the predictions to each other and the recorded data. In general, the predictions based on the valley-edge motion exceed the observed data. Predicted peak ground acceleration at the center of the valley exceeded the observed by about 50% and predicted response spectra exceeded the observed by as much as 3–5 times at periods near 0.5 sec. In the second phase, involving predictions based on the recorded motion beneath the valley sediments, much closer results were obtained. In both phases, the predictions by different investigators were quite similar to each other. The use of nonlinear vs. equivalent-linear models did not significantly improve the predictions for this stiff-soil, relatively low strain motion.

Introduction

In anticipation of an earthquake near Parkfield, the California Geological Survey established a site effects test area across a sedimentary valley at Turkey Flat, east of Parkfield, California in the late 1980s (Tucker and Real, 1986). The geophysical properties of the site were thoroughly characterized in a cooperative effort by CGS, firms in the geotechnical community, and the IASPEI/IAEE Joint Working Group on Effects of Surface Geology on Seismic Motion. The test site was instrumented with a strong motion array by consisting of surface and downhole accelerometers by the California Strong Motion Instrumentation Program of CGS. The array includes surface instruments at the two valley edges, at one quarter the valley width, and at the center of the small, shallow 23 m stiff-soil sedimentary valley. The instrumentation at the valley center also includes a downhole array, with an instrument at mid-height in the sediments and another just below the rock interface. The instrumentation at one valley edge also includes a downhole accelerometer at the same depth as the deep accelerometer at valley center.

The Parkfield earthquake was well recorded throughout the Turkey Flat array, providing the records necessary to conduct the long awaited blind prediction test. In this prediction experiment, acceleration time histories recorded on bedrock near one valley edge were provided

to participants, along with a "Standard" model of the subsurface geotechnical properties defined following measurements made in the 1980s (e.g., Real et al., 2006a,b). Participants were asked to make predictions of the ground motions at the valley center and other recording locations for which, as part of a long-term plan, records were not made public. A workshop at which predictions were compared to each other and the recorded motions was held on September 21, 2006.

The M6.0 Parkfield earthquake of September 28, 2004 was a well-documented event (e.g., Harris and Arrowsmith, 2006) and produced a very extensive, dense set of near-fault strong motion recordings. The strong-motion measurements included unprecedented near-fault coverage, and the measured strong motion includes high variability in the near fault motion, with accelerations as high as 2g or larger (e.g., Shakal et al., 2006a,b). At the distance of the Turkey Flat array, peak acceleration was generally 0.3 g or less.

The Turkey Flat Blind prediction experiment is based on the recordings at the Turkey Flat strong-motion array, shown schematically in Figure 1. The array has a surface site, R1, at the south side of the valley, a downhole array (V1, D2 and D3) at the center of the valley, a surface site farther north in the valley (V2), and a rock site at the north side of the valley (R2). Each location has a triaxial set of force-balance accelerometers, recorded by a digital solid-state recorder (SSA-1).
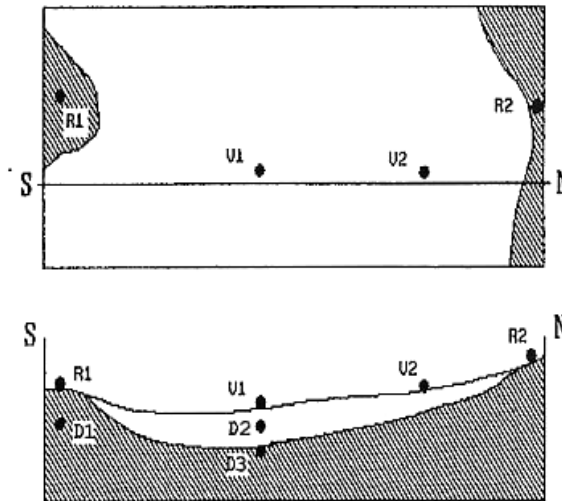
Figure 1. Schematic illustration of the Turkey Flat site effects test area and the strong-motion array stations (after Tucker and Real, 1986). Downhole sensor D3 is about 1 m below the rock interface at valley center. D1 is at a similar depth (24 m, 80 ft) below rock site R1. D2 is at mid-height in the sediments (11 m, or 35 ft). For reference, the distance from V1 to V2 is about 500 m, and from V1 to R1 is about 800 m.

In the first phase of the experiment, the R1 record was released and predictions were to be made for all other sites, though V2 and R2 were optional. In the second phase of the

experiment, starting about 6 months later, the D3 record was released, and the other sites were to be predicted again.

The purpose of the prediction experiment is to assess the state of the practice for predicting site response at a site in California, not to establish winners or losers. The site is of a particular type, thin, stiff alluvium over rock. The site was chosen as a highly likely site to experience strong shaking, being near the Parkfield segment of the San Andreas fault on which an earthquake was predicted to occur soon. The site is about 5 km from the San Andreas fault and ideally should be more distant to be confident of avoiding finite fault effects at the different sites of the array. However, given the moderate magnitude event expected at Parkfield, strong shaking could not be expected at great distances from the event. Clear tradeoffs were necessary for this experiment, but as a result, the first successful blind prediction has been made, described in greater detail in Real et al. (2006a, b).

Recorded Data

The Turkey Flat array, at its closest point, is located approximately 5 km from the fault and approximately 7 km from the epicenter of the Parkfield earthquake. The peak acceleration at the valley center site (Turkey Flat #2) was 0.29g. The acceleration records are shown in Figure 2, which also shows the records at 11 m depth (D2) and 34 m, in the bedrock (D3). The records at the rock site at the south edge of the valley, Rock South, are shown in Figure 3.

A striking difference between Rock South and Valley Center is that the EW record from 23 m depth at Valley Center (D3) is only 0.07g, in contrast with a value of 0.16g at the same depth at Rock South (D1). The rock at D1 and D3 has the same S-wave velocity according to the field measurements performed in 1988 (Real et al., 2006b). As shown in Figure 3, the NS record at D1 looks very similar to that at the surface (R1), but reduced from the 0.19g at the surface to 0.16g. The surface records from Valley North (Turkey Flat 3) and Rock North (Turkey Flat 4) are shown in Figure 4.

The low amplitude of the record at D3 compared to D1 and V1 may raise a question about possible errors in the recording at D3. To confirm the D3 record, in Figure 5 the computed horizontal displacements at Valley Center are shown. The displacements are nearly identical at all depths, with a peak value less than 1.5 cm. Though not shown, the NS displacement at V1 appears very similar to that at R1. The EW displacements at R1 and D1 have amplitudes very similar to that at V1, but they have an additional arrival or reflection in the middle of the simple displacement wavelet. The displacements at the V2 and R2 surface sites look very similar to those at V1. This comparison indicates that at long period the sensors have the same waveform and that there is not an error in gain, etc. At high frequency, on the other hand, the routine sensor tests done at record recovery look very ordinary and nominal. Thus, there is no reason to doubt the D3 recordings.
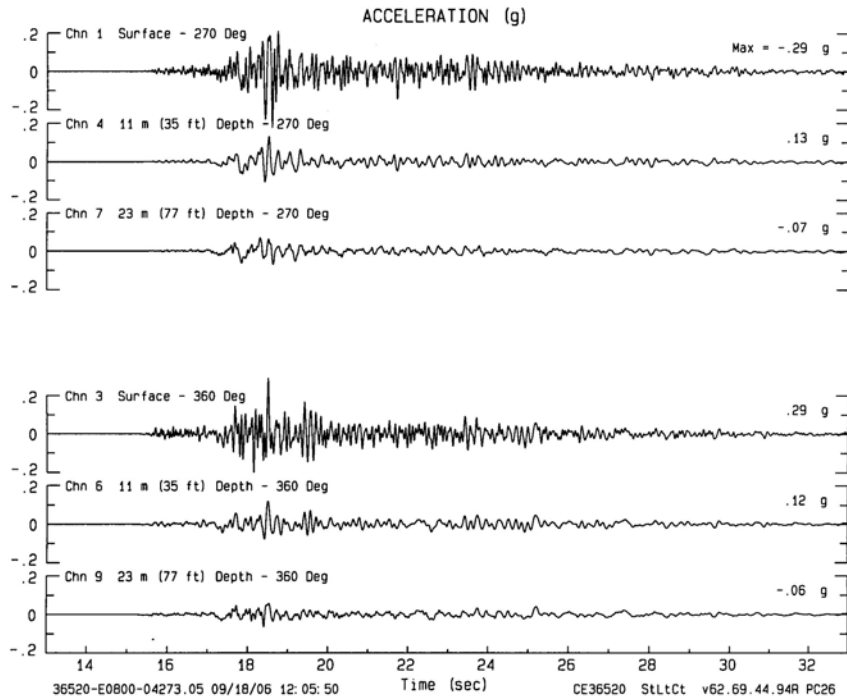
Figure 2. Horizontal accelerations recorded by the downhole array at valley center (station Turkey Flat #2), at the surface, 11 m and 23 m. These are locations V1, D2 and D3, respectively, of the Turkey Flat array.
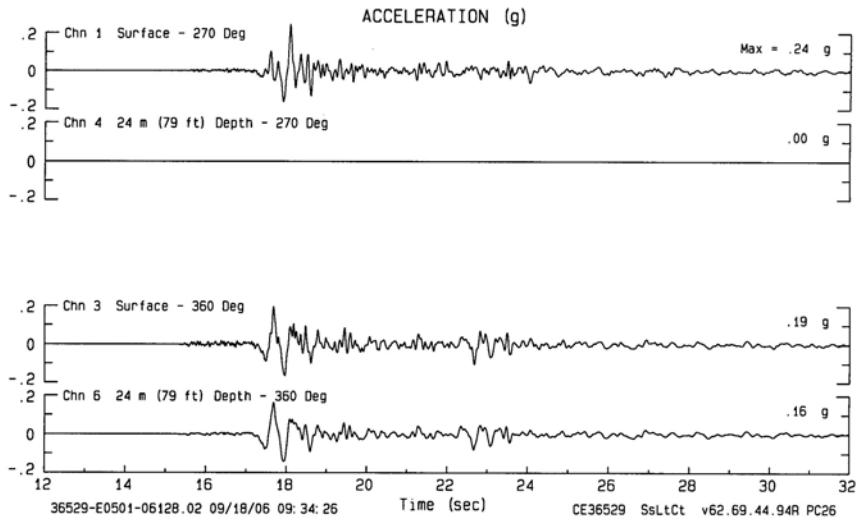

Figure 3. Horizontal accelerations recorded by the downhole array at Rock South, at the south edge of the valley, at the surface and at 24 m depth (locations R1 and D1, respectively). The EW sensor at D1 did not record.
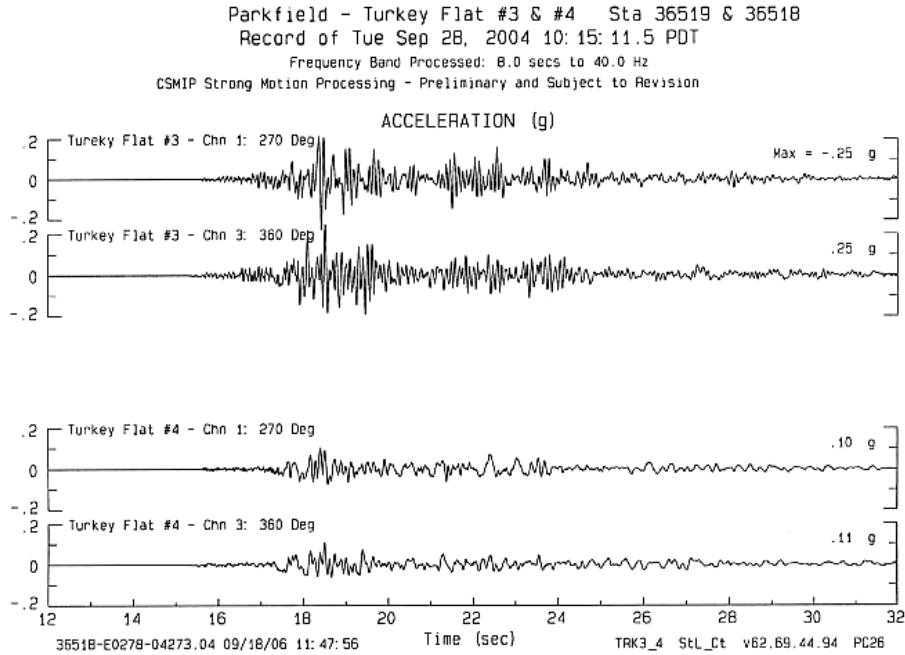
Figure 4. Horizontal accelerations recorded at the surface installations at Valley North (Turkey Flat #3) and Rock North (Turkey Flat #4).
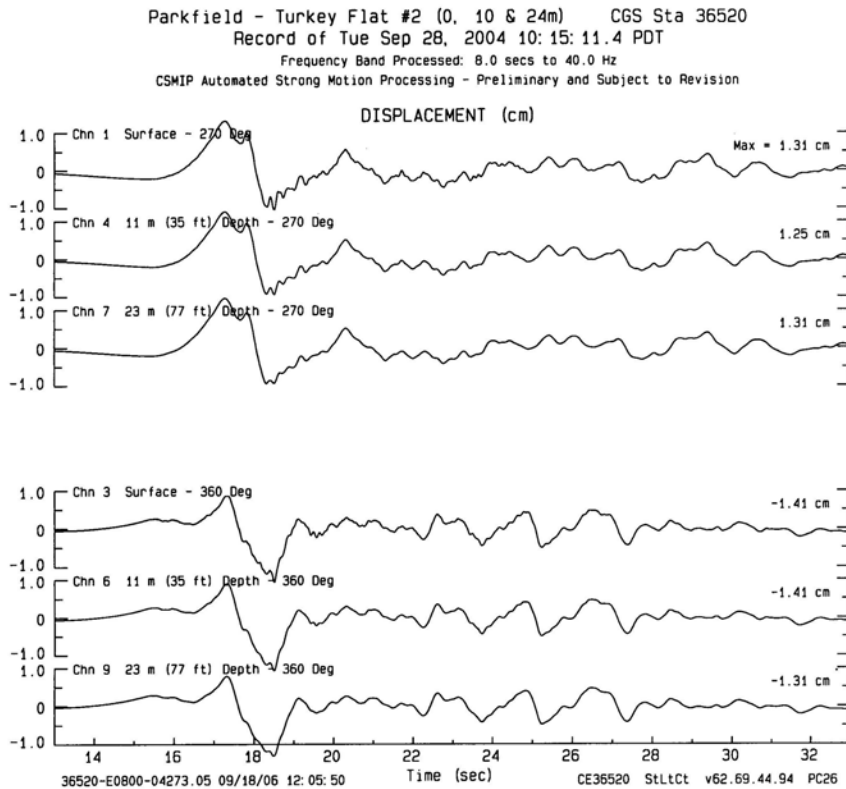
Figure 5. Horizontal displacements at the downhole array at Valley Center (V1, D2, D3).

Phase 1 Predictions – Based on R1

In Phase 1 of the blind prediction test, predictions teams were asked to predict the motion at all sites given the record at Rock South, R1. Fifteen different prediction teams submitted predictions, using one or more methods and soil models. The predictors were asked to submit, for the same computational method, a run made using a Standard soil model provided by CGS as well as a modified soil model, for which they altered parameters as they saw appropriate, and which was called a Preferred soils model. Some predictors used more than one computation method. The methods were divided into the categories of Equivalent–Linear (Shake-like), Nonlinear, and Linear. There were 23 computational methods used, of which 13 were of equivalent-linear type, eight nonlinear, and two linear. The predictors were kept anonymous, and are not identified except by an assigned number.

The predicted peak accelerations (EW component) at center of the valley are shown in Figure 6, along with the observed peak accelerations, for the surface, 11 m and 23 m depths, respectively. Nearly all predictions were high, with most predictions in the 0.40-0.45g range – compared to the observed peak of 0.29g, approximately 50% high. In general, predictions obtained by an investigator when using a Preferred model were lower than for the Standard model (both are shown, in different symbols, where given, in Figure 6). Thus, the use of a modified or Preferred soil model improved investigator predictions slightly.

The over prediction at the surface also occurs at 11 m depth (D2), with many predictions around 0.25g, approximately double the 0.13g value observed. The over prediction is greater at 23 m depth (D3), where most of the predictions are near 0.20g, approximately 3 times the observed value of 0.07g.

The over prediction also occurs for the two other surface sites of the arrays. Figure 7 shows the prediction at Valley North (V2), which is similar, in the difference between the predicted and observed values, to those at Valley Center (V1). Finally, the predicted accelerations for Rock North (R2) are near 0.25g, over double the observed peak of 0.11g.

The over prediction also occurs at D1, at 24 m depth in the rock immediately below the released R1 record as shown in Figure 8. Most of the predictions are near 0.20g, 25% larger than the observed value of 0.16 g.
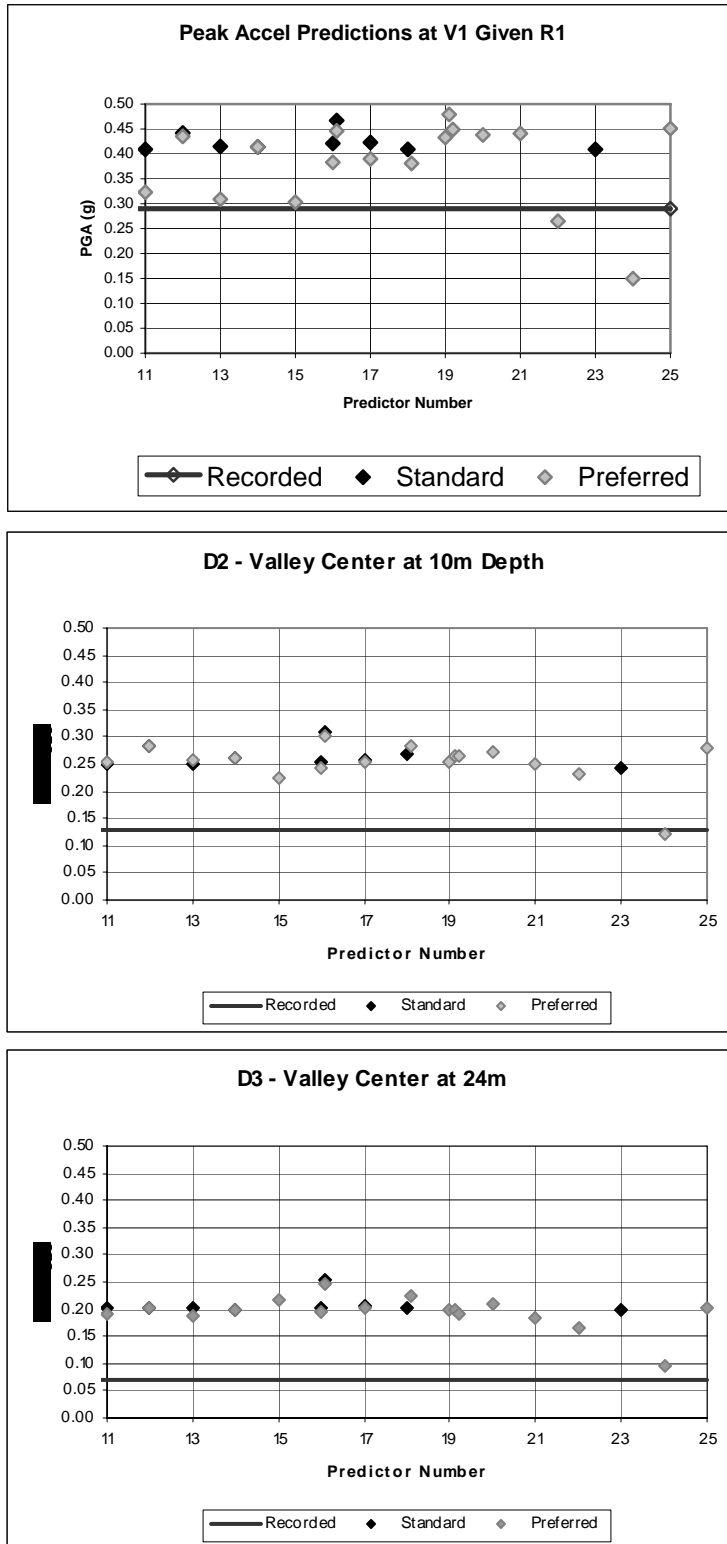
Figure 6. Peak accelerations (EW) predicted at V1, D2 and D3, given the record at R1, by numbered predictor teams compared to the observed values (line), for predictions using the Standard soil model (black), and Preferred models (gray).
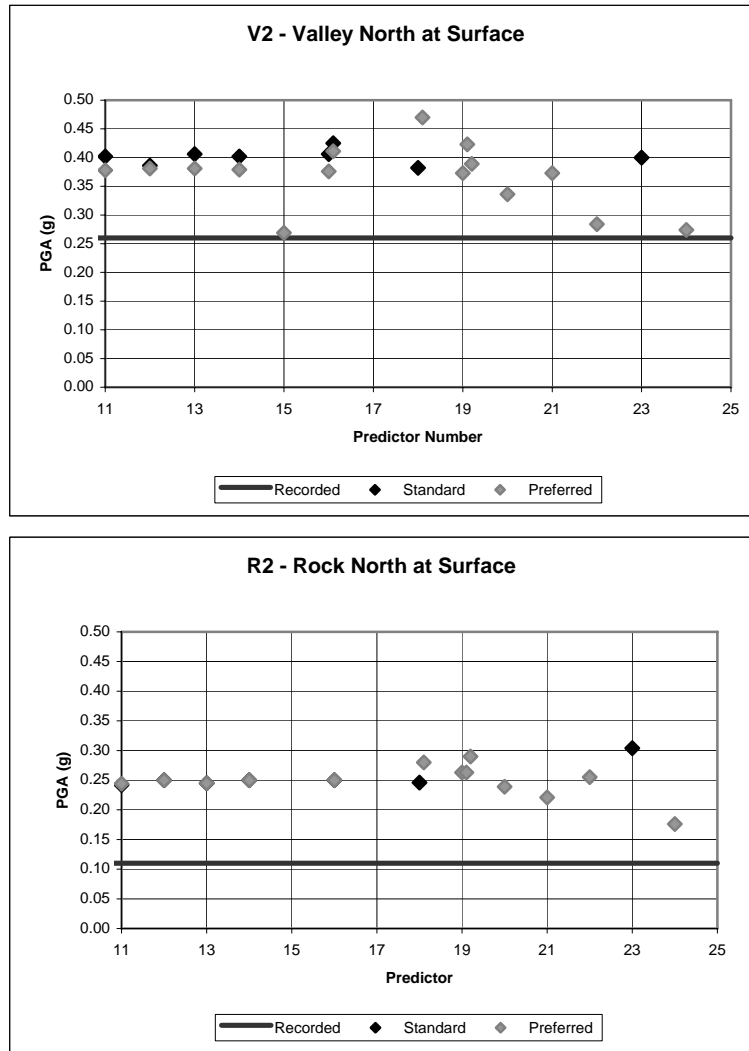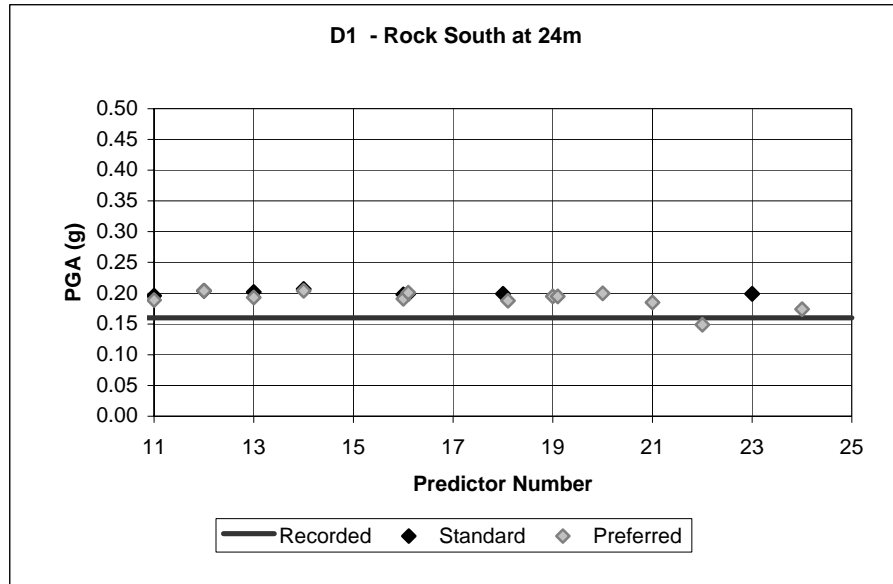
Figure 7. Peak accelerations predicted by numbered prediction teams for the motion at V2 and R2, given the record at R1, compared to the observed values (line). Black symbols are for predictions using the Standard soil model, gray are for Preferred models.

Figure 8. Peak accelerations predicted by numbered predictor teams for the motion at D1, given the record at R1, compared to the observed value (line). Black symbols are for predictions using the Standard soil model, gray for Preferred models.

Time Series Comparisons

Acceleration time series predicted for the valley center site, V1, are compared with the observed in Figure 9, for the Standard soil model. Only a subset is shown, as many of the predicted waveforms look similar. Peak accelerations greater than the observed, noted in Figure 6, are apparent, as well as some increase in apparent duration. Time series generated using Preferred models are somewhat lower in amplitude but the improvement is modest.

The observed record and a subset of the predicted records at D3, at 23 m, is shown in Figure 10. The waveforms are all substantially larger than the observed, which was reflected in the peak acceleration amplitudes in Figure 6.

In general, predicted waveforms in the Phase 1 part experiment are substantially higher than the observed. In addition, they share a high degree of similarity, and are more similar to each other than to the data.
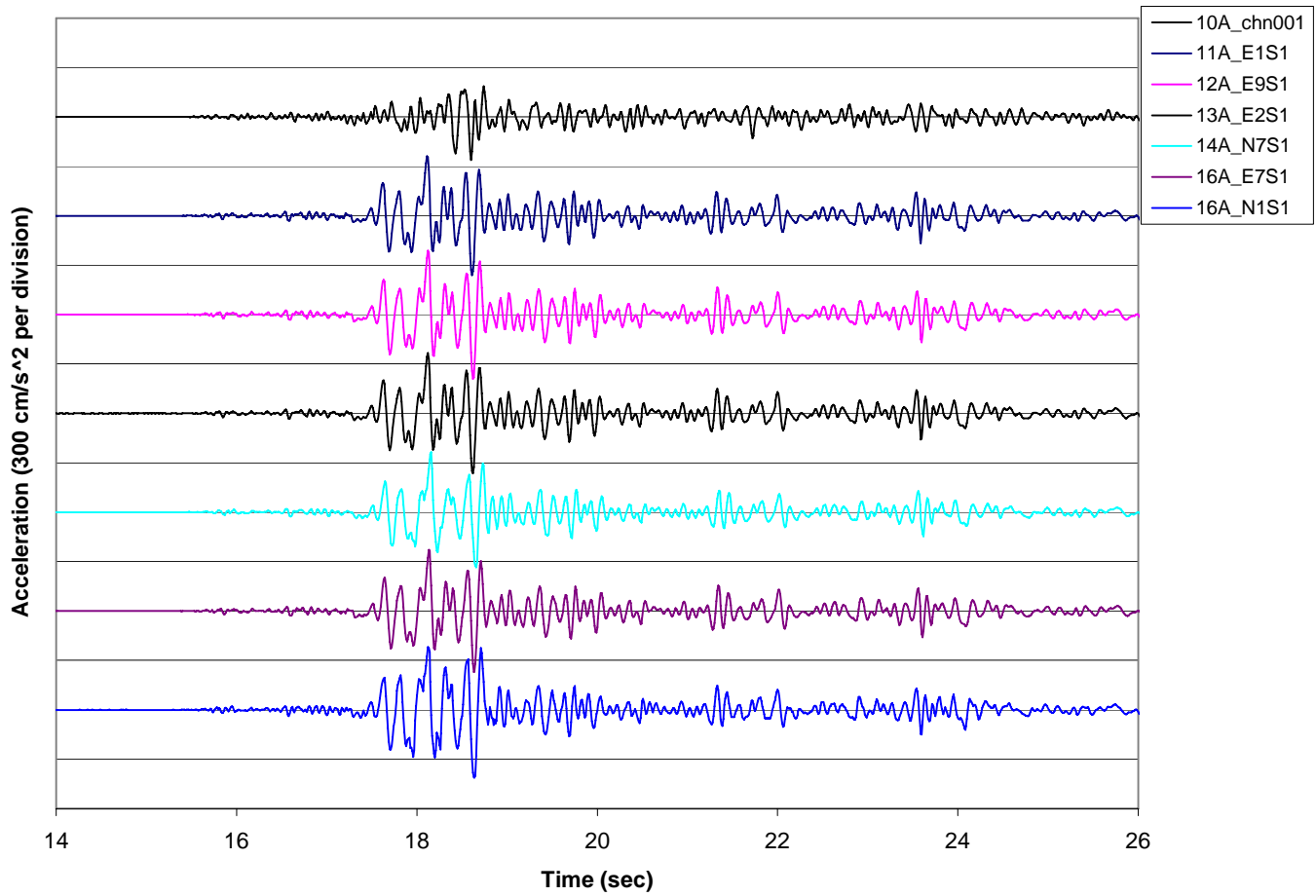
Figure 9. Observed (top) and predicted time series, EW component, for the valley center surface site, V1, based on the valley-edge rock record (R1), generated using the Standard soil model and a variety of computational methods. Only a subset of the predicted waveforms is shown as they look quite similar.
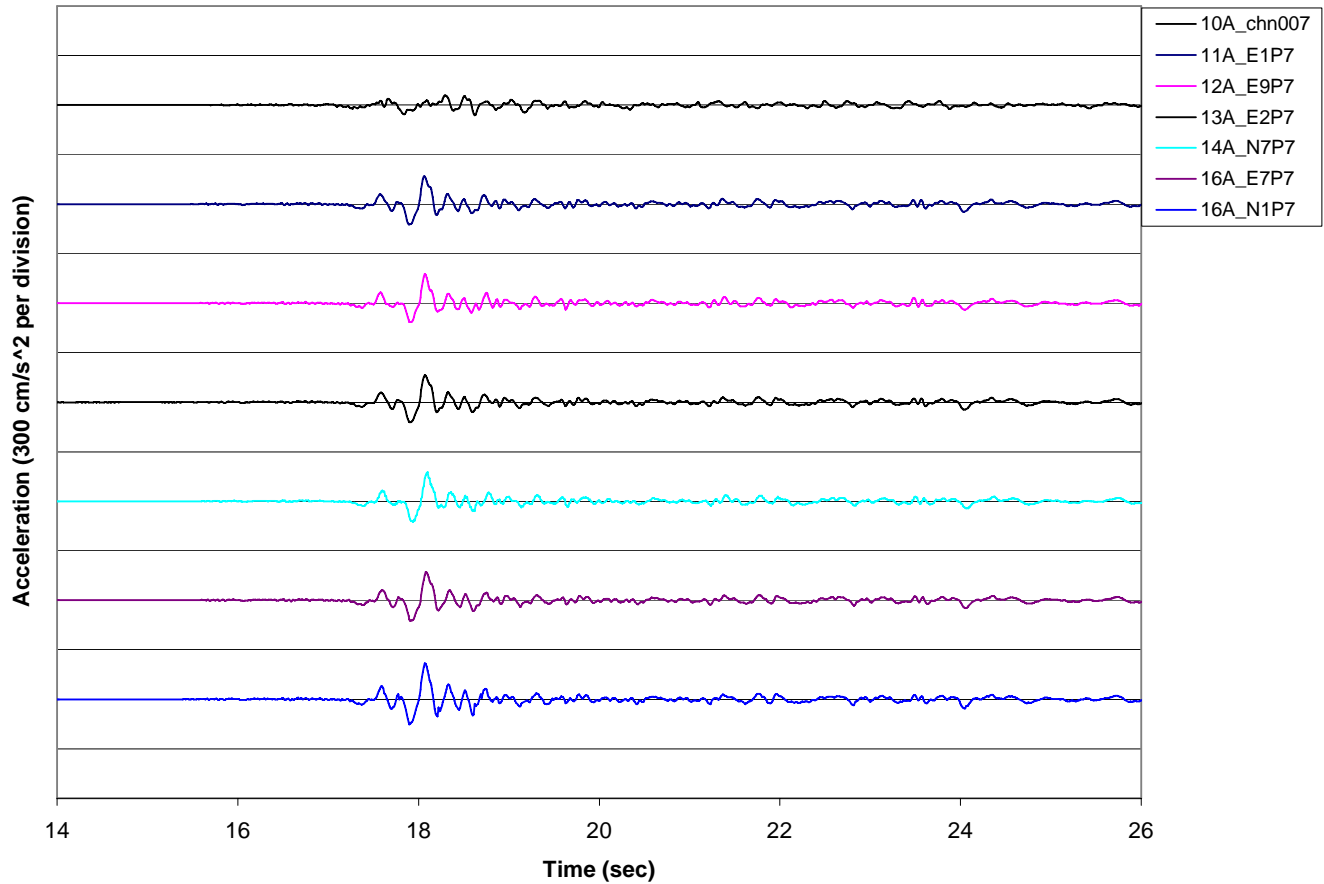
Figure 10. Observed (top) and predicted time series, EW component, at site D3, in the rock at the base of the sediments in the valley, based on the valley-edge rock record (R1), generated using the Standard soil model and a variety of computational methods.

Response Spectra Comparisons

To more completely compare the predictions and the recorded motion, response spectra are compared. Figure 11 shows the response spectra of the EW component for the observed record, and for all predictions obtained using the Standard soil model. In general, the predicted spectra cluster together, and are quite similar to each other, while the observed spectrum is significantly lower over most periods. At high frequencies (short period less than .2sec?), the predicted and observed are quite close (reflecting the difference of 50% or less in the peak values in Figure 6). However, at longer periods, between 0.25 and 0.75 sec, the predictions are several times higher than the observed. The spectra for the predictions based on Preferred soils models are lower, but still well above the observed. Very similar character is shown in the NS component.
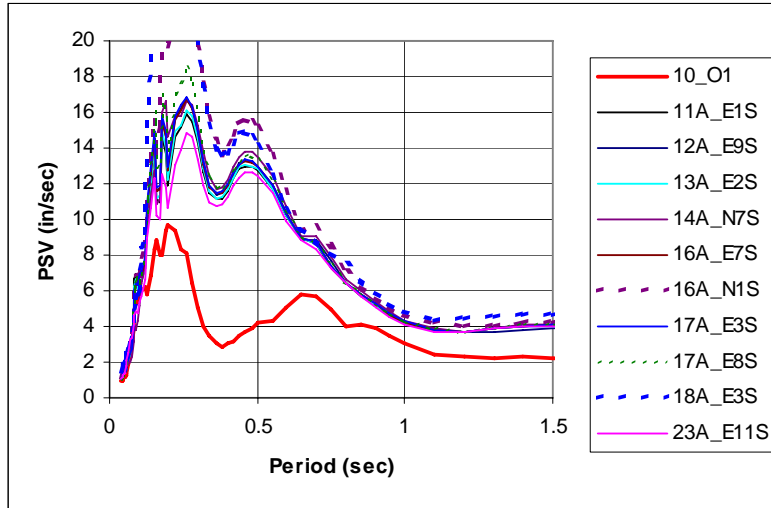
Figure 11. Response spectra of the EW component (5% damping) for the observed record and all predictions, obtained using the R1 valley-edge record and the Standard soil model. The lowest thick line is the observed spectra. The predicted spectra are quite similar to each other and well above the observed spectra at most periods.
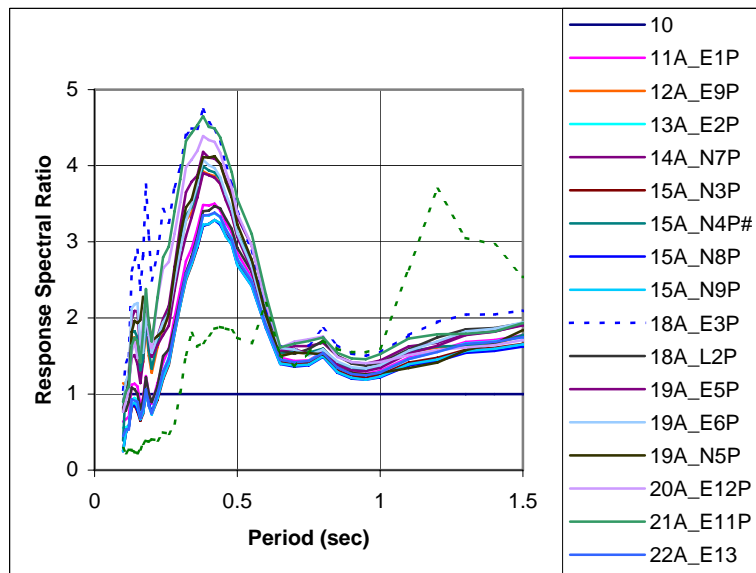

Figure 12. Ratios of the predicted response spectra (EW component, PSV, 5% damping) to the observed at V1, using the R1 valley-edge record and Preferred soil models, for all computational methods. The ratio spectra are quite similar to one another, expect for a few outliers. At periods between about 0.3 to 0.5 second, the predicted spectra are 3 to 4 times larger than the observed.

The difference is clear in the ratios of the predicted to the observed response spectra at V1, shown for the EW component in Figure 12. The ratio spectra are quite similar to one another, expect for a few outliers. At periods from 0.3 to 0.5 second, the spectra are 3 to 4 times

the observed. All methods are shown in Figure 12. There is not a clear difference between the predictions obtained using equivalent linear, nonlinear or linear methods. At long periods, the ratios are somewhat high as well, clustering at a ratio near 2 at 1.5 seconds and increasing slowly for longer periods. For the NS component the ratios are similar, but higher, with the ratios generally being between 5 and 6 in approximately the same period band where the EW component is high.

Phase 2 Predictions – Based on D3

In the second phase of the blind prediction experiment, the predictors were provided with the record from D3, in the rock under the sedimentary valley. The difference between the recording at D1 and D3 is significant, and unexpected by the predictors; this Phase of the experiment avoids this problem.

Peak Accelerations

A comparison of the peak accelerations with each other and the observed, for the EW component, is shown in Figure 13. The predictions cluster around the observed values much better than for the Phase 1 results. Most peak values are somewhat low, surprisingly. For comparison purposes, the Phase 1 predictions are also shown in Figure 13. The spread of predictions is not reduced in Phase 2, though the given record is only 23 meters below the predicted site. It is also clear that some of the predictions which were close to the observed in Phase 1 (e.g., Nos. 13 and 15) are now low.

Response Spectra

The predicted response spectra for the EW component are compared to the observed in Figure 14 and they are quite close to the observed. Beyond about 0.5 second, the predicted and observed spectra are very close to each other, though they drift apart at longer periods. At the spectral peak, around 0.25 second, many of the predicted spectra are smaller than the observed. In the NS direction, the predictions are again quite close to the observed, though at the spectra peak most of the predicted spectra are above the observed.
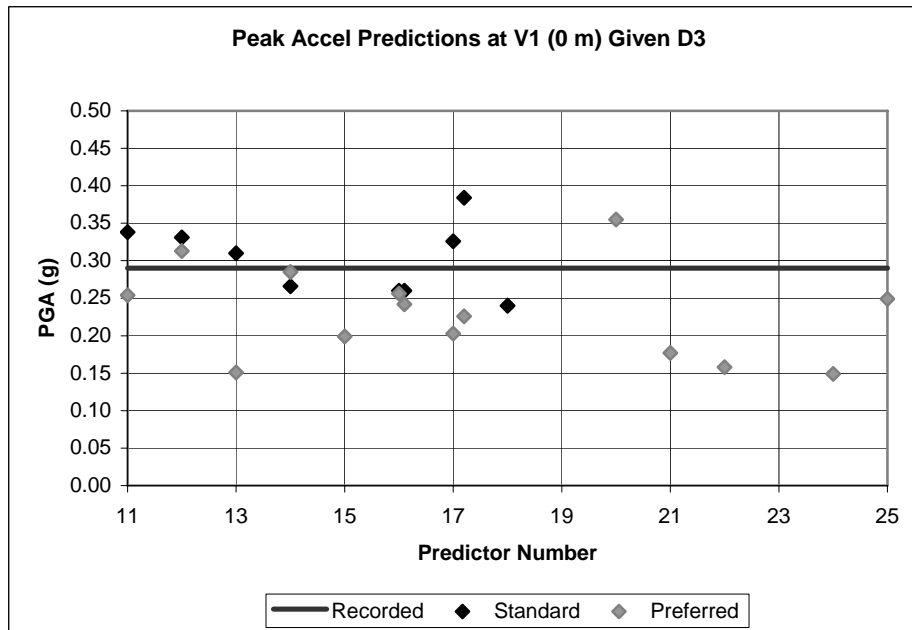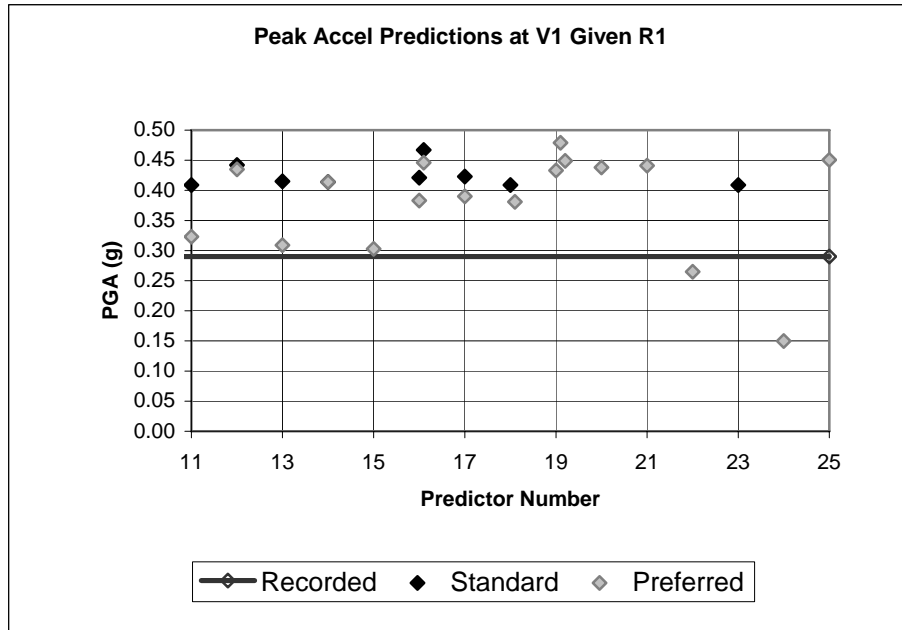
Figure 13. Peak accelerations (EW), observed and predicted, at valley center, V1. Upper: Peak acceleration predictions given the valley-edge record, R1. Lower: Peak acceleration predictions given the record from the rock under the sediments, D3. Predictions were made based on the Standard soil model (black) and Preferred soil models (gray).
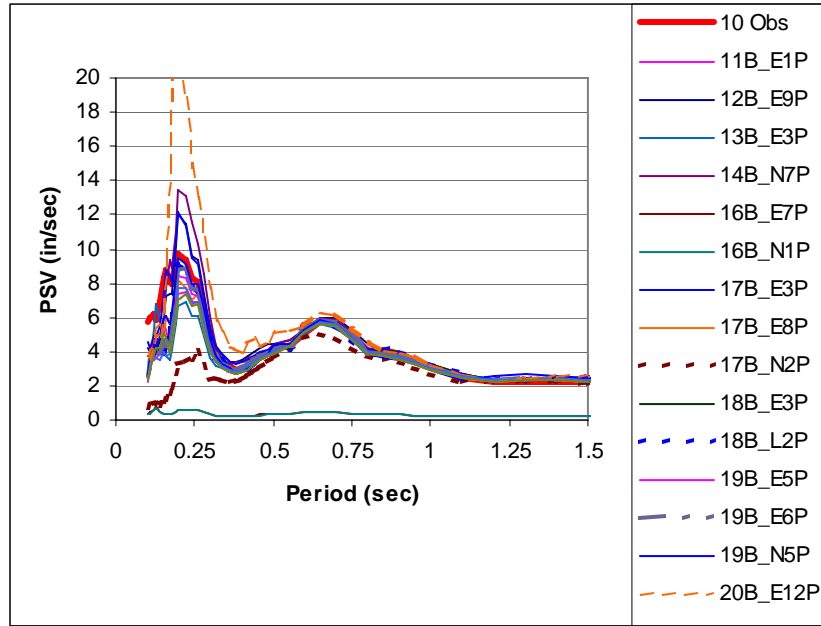
Figure 14. Predicted response spectra (5% damping), given the D3 record, compared to the observed spectra (EW component). Around 0.25 second the observed spectra (at about 9 in/sec) is above most of the predicted spectra (7 to 9 in/sec), but in general the predicted spectra are close to the observed, with some outliers.

Summary

As a result of preparations made two decades ago, continued careful maintenance of the deployed array and the occurrence of the 2004 Parkfield earthquake, an important blind prediction experiment was possible. Fifteen teams participated in the blind prediction; the other key element of the experiment, and in so doing made an important contribution to the community and to the advancement of the science and practice. Analyses of the experiment results have only begun and important advances should result.

Some preliminary assessments can be made. The use of Preferred soil models by the predictors yielded, in general, only limited improvement over the results for the Standard model. The predictions were much more similar to each other than to the observations. The use of nonlinear versus equivalent linear computational methods did not yield dramatic differences for this motion at this site. An experiment with stronger shaking, and/or a softer soil site, may be necessary for the benefit of nonlinear methods to be observed.

The results for the Phase 1 predictions (based on the rock record at the valley edge) showed over prediction of peak accelerations around 50% and of peak response spectra by as much as 3 - 5 times the observed.

The results of the Phase 2 predictions (based on the rock record at the base of the valley sediments) are much closer to the observations. The results show over and under prediction of the peak acceleration and the spectra. The spectra beyond about 0.4 second (frequencies below

2.5 Hz) cluster around each other and the observed spectra well. An important conclusion is that the present ability to predict the motion traveling up through a sedimentary layering is much better than the ability to predict the same motion using an observed surface rock record from about 800 m away, in the Turkey Flat environment.

Data Access

All of the data discussed here is available through the California Integrated Seismic Network's (CISN) Engineering Data Center (EDC), a joint effort of the CGS California Strong Motion Instrumentation Program and the USGS National Strong Motion Program, at http://www.cisn-edc.org. Both the processed and raw data are available for download.

Acknowledgements

The success of a blind experiment like this depends on several key elements. With the initial impetus of B. Tucker in 1986, the Strong Motion Instrumentation Advisory Committee reviewed and recommended the deployment of an array in 1987. Key individuals included C. Stepp, L. Crandall, M. Power, N. Donovan, I. Idriss and W. Joyner. Current members of SMIAC or its subcommittees, including W. Iwan, M. Lew, G. Martin, B. Chiou, B. Tsai, Y. Borzorgnia and A. Abghari, none of whom were involved in any of the prediction teams, helped plan the prediction workshop. Geotechnical properties of the site were measured in the 1980s by Crandall & Assoc., Dames and Moore, Geomatrix, Woodward Clyde, Oyo Corp. and others. Drilling was provided by Pitcher Drilling. W. Thomson of CSMIP maintained the array for the last 10 years, originally installed by C. Petersen and others. The success of the experiment was crucially dependent on the efforts of the predictor teams, whose involvement was critical to real benefit being obtained from the experiment, and the geotechnical community is indebted to their public-spirited participation in the experiment.

References

Harris, R.A. and J.R. Arrowsmith (2006). Introduction to the special issue on the 2004 Parkfield earthquake and the Parkfield earthquake prediction experiment, *Bulletin of the Seismological Society of America* **96**, no. 4B, S1-S10.

Real, C., A. Shakal and B. Tucker (2006a). Turkey Flat, USA site effects test area: Anatomy of a blind ground-motion prediction test, Third Inter. Symp. On Effects of Surface Geology on Seismic Motion, Grenoble, Paper KN3.

Real, C., A. Shakal and B. Tucker (2006b). Overview of the Turkey Flat ground motion prediction experiment, *Proc. SMIP06 Seminar on Utilization of Strong-Motion Data*, p. 117-136, Oakland, California.

Shakal, A., H. Haddadi, V. Graizer, K. Lin and M. Huang (2006a). Some key features of the strong-motion data from the M6.0 Parkfield, California, earthquake of 28 September 2004, *Bulletin of the Seismological Society of America* **96**, no. 4B, S90-S118.

Shakal, A., H. Haddadi and M. Huang (2006b). Note on the very high-acceleration Fault Zone 16 record from the 2004 Parkfield earthquake, *Bulletin of the Seismological Society of America* **96**, no. 4B, S119-S142.

Tucker, B. and C. Real (1986). Turkey Flat, USA Site Effects Test Area – Report 1: Needs, Goals and Objectives, TR 86-1, California Department of Conservation, Division of Mines and Geology.